Thèse de Laura Geoffroy, Université de Lille, 2020

PhD THESIS

DESIGN OF NEW FIRE PROTECTIVE MULTI-MATERIALS

Submitted to and defended at

University of Lille

Doctoral School for Materials, Radiation and Environmental Sciences

Materials and Transformations Unit (UMET), UMR CNRS 8207, ENSCL

For the degree of

DOCTOR OF PHILOSOPHY

in Condensed Matter and Molecules

Specialty: Materials chemistry

by **Laura GEOFFROY**

Graduate Engineer in materials chemistry at École Nationale Supérieure de Chimie de Lille

Master of Science in Engineering Polymer Systems at University of Lille

PhD thesis supervised by

Prof. Serge BOURBIGOT and Prof. Maude JIMENEZ

To be defended on the 24th of September 2020 before an Examination Committee comprised of:

Prof. Yves GROHENS	University of Bretagne Sud, France	President
Prof. Laurent FERRY	IMT Mines d'Alès, France	Reviewer
Prof. Andrea TOLDY	Budapest University of Technology and Economics, Hungary	Reviewer
Ms. Cornaline HUMBERT	Safran Composites, France	Guest
Dr. Fabienne SAMYN	Centrale Lille Institute, France	Examiner
Prof. Serge BOURBIGOT	Centrale Lille Institute, France	Thesis Supervisor
Prof. Maude JIMENEZ	University of Lille, France	Thesis co-supervisor

© 2020 Tous droits réservés.

lilliad.univ-lille.fr

© 2020 Tous droits réservés.

lilliad.univ-lille.fr

Thèse de Laura Geoffroy, Université de Lille, 2020

THESE DE DOCTORAT

NOUVEAUX MULTI-MATERIAUX DE PROTECTION CONTRE LE FEU

Présentée et soutenue publiquement à

l'Université de Lille

École Doctorale Sciences de la Matière, du Rayonnement et de l'Environnement

Unité Matériaux Et Transformation (UMET), UMR CNRS 8207, ENSCL

Pour le grade de

DOCTEUR

en Molécules et Matières Condensée

Spécialité : Chimie des matériaux

Par **Laura GEOFFROY**

Ingénieure diplômée de l'École Nationale Supérieure de Chimie de Lille

Master en Ingénierie des Systèmes Polymères de l'Université de Lille

Thèse dirigée par

Prof. Serge BOURBIGOT et Prof. Maude JIMENEZ

Soutenance prévue le 24 Septembre 2020 devant la Commission d'Examen composée de :

Prof. Yves GROHENS	Université de Bretagne Sud, France	Président
Prof. Laurent FERRY	IMT Mines d'Alès, France	Rapporteur
Prof. Andrea TOLDY	Université de Technologie et d'Économie de Budapest, Hongrie	Rapporteur
Mme. Cornaline HUMBERT	Safran Composites, France	Invitée
Dr. Fabienne SAMYN	Institut Centrale Lille, France	Examinatrice
Prof. Serge BOURBIGOT	Institut Centrale Lille, France	Directeur de thèse
Prof. Maude JIMENEZ	Université de Lille, France	Co-directrice de thèse

© 2020 Tous droits réservés.

lilliad.univ-lille.fr

© 2020 Tous droits réservés.

lilliad.univ-lille.fr

Acknowledgement

Au terme de ce travail de recherche et belle aventure de trois ans, je souhaite avant tout remercier Professeur Patrice Woisel directeur du laboratoire Unité Matériaux Et Transformations (UMET) et Professeur Serge Bourbigot responsable de l'équipe Ingénierie des Systèmes Polymères pour m'avoir donné l'opportunité de rejoindre le laboratoire pour y effectuer mes travaux de recherche.

Je tiens également à exprimer ma gratitude envers mes encadrants Professeur Serge Bourbigot, Professeur Maude Jimenez et Docteur Fabienne Samyn, qui m'ont donné l'occasion de travailler avec eux sur ce projet de recherche. Je vous remercie pour votre soutien scientifique et moral précieux, pour l'ensemble de vos conseils, votre confiance et l'autonomie que vous m'avez laissée tout au long de ce projet. J'ai beaucoup appris et ce fut un réel plaisir de travailler auprès de vous.

I am very grateful to Professor Laurent Ferry, Professor Andrea Toldy, Professor Yves Grohens and Cornaline Humbert who accepted to take their time to review this manuscript and be part of the jury.

Je souhaite également remercier l'« European Research Council » ERC pour le financement du projet FIREBAR concept (ERC Advanced Grant Agreement no. 670747) dans laquelle ma thèse s'est inscrite, ainsi que tous les membres du projet pour leurs contributions et leurs retours durant nos réunions mensuelles : Gaëlle, Gizem, Pauline, Kay, Johan, Tatenda, Adi, Roland et Anne-lise.

Des collaborations ont également permis de mener à bien ce travail de recherche. Par conséquent, je souhaite remercier (i) Séverine Bellayer de l'UMET pour son aide essentielle lors des observations au microscope électronique à balayage (SEM) et à la microsonde électronique (EPMA), (ii) Pascal Roussel, Laurence Burylo et Florent Blanchard de l'Unité de Catalyse et Chimie du Solide (UCCS) pour leur expertise indispensable lors des analyses par diffraction aux rayons X (XRD), (iii) Frédéric Sanchette et Fabrice Parent de l'université de Technologie de Troyes (UTT) pour leur collaboration ayant permis la réalisation des revêtements basse émissivité par dépôt physique en phase vapeur (PVD), (iv) Elodie Richard de la Plateforme d'Imagerie Cellulaire Sciences et Technologies (BIcel) pour son aide technique lors des observations au microscope confocal ainsi que (v) Bertrand Doumert et

© 2020 Tous droits réservés.
lilliad.univ-lille.fr

Bertrand Revel de l'UMET pour leurs conseils lors des analyses spectroscopiques par résonance magnétique nucléaire (NMR).

De plus, je remercie l'ensemble des membres du laboratoire actuels et précédents (Tsilla, Sophie, Mathilde, Guillaume, Fanny, …) et tout particulièrement Pierre, Johan et Benjamin pour leur assistance technique dans la résolution des problèmes pouvant subvenir au laboratoire ainsi que Corinne et Angélique pour leur aide administrative sans failles ayant permis des départs en congrès plus serein.

Une pensée émue envers l'ensemble de mes camarades de thèse présents tout au long de ces trois ans : mon acolyte de thèse Anne-lise, mes collègues de bureau (la bat team) Manon, Charlotte, Tatenda, Adi, Soso, Chi, et les petites dernières Marie et Mariette ainsi qu'à tous les autres Roro, Angeline, Alex, Jérôme, Morgane, Elodie, Solène, Nittaya, Louis, Fei, Maryam, Imane, Yasser, Sana. Merci pour votre soutien, votre bonne humeur et pour tous ces bons moments partagés ensemble.

Je tiens également à remercier l'ensemble de mes amis qui me soutiennent à chaque étape et plus particulièrement Camille V, Marina, Mathilde, Vilayvone, Chloé et Camille T. Merci pour toute votre bienveillance.

Enfin, je tiens à remercier et exprimer ma profonde gratitude envers ceux sans qui tout ça n'aurait pas été possible ma famille : mes grands-parents et surtout ma sœur jumelle, ma mère, NB et NR. Infiniment merci d'être ce que vous êtes.

© 2020 Tous droits réservés.

lilliad.univ-lille.fr

Thèse de Laura Geoffroy, Université de Lille, 2020

Table of content

ACKNOWLEDGEMENT ..... **I**

TABLE OF CONTENT ..... **III**

ABBREVIATIONS ..... **VIII**

GENERAL INTRODUCTION **1**

PART 1: CONTEXT & STRATEGIES **3**

1. FIRE: A REAL ISSUE 5
2. FIREPROOFING SOLUTIONS: ACTIVE AND PASSIVE APPROACHES 6
Active fire protections 6
Passive fire protections 7
3. STRATEGY TO DEVELOP HIGHLY EFFECTIVE FIRE BARRIER 9

PART 2: DESIGN OF FLAME RETARDANT MULTI-MATERIALS **11**

CHAPTER 1: COMPLEX SHAPE AND MULTI-MATERIAL PROCESSING **14**
1. STANDARD POLYMER SHAPING PROCESSES 16
2. ADDITIVE MANUFACTURING 18
2.1. Additive manufacturing techniques 19
2.1.1. Vat photo—polymerization 19
2.1.2. Powder bed 21
2.1.3. Material extrusion 22
2.1.4. Sheet lamination 23
2.1.5. Material and binder jetting 24
2.2. Challenges, research and applications of additive manufacturing process 26
2.2.1. Mechanical properties 27
2.2.2. Flame-retardant 3D printed materials 29
3. CONCLUSION & STRATEGIES OF THIS PART 34
CHAPTER 2: INNOVATIVE 3D PRINTED DESIGN TO CONCEIVE HIGHLY FLAME RETARDANT MULTI-MATERIAL **36**
1. SAMPLES DESCRIPTION 38
2. RESULTS 40
2.1. New design of lighter flame-retardant materials with empty cells 40
2.1.1. Characterizations before fire testing 40
2.1.2. Fire protection performances 42
2.2. Flame retardant biphasic sandwich multi-materials elaboration 47
2.2.1. Characterization before fire testing 47
2.2.2. MLCC fire testing 48

© 2020 Tous droits réservés.

lilliad.univ-lille.fr

Thèse de Laura Geoffroy, Université de Lille, 2020

2.2.3. Mechanism investigation 52
2.2.3.1. Gas phase analysis 52
2.2.3.2. Condensed phase analysis after fire testing 55
3. Discussion 59
4. Conclusion 62
Chapter 3: 3D Printed Sandwich Materials Filled with Hydrogels for Extremely Low Heat Release Rate 64
1. Samples description 66
2. Results 67
2.1. Characterizations before fire test 67
2.2. Fire behavior 70
2.3. Mechanism investigation 74
2.3.1. Clay influence investigation on the fireproofing 74
2.3.1.1. EPMA Observations 74
2.3.1.2. XRD analysis 77
2.3.2. K_2CO_3 influence on fireproofing 80
2.3.2.1. Gas phase mechanism 80
2.3.2.2. Condensed phase mechanism 80
3. General discussion 82
4. Conclusion 85
Chapter 4: Combining low emissivity thin coating and 3D printed original designs for superior fire protective performance 87
1. 3D printed sandwich multi-materials description 88
2. Results 90
2.1. Characterization before fire testing 90
2.2. Fire testing 91
2.3. Mechanism of action 94
3. Conclusions 95
General conclusion & Outlook part 2 97

PART 3: DESIGN OF FIRE RESISTANT MULTI-MATERIALS 99

Chapter 1: Intumescence and Polymer metal laminate as fire proofing layers: State of the art 101
1. Intumescent materials and coatings 102
1.1. Intumescence background 102
1.2. Intumescence process and key factors 102
1.3. Novels ingredients developed for intumescent coatings 104
2. Laminated composites 106
3. Conclusion 109
Chapter 2: Intumescent Polymer Metal Laminate for fire protection 110
1. Samples description 111
2. Results 112
2.1. IPML characterizations before fire test 112
2.2. Fire performances 112
2.3. Expansion measurements 116

© 2020 Tous droits réservés.

lilliad.univ-lille.fr

2.4. Char morphology analysis 117
2.5. Thermal and carbonization gradients 118
3. DISCUSSION 122
4. CONCLUSIONS 124
CHAPTER 3: BI-LAYER INTUMESCENT PAINT METAL LAMINATE: A NOVEL DESIGN FOR A HIGH PERFORMANCE FIRE BARRIER 126
1. SAMPLES DESCRIPTION 127
2. RESULTS 128
2.1. Intumescent bilayer metal laminate characterizations before fire test 128
2.2. Fire behavior 130
2.3. Mechanism investigation 135
3. CONCLUSIONS 139
CHAPTER 4: EXTENSION TO OTHER APPLICATIONS: SUBSTRATE CHANGING 141
1. SAMPLES DESCRIPTION 142
2. RESULTS 143
2.1. Characterizations before fire testing 143
2.2. Fire testing 144
3. CONCLUSION 149
GENERAL CONCLUSION & OUTLOOK PART 3 151

GENERAL CONCLUSION & OUTLOOK 153

PHD COMMUNICATIONS 157

WRITTEN COMMUNICATIONS 157
Peer-reviewed scientific articles 157
ORAL COMMUNICATIONS 157
International congress 157
Seminar 158
Poster 158

MATERIALS & METHODS 159

CHAPTER 1: MATERIALS & METHODS OF PART 2 FOR DESIGNING THE NEW 3D PRINTED FLAME-RETARDANT MULTI-MATERIAL 162
1. MATERIALS 162
2. MATERIAL ELABORATION: EXTRUSION PROCESS 163
3. SHAPING PROCESSES 164
3.1. Thermocompression 164
3.2. Additive manufacturing / 3D printing 164
4. SAMPLE PROCESSING 166
4.1. Biphasic sandwich multi-materials elaboration process 167
4.2. Hydrogel and sandwich multi-materials elaboration process 167
4.2.1. Reference hydrogels 167
4.2.2. Hydrogels containing vermiculite and vermiculite/K_2CO_3 168
4.3. Low emissivity coating deposition 169

© 2020 Tous droits réservés.
lilliad.univ-lille.fr

Thèse de Laura Geoffroy, Université de Lille, 2020

5. FIRE TESTING 170
5.1. Mass Loss Cone Calorimeter 170
5.2. Temperature versus time measurement 171
5.3. Gas phase analysis 171
5.4. Soot picking in the flame 172
6. CHARACTERIZATIONS 172
6.1. Weight, thickness and apparent density measurements 172
6.2. Optical microscopy 172
6.3. Confocal microscopy 173
6.4. Electron Probe Micro-Analysis 173
6.5. Scanning Electron Microscopy 174
6.5.1. Scanning Electron Microscopy for observation 174
6.5.2. Scanning Electron Microscopy for EDS analysis and X-ray mappings 174
6.6. X-Ray Diffraction and/or High Temperature X-ray Diffraction 174
6.7. Thermal conductivity measurements 175
6.8. Emissivity measurements 175
CHAPTER 2: MATERIALS & METHODS OF PART 3 FOR DESIGNING THE NEW INTUMESCENT METAL LAMINATE FIRE BARRIER 176
1. PROCESSING OF SAMPLES 176
1.1. Materials 176
1.2. Intumescent Polymer Metal Laminate (IPML) samples elaboration 177
1.3. Bilayer Metal Laminate samples elaboration 177
2. FIRE TESTING 179
2.1. Burn-Through test 179
2.2. Temperature versus time measurements 180
2.2.1. For steel plate as substrate 180
2.2.2. For composite plate as substrate 180
2.3. Thermal gradient measurement 180
3. CHARACTERIZATIONS 181
3.1. Mass loss measurements 181
3.2. Expansion measurements 181
3.3. Optical microscopy 181
3.4. Scanning Electron Microscopy observations 182
3.5. Thermal analyses 182
3.6. Pull-off test 182

APPENDIX 183

APPENDIX 1 – PART 2, CHAPTER 1 183
1. PLASTIC EXTRUSION 183
2. INJECTION MOLDING 183
3. BLOW MOLDING 184
4. THERMOFORMING AND COMPRESSION MOLDING 185
5. ROTATIONAL MOLDING 186
APPENDIX 2 – PART 2, CHAPTER 1 188
1. SAMPLES DESCRIPTION 189

© 2020 Tous droits réservés.

lilliad.univ-lille.fr

2. RESULTS 190
2.1. Thermocompressed and 3D-materials before fire testing 190
2.2. Morphological analysis before fire test 191
2.2.1. Surface characterizations 191
2.2.2. Cross-section analyses 192
2.3. Fire behavior 194
3. CONCLUSION 199
APPENDIX – APPENDIX 1 200
APPENDIX 3 – PART 2, CHAPTER 3 201
APPENDIX 4 – PART 3, CHAPTER 2 205
APPENDIX 5 – PART 3, CHAPTER 3 206
APPENDIX 6 – PART 3, CHAPTER 4 208

REFERENCES 209

LIST OF FIGURES 227

LIST OF TABLES 235

ABSTRACT 237

© 2020 Tous droits réservés.
lilliad.univ-lille.fr

Abbreviations

A	
ABS	Acrylonitrile Butadiene Styrene
Al	Aluminum
Al_2O_3	Alumina
APP	Ammonium PolyPhosphate
ARALL	Aramid Reinforced Aluminum Laminate
ASTM	American Society for Testing Materials
ATH	Aluminum TriHydroxide
C	
C	Carbon
C-30B	Cloisite-30B
$CaCl_2$	Calcium chloride
CAD	Computer Aide of Design
CARALL	Carbon Reinforced Aluminum Laminate
CLIP	Continuous Liquid Interface Production
CO	Carbone Monoxide
CO_2	Carbon dioxide
Co_3O_4	Cobalt tetraoxide
CoO	Cobalt Oxide
Cr	Chromium
Cu	Copper
D	
DLP	Digital Light Processing
DMLS	Direct Metal Laser Sintering
DOD	Drop On Demand
E	
E	Expansion
EBM	Electron Beam Melting
EDS	Energy-Dispersive X-ray Spectroscopy
EG	Expandable Graphite

© 2020 Tous droits réservés.

lilliad.univ-lille.fr

EPMA	Electron Probe Micro-Analyzer
ERC	European Research Council
EU	European Union
EVA	Etylene VinylAcetate
F	
FAR	Federal Aviation Regulations
FDM	Fused Deposition Modeling
Fe	Iron
FeO	Iron oxide
FFF	Fused Filament Fabrication
FML	Fiber Metal Laminate
FR	Flame-retardants
FTT	Fire Testing Technology
FTIR	Fourier Transform Infrared
G	
GLARE	Glass Laminate Aluminum Reinforced Epoxy
H	
H_2O	Water
HO	Hydroxide
HRR	Heat Release Rate
I	
IPML	Intumescent Polymer Metal Laminate
IR	Infrared
ISO	International Organization for Standardization
ITO	Indium Tin Oxide
K	
K	Potassium
KBr	Potassium Bromide
K_2CO_3	Potassium carbonate
$KHCO_3$	Potassium hydrogencarbonate
KOH	Potassium hydroxide
L	
LENS	Laser Engineered Net Shaping
LIF	Lithium Fluoride

© 2020 Tous droits réservés.
lilliad.univ-lille.fr

LOM	Laminated Object Manufacturing
M	
M	Mass Loss
MAHRR	Mean Average Heat Release Rate
Mg	Magnesium
MLCC	Mass Loss Cone Calorimeter
MMT	Montmorillonite
Mo	Molybdenum
MPP	Melamine PolyPhosphate
N	
Na_2CO_3	Sodium carbonate
Ni	Nickel
O	
OMMT	Organic Montmorillonite
O_2	Oxygen
P	
PA	PolyAmide
PAM	Polymer Additive Manufacturing
PC2	multilayer of Ni/C
PEEK	Polyether ether ketone
PEI	Polyethylenimine
PET	Pentaerythritol
pH	Potential for Hydrogen or Power of Hydrogen
pHRR	Peak of Heat Release Rate
PLA	PolyActic Acid
PMMA	Poly(Methyl MethAcrylate)
PML	Polymer Metal Laminate
PPDA	Poly(phenylphosphoryl phenylenediamine)
PVA	PolyVinyl Acetate
PVD	Physical Vapor Deposition
PVDF	PolyVinyliDene Fluoride
S	
S	Steel
SDL	Selective Deposition Lamination

© 2020 Tous droits réservés.

lilliad.univ-lille.fr

SEM	Scanning Electron Microscope
SFPE	Society of Fire Protection Engineers
Si	Silicium
SiC	Silicon Carbide
SiO_2	Silicon Dioxide
SLA	Stereolithography
SLM	Selective Laser Melting
SLS	Selective Laser Sintering
T	
T	Temperature
TAP	Thallium Acid Phtalate
TC	ThermoCouple
TGA	ThermoGravimetric Analysis
THR	Total of Heat Release Rate
Ti	Titanium
TiO_2	Titanium oxide
TPP	Two Photon Polymerization
TTI	Time To Ignition
U	
UL	Flammability standard
ULTEM	high-performance polyetherimide
US	United States
UV	UltraViolet
V	
VMT	Vermiculite
VO_2	Vanadium dioxide
X	
$X^{\bullet}$	Halogenate radical
XRD	X-Ray Diffraction
Other	
3D	Three-dimensional

© 2020 Tous droits réservés.
lilliad.univ-lille.fr

© 2020 Tous droits réservés.

lilliad.univ-lille.fr

General introduction

The development of science and technology provides the availability of advanced products but concurrently increases the use of flammable materials, in particular organic materials. Indeed, polymeric materials (plastics) have been increasingly used as alternatives to traditional materials such as wood or metals in various applications, especially due to their benefits (their versatility[1], [2], their lightness [1], and the numerous possibilities offered in terms of processability and design such as solids, foams, fibers or film [2]). However, most of polymeric materials in their virgin form are highly flammable upon heating [3]–[10]. This can cause severe material damage as well as human casualties and deaths. As a result, the development of safe and effective flame retardants materials must be a priority. In case of fire, people must be protected by materials confining fire and forming fire barriers. The design of smart fire barriers triggering at the right time, at the right location and responding accordingly to the type of fire exposure is consequently of prime importance. The European project FireBar-Concept (2014–2020 ERC Advanced Grant Agreement no. 670747) is dedicated to the development of such smart barriers [11]. This project is multidisciplinary and is divided into 5 actions: (i) fundamental numerical and experimental approaches to conceptualize fire barrier, (ii) synthesis and design of conceptualized flame retardants, (iii) smart measurements at reduced scale mimicking fire scenarios, (iv) multi-materials and combination of concepts, (v) thin coatings for fire protection. As a consequence, these actions gather:

- modeling and numerical simulation,
- design and development of concepts (flame retardants, and multi-materials),
- development of experimental protocols at reduced scale.

This PhD work is in the frame of this project, and concerns especially the action (iv). **The objective of this work is to design new fire protective multi-materials to achieve low flammability and limit fire spread. To manage this, an original approach is considered: instead of changing the formulation of materials as it is usually done, the modification of the design/assembly and the combination of materials and concepts are investigated to conceive innovative multi-materials. Moreover, in order to have a fire protection in various fire scenarios, two concepts have been elaborated to improve the flame retardancy**

© 2020 Tous droits réservés.
lilliad.univ-lille.fr

Thèse de Laura Geoffroy, Université de Lille, 2020

(i.e. delay or suppress the materials ignition and reduce its rate of combustion) and the flame resistance (i.e. give a protection from fire for a period of time), respectively.

To report the strategy and results obtained in the present work, the manuscript has been divided into three main parts. The first part deals with the context and some scientific backgrounds regarding the thermal decomposition and combustion of materials, as well as the ways to fire protect them. The strategies and approaches considered in this work are also described.

The second part, divided into four chapters, describes the conception of a novel fire retardant multi-material using 3D printing process, which allows to design freely a material with a given shape. Scientific backgrounds including standard polymer processing and an overview of additive manufacturing techniques is first detailed. The objective of other chapters is to conceive an original 3D printed multi-material, with an innovative design and combining various phases to reach the lowest reaction to fire as possible. The fire behavior was assessed using mass loss cone calorimetry and full characterizations were undertaken to elucidate the fire protective mechanism.

The third part, organized in four chapters, deals with the second concept which aims at elaborating a new solution to fire protect a substrate. As in the first part, scientific background on intumescent coatings and metal laminated structure were firstly reviewed. This concept, inspired from laminated structures, and combined different materials (thin metallic layers and intumescent paints) with different designs and assemblies were described, characterized and optimized in other chapters. The fire protective performances were evaluated by impacting a flame at a severe heat fluxes (e.g. burn through test). In all the cases, fire protective mechanisms were investigated using various characterization techniques.

Finally, a general conclusion pertaining to the work is provided and perspectives for further work concerning this study are proposed.

© 2020 Tous droits réservés.

lilliad.univ-lille.fr

Part 1: Context & Strategies

The objective of this part is to present the scientific background of the project that led to the scientific approach and experimental strategy of this PhD thesis (Figure 1).

This part is divided into 3 sections. The fire behavior of polymeric materials is firstly and briefly explained from literature. Then, the current fireproofing solutions are discussed. Finally, the strategies and scientific approach considered are fully detailed.

Figure 1. Scientific approach and strategies.

© 2020 Tous droits réservés.
lilliad.univ-lille.fr

Table of Content part 1

PART 1: CONTEXT & STRATEGIES **3**

1. FIRE: A REAL ISSUE 5
2. FIREPROOFING SOLUTIONS: ACTIVE AND PASSIVE APPROACHES 6

Active fire protections 6
Passive fire protections 7

3. STRATEGY TO DEVELOP HIGHLY EFFECTIVE FIRE BARRIER 9

© 2020 Tous droits réservés.
lilliad.univ-lille.fr

1. Fire: a real issue

Damage and injuries from fire lead to enormous loss of life and property worldwide each year. Between 2012 and 2016, over 17.5 million fires were reported around the world, leading to 220,000 fatalities and nearly 350,000 injuries [12]. The dangers of fires to lives, planet and historical buildings have been cruelly illustrated by for example the Grenfell Tower catastrophe in London in 2017 [13], the tragic Amazon rainforest wildfires in 2019, which have seen large areas of the Amazon rainforest go up in smoke, particularly in Bolivia, Venezuela and Colombia [14], and the fire at Notre-Dame Cathedral in Paris in 2019 [15].

Fire results from the thermal decomposition and combustion processes of flammable materials, as for example polymeric materials [3]–[10]. Indeed, despite their widespread use, polymers still have some major drawbacks such as environmental degradation (e.g. under UV light), hydrolysis due to water in air, mechanical erosion and high flammability [3]–[10]. To get fire to occur, the contribution of four key parameters is required: fuel, oxygen, heat and a chain reaction (Figure 2) [5]–[10], [16]. When a polymeric material is exposed to an amount of heat high enough, thermal decomposition occurs resulting in chemical bounds breaking (homolytic or heterolytic) and volatile gases (radicals, ions) release [17]. Four chemical bounds breaking processes can take place, depending on the materials: i) Random chain scission on the polymer backbone; ii) End chain scission, in which individual monomer units are stripped successively at chain ends; iii) Chain-stripping, whereby individual atoms or groups which are not part of the backbone of the polymer are cleaved; iv) Cross-linking, in which covalent bonds are created between polymer chains. The volatile gases produced act as fuel when they come in contact with sufficient oxygen from the air, causing them to ignite in the presence of an ignition source like a faulty electrical appliance (Figure 2). This endothermic reaction corresponds to the thermal decomposition in the condensed phase. Then, a transition occurs and the endothermic reaction is followed by an exothermic reaction, which corresponds to combustion in the gas phase. This exothermic reaction releases gases (CO, CO_2, …), soot, smoke and heat, degrading further the material, and leading to the fire propagation through a chain reaction (Figure 2) [5]–[10].

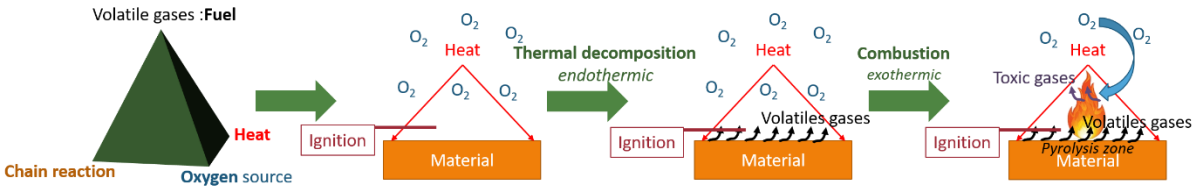

Figure 2. Illustration of thermal decomposition and combustion of flammable materials.

© 2020 Tous droits réservés.

2. Fireproofing solutions: active and passive approaches

To fight or prevent fire, it is necessary to remove one of the four contributors. As a consequence, fireproofing solutions are developed and classified into two main categories: active and passive fireproofing solutions (Figure 3) [18]. It is essential that both systems properly and simultaneously work in the event of a fire.

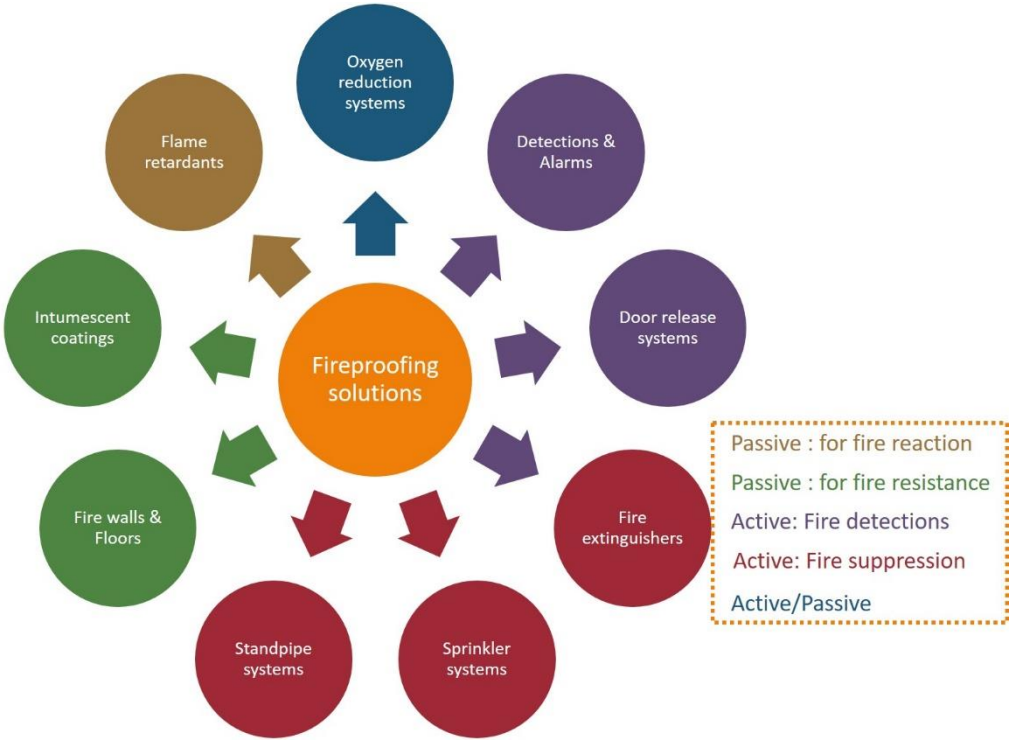

Figure 3. Active and passive fireproofing solutions.

Active fire protections

The role of active fire protection within the fire containment process is to detect, alert about, and seek for eliminating the fire hazard. These active solutions are typically divided into two categories:

(i) fire detectors (Figure 3), which act as a signal to warn that a fire has broken out. Common fire detection solutions include smoke alarms, to bring attention to a fire, and door release systems, to ensure individuals within fire-threatened premises are able to evacuate them safely [18], [19].

(ii) fire suppressors (Figure 3), which ensure that fire is extinguished quickly and efficiently. Fire suppression measures include fire extinguishers, automatic or manual sprinkler systems, standpipe systems, preventive foam or even a non-toxic gaseous agent which acts upon and extinguishes the flames [18], [19].

© 2020 Tous droits réservés.
lilliad.univ-lille.fr

Another additional active fireproofing solution, which cannot be considered to fit within either of these categories, is oxygen reduction (Figure 3). Oxygen reduction systems are hypoxic air systems, and are usually put into place as a preventive measure, rather than to detect or suppress a fire. These new systems operate by reducing the oxygen levels within a certain space where a fire hazard is suspected, thus preventing ignition [20]. As a consequence, the fire can be inhibited ahead of time, rather than dealt with when it is already too late.

Passive fire protections

In addition to these active solutions, passive fireproofing solutions can reinforce fire protection. Their purpose is to maximize the time available to evacuate by restricting the growth and spread of fire [18]. Such protection is either provided by the materials from which the building is constructed, or is added to the building to protect a material and enhance its fire protection. Passive fire protections do not require to be activated in the same way as active protection, which needs to be triggered manually or automatically in order to have an effect against fire. These passive fire protections can be divided into two categories (Figure 3), which depend on the fire testing considered: those for lowering the fire reaction(1) and those for improving the fire resistance.

These different solutions are described hereafter.

On one hand, the resistance to fire assesses a material or system ability to withstand and prevent the penetration of fire through the system (defined according to the ISO 13943:2088) [9], [21], [22]. It also gives information on the temperature rise between the exposed and unexposed sides in a fully developed fire situation. Fire resistance tests consist in putting materials into contact with fire, such as for example in big furnaces (ISO834 and UL1709) or burn-through test (according to two aeronautical certification fire tests ISO2685:1998(E) and FAR25.856(b):2003 and fully described in materials & methods part (page 179)). Some of

(1) It is important to notice that passive fire protections are traditionally considered for fire resistance. However, flame retardants act on material's behavior upon heating (i.e. in the case of fire reaction) and prevent the spread of fire or delay its ignition without manually or automatically activation as for active fire protection. As a consequence, it makes sense to consider that flame retardants offer one way of providing passive fire protection (confirmed by the Society of Fire Protection Engineers (SFPE) [274]) and thus distinguish the passive fireproofing solutions for fire resistance and for fire reaction.

© 2020 Tous droits réservés.
lilliad.univ-lille.fr

Thèse de Laura Geoffroy, Université de Lille, 2020

existing fire resistant passive protections, often used to protect a substrate, are gathered in Table 1.

Table 1. Examples of fire resistant passive fire protections.

Fire resistant passive protections	Advantages	Drawbacks	Ref
Cementitious coatings	low cost, show great weather exposure resistance, easy to apply on substrate	require high thickness and weight to reach sufficient level of fire protection	[23]
Intumescent coatings	high fire protection with low weight and thickness deposition, easily applied on many substrates for indoor or outdoor applications	Can have ageing issue and be expensive	[24]–[28]
Fibrous materials (boards and blankets of mineral wood and ceramic fibers)	Inorganic binders not burn and decompose at high temperature	absorb water easily, which limits applications	[29], [30]
Composites or fire protective panels	Various types of materials	high thickness and thus high weight needed to reach high insulative properties	[31], [32]

On the other hand, fire reaction is the measurement of how an individual material or system will contribute to the development and spread of a fire, particularly in the very early stages when evacuation is crucial [9], [21], [22]. Specific fire tests can be used to characterize the reaction to fire performances of materials such as flammability tests (UL-94 (ISO1210 standard), Limited Oxygen Index (ISO4589-2 standard)), mass loss cone calorimetry test (according to standard ISO13927 or ASTM E906 and fully described in materials & methods part (page 170)) or Smoke test (as smoke density chamber (Railway (ISO5659) and aeronautical (ASTM E 662) tests), which measures the smoke opacity and gases toxicity).

For the fire reaction passive protections, flame retardants [31]–[34] are usually incorporated in polymeric materials to improve their fire behavior and make them less flammable. These chemicals can be halogenated [35], [36], phosphorous [37]–[39], nitrogenous [40]–[42] and boron [43], [44] compounds, metal oxides and hydrates [45]–[47], silicon additives [48], [49], nanoparticles [50]. These flame-retardants prevent one or more of the key parameters from taking part in combustion: thus limiting flame spread, suppressing the production of toxic smoke [51], limiting the oxygen consumed by the flame or inhibiting the chain reaction of the combustible decomposition products [52]–[55]. There are many ways to flame retard a polymeric material. These include: i) physical methods, whereby flame-retardants are incorporated into a polymer by melt blending, ii) chemical methods, whereby fire retardant

© 2020 Tous droits réservés.

lilliad.univ-lille.fr

groups are added into the structure of the polymeric material as a functionalized part of the polymer, or iii) surface treatment methods, whereby a fire retardant is grafted/added to the surface of the material [16]. Depending on their nature, the flame-retardant mode of action can operate at different stages simultaneously, chemically or/and physically in gas or/and condensed phase [51]–[55]. For example, Table 2 gathers some of existing fire reaction passive protections. These flame retardant additives can be used alone or in combination to obtain synergistic effects.

Table 2. Examples of fire reaction passive fire protections.

Fire reaction passive protections	Action	Mechanism	Ref
Halogenated flame retardants	Chemically in gas phase	Unstable radicals ($HO^{\bullet}$ and $H^{\bullet}$) released from polymer combustion, react with other radicals such as halogenated $X^{\bullet}$ (produced from the thermal degradation of the flame retardant) and create less reactive radicals, which interrupt the combustion chain reaction.	[35], [36]
Metallic oxides	Chemically in gas phase	Act as flame inhibitors, provoking a flame extinguishment and disturbing the combustion reaction, such as halogenated flame retardants.	[35], [45]–[47]
Carbonate	Physically and chemically in gas phase	Mitigation of combustible gases through an endothermic release of non-flammable gases (such as H_2O and CO_2). Fuel is thus diluted and material is thermal stabilized with a flame extinguishment.	[56], [57]
Clay (such as montmorillonite or vermiculite)	Physically in condensed phase	Formation of an insulating, thermally stable barrier, which reduce the fuel amount and the decomposition rate of polymer, and thus disturb the flame propagation.	[58]–[61]
Intumescent additives	Chemically and physically in condensed phase	Additives promote charring of the material and form an expanding carbonaceous protective layer, which reduce the heat and mass transfer from the heat source to the flammable materials.	[24], [58], [62]–[64]

3. Strategy to develop highly effective fire barrier

It was shown previously that many fireproofing solutions (active and passive) exist to improve fire protective performances of materials. However, the need to find more efficient solution is still stimulating researches that are today mainly focused on the development of new flame-retardant additives such as nanoparticles [50], or metal oxides [45]–[47] or improvement of the materials formulation to promote synergism. In this work, done in the framework of the European project FireBar-Concept, an original approach was considered to design new fire protective multi-materials. It consists in **changing the design of materials**, i.e., the materials

© 2020 Tous droits réservés.
lilliad.univ-lille.fr

Thèse de Laura Geoffroy, Université de Lille, 2020

assembly instead of changing the chemistry (as it is usually done), to reach better fireproofing properties. Moreover, it is noteworthy that the combination of various materials usually allows to obtain advanced materials (such as composite or hybrid materials) with special functionality and novel properties [65]–[67]. For example, the incorporation of glass fibers in polymer matrix allows to reinforce the mechanical properties of the material [66]. As a consequence, in addition to changing the design of materials, a **combination of different materials, phases (liquid, solid, gel) and fireproofing concepts** have been investigated to improve the fire protection. Furthermore, in order to attempt these strategies (changing design and combining materials and concepts) in different situations, two fireproofed multi-materials (one acting for lowering fire reaction and another for increasing fire resistance) were elaborated and evaluated under different thermal constraints. In the two next parts, different concepts are considered such as the use of 3D printing process to elaborate new design or the modification of fire barrier design by combining intumescence and delamination phenomena to reach superior fire protection. With these two concepts, purpose is to demonstrate to the scientific community that changing the design and playing with the combination of various materials can be an innovative and effective way to elaborate efficient multi-materials for different fire scenarios.

© 2020 Tous droits réservés.

lilliad.univ-lille.fr

Part 2: Design of flame retardant multi-materials

As described in previous part, the demand for polymeric materials exhibiting low reaction to fire is in constant increase. To elaborate such materials, conventional solutions involve adding fire retardant fillers in the bulk of the polymeric materials for enhancing their fire behavior [68]–[71]. However, the development of new flame retardants remains challenging and sometimes limited in view of the amount of work already undertaken on them. For this reason, in this work, another way of thinking has been considered. It consists in elaborating new materials with improved flame retardancy by modifying the design and combining various materials (and concepts) rather than changing chemistry as it is usually done (Figure 4). Some approaches were already considered, such as skin-core structure or flame retardant gradient in the materials [72]–[74]. But the preparation of sophisticated structures using standard shaping processes is not straightforward. For this reason, in this part, the advantage of the flexibility of additive manufacturing (i.e. 3D printing) as process to prepare and design efficient flame retarded multi-materials was considered.

This part is divided into four chapters. The purpose of the first chapter is to provide an overview of the polymer processes used to develop complex designs, with a particular focus on the 3D printing process. The second chapter focuses on the elaboration of a new 3D printed design and the development of innovative flame-retardant materials by combining liquid and solid phases. The fabrication process of the best biphasic material is optimized in the third chapter. Finally, in the last and fourth chapter, the design is improved to achieve outstanding fire properties. Materials and methods used in this work are described at the end of this manuscript (beginning on page 162), and easily spotted on color papers.

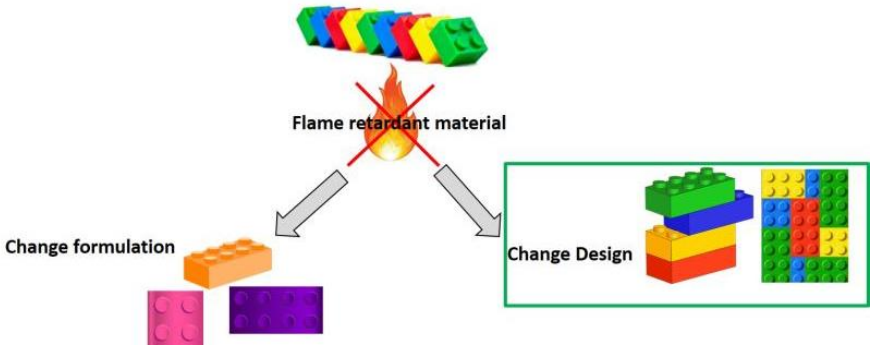

Figure 4. Design of flame retardant material.

© 2020 Tous droits réservés.
lilliad.univ-lille.fr

Thèse de Laura Geoffroy, Université de Lille, 2020

Table of Content part 2

PART 2: DESIGN OF FLAME RETARDANT MULTI-MATERIALS **11**

CHAPTER 1: COMPLEX SHAPE AND MULTI-MATERIAL PROCESSING **14**
1. STANDARD POLYMER SHAPING PROCESSES 16
2. ADDITIVE MANUFACTURING 18
2.1. Additive manufacturing techniques 19
2.1.1. Vat photo—polymerization 19
2.1.2. Powder bed 21
2.1.3. Material extrusion 22
2.1.4. Sheet lamination 23
2.1.5. Material and binder jetting 24
2.2. Challenges, research and applications of additive manufacturing process 26
2.2.1. Mechanical properties 27
2.2.2. Flame-retardant 3D printed materials 29
3. CONCLUSION & STRATEGIES OF THIS PART 34

CHAPTER 2: INNOVATIVE 3D PRINTED DESIGN TO CONCEIVE HIGHLY FLAME RETARDANT MULTI-MATERIAL **36**
1. SAMPLES DESCRIPTION 38
2. RESULTS 40
2.1. New design of lighter flame-retardant materials with empty cells 40
2.1.1. Characterizations before fire testing 40
2.1.2. Fire protection performances 42
2.2. Flame retardant biphasic sandwich multi-materials elaboration 47
2.2.1. Characterization before fire testing 47
2.2.2. MLCC fire testing 48
2.2.3. Mechanism investigation 52
2.2.3.1. Gas phase analysis 52
2.2.3.2. Condensed phase analysis after fire testing 55
3. DISCUSSION 59
4. CONCLUSION 62

CHAPTER 3: 3D PRINTED SANDWICH MATERIALS FILLED WITH HYDROGELS FOR EXTREMELY LOW HEAT RELEASE RATE **64**
1. SAMPLES DESCRIPTION 66
2. RESULTS 67
2.1. Characterizations before fire test 67
2.2. Fire behavior 70
2.3. Mechanism investigation 74
2.3.1. Clay influence investigation on the fireproofing 74
2.3.1.1. EPMA Observations 74
2.3.1.2. XRD analysis 77
2.3.2. K_2CO_3 influence on fireproofing 80
2.3.2.1. Gas phase mechanism 80
2.3.2.2. Condensed phase mechanism 80

© 2020 Tous droits réservés.

lilliad.univ-lille.fr

3. GENERAL DISCUSSION 82
4. CONCLUSION 85
CHAPTER 4: COMBINING LOW EMISSIVITY THIN COATING AND 3D PRINTED ORIGINAL DESIGNS FOR SUPERIOR FIRE PROTECTIVE PERFORMANCE **87**
1. 3D PRINTED SANDWICH MULTI-MATERIALS DESCRIPTION 88
2. RESULTS 90
2.1. Characterization before fire testing 90
2.2. Fire testing 91
2.3. Mechanism of action 94
3. CONCLUSIONS 95
GENERAL CONCLUSION & OUTLOOK PART 2 97

© 2020 Tous droits réservés.
lilliad.univ-lille.fr

Thèse de Laura Geoffroy, Université de Lille, 2020

Chapter 1: Complex shape and multi-material processing

The light weight and functional properties of polymers have made their use constant and in perpetual growth, for example in building, transportation and cable and wire fields [1], [2]. Unfortunately, the high flammability of most of them [3]–[10] threatens human lives as well as infrastructures and fire retardant solutions are therefore an absolute necessity to avoid these materials to contribute to the development and spread of fire [16], [17], [51]–[55].

In this work, an original approach was considered (as detailed in part 1) and consisted in studying the influence of the design and the combination of materials (and concepts) to reach high fire performance. To elaborate sophisticated structures and combine various materials, numerous processes exist, such as injection molding [75], thermocompression [75]–[79], or additive manufacturing [80]–[90]. This latter process has gathered a lot of interest because of its versatility and its capability to create easily original designs. Additive manufacturing has been opening since a few years a wide range of prospects for the creation of innovative materials [85], [89].

In this chapter, an overview of standard polymer processes and of some additive manufacturing techniques is presented to highlight processes available for designing complex (and potentially multi) polymeric materials; this overview concludes by a rapid survey of the use of 3D printing process in the fire protection field (Figure 5).

KEYWORDS: Polymer processing, 3D printing, Flame retardancy

Aims

- ✓ Comparison of some standard polymer processes, including extrusion, injection molding, blow molding, thermoforming, thermocompression and rotational molding.
- ✓ Description of some additive manufacturing techniques.
- ✓ Survey on flame-retardant 3D printed polymers.

© 2020 Tous droits réservés.

lilliad.univ-lille.fr

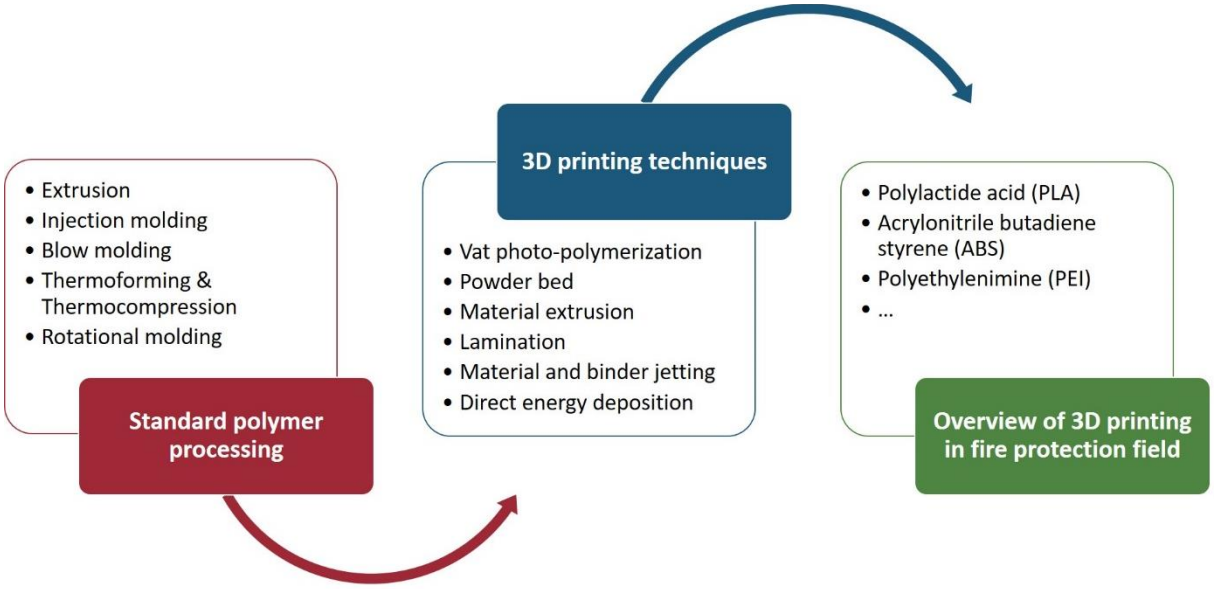

Figure 5. Polymer processing.

© 2020 Tous droits réservés.
lilliad.univ-lille.fr

1. Standard polymer shaping processes

Thermoplastic polymers are usually processed through thermo-mechanical forming methods consisting in three main steps: (i) heating, to soften or melt the solid polymer, (ii) shaping, under a constraint or using a mold, (iii) cooling to retain the shape. The existing polymer forming methods can be classified according to the initial form of the polymer (Figure 6). The selection of a polymer shaping process depends on many factors such as quantity and production rate, form and detail of the product, size of final product and nature of the material [77]. Simple or complex shapes can be made, as well as parts from one or several polymers. Some of them can be used to elaborate multi-materials such as molding with multi-component injection molding as an example. Currently, to elaborate a product with a complex shape, standard polymer shaping processes are used, such as: plastic extrusion, injection molding, blow molding, thermoforming, compression molding and rotational molding. A comparison between these well-known traditional processes (fully described in the literature [75]–[79], [91] and in appendix 1 (page 183)) is detailed in Table 3.

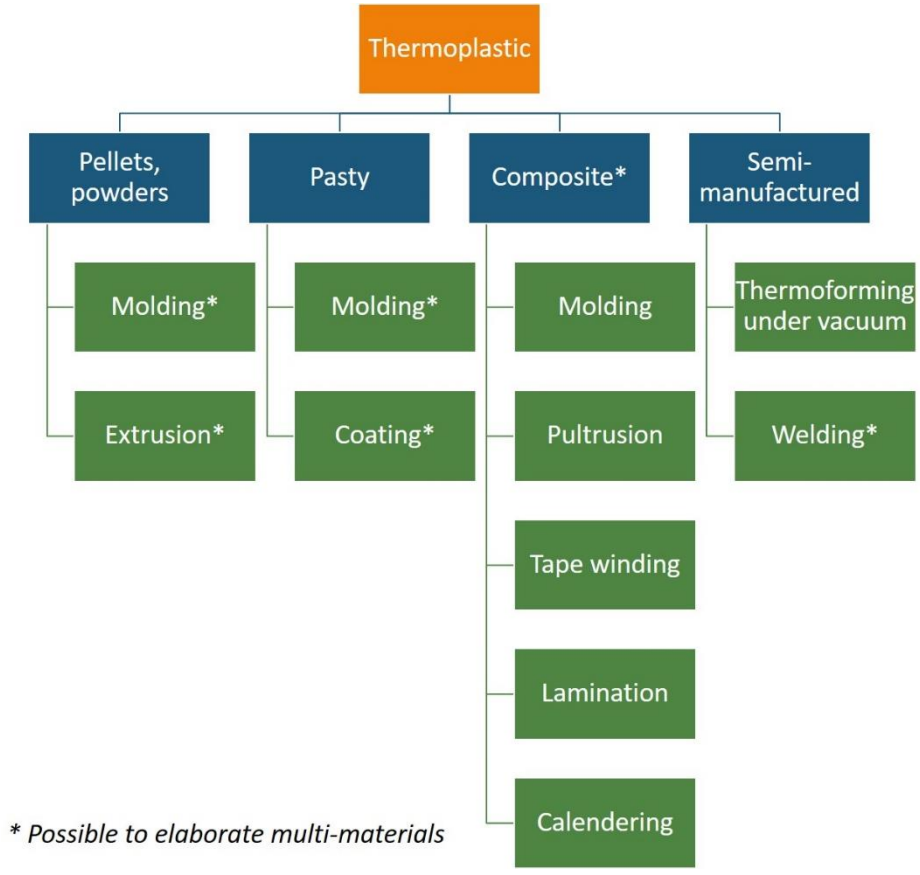

Figure 6. Classification of standard polymer processing.

© 2020 Tous droits réservés.

lilliad.univ-lille.fr

Table 3. Polymer processing comparison [91], [92].

Molding process	Process description	Complex shape	Multi-materials processing	Equipment cost	Tooling cost	Cycle time	Precision	Pros	Cons
Extrusion	Heated plastic is forced through a die creating a part	Yes	Yes: co-extrusion	High	Moderate	Continuous	Good	Short process time	High costs
Injection Molding	Heated plastic is injected into mold	Yes	Yes	High	High	Quick	Good	Short process time and detailed parts	High costs
Blow Molding	A parison (tubular plastic charge) is attached to a mold and then filled with air and cooled to have the desired shape and dimensions	Yes but limited	Yes possible in several steps	High	Moderate	Quick	Moderate	Short process time	Limited geometry
Rotational molding	The polymer is placed into a mold which rotates around both vertical and horizontal axes, while being heated and then cooled	Yes but limited	No	Moderate	Low	Moderate	Moderate	Complex geometries are possible	Slower than high-speed processes
Thermoforming under vacuum	Polymer is softened by heat, flowed by forming by the application of vacuum	No	Yes	Moderate	Low	Moderate	Low	Flexibility in molding structures	Limited geometry
Thermo-compression	Polymer is softened by heat, flowed by forming by the application of pressure	No	Yes	Low	Moderate	Quick	Low	Low cost, can mold large patterns	Limited geometry
Additive manufacturing	Use computer-Aided Design to build objects layer by layer	Yes	Yes	Depending of the techniques	None	Long	Good	Very detailed part, no mold costs, rapid prototyping	Slow process, size limitations

This comparison of standard shaping processes highlights that the design of polymeric materials with a complex shape has some constraints. Indeed, among all of these processes, the use of a complex mold is needed. This leads to an increase in the time required to manufacture the final product and an increase in manufacturing and shipping costs. As a consequence, due to cost constraints, less innovative designs are possible with these processes. Moreover, these standard processes create material wastes. One way to overcome these drawbacks consists in using another process, named additive manufacturing, as this technology builds 3D products without using complex mold. This process is fully described in the next section.

2. Additive manufacturing

First introduced in 1981 by Dr. Hideo Kodama as a "rapid prototyping" technique, additive manufacturing, also named 3D printing, has emerged as a versatile technology [93]. According to ISO/ASTM international standard (ISO/ASTM 52900:2015), additive manufacturing uses Computer-Aided Design (CAD) to build objects layer by layer [94]. This process is divided into three mains steps. The 3D part is first numerically drawn with the right dimension using CAD software (Figure 7 a). Then, the 3D model is sliced in many sections, corresponding to the layers that will be printed (Figure 7 b). Finally, the 3D model sliced is sent to additive manufacturing device software and printed one layer on top of the other to form the finished 3D part (Figure 7 c). Some post-processing can be done like annealing or painting, afterwards (Figure 7 d).

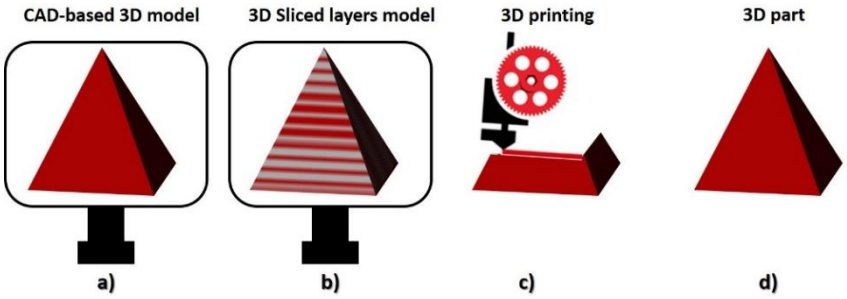

Figure 7. Steps of 3D printing process.

Additive manufacturing process has three main advantages. It allows: (i) to save materials, because the exact amount of needed polymer is used, (ii) to save money, because no tools or molds are required to elaborate sophisticated shapes and (iii) to be flexible to design 3D objects. Due to these advantages, several 3D printing technologies have emerged these last years and were classified in 2009 into seven categories listed in Table 4 according to the ASTM International Committee F42 on additive manufacturing technology [93]. These techniques are

© 2020 Tous droits réservés.

lilliad.univ-lille.fr

further described in the next section, except direct energy deposition technique which is currently only used for metals [83].

Table 4. 3D printing techniques [95].

3D printing technology	Example of 3D printing techniques
Vat photo-polymerization	Stereolithography (SLA), Continuous Liquid Interface Production (CLIP), Digital Light Processing (DLP), Two Photon Polymerization (TPP)
Powder bed	Selective Lase Sintering (SLS), Selective Laser Melting (SLM), Electron Beam melting (EBM), Direct Metal Laser Sintering (DMLS)
Material extrusion	Fused Deposition Modelling (FDM), 3D bio-plotting
Sheet lamination	Laminated Object Manufacturing (LOM), Selective Deposition Lamination (SDL)
Direct energy deposition	Laser Engineered Net Shaping (LENS)
Material jetting	Drop On Demand (DOD), Polyjet
Binder jetting	Indirect Inkjet Printing (Binder 3DP)

2.1. Additive manufacturing techniques

2.1.1. Vat photo—polymerization

Vat photo-polymerization 3D printing techniques use a vat of liquid photopolymer resin and an ultraviolet (UV) light to selectively cure or harden the resin where it is required to form the 3D object layer by layer [80]–[87], [93]. Four main techniques were developed over time. Stereolithography (SLA) is one of the earliest techniques of additive manufacturing, developed in 1986 by Chuck Hull [85] (Figure 8 a). A UV laser is used to trace point by point the predefined numerical model's cross-section in the liquid resin. UV light initiates a chain reaction on a layer of photosensitive resin or photosensitive monomer solution by linking chains of molecules, and forming polymers. Once the trace is completed, the platform is lowered and the part is coated with a new layer of resin. These steps are repeated until the entire three dimensional part is finished. The unreacted resin remains in liquid form and is removed after the completion of printing. Finally, the final 3D part is put in an UV oven to complete the curing process. On the same photo-polymerization principle than SLA, Digital Light processing (DLP) technique was proposed by Pomerantz in 1996 [80] (Figure 8 b). Unlike the SLA technique where a UV laser is used to cure the photosensitive resin, the DLP technique uses a DLP projector (liquid crystal display panel) to project the entire cross-sectional layer of the 3D structure. As a consequence, photosensitive layer resin is cured all at once between each scan

© 2020 Tous droits réservés.
lilliad.univ-lille.fr

compared to point by points. Due to this new curing process, printing time of DLP technique is faster than that of SLA. However, the cured layer obtained by DLP technique has to be mechanically removed from the bottom of the vat containing the resin, followed by resin re-coating before the next scan, i.e. the next layer exposed. To move even faster, another technique similar to DLP was thus developed and named Continuous Liquid Interface Production (CLIP). This continuous 3D printing technique diminishes the additional mechanical movement by the presence of an oxygen-permeable membrane below the resin [80], [81] (Figure 8 c). This membrane creates a persistent liquid interface, preventing a thin layer of resin to cure at the build point. As a consequence, the oxygen membrane prevents the resin adhesion to the vat. The end result is super-fast 3D printing, quicker than any other photo-polymerization based printers. Recently, and to achieve higher resolution, another technique named Two Photon Polymerization (TPP) was developed (Figure 8 d). This technique is fully described in paper [81]. Briefly, it is based on the simultaneous absorption of two photons by a photo-activated monomer. This absorption leads to photochemical or physical reactions and forms a polymer, in a very thin region. Table 5 gathers the advantages and disadvantages of these vat photo-polymerization 3D printing techniques.

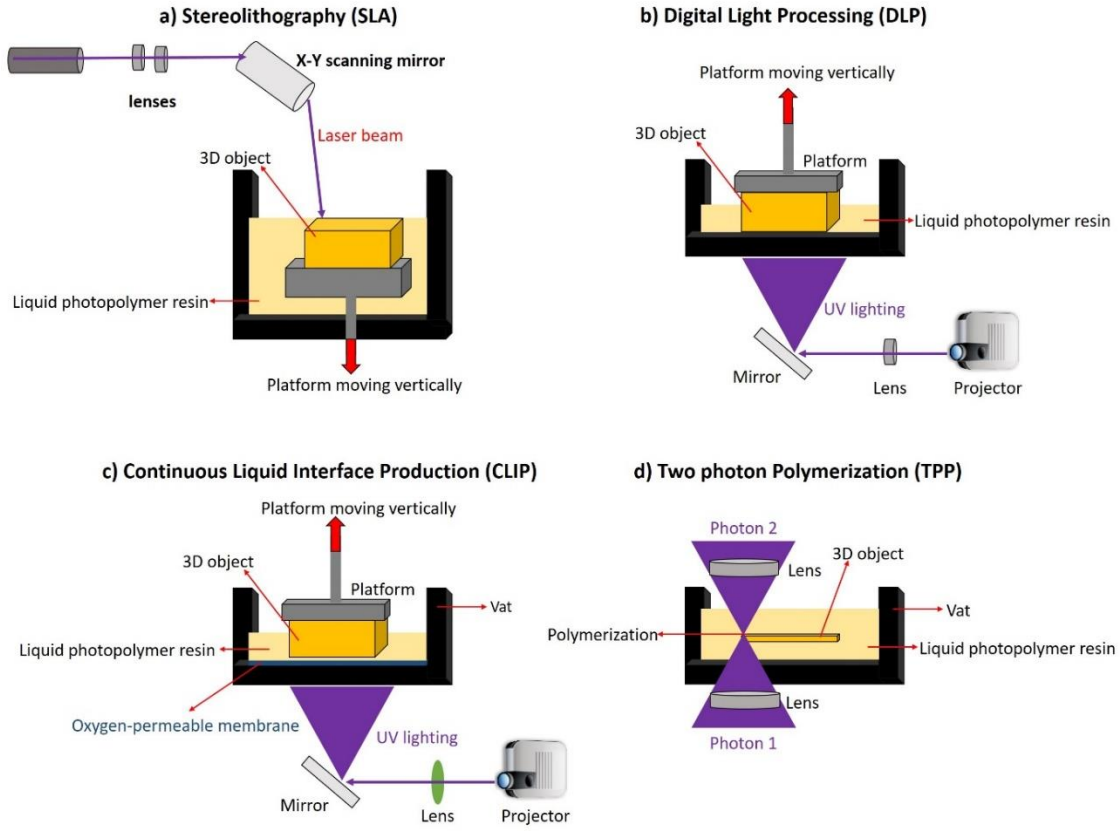

Figure 8. Illustration of vat photo-polymerization 3D printing techniques: a) Stereolithography (SLA), b) Digital Light Processing (DLP), c) Continuous Liquid Interface Production (CLIP), d) Two Photon Polymerization (TPP).

© 2020 Tous droits réservés.

lilliad.univ-lille.fr

Many vat photo-polymerizations techniques exist, but their use requires working with a photosensitive resin or liquid. Therefore, the limited range of materials available has led to new techniques, such as powder bed 3D printing techniques.

2.1.2. Powder bed

In 1988, Selective Laser Sintering (SLS), the first powder bed 3D printing technique, was developed and patented by Carl Deckard [82]. Thermal energy from a laser, which acts as a power source, is used to selectively sinter and bind powdered material (metal or polymer) to create a solid structure (Figure 9 a). To manage this, a thin layer of powder is first spread and packed on a platform. Then, a laser beam is used to sinter a thin layer of powders according to a certain pattern predefined by the numerical 3D model. After that, subsequent layers of powders are rolled on top of previous layers, and sintered as previously. These steps are repeated until the final 3D part is built. Finally, the excess powder is removed using vacuum. This technique could also be used for metals, and is named in that case Direct Metal Laser Sintering (DMLS) [81]. At the end of the 1990s, two other comparable techniques were developed: Selective Laser Melting (SLM) and Electron Beam Melting (EBM). The first one is similar to the SLS technique. Instead of sinter and bind the powder as it is the case in SLS, powder is fully melted in SLM [80], [81], [85]. This difference leads to a modification of properties like crystal structure and porosity (which is less important). Regarding EBM technique, an electron beam source is used instead of a high-powered laser [81], [85] (Figure 9 b). In addition, the electron beam fully melts the metal powder to form the desired object. EBM technique is slower and more expensive than SLM with a high limitation on the available materials. Moreover, the powder size, distribution and packing are of prime importance for these powdered bed 3D printing techniques because they determine the density of the final printed part.

© 2020 Tous droits réservés.
lilliad.univ-lille.fr

Thèse de Laura Geoffroy, Université de Lille, 2020

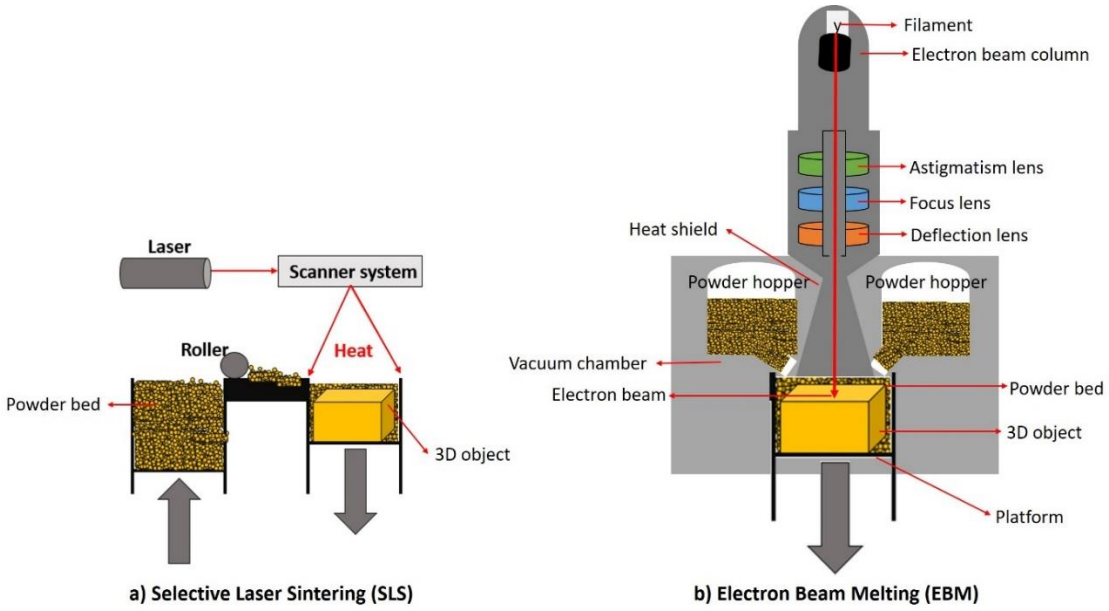

Figure 9. Illustration of powder bed 3D printing techniques: a) Selective Lase Sintering (SLS), b) Electron Beam melting (EBM).

Advantages and disadvantages of powder bed 3D printing techniques are gathered in Table 5. The main advantages of these techniques are their fine resolution and that support is not necessary when a complex geometry is developed, which overcomes difficulties in removing supporting material. Indeed, the powder bed not sintered by the laser acts as a support. However, these techniques are expensive, and can only be used for powdered materials with low melting/sintering temperature.

2.1.3. Material extrusion

In 1989, material extrusion-based 3D printing system appears with Fused Deposition Modelling (FDM) technique, otherwise known as Fused Filament Fabrication (FFF) by Scott Crump [80]. The principle consists in heating and softening a thermoplastic filament through a nozzle to depose it on a substrate or support layer by layer to form the final 3D object (Figure 10 a). Special techniques can be used to create complex structures. For example, the printer can extrude a second material that will serve as support material for the object being formed during the printing process. This support material can later be removed or dissolved. Due to the limited range of filament commercially available, and also to the issue related to the use of filament (filament breaking, diameter restriction, …), a novel technology, capable of printing raw materials from pellets is now on the market [80]–[85]. Polymer pellets are extruded before being deposed as for the FDM technique on a platform (Figure 10 b). This technique has the best quality to cost ratio (Table 5) and highlights its high potential for polymer manufacturing. Paste, solution, hydrogels and dispersions of polymers and blends can also be printed using

© 2020 Tous droits réservés.

lilliad.univ-lille.fr

another extrusion-based printer named 3D bioplotter [88], [93]. This technique dispenses viscous plotting material into a liquid medium with a matching density to form the 3D object.

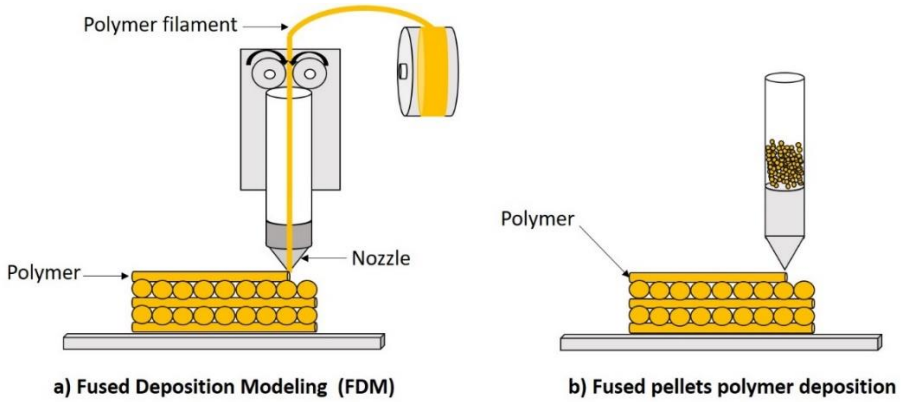

Figure 10. Illustration of material extrusion 3D printing techniques: a) Fused Deposition Modelling (FDM), b) Fused pellets polymer deposition.

2.1.4. Sheet lamination

Laminated 3D printing technology appears with Laminated Object Manufacturing (LOM) method (Figure 11 a). This 3D printing technique consists of superposing and bonding sheet materials together, which are then cut to form an object [81], [85], [93]. The process is divided into four main steps: (i) a sheet is collected and adhered to a substrate with a heated roller, (ii) an adhesive is applied on a sheet, (iii) a laser traces desired dimensions predefined by the numerical model and cross hatches the excess area to facilitate waste removal, (iv) a new sheet is deposed and rolled using the heater roller. These five steps are repeated until full 3D object is prepared. Selective Deposition Laminate (SDL) based on LOM technique is another laminated 3D printing technology (Figure 11 b). SDL differs from LOM notably in the gluing process. Indeed, using SDL, only the parts of the object that prepare the final object are glued, whereas LOM glues the whole sheet uniformly [81]. Advantages and disadvantages of these sheet lamination 3D printing techniques are gathered in Table 5 and can be easily compared with other 3D printing processes.

© 2020 Tous droits réservés.
lilliad.univ-lille.fr

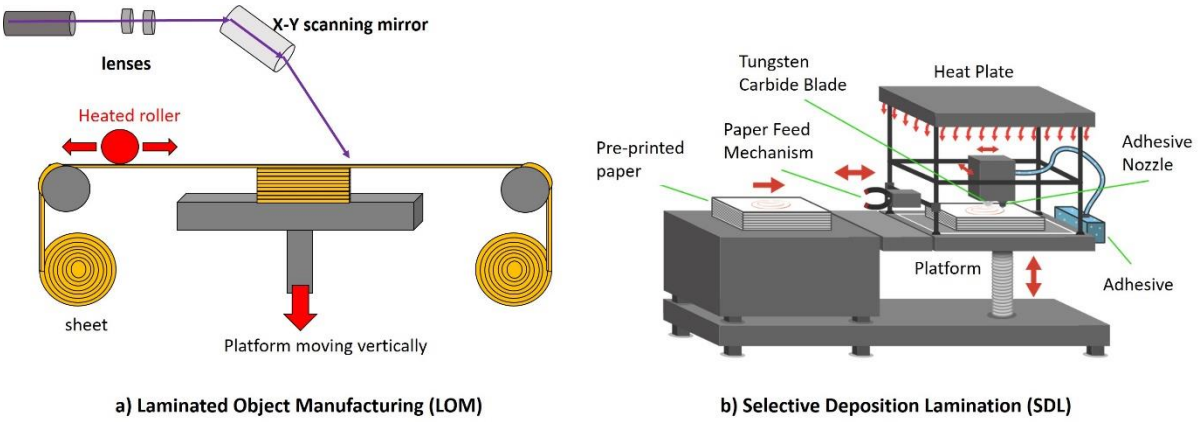

Figure 11. Illustration of lamination 3D printing techniques: a) Laminated Object Manufacturing (LOM), b) Selective Deposition Lamination (SDL) [96].

2.1.5. Material and binder jetting

Material jetting and binder jetting 3D printing techniques are systems based on traditional inkjet-printing. The first one, material jetting technique, consists in depositing droplets to build 3D part. As an example, Drop On Demand (DOD) method uses a photosensitive resin instead of the usual ink, which is cured using a UV light [80], [93] (Figure 12 a). The support moves down between each scan to build the 3D object. PolyJet is a similar technique as DOD except that thousands of photopolymer droplets are jetted simultaneously onto a build platform which significantly improves the printing speed. Other techniques using thermoplastic materials and working as inkjet-printing also fall into this category. Regarding binder jetting technique, a chemical binder, acting as the usual ink in standard inkjet printing, is deposed onto the spread powder to form the solid layer [80], [81], [83], [87], [93] (Figure 12 b). Table 5 gathers the advantages and disadvantages of these material and binder jetting 3D printing techniques, and compared all 3D printing processes with each other.

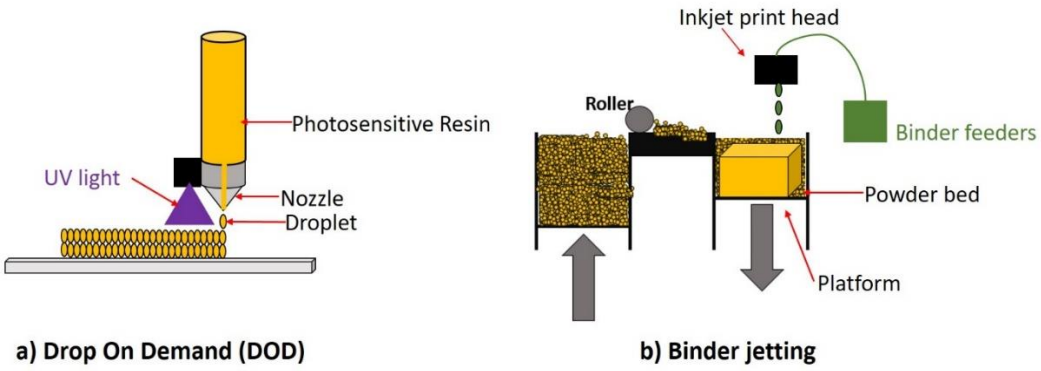

Figure 12. Illustration of material jetting 3D printing techniques a) Drop On Demand, and b) Binder Jetting.

© 2020 Tous droits réservés.

lilliad.univ-lille.fr

Table 5. Advantages and disadvantages of vat photo-polymerization 3D printing techniques.

3D printing technology	3D printing techniques	Materials	Advantages	Disadvantages
Vat photo-polymerization	SLA	Photopolymer (Acrylates/epoxides)	Excellent surface quality and precision	Expensive, slow printing speed, limited materials
	DLP, CLIP	Photopolymer (Acrylates/epoxides)	High (DLP) and very high (CLIP) printing speed, low initial vat volume, better surface quality	Expensive, limited materials, low-viscosity resins required, Small build size
	TPP	Photoresists (such as: PEG-DA, IP-L, IP-G, SU-8, chalcogenide glass, …)	Very high resolution (nanometer)	Expensive, limited materials, slow printing speed, small build size, required materials with high optical transparency
Powder bed fusion	SLS, DMLS, SLM, EBM	Thermoplastics or ceramics powders for SLS and SLM (such as PA12, PEEK, …) and metal powders for DMLS and EBM (such as titanium, nickel-base alloys, stainless steel, aluminum, …)	Fine resolution, high quality, no support required	Rough surfaces, poor reusability of un-sintered powder, expensive, slow printing
Material extrusion	FDM, FFF	Thermoplastics (ABS, PLA, PC, …) or fiber-reinforces thermoplastics	Low cost, simplicity, multi-material capability, quick printing	Rough surfaces (layer by layer finish), nozzle clogging, limited materials (only thermoplastics)
	3D bio-plotter	Hot melts, solutions, pastes, dispersions, polymers, monomers, hydrogels, reactive oligomers	Vast range of materials including biocompatible and medical grade materials	Small build size, time consuming technique to requirement of optimization of the plotting conditions for each different material
Sheet lamination	LOM, SDL	Paper, metal foil, plastic film (PVC) Only paper for (SDL)	Relatively low cost, reduces manufacturing time (excellent for manufacturing of larger structures)	Limitation in manufacturing of complex shapes, limited materials, low resolution
Direct energy deposition		Metals and alloys in the form of powder or wire	Reduced manufacturing time and cost, controlled microstructure, excellent for repairing and retrofitting	Low surface quality, structure, limitation in printing complex shapes with fine details
Materials and binder jetting		A concentrated dispersion of particles in a liquid (polymer, metal, alloy, ceramic)	Multi-material capability, low cost, quick printing, no heat required	Low viscosity ink required, rough surfaces (layer by layer finish), coarse resolution

Thèse de Laura Geoffroy, Université de Lille, 2020

This overview highlights that many additive manufacturing techniques have been developed over these years, and the choice of the technique used strongly depends on the nature (metal, polymer, …) and form of material (solid, powder, liquid).

2.2. Challenges, research and applications of additive manufacturing process

With the development of 3D printing techniques increasingly efficient and enabling to print a large diversity of materials (metals, polymer, liquid, ceramics, hydrogels) (Table 5), 3D printing applications have enlarged from prototyping to manufacturing of end user parts. As a consequence, the scientific and technological impact of additive manufacturing process has steadily increased. Figure 13 represents the number of scientific publications and patents from 1993 to 2019 using the terms “3D printing”. An exponential evolution is observed, particularly these last ten years, that reveals the recent strong interest on that technology. Indeed, 3D printing process is applied in various fields such as: engineering, architecture, food processing, optics, energy, dentistry, drug delivery, personalized medicine [93] and biological systems [97], [98], highlighting the versatility of this process. In addition, the many advantages and strong potential of 3D printing is also noticeable through further research and the recent emergence of a new generation of 4D printed objects. Indeed, 4D printing pioneered by skylar Tibbits at the self-assembly laboratory of MIT in collaboration with Stratasys recently appeared and uses time as fourth dimension for 3D parts to elaborate “smart structures” [99], [100]. This 4D process is based on a 3D printed part which can modify itself into another structure over the influence of external energy input such as temperature, light or other environmental stimuli. This technique, still in its early stage of development, highlights even more the high interest and technological impact of 3D printing process.

However, with the increasingly widespread use of additive manufacturing in ever more challenging applications, the demands and performances of the finished object raise and have to match or surpass the performance of products fabricated using standard processes, such as mechanical or flame retardant properties.

© 2020 Tous droits réservés.

lilliad.univ-lille.fr

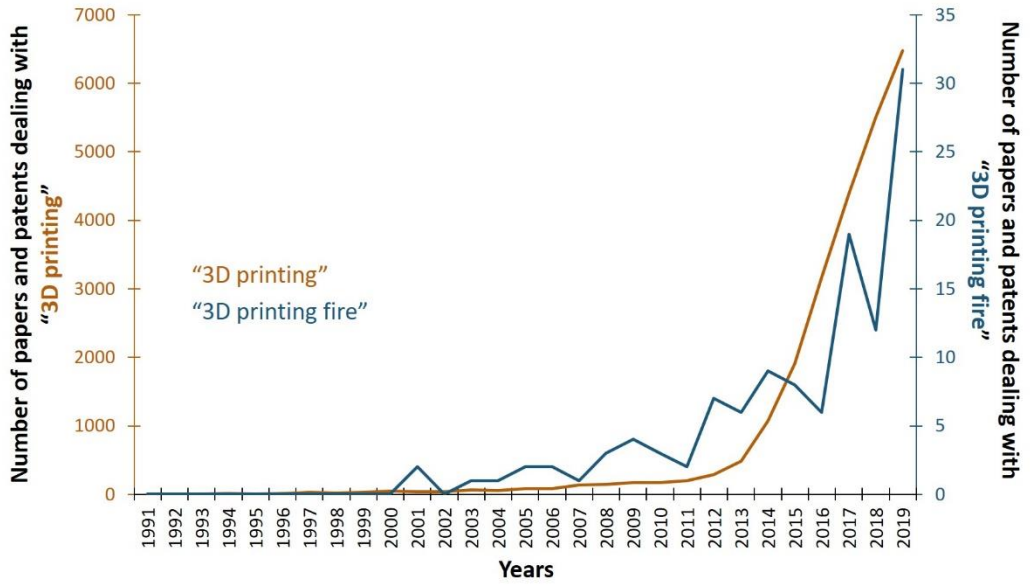

Figure 13. Illustration of the number of papers and patents on "3D printing" and "3D printing fire" according to web of science databased accessed April 13th 2020.

2.2.1. Mechanical properties

A lot of work on 3D printing investigates the mechanical properties of printed parts. Unfortunately, they are often lower than those obtained with standard manufactured parts (such as injected or thermocompressed ones) [101], [102]. This is mainly explained by an unavoidable porosity [101], [103]–[107] and a large anisotropy [101], [102], [108] resulting from the layered printing process. Both phenomena are more or less significant according to the materials and the 3D printing technique used. For example, anisotropy is usually higher for LOM and lower for SLS techniques [101].

More and more works are thus done in an attempt to improve these mechanical properties. For example, some of them try to change the formulation of material by adding nanoparticles or reinforcement, that have proven to be effective [109]–[111]. However, these works were limited by the range of materials available. Alternatively, to the modification of the material chemistry, an optimization of the 3D printing parameters [101], [112]–[120] is another approach to achieve better mechanical performances, which have drawn a lot of interest. To illustrate this point, the influence of some of them is detailed hereafter in the case of FDM technique.

Some papers highlight that the layer thickness, corresponding to the layer height of each successive addition of material (Figure 14 a), affects the mechanical properties. Indeed, it was for example demonstrated that a layer thickness of 0.2 mm allows achieving higher stiffness and tensile strength than a layer thickness equal at 0.4 mm [101], [121].

© 2020 Tous droits réservés.
lilliad.univ-lille.fr

The impact of the air gap (i.e. the space between the roads and the rasters (Figure 14 a) was also studied [101]. Three cases can be distinguished: (i) zero air gap, where two roads just touch, (ii) positive gap, where roads do not touch and (iii) negative gap, where two roads overlap. According to paper [114], a higher tensile strength was obtained for a negative air gap, because of the reduction of porosity in the 3D printed sample. However, a negative air gap leads to a dense structure, which requires a longer printing time. Thus, to avoid damaging the appearance of the 3D printed part, it is important that this negative air gap is not too high.

Moreover, the raster angle which refers to the angle between the roads (i.e. the path of the nozzle) and the loading of the part (Figure 14), has also an influence on mechanical properties of 3D printed product and strongly depends on materials studied. For PLA, a higher tensile strength was obtained for a raster angle of 45° (Figure 14 b_3) than 0° (Figure 14 b_1) or 90° (Figure 14 b_2) [101], [117]. In contrast to PLA, for ABS [101], [112], [118], [122] and PEEK [101], [123], the tensile strength is higher with a raster angle equal at 0° than with 45° or 90°. In addition to being material-dependent, the effect of the raster angle also varies according to the mechanical stress applied (such as tensile strength, compression, bending, fatigue and impact strength). For example, in the case of PLA, a raster angle of 45° should be preferred to reach high tensile strength [101], [117] while for a raster angle equal to 0° should be favored to achieve the best performance at a bending test [101], [117]. Therefore, it is noteworthy that it is important to well define the stress to which material will be subjected in order to optimized its elaboration.

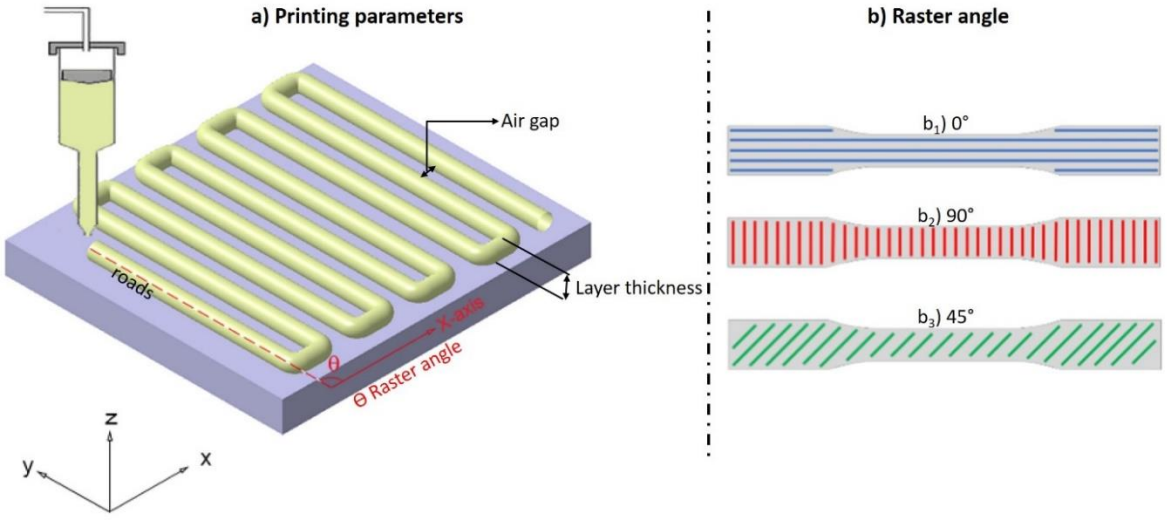

Figure 14. Illustration of a) printing parameters and b) raster angle (b_1) 0°, b_2) 90°, b_3) 45°).

Although some studies try to improve the mechanical properties of 3D printed parts, these remain weaker than parts manufactured by standard processes such as injection or

© 2020 Tous droits réservés.

lilliad.univ-lille.fr

thermocompression [101], [102]. As a consequence, to be able to use 3D printing parts, new specific tests for additive manufacturing parts have to be created and imposed. The aim is to change the way of design thinking, and use additive manufacturing process for certain part of the finish object. Committee discussions are still ongoing with regards to implementing new specific standards.

2.2.2. Flame-retardant 3D printed materials

As far as flame retardant properties are concerned, very few works have been done on 3D printed parts and the first studies have only been carried out recently (within the last 10 years), as Figure 13 illustrated. These studies can be divided into three main categories.

In the first instance, academics and industrials (such as Arkema, Solvay, BASF, Evonik, or Clariant) worked to increase the range of flame-retardant materials available for 3D printing applications like FFF, SLS and SLA, using two approaches.

On the one hand, works favored the development of inherently thermally stable polymers such as Arkema with Kepstan PEKK (for material extruded and powdered bed 3D printer application) [124] and Kynar PVDF (for material extruded 3D printing technique) [124], Solvay with ketaspire PEEK [125], ketaspire carbon-filled PEEK [125], or Radel PPSU (for material extruded 3D printer) [125] and NovaSpire PEEK (for powdered bed 3D printer) [125].

On the other hand, the strategy was to change the formulation of materials to achieve a better thermal protective performance of 3D printed materials. As a consequence, various additives (like nanoparticles, nanoclays, or flame-retardants) were incorporated in different matrices such as polyetherimide (PEI) [126]–[128], polylactic acid (PLA) [129], acrylonitrile butadiene styrene (ABS) [126], [128], [130]–[132], Nylon 6 [133], polyimide [134] poly(ethylene terephthalate) [135] and even cementitious materials [136] and aerogels [137] to reach flame retardant properties. Table 6 gathers and summarizes some of them. As an example, the work of Lao et al. consisted in developing fire-retardant polyamide 11 and 12 (PA11 and PA12) for SLS applications [138] (Table 6). The aim of this study was to improve simultaneously the flame retardant and mechanical properties of PA11 and PA12 by adding different types of nanoparticles (nanoclays, carbon nanofibers nanosilicas and phosphorous flame-retardant additives). This study revealed that phosphorous flame-retardant and carbon nanofibers induce a synergistic mechanism for flame retardancy. Regarding the mechanical properties, the phosphorous flame-retardant in high amount tends to decrease them in the case of PA11

© 2020 Tous droits réservés.
lilliad.univ-lille.fr

Thèse de Laura Geoffroy, Université de Lille, 2020

polymeric material. However, by adding nanoparticles and reducing the proportion of flame-retardant, the mechanical performances were improved (except for elongation at break). Another example in the case of SLA application can be mentioned and concerns the work of Mubarak et al., who added TiO_2 nanoparticles in a resin (different crystalline phases: anatase and rutile forms) to improve the thermal and mechanical properties of the material for SLA application [139] (Table 6). With regards to extrusion printer applications, several materials were also investigated (Table 6). For example, in the case of Poly(phenylphosphoryl phenylenediamine) (PPDA), Wu et al. revealed that 3 wt.-% PPPDA in PLA allowed to (i) increase the limited oxygen index from 20% (for neat PLA) to 25.5% for PLA with PPDA, (ii) reach V0-rating at UL-94 test, (iii) reduce the THR and pHRR respectively by 10% and 21% compared to neat PLA and (iv) improve the fire performance index from 0.081 (for neat PLA) to 0.132 m^2s/kW for PLA with PPDA (Table 6). Moreover, the elaboration of a new formulation of fiber reinforced cementitious materials for 3D printing application [136] and the development of novel methods of large-scale printing using pellets of flame-retarded ABS and PLA [140] were also considered.

So, over the years and because of these works, an enlargement of the range of flame retardant materials available for 3D printing applications has been observed.

© 2020 Tous droits réservés.

lilliad.univ-lille.fr

Table 6. Examples of flame-retardant 3D printed materials developed.

3D printing technique	Polymer	Additives	Targeted properties	ref
SLS	PA6	Phosphorus-based flame retardant	Improve the flame retardancy	Clariant [141]
	PA11 and PA12	Phosphorous flame-retardant, nanoclays, carbon nanofibers, nanosilicas	Enhance simultaneously the fire-retardant and mechanical properties	[138]
	PA12	multiwalled carbon nanotubes (MWCNTs)		[142]
	Polymeric or ceramic matrix	nanooxides such as Al_2O_3, FeO, CoO and Co_3O_4		[143]
SLA	Resin of anatase and rutile	TiO_2 nanoparticles	Improve the fire-retardant and mechanical properties	[139]
FDM	ABS	Graphene nanoplatelets	Enhance the thermal stability by reducing the linear thermal expansion and the creep compliance coefficient	[130]
	ABS	Organic modified montmorillonite (OMMT)	Reach a higher thermal stability	[131]
	82 wt.-% PLA	17 wt.-% Melamine PolyPhosphate (MPP) and 1 wt.-% Cloisite-30B (C-30B)	Improve flame retardancy	[129]
FFF	PLA	Graphene nanoplatelets	Mechanical properties, dimensional accuracy and texture	[144]
	PLA	3 wt.-% Poly(phenylphosphoryl phenylenediamine) (PPDA)	• LOI: 25.5% (compared to 20% for PLA) • UL-94 test: reach V0-rating • Cone calorimeter: -10% THR and -21% pHRR • Fire performance index: 0.132 m^2s/kW (0.081 for PLA)	[145]
	PEI	10 wt.-% hollow glass microspheres, 5 wt.-% nanoclays and 10 wt.-% non-halogenated flame retardant	• Low density • +10.7% char yield • Heat release capacity -52%	[127]
	75wt.-% Nylon 6	15 wt.-% of a flame retardant OP1312, 5 wt.-% montmorillonite (MMT), 5 wt.-% elastomer (a maleated triblock copolymer containing styrenehydrogenated butadiene-styrene (SEBS-g-MA))	Able to print and improve the flame retardancy	[133]
	Polyimide	1 wt.-% of carbon nanofibers		[134]

Thèse de Laura Geoffroy, Université de Lille, 2020

In the second instance, other studies compared the fire protection properties of 3D printed and conventional manufactured product (such as injection molding [126], [129], [131] or compression molding [130]). The objective of these works was to determine if disadvantages resulting of 3D printing process (such as higher porosity and anisotropy as previously introduced in previous section 2.2.1.) have an influence on the fire protection performances of materials. These studies revealed slight differences in terms of heat release rate and time to ignition between 3D printed and standard manufactured samples. A shorter time to ignition was often observed for 3D printed materials compared to injected or thermocompressed ones. For example, Regazzi et al. [146], [147], focusing on flame-retardant PLA for FFF applications revealed that same thermal behavior occurs between 3D printed and injected samples, but a shorter time to ignition was measured for 3D printed samples. Regarding HRR, results strongly depend on materials studied. 3D printing process can have no influence on the heat release rate [129], [146], [147], or can improve [126] (the mean average HRR (MAHRR) of 3D printed ULTEM is 13% lower than ULTEM molded sample) or conversely reduce [126] (the MAHRR of 3D printed ABS is 17% higher than ABS molded sample) the fire protection performances of flame-retardant materials). These fire behavior differences are mainly explained by the higher porosity and the anisotropy related to the 3D printing process [146], [147]. It is important to note that we also compared the fire behavior of Ethylene Vinyl Acetate (EVA) polymeric materials 3D printed with thermocompressed ones. On this preliminary work to the current PhD thesis, four polymers matrices were elaborated and composed of neat EVA, or EVA flame retarded with Aluminum TriHydroxyde (ATH) (at different loading: 30 wt.-% and 65 wt.-%) or expandable graphite (EG) (at 10 wt.-%). All plates were characterized and compared quantitatively (mass, thickness and apparent density) and qualitatively by optical microscopy and Electron Microprobe analyses (EPMA). Comparison of flame retardant properties of 3D printed and thermocompressed plates were carried out by mass loss cone calorimeter test (MLCC) using an external heat flux of 50 kW/m². Results have shown that the fire behavior of EVA and flame-retardant EVA materials was not particularly affected by the shaping process. The porosity inherent to the successive filaments deposition during the 3D printing process has no influence on the burning mechanism of the EVA and EVA/ATH polymer matrices studied. However, the porosity combined with the nozzle size and “re-extrusion” of the filaments inside the 3D printer can have some harmful influence on some flame retardant fillers, such as expandable graphite. For example, the smaller size of the EG particles as well as the horizontal preferential orientation induced by filaments deposition, lead to decreased fire-retardant

© 2020 Tous droits réservés.

lilliad.univ-lille.fr

properties of the 3D printed plates compared to thermocompressed ones. More information on this preliminary study can be found in appendix 2 (page 188) and paper [148].

Finally and in addition to these works, other investigations were done in 2018 by Rehn et al. [149]. These studies focused on the influence of printing conditions (such as layer thickness, raster angle, infill density) on the fire behavior of PEI. According to the raster angle (0° (Figure 14 b_1), 90° (Figure 14 b_2) or 45° (Figure 14 b_3)), different fire behaviors and flammability were observed using UL-94 test. Other studies demonstrated the influence of the build orientation (Figure 15). Indeed, Dul et al. [130] highlighted that a vertical orientation (Figure 15 b) or a horizontal orientation (Figure 15 a) are better than a perpendicular orientation (Figure 15 c) for ABS-graphene nanocomposite. At the same time, Fabian et al. [128] confirmed that the build orientation is the most influential printing parameters for flame-retarded ABS and PEI materials.

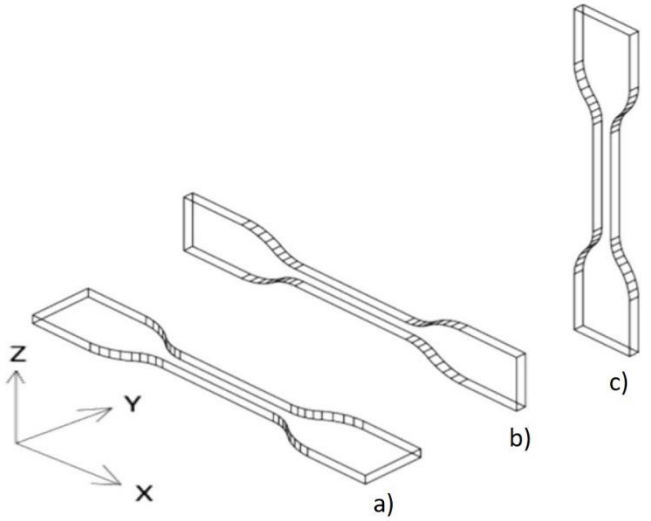

Figure 15. Illustration of different printing directions (a) horizontal, b) vertical, c) perpendicular).

This overview highlights that the literature is rather scarce on the use of 3D printing in fire protection field. Most of the studies focus on the development of new flame-retardant polymer formulations and the comparison between 3D printed plates and injected or thermocompressed plates. Indeed, these works show that the disadvantage related to 3D printing process, such as higher porosity and anisotropy can have a slight influence on the fire behavior of materials and especially on the reduction of TTI. This overview also reveals that printing parameters may influence the fire retardancy, especially the printing direction. Finally, among the paper published, very few of them considered the modification of design to improve the flame-retardancy. Only Regazzi et al. [146], [147] focused on that point. In these works, a new design

© 2020 Tous droits réservés.
lilliad.univ-lille.fr

Thèse de Laura Geoffroy, Université de Lille, 2020

was tested by concentrating flame-retardant additive on the heated surface of PLA using core-skin structure elaborated by FFF printer. This design changing seems to improve the fire protective performance of materials for a given flame-retardant loading.

3. Conclusion & Strategies of this part

To conclude, unlike additive manufacturing process, the use of complex mold is required with standard processes to design a material with a sophisticated shape. Thanks to its many advantages, 3D printing has reached an increasingly widespread use in several fields over the years and even led to a recent development of 4D printing. However, most studies are focused on improving the mechanical properties of 3D printed parts and very few papers used additive manufacturing to improve the fire protection of materials. Comparison of the fire behavior of 3D printed and injected or thermocompressed plates were made and the development of fire retardant 3D printed materials is limited to formulating matrices with additives. With such approach, the specificities of this processing technology are not exploited to its full extent for flame retardant purposes.

The aim of this work was consequently to fully take advantage of the freedom offered by 3D printing to develop new designs enabling to optimize the flame-retardant performances. Fused pellets polymer deposition technique was more specifically selected because of its versatility and its good quality to cost ratio (fully described in materials & methods part (page 164)). A copolymer of Ehtylene Vinyl Acetate (EVA) was chosen as model matrix to prove our concepts, because of its softness, flexibility and polarity which make it easy to be extruded. Moreover, the fire behavior of this polyolefin widely used in some industrial sectors (aerospace, microelectronics, cable and wire manufacture) was extensively studied in our laboratory [150]–[154]. Aluminum Tri-Hydroxide (ATH), and Expandable Graphite (EG) were chosen as flame-retardant additives because of their different chemistries and modes of action under heat flux exposure. On the one side, ATH acts in condensed phase to protect material with the formation of protective ceramic-like residue (alumina) according to an endothermic decomposition reaction coupled with a dilution effect due to water emission into gas phase [150]–[153]. On the other side, EG has an intumescent behavior due to the physical expansion of the graphite worms caused by the sublimation of inserted compounds trapped between the layers [154]. An entangled network ensures a protective barrier formation. Four formulations, i.e. EVA, EVA loaded with 30 or 65% of ATH and EVA containing 10% EG were thus studied (and their development is fully described in materials & methods part (page 162)). As it was briefly described in previous section 2.2.2. (and fully detailed in appendix 2 (page 188)), a preliminary

© 2020 Tous droits réservés.

lilliad.univ-lille.fr

study was focused on the fire protection performances comparison between 3D printed and thermocompressed samples with EVA polymeric material. This work fully characterized the formulations of materials studied and highlighted that 3D printing process has a negligible effect on their flame retardant mechanisms. The advantage of 3D printing process in term of design will thus investigated in the next chapter, leading to a new type of multi-materials combining an original design with various materials and phases.

Key points

- ✓ Standard polymer processing must use a complex mold to elaborate material with a sophisticated shape.
- ✓ Additive manufacturing is a flexible process, which allows designing original structures without using a mold. However, higher porosity and anisotropy is expected.
- ✓ Most of 3D printing studies focus on mechanical properties.
- ✓ Very few 3D printing studies are related to fire protection field: just to compare the fire behavior of 3D printed and standard parts and to develop flame-retardant materials for 3D printing applications.
- ✓ A preliminary study (appendix 2 (page 188)) to characterize and compare EVA and flame-retardant EVA 3D printed materials in relation to thermocompressed ones was done: it highlighted that the impact of 3D printing process on the EVA polymeric materials fire behavior is negligible.
- ✓ **Strategies:** Elaboration of an original design using 3D printing process to improve the fire protection performance of materials.

© 2020 Tous droits réservés.
lilliad.univ-lille.fr

Thèse de Laura Geoffroy, Université de Lille, 2020

Chapter 2: Innovative 3D printed design to conceive highly flame retardant multi-material

As highlighted in the previous chapter, flame-retardant materials can be designed using fused pellets polymer deposition 3D printing process. However, flame-retardancy was only provided by changing the formulation of materials and adding flame-retardant molecules. According to the strategies defined in this PhD work (part 1), the objective is to go a step further and to investigate the modification of materials design as an alternative approach to reach optimized fire protection performances. For such purpose, the freedom of designing objects offered by 3D printing process was used and several designs were investigated (Figure 16).

Amongst the different designs imagined, the first approach considered to play with the distribution of flame-retardants in a sample printed as a plate. Two solutions were investigated. Firstly, the use of a protective flame-retardant layer on top of an untreated matrix was proposed in order to concentrate the active flame-retardant on the surface of the plate where it is needed in case of fire (Figure 16 b). Then multi-materials plates were made in order to combine two formulations containing flame-retardants presenting different modes of action. The idea of the distribution (concentric squares or snail like) was to maximize the contact area between them to favor eventual interaction and/ or to have formulations that could react at different times during the heat exposure and protect better from the decomposition (Figure 16 a). These solutions were however not satisfactory with the chosen flame-retardants and are consequently not detailed in the manuscript.

Finally, a skin / porous core sandwich structure (Figure 16 c) appears as an interesting design that can be easily prepared using fused polymer deposition technique. This design, bio-inspired (honeycomb like structure), presents several interesting features such as a weight reduction of material and a high versatility. Indeed, the empty cells, created in the core of the sample, could be beneficial for flame-retardant properties, as a component can easily be incorporated in them to improve the global performances of the materials. The development of an optimized flame-retardant sandwich design (Figure 16 c) is fully described in the following chapters.

© 2020 Tous droits réservés.

lilliad.univ-lille.fr

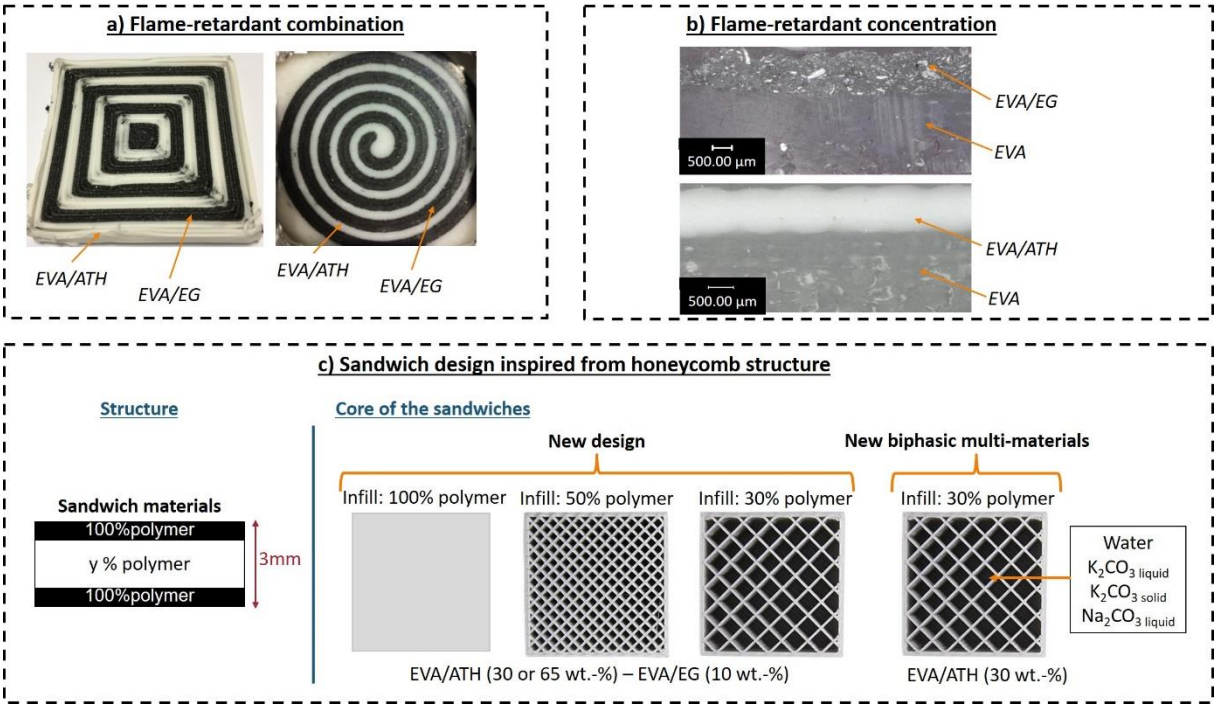

Figure 16. Concepts of flame-retardant designs printed using additive manufacturing (a) Design combining various flame-retardants, b) Design concentrating flame-retardants, c) Sandwich design inspired from honeycomb structure).

To elaborate the sandwich designs, the possibility to print samples using different infill density of polymer was used. The skins of the sandwich were thereby made of 100% filled layers (because one of the skin is the most exposed to the heat) whereas the core was partially filled (Figure 16 c). A grid pattern was chosen for the core. It is important to notice that the sides of the porous core were covered by the skin material.

The first approach of this chapter was to compare the fire performances of sandwiches having grid patterned designs partially filled with 30% or 50% of flame retarded polymers with those of standard designs (plate completely filled with 100% flame retarded polymers).

Then, the possibility of using the core materials as flame retardant carrier was investigated as illustrated in Figure 16 c. Biphasic sandwich multi-materials containing various liquid or solid phase in the cells was suggested (fully described in this chapter) and their fire performances were assessed.

These new designs were elaborated using the previously described flame-retarded EVA formulations composed of respectively of 30 wt.-% ATH, 65 wt.-% ATH and 10 wt.-%. EG loading. A full characterization of these innovative 3D designs was performed using optical microscopy, XRD, EDS analysis and Mass Loss Calorimeter Test (MLCC).

© 2020 Tous droits réservés.
lilliad.univ-lille.fr

Thèse de Laura Geoffroy, Université de Lille, 2020

The results and discussion of this chapter were published in ***Polymer Degradation and Stability*** journal: **https://doi.org/10.1016/j.polymdegradstab.2019.108992** [155].

KEYWORDS: Additive manufacturing, Design, Biphasic multi-materials, Flame retardancy

Aims

- ✓ Development of new design of flame retardant materials using fused polymer 3D printing process to improve fire protection performances.
- ✓ Based on this new design, combination of various solid and liquid phases to reach better fire insulation properties: biphasic sandwich multi-materials conception.
- ✓ Evaluation of fire protection performances of biphasic sandwich multi-materials and mechanism investigation.

1. Samples description

The Table 7 summarizes the prepared samples. The materials, materials' formulations and 3D printing process are fully described in materials & methods part (pages 162 and 164). Two sets of samples can be distinguished. The first nine samples concern the samples made with the three different formulations and the three infill densities (100, 50 and 30%). The empty cells in the core are let unfilled and consequently just contain air. The second set of samples gathers biphasic sandwich multi-materials, which use the core materials as flame retardant carrier. The sandwich structures are printed with the formulation EVA/ATH (30 wt.-%) as two parts subsequently filled and sealed as illustrated in Figure 16. The bottom skin and the grid pattern core having an infill density of 30% are printed as one piece while the top skin is printed separately. Then, the empty cells in the core are filled in with a controlled weight of liquid or solid. Distilled water, potassium carbonate used as a powder or diluted in water (saturated solution or 0.05 g/mL solution) and anhydrous sodium carbonate diluted in water (0.05 g/ml solution) were used (more details on biphasic sandwich multi-materials elaboration in materials & methods part (pages 162 and 167)). Potassium and sodium carbonates were selected because both are used in fire extinguishing systems as powders in dry fire extinguishers [156] or diluted in water (as for example in the fire vase developed by Samsun (Seoul, South Korea) for potassium carbonate) [57], [157]. These two carbonates have indeed high solubility coefficient in water (138 g/l and 212 g/l, respectively) compared to other carbonates. In the different systems, these carbonates have similar mode of action. They generate CO_2 when heated, suppressing oxygen and smothering the flame. Moreover, these two carbonates were studied to

© 2020 Tous droits réservés.

lilliad.univ-lille.fr

examine the influence, if any, of the counter ion (K^+ or Na^+) in terms of fire behavior. Finally, the design was sealed by fusing the edges of the polymer top skin to the polymer plate at 200°C, thereby forming the final biphasic sandwich multi-material.

Table 7. Name and description of samples prepared.

	Name of the sample	Phase 1		Phase 2
		Infill density (%)	Formulation	
1	3D-EVA/EG (10 wt.-%)-0%air	100	EVA/ EG (10 wt.-%)	Air
2	3D-EVA/EG (10 wt.-%)-50%air	50		
3	3D-EVA/EG (10 wt.-%)-70%air	30		
4	3D-EVA/ATH (65 wt.-%)-0%air	100	EVA/ ATH (65 wt.-%)	
5	3D-EVA/ATH (65 wt.-%)-50%air	50		
6	3D-EVA/ATH (65 wt.-%)-70%air	30		
7	3D-EVA/ATH (30 wt.-%)-0%air	100	EVA/ ATH (30 wt.-%)	
8	3D-EVA/ATH (30 wt.-%)-50%air	50		
9	3D-EVA/ATH (30 wt.-%)-70%air	30		
10	3D-EVA/ATH (30 wt.-%)-70%water	30		Water
11	3D-EVA/ATH (30 wt.-%)-70%$K_2CO_{3\ sat.-liquid}$	30		Saturated solution of K_2CO_3
12	3D-EVA/ATH (30 wt.-%)-70%$K_2CO_{3\ liquid}$	30		0.050 g/mL solution of K_2CO_3
13	3D-EVA/ATH (30 wt.-%)-70%$K_2CO_{3\ solid}$	30		$K_2CO_{3\ solid}$
14	3D-EVA/ATH (30 wt.-%)-70%$Na_2CO_{3\ liquid}$	30		0.05 g/ml solution of Na_2CO_3

© 2020 Tous droits réservés.
lilliad.univ-lille.fr

Thèse de Laura Geoffroy, Université de Lille, 2020

2. Results

2.1. New design of lighter flame-retardant materials with empty cells

2.1.1. Characterizations before fire testing

Top and cross-section of each sample before fire testing was observed using an optical microscope (following the set-up fully described in materials & methods part (page 172)) and the resulting pictures are gathered in Figure 17 and Figure 18. All samples seem quite homogeneous exhibiting the same thickness (average measured values reported in Table 8). As expected, the mass decreases according to the percentage of polymer in each printed plate. Whatever the formulations, the mass of polymer plates filled at 50% (with 50% air) are 24 to 27% lower than 100% filled plates and for the infill density of 30% (with 70% air) 34 to 39% lower. Lighter materials were thus elaborated. Moreover, the created grid patterns exhibit square empty cells of dimension around 800 µm and 1800 µm for respectively 50 and 30% infills (Table 8), whatever the materials. The empty cells in the grid with 50% air have length roughly half the size of the one of the grid with 70% air (Figure 17). The top and bottom thickness layers for each plate were calculated giving an averaged value equal to 604 µm, (Table 8).

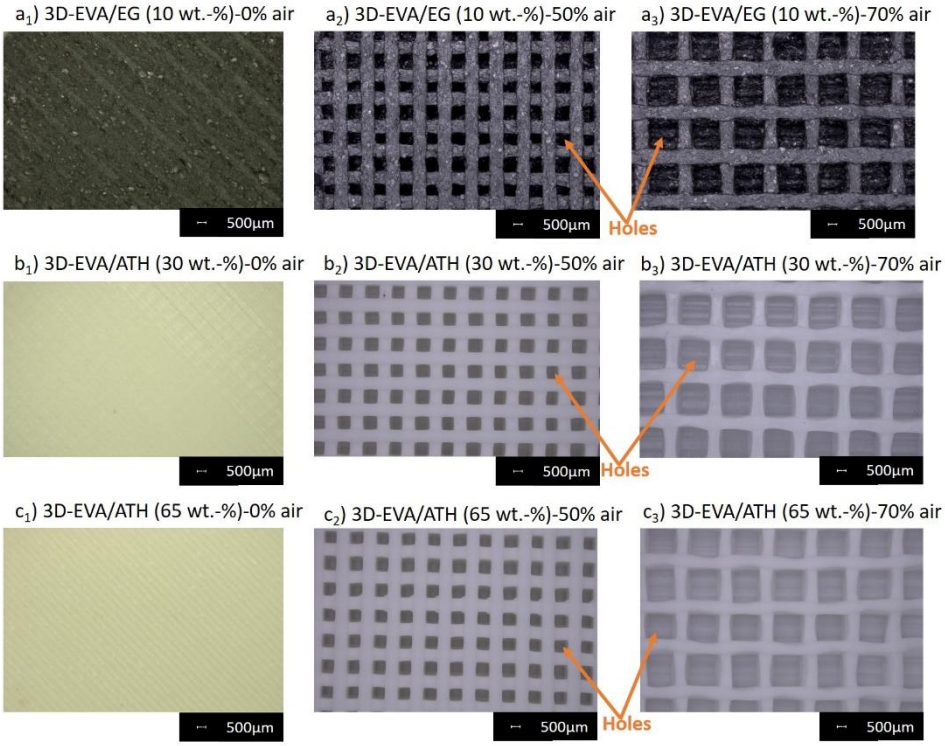

Figure 17. Top section observation using optical microscopy (x20) before MLCC test (a_1) 3D-EVA/EG (10 wt.-%)-0% air, a_2) 3D-EVA/EG (10 wt.-%)-50%, a_3) 3D-EVA/EG (10 wt.-%)-70% air, b_1) 3D-EVA/ATH (30 wt.-%)-0% air, b_2) 3D-EVA/ATH (30 wt.-%)-50% air, b_3) 3D-

© 2020 Tous droits réservés.

lilliad.univ-lille.fr

EVA/ATH (30 wt.-%)-70% air, c_1) 3D-EVA/ATH (65 wt.-%)-0%air, c_2) 3D-EVA/ATH (65 wt.-%)-50%air, c_3) 3D-EVA/ATH (65 wt.-%)-70% air).

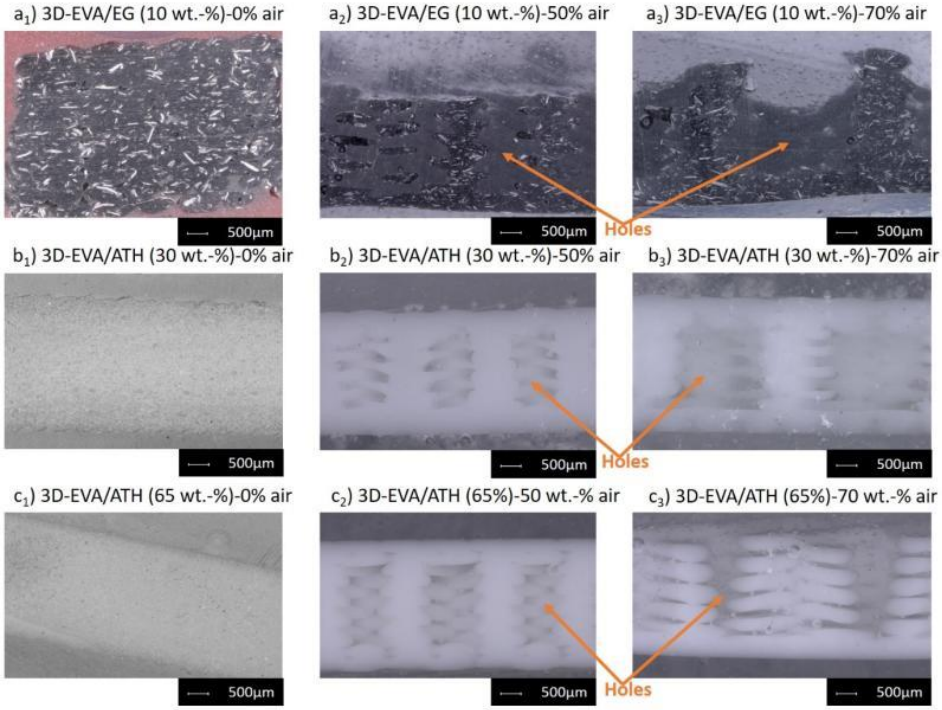

Figure 18. Cross section observations using optical microscopy (x50) before MLCC test (a_1) 3D-EVA/EG (10 wt.-%)-0% air, a_2) 3D-EVA/EG (10 wt.-%)-50%, a_3) 3D-EVA/EG (10 wt.-%)-70% air, b_1) 3D-EVA/ATH (30 wt.-%)-0% air, b_2) 3D-EVA/ATH (30 wt.-%)-50% air, b_3) 3D-EVA/ATH (30 wt.-%)-70% air, c_1) 3D-EVA/ATH (65 wt.-%)-0% air, c_2) 3D-EVA/ATH (65 wt.-%)-50% air, c_3) 3D-EVA/ATH (65 wt.-%)-70% air).

© 2020 Tous droits réservés.
lilliad.univ-lille.fr

Thèse de Laura Geoffroy, Université de Lille, 2020

Table 8. Quantitative characterization of each sample studied.

Formulation	Mass (g)	Thickness (mm)	Square hole dimension (µm)	Fused filament diameter (mm)	Bottom layer thickness (mm)
3D-EVA/EG (10 wt.-%)-0% air	7.07 ± 0.02	3 ± 0	/	/	/
3D-EVA/EG (10 wt.-%)-50% air	5.4 ± 0.2	3 ± 0	840	800	580
3D-EVA/EG (10 wt.-%)-70% air	4.67 ± 0.04	3 ± 0	1800	840	605
3D-EVA/ATH (30 wt.-%)-0% air	9.2 ± 0.3	3 ± 0	/	/	/
3D-EVA/ATH (30 wt.-%)-50% air	6.72 ± 0.03	3 ± 0	900	820	640
3D-EVA/ATH (30 wt.-%)-70% air	5.82 ± 0.03	3 ± 0	1770	820	590
3D-EVA/ATH (65 wt.-%)-0% air	12.18 ± 0.04	3 ± 0	/	/	/
3D-EVA/ATH (65 wt.-%)-50% air	9.13 ± 0.03	3 ± 0	787	820	620
3D-EVA/ATH (65 wt.-%)-70% air	7.4 ± 0.2	3 ± 0	1830	840	590

2.1.2. Fire protection performances

Reaction to fire performances of the references and sandwich plates were compared (fire testing fully described in materials & methods part (page 170)). Figure 20 and Table 9 show HRR as a function of time curves and the averaged values of pHRR, THR and TTI for the different systems.

It is observed that systems with 65 wt.-% ATH and 10 wt.-% EG were very efficient compared to system with 30 wt.-% ATH whatever the design studied. pHRR of standard design plate (100% polymers) of 3D-EVA/ATH (30 wt.-%) were 88% and 150% higher than that of systems with the standard design containing 10 wt.-% of expandable graphite and 65 wt.-% ATH, respectively (an increase of 65% and 71% was also obtained for the THR of both materials with EG and 65 wt.-% ATH respectively). It is consistent with results reported in preliminary study

© 2020 Tous droits réservés.

lilliad.univ-lille.fr

in appendix 2 (page 188) (and paper [148]). It is noteworthy that sandwich designs containing empty cells exhibit better performance than the 100% filled reference plates whatever the material. It makes sense because in these cases there is less polymer and consequently less fuel.

For the 3D-EVA/EG (10 wt.-%) material (Figure 20 a), the results are identical for the two infills (70% air compared to 50% air) in terms of THR, pHRR and TTI (-6%, -1% and 3%, respectively). Compared to the reference plate without cells, pHRR and THR of plate with 70% air are decreased (by -20% and -65% respectively) but the TTI remains unchanged. The decrease of HRR when empty cells are incorporated inside materials can be explained by the compacity changing of the entangled network structure caused by the empty cells (due to the design modification), and also by the reduction of 'fuel' load in the system. Indeed, air inside materials and thus higher porosity creates higher gap to be filled by the graphite worms and hence, it modifies the compacity of the graphite worms network (Figure 19) [148]. This structure modification can have an influence on fire protection properties as it is the case for intumescent systems [158]. Moreover, hollow structure has much lower thermal conductivity compared to non-hollow structure. Therefore, as long as the empty cells stand during burning, it is reasonable to assume that cells slow down the heat transfer within the material and thus decrease the THR. Furthermore, the reduction of 'fuel' load modifies the combustion and improves the fire performance.

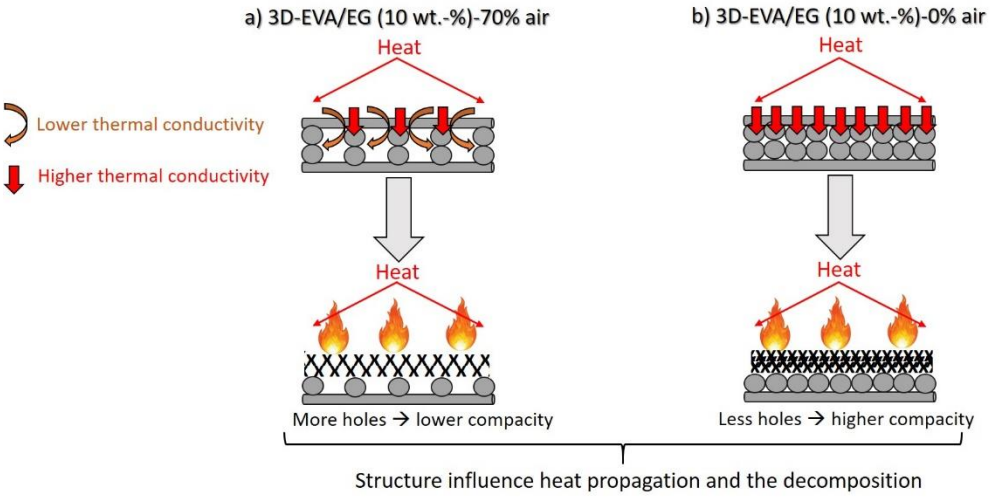

Figure 19. Compacity difference and influence in heat propagation for system (a) 3D-EVA/EG (10 wt.-%)-70% air, b) 3D-EVA/EG (10 wt.-%)-0% air).

In the case of 3D-EVA/ATH (30 wt.-%) (Figure 20 b), the THR, and the pHRR differences between the plate with 30% polymer and the plate completely filled are respectively of -37% and -12%, with a TTI reduced by 15 seconds (about 1.6 times shorter). Regarding the

© 2020 Tous droits réservés.
lilliad.univ-lille.fr

Thèse de Laura Geoffroy, Université de Lille, 2020

comparison between 3D-EVA/ATH (30 wt.-%)-50% air and 3D-EVA/ATH (30 wt.-%)-0% air, the difference in terms of THR, and pHRR is -19% and -10% respectively, with a TTI reduced by 5 seconds (about 1.14 times shorter). Thus, for this material, the design modification does not allow to reach a significant improvement in terms of reaction to fire. In this case it seems that the flame-retardant used at this loading is not high enough to be efficient. Consequently, the sample under heat exposure, melts and burns and hence, all the cells collapse: the design is then no longer a governing parameter.

For the materials containing 65 wt.-% ATH (Figure 20 c), there is a huge impact of the infill density on the fire performances. THR difference between 70% air plate and 50% air plate is -8 MJ/m^2, (corresponding to -29% difference) but the pHRR and TTI remain similar. Furthermore, the comparison between plain plate (standard design) and plate with 70% air revealed unexpected results. During the fire testing of 3D-EVA/ATH (65 wt.-%)-70% air, ignition started quickly when the sample was exposed to heat flux. EVA melts, burns and concurrently ATH dehydrates releasing water leading to a dilution effect in the gas phase and makes an alumina-type ceramic in the condensed phase. The combination of water evolution, ceramization and lower 'fuel' load makes the material poorly flammable and flame extinguishment is rapidly observed. Moreover, the new design with empty cells inside (3D-EVA/ATH (65 wt.-%)-70% air and 3D-EVA/ATH (65 wt.-%)-50% air) reduces the thermal conductivity of the system compared to standard design (3D-EVA/ATH (65% wt.-%)-0% air). Indeed, while the empty cells (created by the design) are maintained during the combustion, they can slow down the heat propagation, and thus improve the fire protection. So, the pHRR of 3D-EVA/ATH (65 wt.-%)-70% air was decreased by 23% compared to 3D-EVA/ATH (65 wt.-%)-0% air. Moreover, a significant reduction of THR (by 57%) was also measured but TTI is decreased by 35.5 seconds (about 1.95 times shorter) for the design with 70% air inside materials (probably due to higher concentration of oxidizer (O_2 of the air filling the cells). TTI reduction for 3D printed plates was expected as it was previously reported [146]. Overall, the design has a strong influence and can improve the fire retardancy of materials.

A THR comparison of all systems studied was also done (Table 9) with the normalization of THR by sample weight to rule out the influence of mass. The same trend is found and thus a reduction of THR is obtained for 3D-EVA/EG (10 wt.-%) and 3D-EVA/ATH (65 wt.-%) with 50% air and 70% air. Indeed, THR of 3D-EVA/EG (10 wt.-%)-70% air and 3D-EVA/EG (10 wt.-%)-50% air is reduced by 46% and 51% respectively, compared to 3D-EVA/EG (10 wt.-%)-0% air. Concerning 3D-EVA/ATH (65 wt.-%)-70% air and 3D-EVA/ATH (65 wt.-%)-50%

© 2020 Tous droits réservés.

lilliad.univ-lille.fr

air, THR is decreased by 29 and 19% respectively, compared to 3D-EVA/ATH (65 wt.-%)-0% air. No improvement of THR is measured for 3D-EVA/ATH (30 wt.-%) whatever the percentage of infill.

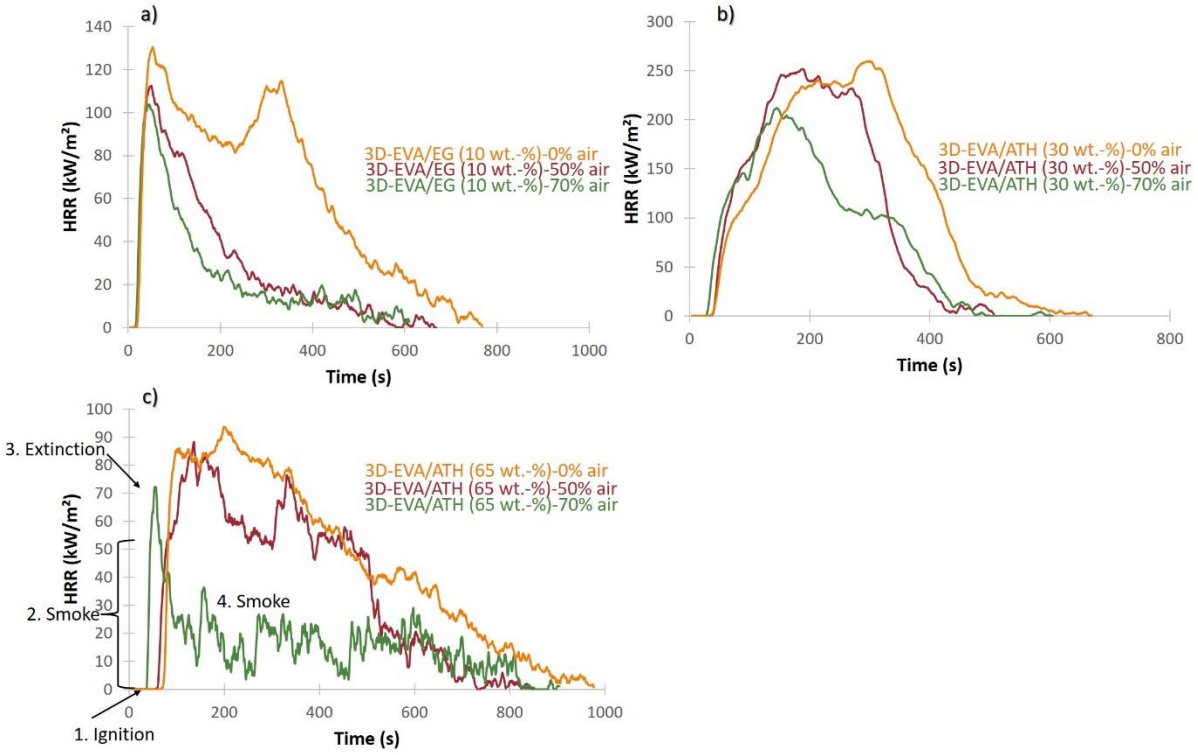

Figure 20. Influence of the design and the amount of empty cells on fire behavior (a) 3D-EVA/EG (10 wt.-%), b) 3D-EVA/ATH (30 wt.-%), c) 3D-EVA/ATH (65 wt.-%)).

Table 9. Fire performance values of each design studied for the different formulations.

Polymer matrix	TTI (s)	THR (MJ/m²)	THR/mass (MJ/m².g)	pHRR (kW/m²)
3D-EVA/EG(10 wt.-%)-0% air	17	48	6.8	137
3D-EVA/EG (10 wt.-%)-50% air	14.5 (÷1.17)	18 (-63%)	3.3 (-51%)	110 (-20%)
3D-EVA/EG (10 wt.-%)-70% air	15 (÷1.13)	17 (-65%)	3.6 (-46%)	109 (-20%)
3D-EVA/ATH (30 wt.-%)-0% air	41	79	8.6	257
3D-EVA/ATH (30 wt.-%)-50% air	36 (÷1.14)	61 (-23%)	9.1 (6%)	249 (-3%)
3D-EVA/ATH (30 wt.-%)-70% air	26 (÷1.58)	49.4 (-37%)	8.5 (-1%)	225 (-12%)
3D-EVA/ATH (65 wt.-%)-0% air	73	46	3.8	103
3D-EVA/ATH (65 wt.-%)-50% air	43.5 (÷1.68)	28 (-39%)	3.1 (-19%)	95 (-8%)
3D-EVA/ATH (65 wt.-%)-70% air	37.5 (÷1.95)	20 (-57%)	2.7 (-29%)	79 (-23%)

© 2020 Tous droits réservés.
lilliad.univ-lille.fr

Thèse de Laura Geoffroy, Université de Lille, 2020

Pictures of the residues after fire testing are presented on Figure 21. No additional information was obtained from the observation of the residues of 3D-EVA/EG (10 wt.-%) and 3D-EVA/ATH (30 wt.-%). For these formulations, residues are the same whatever the infill density. But, in the case of 3D-EVA/ATH (65 wt.-%), the structure is kept as observed during the MLCC test. Indeed, the structure of the residue exhibits holes (induced by the design) below the top layer (Figure 21 c_3). Table 10 gathers the mass loss of each sample studied. It is noteworthy that whatever the materials studied, the mass loss is almost the same for each design studied (0% air, 50% air, 70% air).

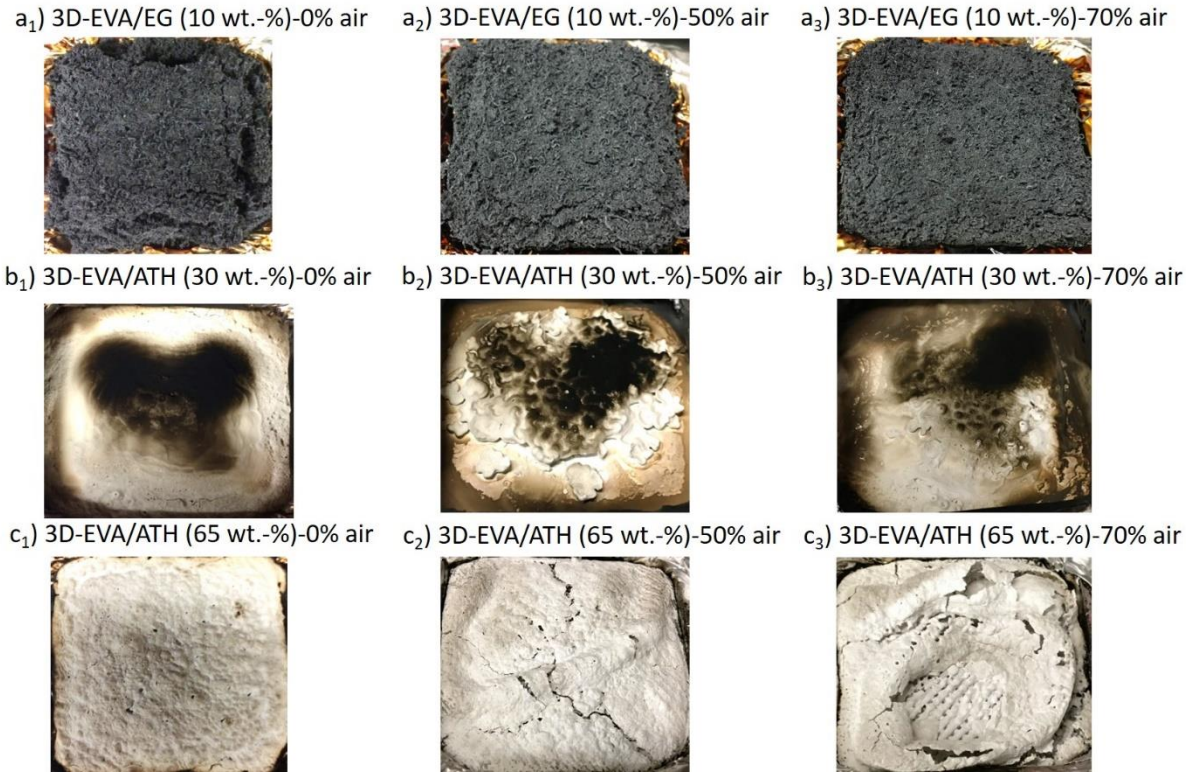

Figure 21. Residue after fire testing (a_1) 3D-EVA/EG (10 wt.-%)-0% air, a_2) 3D-EVA/EG (10 wt.-%)-50% air, a_3) 3D-EVA/EG (10 wt.-%)-70% air, b_1) 3D-EVA/ATH (30 wt.-%)-0% air, b_2) 3D-EVA/ATH (30 wt.-%)-50% air, b_3) 3D-EVA/ATH (30 wt.-%)-70% air, c_1) 3D-EVA/ATH (65 wt.-%)-0% air, c_2) 3D-EVA/ATH (65 wt.-%)-50% air, c_3) 3D-EVA/ATH (65 wt.-%)-70% air).

© 2020 Tous droits réservés.

lilliad.univ-lille.fr

Table 10. Mass loss comparison between different design studied for each material (3D-EVA/EG (10 wt.-%), 3D-EVA/ATH (30 wt.-%), 3D-EVA/ATH (65 wt.-%)).

Polymer matrix	Mass (g)	Residual mass (g)	Mass Loss (%)
3D-EVA/EG(10 wt.-%)-0% air	7.07 ± 0.02	2.675 ± 0.003	62
3D-EVA/EG (10 wt.-%)-50% air	5.4 ± 0.2	2.61 ± 0.05	52
3D-EVA/EG (10 wt.-%)-70% air	4.67 ± 0.03	1.7 ± 0.1	57
3D-EVA/ATH (30 wt.-%)-0% air	9.2 ± 0.3	1.7 ± 0.1	81
3D-EVA/ATH (30 wt.-%)-50% air	6.72 ± 0.03	1.338 ± 0.006	80
3D-EVA/ATH (30 wt.-%)-70% air	5.82 ± 0.03	1.2 ± 0.1	79
3D-EVA/ATH (65 wt.-%)-0% air	12.18 ± 0.04	6.6 ± 0.3	46
3D-EVA/ATH (65 wt.-%)-50% air	9.13 ± 0.03	4.1 ± 0.2	55
3D-EVA/ATH (65 wt.-%)-70% air	7.7 ± 0.1	3.7 ± 0.3	52

In the second part of this chapter, the work focuses on the design containing with 70% air made using 3D-EVA/ATH (30 wt.-%) formulation. 3D-EVA/ATH (65 wt.-%)-70% air already exhibiting extremely high fire retardancy. Thus, it does not need any further enhancement. Regarding 3D-EVA/EG (10 wt.-%), it makes an expanded intumescent coating (and powdered residue) which is not compatible with the strategy of flame retardancy we wanted to examine (see the next section).

2.2. Flame retardant biphasic sandwich multi-materials elaboration

2.2.1. Characterization before fire testing

Based on the design described in the previous section, 3D-EVA/ATH (30 wt.-%)-70% air plates were elaborated (Figure 16 c). These plates were filled with water, potassium carbonate in liquid and solid phase, and sodium carbonate in liquid phase, hereafter called: 3D-EVA/ATH (30 wt.-%)-70% water, 3D-EVA/ATH (30 wt.-%)-70% $K_2CO_{3\ sat.\text{-}liquid}$, 3D-EVA/ATH (30 wt.-%)-70% $K_2CO_{3\ liquid}$, 3D-EVA/ATH (30 wt.-%)-70% $K_2CO_{3\ solid}$, 3D-EVA/ATH (30 wt.-%)-70% $Na_2CO_{3\ liquid}$, respectively. These plates were characterized in terms of mass, thickness and liquid (or solid) phase amount, and all data are gathered in Table 11. Based on Table 11, the amount of liquid (solid) is similar regardless of the system studied (1.5 ml, 1.2 g, 1.7 ml, 1.7 ml for water, $K_2CO_{3\ solid}$, $K_2CO_{3\ liquid}$ and $Na_2CO_{3\ liquid}$, respectively), except for the system with a saturate concentration of $K_2CO_{3\ sat.\text{-}liquid}$ due to the higher density of the solution.

© 2020 Tous droits réservés.
lilliad.univ-lille.fr

Thèse de Laura Geoffroy, Université de Lille, 2020

Table 11. Quantitative values of each biphasic sandwich multi-material studied.

Polymer matrix	Mass (g)	Thickness (mm)	Liquid / solid amount (ml or g)
3D-EVA/ATH (30 wt.-%)-0% air	9.2 ± 0.3	3 ± 0	/
3D-EVA/ATH (30 wt.-%)-70% air	5.82 ± 0.03	3 ± 0	/
3D-EVA/ATH (30 wt.-%)-70% water	8.3 ± 0.2	3 ± 0.2	1.51 ± 0.1
3D-EVA/ATH (30 wt.-%)-70% $K_2CO_{3\ solid}$	7.33 ± 0.01	3 ± 0.2	1.204 ± 0.008
3D-EVA/ATH (30 wt.-%)-70% $K_2CO_{3\ sat.-liquid}$	9.4 ± 0.2	3 ± 0.2	2.6 ± 0.2
3D-EVA/ATH (30 wt.-%)-70% $K_2CO_{3\ liquid}$	8.2 ± 0.4	3 ± 0.2	1.7 ± 0.5
3D-EVA/ATH (30 wt.-%)-70% $Na_2CO_{3\ liquid}$	8.2 ± 0.4	3 ± 0.2	1.7 ± 0.5

2.2.2. MLCC fire testing

Figure 22 and Table 12 show the fire behavior of each filled sample (HRR vs time) and the associated fire parameters (TTI, THR and pHRR). The graph clearly evidences a difference of behavior between the samples.

On one hand, when empty cells were filled with water or powdered K_2CO_3, no significant improvement were recorded compared to 3D-EVA/ATH (30 wt.-%)-70% air. All TTI were either similar (for water) or reduced by 5 seconds (about 1.24 times shorter) for system with powdered K_2CO_3 than unfilled core sample. The THR as well as the pHRR of samples filled with water or powdered K_2CO_3 are of the same order of magnitude or even slightly higher (32% and 7% for the THR respectively, and 13% and 4% for the pHRR respectively) than 3D-EVA/ATH (30 wt.-%)-70% air. Therefore, no benefits are achieved when air is substituted by water or powdered K_2CO_3.

On the other hand, when solutions with same mass concentration of K_2CO_3 or Na_2CO_3 are used, a dramatic decrease of the pHRR (by -80% and -72% respectively) and THR (by -75% and -71% respectively) as well as an increase of the TTI by 8 and 11 seconds (about 1.31 and 1.42 times longer, respectively) are achieved. These enhanced performances can be explained by the fast flame extinction observed during the experiments (visual observation). This extinction is obtained using saturated (112 g/L) and diluted (50 g/L) solution of K_2CO_3. Therefore, it is reasonable to assume that the concentration difference between these two solutions does not

© 2020 Tous droits réservés.

lilliad.univ-lille.fr

influence significantly the fire performance of the material and neither does the cation of the carbonate salts used.

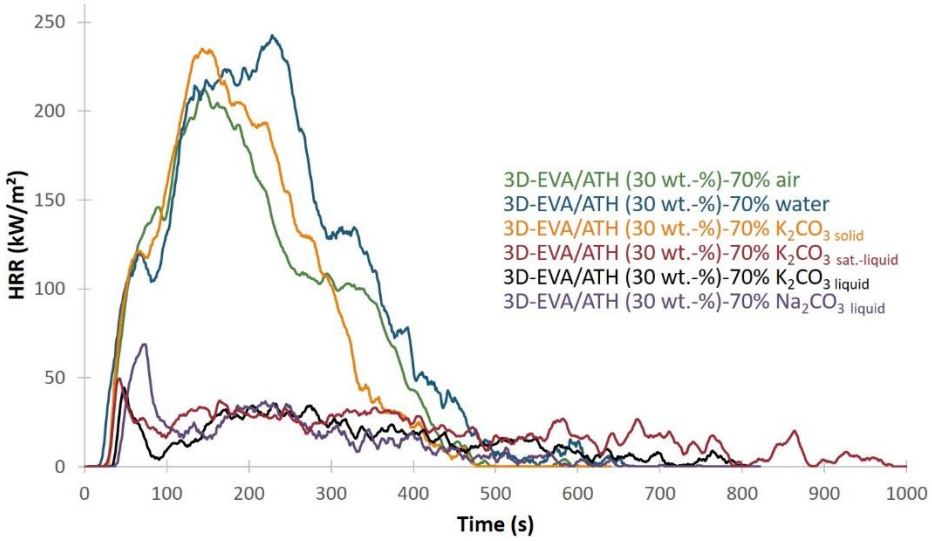

Figure 22. Comparison of the fire behavior of biphasic sandwich multi-materials.

Table 12. Fire protection performances values of each system studied.

Polymer matrix	TTI (s)	THR (MJ/m²)	pHRR (kW/m²)
3D-EVA/ATH (30 wt.-%)-70% air	26	49.4	225
3D-EVA/ATH (30 wt.-%)-70% water	21 (÷1.24))	65 (32%)	255 (13%)
3D-EVA/ATH (30 wt.-%)-70% $K_2CO_{3\ solid}$	26.5 (x1)	53 (7%)	235 (4%)
3D-EVA/ATH (30 wt.-%)-70% $K_2CO_{3\ sat.-liquid}$	34 (x1.31)	17.5 (-65%)	52 (-77%)
3D-EVA/ATH (30 wt.-%)-70% $K_2CO_{3\ liquid}$	34 (x1.31)	12.4 (-75%)	46 (-80%)
3D-EVA/ATH (30 wt.-%)-70% $Na_2CO_{3\ liquid}$	37 (x1.42)	14 (-71%)	62 (-72%)

During the MLCC test, a thermocouple was embedded on the backside of the material and temperature was recorded as a function of time for all systems (Figure 23, note Na_2CO_3 was not considered because of the negligible influence of the cation). Temperature progressively increases from the system with $K_2CO_{3\ sat.-liquid}$, $K_2CO_{3\ solid}$, water to the system with air (Figure 23). In the case of 3D-EVA/ATH (30 wt.-%)-70% air, and 3D-EVA/ATH (30 wt.-%)-70% water, four rates of change of temperature are observed until the plateau at 500°C for all samples. For the system with $K_2CO_{3\ sat.-liquid}$ and $K_2CO_{3\ solid}$, five main changes in the slope of the temperature/time curve can be distinguished (Table 13). From 0 s to 70 s, the heating rate of the system with K_2CO_3 in liquid and solid phase is twice as low as for 3D-EVA/ATH (30

© 2020 Tous droits réservés.
lilliad.univ-lille.fr

wt.-%)-70% air. For 3D-EVA/ATH (30 wt.-%)-70% water, the heating rate from 0 s to 70 s is 1.7-time lower than that for system with air. From 70 s to 120 s, the heating rate of 3D-EVA/ATH (30 wt.-%)-70% air is 10, 2.7 and 1.9 times higher than those of the systems with $K_2CO_{3\ sat.liquid}$, $K_2CO_{3\ solid}$ and water, respectively.

For 3D-EVA/ATH (30 wt.-%)-70% air, the temperature rise can be explained by the fact that, when the sample ignites, EVA melts and burns, thus, all cells collapse, and thus temperature grows rapidly. Comparatively, the system with water ignites and burns and at 100°C water boils (vaporization of water) but no plateau is observed (Figure 23). For the system with K_2CO_3 in solid phase, when the sample ignites, EVA melts and burns, but K_2CO_3 powdered does not decarbonize because the external heat flux is too low to make the decarbonation of K_2CO_3 (891°C). So, the powdered K_2CO_3 keeps the design at the beginning of the test and hence, it limits the temperature rise in the system. For 3D-EVA/ATH (30 wt.-%)-70% $K_2CO_{3\ sat.-liquid}$, a plateau is clearly observed at 100 s – 120 s. Temperature rise is delayed and highlights the benefit of this systems compared to the others. After 300 s, systems with water and K_2CO_3 in liquid and solid phase reach the same temperature (400°C). All the systems reach a steady-state temperature of 500°C after 450 s.

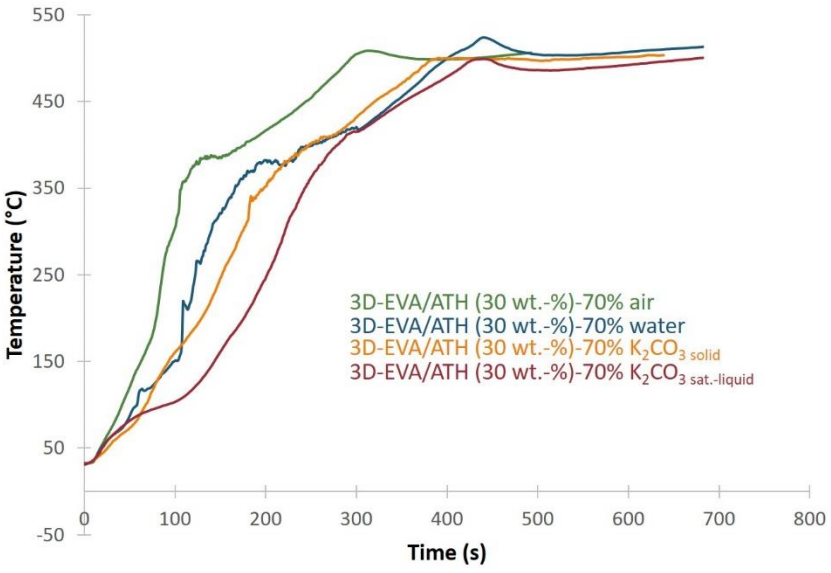

Figure 23. Evolution of temperature vs time for each biphasic sandwich multi-material studied.

© 2020 Tous droits réservés.

lilliad.univ-lille.fr

Table 13. Rate of change of temperature for each sample studied.

Polymer matrix	Rates of change of Temperature (°C/s)				
	0 s – 70 s	**70 s – 120 s**	**120 s – 200 s**	**200 s -300 s**	**300 s - 400 s**
3D-EVA/ATH (30 wt.-%)-70% air	2.14	4.51	0.73	0.73	
3D-EVA/ATH (30 wt.-%)-70% water	1.29	2.41	2.41	0.53	0.53
3D-EVA/ATH (30 wt.-%)-70% $K_2CO_{3\ solid}$	0.94	1.68	2.27	0.69	0.72
3D-EVA/ATH (30 wt.-%)-70% $K_2CO_{3\ sat.-liquid}$	1.07	0.44	1.86	1.86	0.61

Pictures of the residues after fire testing and the percentage of mass loss are gathered on Figure 24 and Table 14. According to Table 14, the mass loss of sample with water is almost the same as 3D-EVA/ATH (30 wt.-%)-70% air. A slight lower mass loss is obtained for sample with K_2CO_3 in solid and liquid phase (60% and 69% respectively) compared to 79% for 3D-EVA/ATH (30 wt.-%)-70% air. A small difference is observed for the systems containing K_2CO_3 solid and K_2CO_3 liquid despite the strong THR reduction obtained for 3D-EVA/ATH (30 wt.-%)-70% $K_2CO_{3\ sat.-liquid}$. This comparison emphasizes that 3D-EVA/ATH (30 wt.-%)-70% $K_2CO_{3\ sat.-liquid}$ limits the contribution of fire growth but it does not allow protecting the material against combustion (no limitation of mass loss compared to the other systems). Moreover, a ceramic residue is obtained for each sample (Figure 24), but a different aspect is observed in the case of system with K_2CO_3 in liquid or solid phase. For 3D-EVA/ATH (65 wt.-%)-70% $K_2CO_{3\ solid}$, the residue is grayer than the others. For 3D-EVA/ATH (30 wt.-%)-70% $K_2CO_{3\ sat.-liquid}$, some white color areas are observed in comparison with the other residues. Further investigations are needed to explain these differences and they are done in the next part.

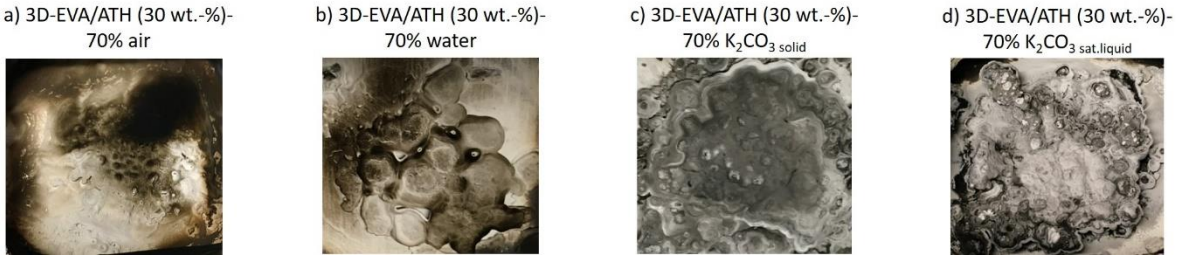

© 2020 Tous droits réservés.
lilliad.univ-lille.fr

Thèse de Laura Geoffroy, Université de Lille, 2020

Figure 24. Residues after fire testing (a) 3D-EVA/ATH (30 wt.-%)-70% air, b) 3D-EVA/ATH (30 wt.-%)-70% water, c) 3D-EVA/ATH (30 wt.-%)-70% $K_2CO_{3\ solid}$, d) 3D-EVA/ATH (30 wt.-%)-70% $K_2CO_{3\ sat.-liquid}$).

Table 14. Mass loss comparison between each sample studied.

Polymer matrix	Mass (g)	Residual mass (g)	Mass loss (%)
3D-EVA/ATH (30 wt.-%)-70% air	5.82 ± 0.03	1.2 ± 0.1	79
3D-EVA/ATH (30 wt.-%)-70% water	8.3 ± 0.2	1.5 ± 0.08	82
3D-EVA/ATH (30 wt.-%)-70% $K_2CO_{3\ solid}$	7.33 ± 0.01	2.6 ± 0.3	60
3D-EVA/ATH (30 wt.-%)-70% $K_2CO_{3\ sat.-liquid}$	9.3 ± 0.2	2.9 ±0.2	69

2.2.3. Mechanism investigation

2.2.3.1. Gas phase analysis

The system containing diluted K_2CO_3 in water exhibits an unusual behavior and the mechanism of action were investigated in the gas and condensed phases. The flame aspect was firstly visually observed as illustrated in Figure 25. It is clearly seen that the flame obtained for 3D-EVA/ATH (30 wt.-%)-70% $K_2CO_{3\ sat.-liquid}$ is purple compared to the flame with 3D-EVA/ATH (30 wt.-%) and 3D-EVA/ATH (30 wt.-%)-70% $K_2CO_{3\ solid}$ which is more yellowish in both cases. This flame color difference might be explained by the presence of potassium ion in the flame. Indeed, the flame color is related to the de-excitation of thermally excited electrons in the form of radiation [159]. The electrons of the atoms are placed on levels with a specific energy. During heat excitation, electrons move from stable to unstable levels (higher in energy). By de-exciting themselves, they return to their original level and emit a photon (light) of a very precise wavelength (color). The wavelength of this radiation thus depends on the electronic structure of the chemical element. Therefore, certain cations such as Cu^{2+}, Sr^{2+}, Na^+, or K^+ have a specific line spectrum and therefore a specific flame color associated (which is green, red, yellow/orange, and purple respectively). This observation (Figure 25) suggests therefore the presence of potassium in flame, and thus in the gas phase.

© 2020 Tous droits réservés.

lilliad.univ-lille.fr

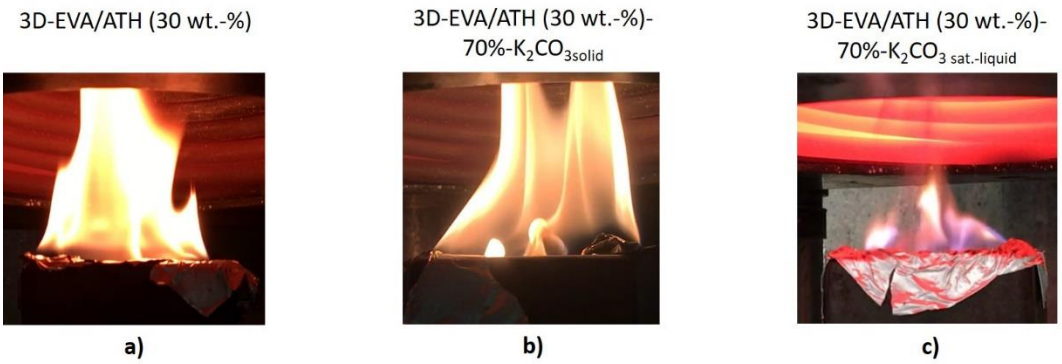

Figure 25. Flame aspect after almost 40s MLCC test (a) 3D-EVA/ATH (30 wt.-%), b) 3D-EVA/ATH (30 wt.-%)-70%-$K_2CO_{3\ solid}$, c) 3D-EVA/ATH (30 wt.-%)-70% $K_2CO_{3\ sat.-liquid}$).

To make sure of the presence of potassium in gas phase, soot was collected at pHRR during the MLCC tests (because of the higher soot particles emission [160]) using mirror polished stainless-steel plate (set-up fully described in materials & methods part (page 172)). Then, soot particles were observed by SEM and qualitatively characterized using EDS analysis (following the set-up described in materials & methods part (page 174)). Note that quantitative element analysis could not be done due to the difference of soot thickness deposition onto the mirror polished stainless steel. Indeed, electron beam does not impact the soot at the same electronic interaction distance. Therefore, the generation of X-rays is affected by the local specimen due to the electron penetration differences [161], and thus the quantitative comparison cannot be done in our case. Figure 26 shows the characterization of soot from 3D-EVA/ATH (30 wt.-%)-70% air, 3D-EVA/ATH (30 wt.-%)-70% water, 3D-EVA/ATH (30 wt.-%)-70% $K_2CO_{3\ sat.-liquid}$ and 3D-EVA/ATH (30 wt.-%)-70% $K_2CO_{3\ solid}$. On these graphs, Cr, Fe, Ni, Mo, Al, C and O elements are identified and come from mirror polished stainless steel, as illustrated in Figure 26 e. The presence of C and O is also due to the soot composition. In the case of the system with K_2CO_3 in liquid phase, the characteristic peak of potassium (between 3.2 and 3.4 keV) is clearly detected in the soot particles contrary to all the other systems including that with K_2CO_3 in solid phase (Figure 26).

© 2020 Tous droits réservés.
lilliad.univ-lille.fr

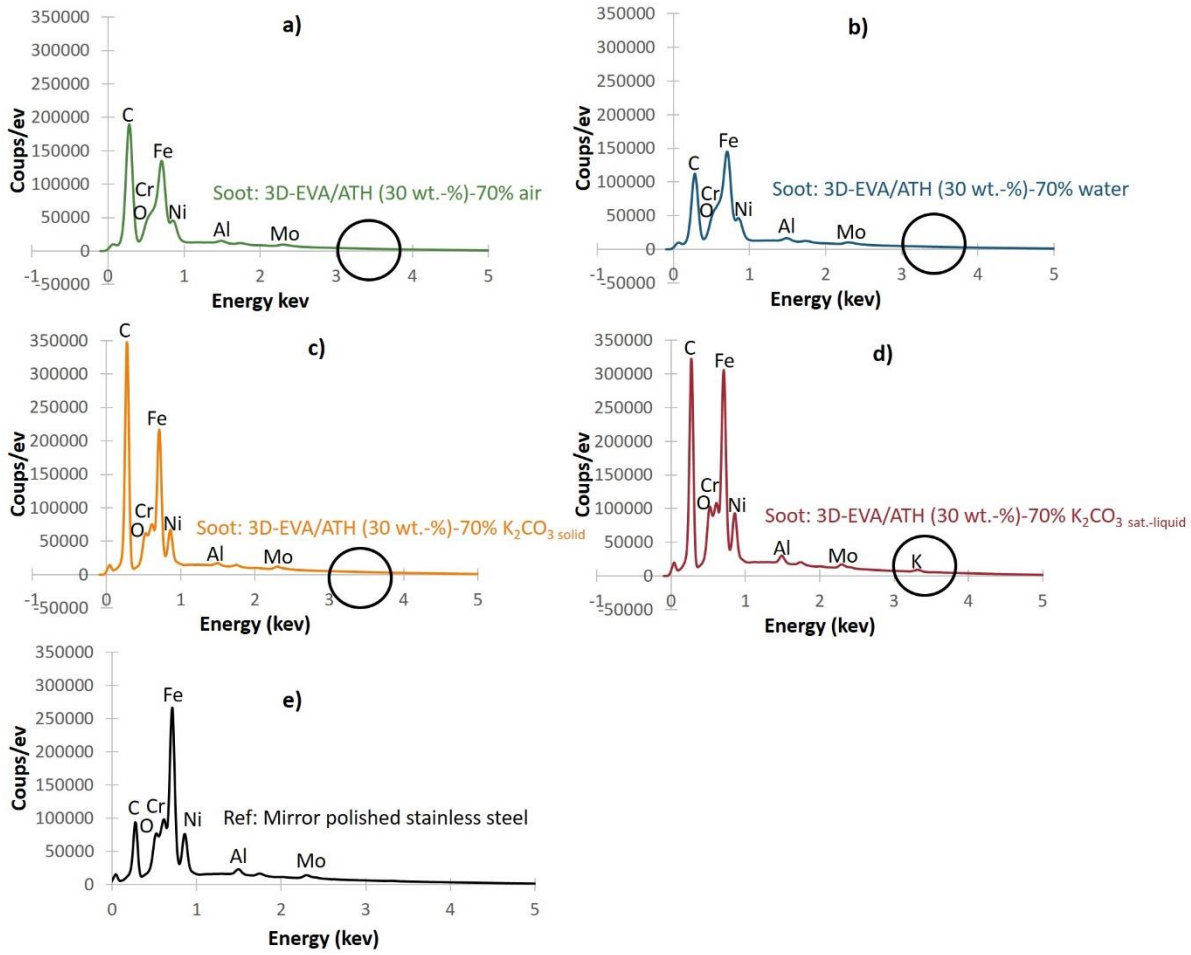

Figure 26. Soot particles EDS spectra of: a) 3D-EVA/ATH (30 wt.-%)-70% air, b) 3D-EVA/ATH (30 wt.-%)-70% water, c) 3D-EVA/ATH (30 wt.-%)-70% $K_2CO_{3\ solid}$, d) 3D-EVA/ATH (30 wt.-%)-70% $K_2CO_{3\ sat.-liquid}$, e) Mirror polished stainless steel.

Finally, to better understand the gas phase combustion mechanism, the amount CO, CO_2 and H_2O evolved as a function of time during the cone experiments were plotted for each sample studied (Figure 27) (gas phase measurements described in materials & methods part (page 171)). Whatever the gas, 3D-EVA/ATH (30 wt.-%)-70% air, 3D-EVA/ATH (30 wt.-%)-70% water and 3D-EVA/ATH (30 wt.-%)-70% $K_2CO_{3\ solid}$ exhibit the same behavior and the curves are almost superimposed. 3D-EVA/ATH (30 wt.-%)70% $K_2CO_{3\ sat.-liquid}$ releases less quantity of water (peaks at 2.5 10^7 ppm compared to 3.5 10^7 ppm for other system studied). But, the water emission of 3D-EVA/ATH (30 wt.-%)70% $K_2CO_{3\ sat.-liquid}$ is spread over time (from 2.5 10^7 to 1.5 10^7 ppm, until 500 s MLCC test) compared to the other systems where a peak is reached at 200 s and decreasing rapidly after. The comparison of CO_2 and CO release points out that 3D-EVA/ATH (30 wt.-%)-70% $K_2CO_{3\ sat.-liquid}$ has a different behavior compared to the other samples. The system with $K_2CO_{3\ sat.-liquid}$ releases less CO_2 and more CO gases compared to the other systems (Figure 27 a and Figure 27 b). Indeed, as regards CO_2 release for 3D-

© 2020 Tous droits réservés.

lilliad.univ-lille.fr

EVA/ATH (30 wt.-%)-70% $K_2CO_{3\ sat.-liquid}$, a peak at 10^7 ppm is reached after 30 s MLCC test and dramatically reduced afterward, unlike other systems where a 3.5 times higher peak is reached and maintained to $2.5.10^7$ ppm until 400 s. Regarding CO release (Figure 27 a), a higher CO emission is observed for 3D-EVA/ATH (30 wt.-%)-70% $K_2CO_{3\ sat.-liquid}$ (peak at 90 ppm), compared to the other systems. Based on the comparison between CO and CO_2 emission release, a more incomplete combustion occurred for 3D-EVA/ATH (30 wt.-%)-70% $K_2CO_{3\ sat.-liquid}$, compared to the other systems. Indeed, Figure 27 d shows the CO/CO_2 ratio evolution during the MLCC test. For 3D-EVA/ATH (30 wt.-%)-70% $K_2CO_{3\ sat.-liquid}$, the CO/CO_2 ratio immediately increases when sample ignites, and remains high during the MLCC test. In comparison, this ratio is low until 300 s for 3D-EVA/ATH (30 wt.-%)-70% air and until 400 s for 3D-EVA/ATH (30 wt.-%)-70% water and 3D-EVA/ATH (30 wt.-%)-70% $K_2CO_{3\ solid}$, and then increases and reaches the same value as 3D-EVA/ATH (30 wt.-%)-70% $K_2CO_{3\ sat.-liquid}$. These differences highlight that reactions in gas phase at the beginning of test, release less energy because of the higher CO/CO_2 ratio, and thus a more incomplete combustion occurs for the system with K_2CO_3 liquid, compared to the other samples.

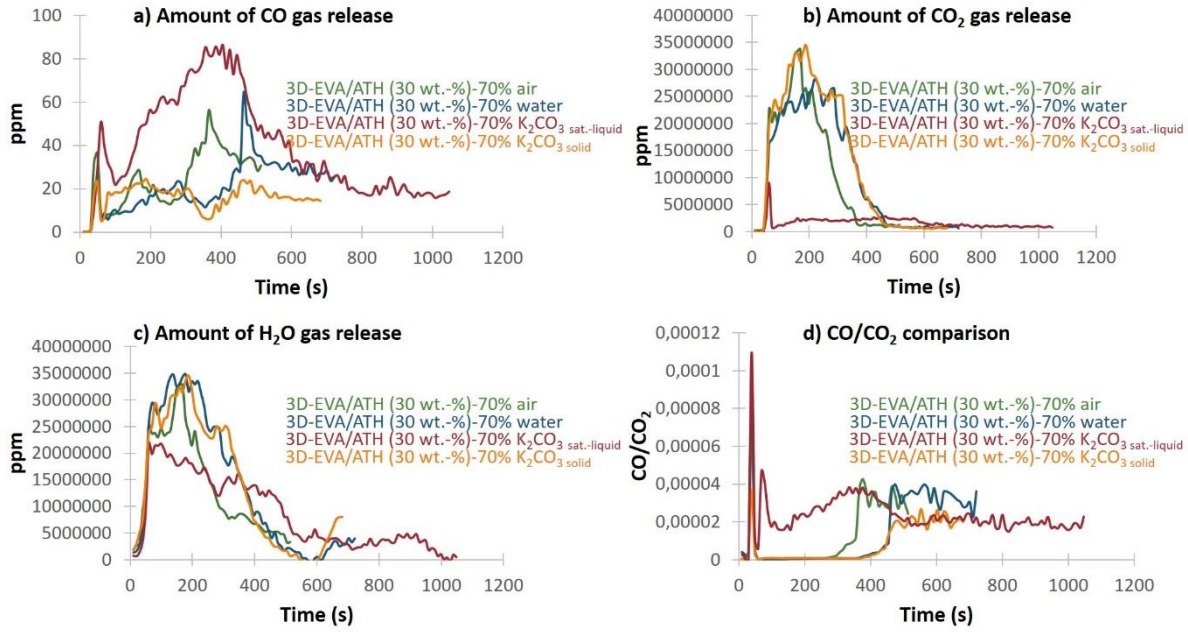

Figure 27. Amount of gas release during MLCC test for each sample studied (a) for CO, b) for CO_2, c) for H_2O).

2.2.3.2. Condensed phase analysis after fire testing

The mechanism of protection of the materials containing K_2CO_3 was investigated analyzing the condensed phase. Figure 28 shows energy spectra from EDS analysis of all residues obtained after MLCC tests (fully described in materials & methods part (page 174)). First of all, C, O

© 2020 Tous droits réservés.
lilliad.univ-lille.fr

Thèse de Laura Geoffroy, Université de Lille, 2020

and Al were detected for all systems. These elements were expected and come from alumina (dehydration of ATH) and EVA decomposition [150]–[154]. Moreover, no peak between 3.2 and 3.4 keV (K element) was detected for sample with air and water (as expected) while a peak is clearly observed between 3.2 and 3.4 keV. for 3D-EVA/ATH (30 wt.-%)-70% $K_2CO_{3\ solid}$ and 3D-EVA/ATH (30 wt.-%)-70% $K_2CO_{3\ sat.-liquid}$. These results were confirmed by EDS mapping of K element for each sample studied (Figure 28). In Figure 28 a and Figure 29 b, the few yellow points observed correspond to the continuous background. In Figure 29 c and Figure 29 d, K element is clearly identified and observed in these both residues. It evidences that K-based molecules also remain in the condensed phase and they are not all transported into the gas phase.

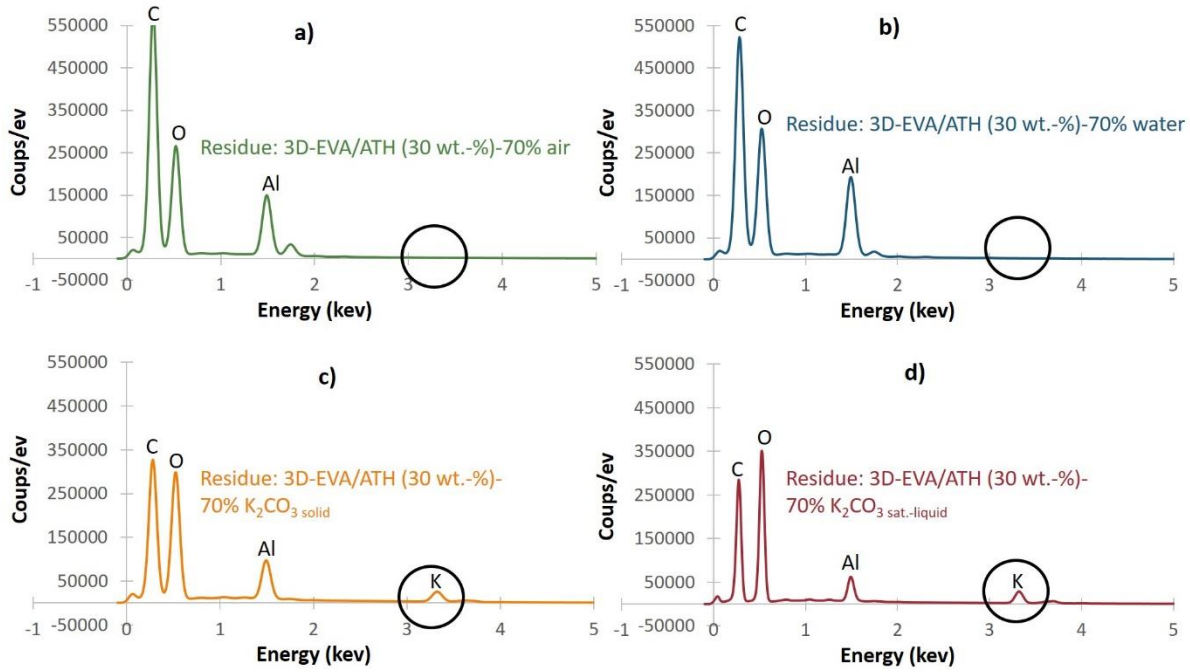

Figure 28. Residue EDS spectra of: a) 3D-EVA/ATH (30 wt.-%)-70% air, b) 3D-EVA/ATH (30 wt.-%)-70% water, c) 3D-EVA/ATH (30 wt.-%)-70% $K_2CO_{3\ solid}$, d) 3D-EVA/ATH (30 wt.-%)-70% $K_2CO_{3\ sat.-liquid}$.

© 2020 Tous droits réservés.

lilliad.univ-lille.fr

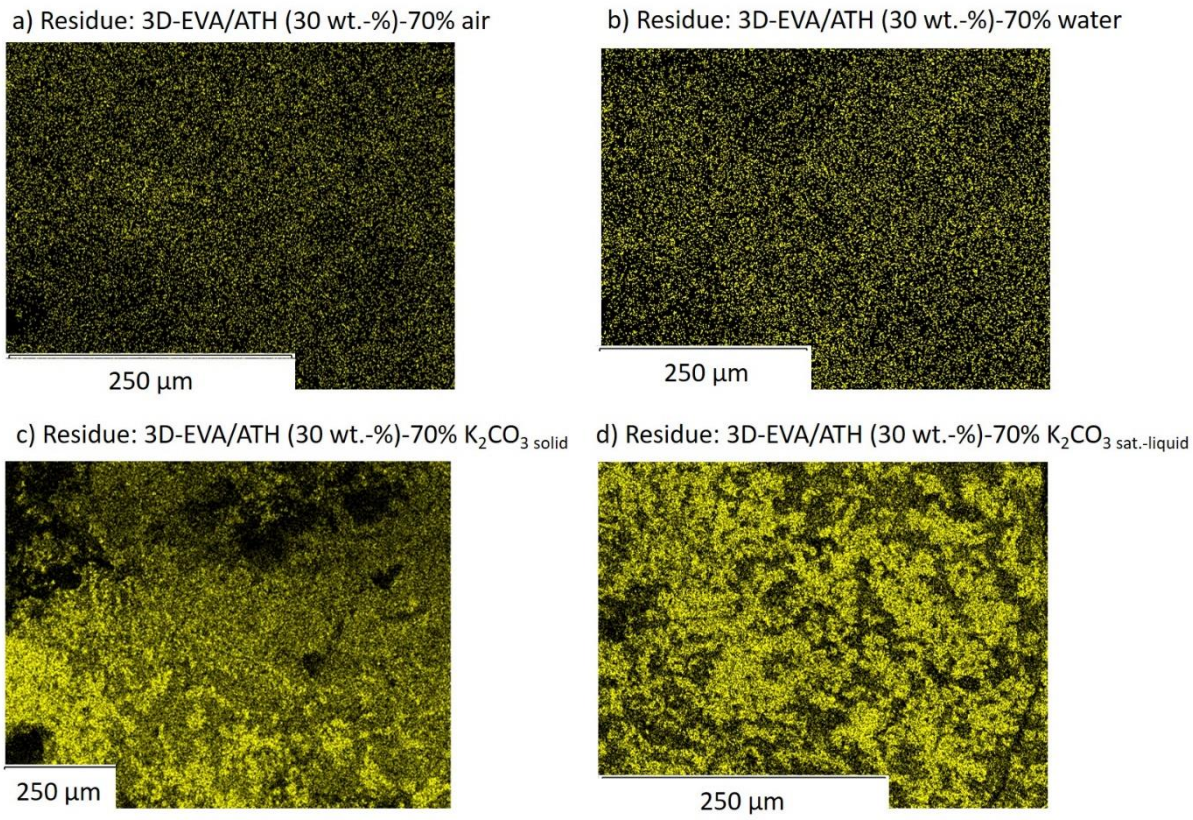

Figure 29. EDS mapping of K after MLCC test in residue of: a) 3D-EVA/ATH (30 wt.-%)-70% air, b) 3D-EVA/ATH (30 wt.-%)-70% water, c) 3D-EVA/ATH (30 wt.-%)-70% K_2CO_3 solid, d) 3D-EVA/ATH (30 wt.-%)-70% K_2CO_3 sat.-liquid.

The 3D-EVA/ATH (30 wt.-%)-70% K_2CO_3 solid and 3D-EVA/ATH (30 wt.-%)-70% K_2CO_3 sat.-liquid residues were analyzed by XRD to investigate the changes of K_2CO_3 (following the set-up described in materials & methods part (page 174)). Figure 30, Figure 31 and Figure 32 show the X –ray spectra (counts per second as function of $\theta/2\theta$). The two residues exhibit the same spectra (Figure 30) and almost no difference can be distinguished. For the system with K_2CO_3 sat.-liquid, broader bands were obtained compared to system with K_2CO_3 solid. It suggests 3D-EVA/ATH (30 wt.-%)-70% K_2CO_3 sat.-liquid residue has a higher amorphous phase than 3D-EVA/ATH (30 wt.-%)-70% K_2CO_3 solid residue. The amorphous phase detected could be assigned to Al_2O_3 from the ATH dehydration in EVA [150]. In the two residues, three crystalline phases were identified: $KAl(CO_3)(OH)_2$, $KHCO_3$ and $Al(OH)_3$ (Figure 31 and Figure 32). These crystalline structures suggest that: i) K_2CO_3 reacts with ATH and/or alumina to form a potassium aluminum carbonate hydroxide, ii) a part of alumina residue is rehydrated to form $Al(OH)_3$ (according to this reaction: $Al_2O_3 + 3\ H_2O \rightarrow 2\ Al(OH)_3$ [162]), due to water evolution. As a consequence, as the same species are formed in the residues of the two system, it is reasonable to assume that the THR reduction is mainly due to gas phase action of K_2CO_3.

© 2020 Tous droits réservés.
lilliad.univ-lille.fr

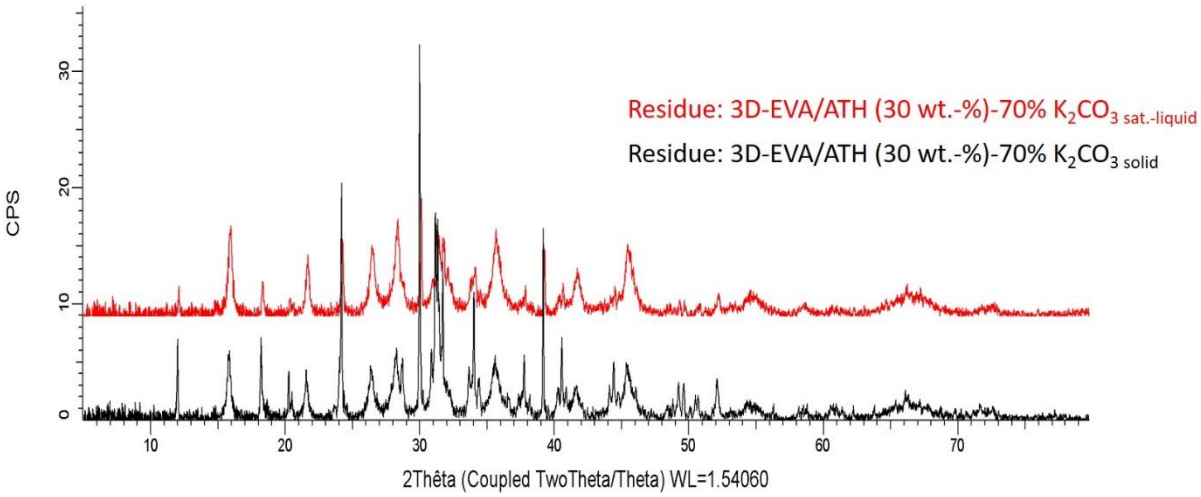

Figure 30. XDR spectra comparison between 3D-EVA/ATH (30 wt.-%)-70% $K_2CO_{3\ solid}$ residue and 3D-EVA/ATH (30 wt.-%)-70% $K_2CO_{3\ sat.-liquid}$ residue.

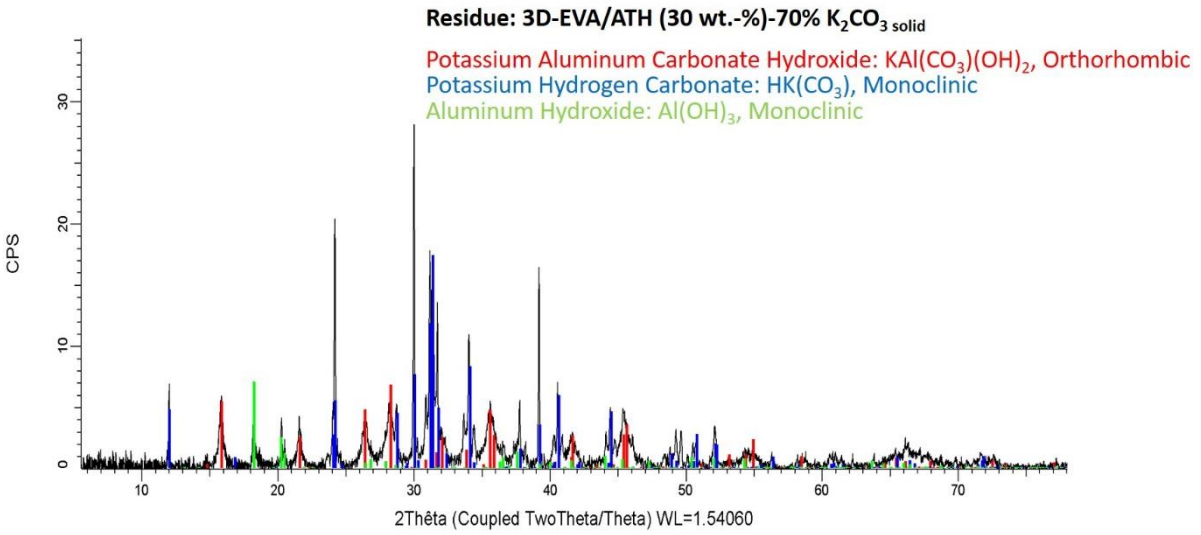

Figure 31. XDR spectrum of 3D-EVA/ATH (30 wt.-%)-70% $K_2CO_{3\ solid}$ residue.

© 2020 Tous droits réservés.

lilliad.univ-lille.fr

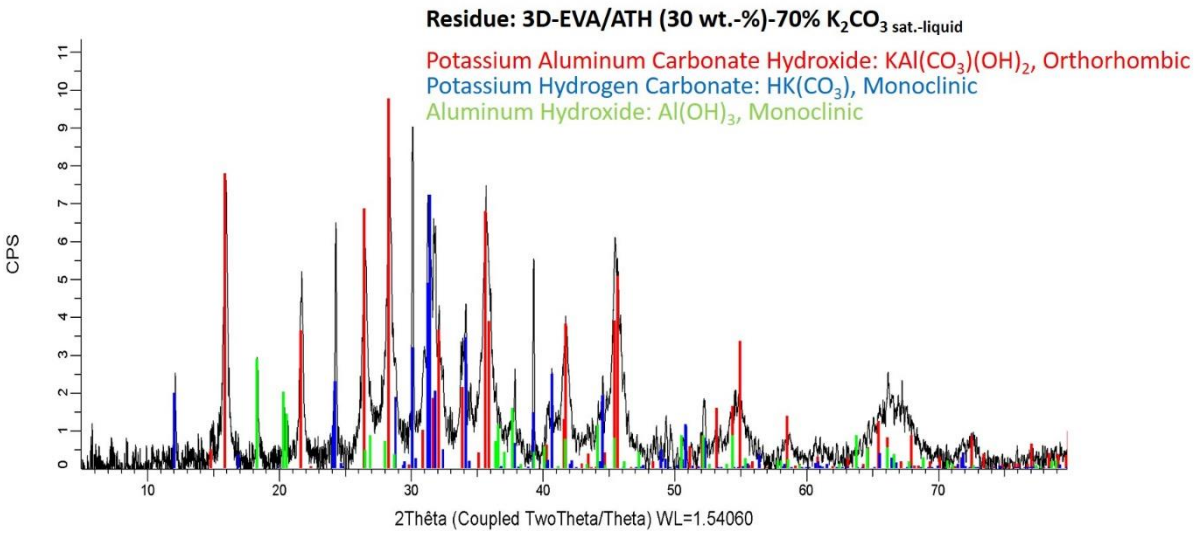

Figure 32. XDR spectrum of 3D-EVA/ATH (30 wt.-%)-70% $K_2CO_{3\ sat.-liquid}$ residue.

3. Discussion

In this work, the influence of the design of materials in terms of reaction to fire was studied. A lightweight design was tested with empty cells inside material. In case of 3D-EVA/EG (10 wt.-%) a strong decrease of HRR was measured when voids are incorporated inside materials. These differences can be explained by (Figure 33 a): i) the compacity of entangled network (caused by the graphite expansion) changing, ii) the reduction of the 'fuel' load caused by the design modification, and iii) the lower thermal conductivity of hollow structure comparing to non-hollow structure can delay the heat transfer as long as the cells stand during burning, and hence HRR is decreased. For the material with 3D-EVA/ATH (30 wt.-%)-70% air, flame-retardant polymer melts and burns, and the cells (created by the new design) are filled. As a consequence, the design is no longer maintained and does not enhance the performance (Figure 33 b). In the case of 3D-EVA/ATH (65 wt.-%), EVA also melts and burns but concurrently ATH dehydrates and makes an alumina-type ceramic (Figure 33 c). In addition to that, fuel load generated by the new design is less. Moreover, as Figure 21 illustrated, the hollow structure is kept during burning. So, it is possible to assume that empty cells reduce the heat propagation (due to their lower thermal conductivity) and improve the fire retardancy of the materials. Therefore, the combination of water evolution (dilution), ceramization (physical mass transfer barrier) and lower 'fuel' load (caused by the new design) stops the combustion. Thus, with this sandwich material, the change of design allows to increase the fire protection without any formulation modification.

© 2020 Tous droits réservés.
lilliad.univ-lille.fr

Thèse de Laura Geoffroy, Université de Lille, 2020

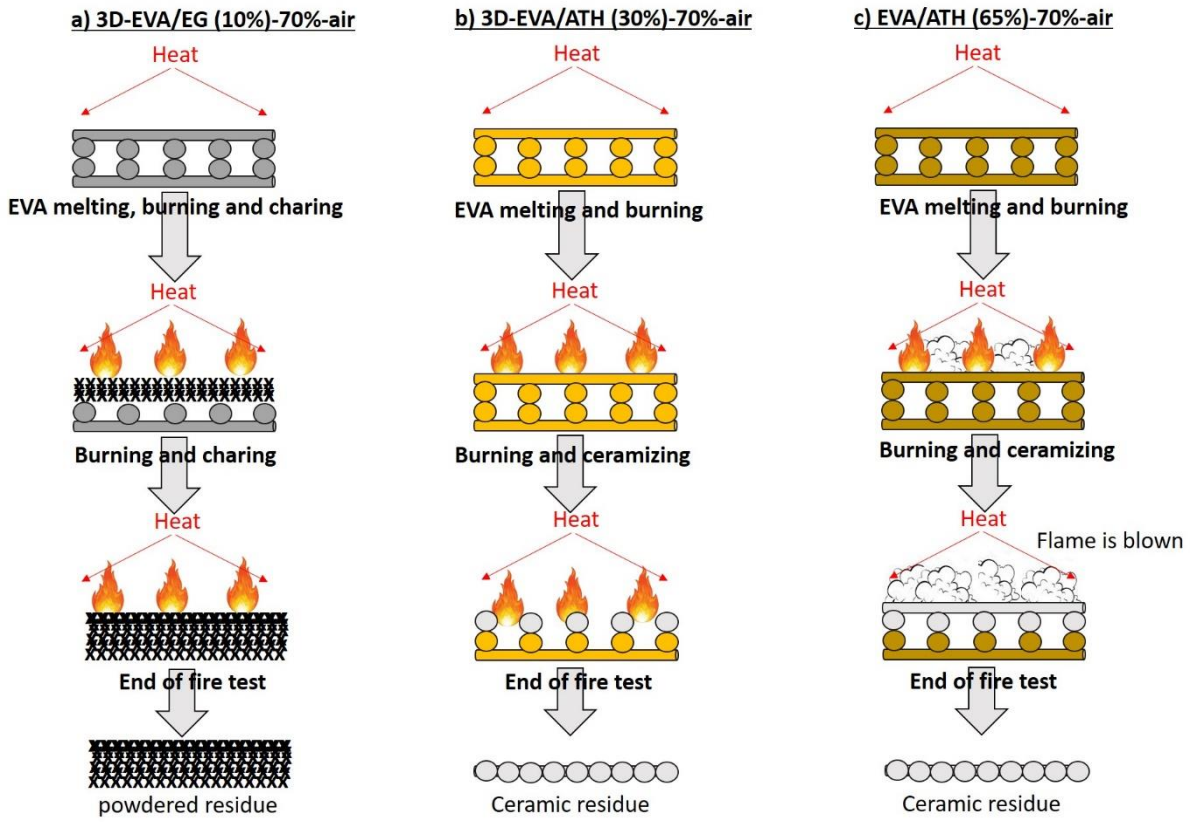

Figure 33. Illustration of fire behavior mechanism for 3D printed plate with 30%polymer (70% voids inside materials) for a) 3D-EVA/ATH (30 wt.-%), b) 3D-EVA/ATH (65 wt.-%), c) 3D-EVA/EG (10 wt.-%).

Based on this very promising design, air was substituted by another phase to create biphasic sandwich multi-materials in the case of 3D-EVA/ATH (30 wt.-%). As it was previously highlighted, the design of 3D-EVA/ATH (30 wt.-%)-70% air has not a significant influence compared to standard design (3D-EVA/ATH (30 wt.-%)-0% air). (Figure 34 a). In the case of the sample containing only water (Figure 34 b), EVA melts and burns and water vaporizes. But the amount of water is not enough to play a significant role for enhancing the fire performance (no reduction of HRR). Figure 34 c) illustrates the case where cells are filled with powdered K_2CO_3. When this sample is heat exposed: the EVA matrix melts and burns, but K_2CO_3 powdered does not decarbonize because the external heat flux is too low to make the decarbonation of K_2CO_3 (891°C). So, no improvement of the fire performance is observed. No potassium-based compound was transported into the gas phase but ATH and/or alumina residue react with powdered K_2CO_3 and form a potassium aluminum carbonate hydroxide which remains in the condensed phase. On the opposite, when K_2CO_3 is solubilized in water, K_2CO_3 is dissociated as: $K_2CO_{3(s)} + H_2O \rightarrow KOH + KHCO_3$. When sample ignites, a lot of gases is evolved (visual observation). The solution reaches its boiling temperature and vaporizes leading

© 2020 Tous droits réservés.

lilliad.univ-lille.fr

to the transportation of KOH (or K/H_2O) into the flame (Figure 34 d) (proven by the color change of flame and soot analysis by EDS). At the same time $KHCO_3$ (transported into the flame by the vapor when the solution evaporated upon heating) decomposes between 100 and 120°C according to the endothermic reaction: $2\ KHCO_3 \rightarrow K_2CO_{3\,(s)} + CO_{2\,(g)} + H_2O_{\,(g)}$. Thus, two nonflammable gases ($CO_{2\,(g)}$ and $H_2O_{\,(g)}$) were produced and absorbed heat from the fire (dilution of the flame) [163]–[166]. In the same time, the remaining $K_2CO_{3(s)}$ also react with ATH and/or alumina residue and form a potassium aluminum carbonate hydroxide (as 3D-EVA/ATH (30 wt.-%)-70% $K_2CO_{3\ solid}$). Overall, the mechanism of action is then: i) KOH (or K/H_2O) is transported into the flame by the vapor (when the solution evaporated upon heating) and react via free radical reactions [164], [165], and ii) the additional release of $CO_{2\,(g)}$ and $H_2O_{\,(g)}$ dilutes the flame and (iii) the combination of these two effects permits the rapid extinguishment of the flame and THR and pHRR are strongly reduced. The main step responsible to the flame extinction is mainly due to the transport of K_2CO_3 (K^+ ionized in water) by the vapor upon heating. It favors then K^+ to interact in the gas phase as it was evidenced in Figure 25 observing the flame color changes.

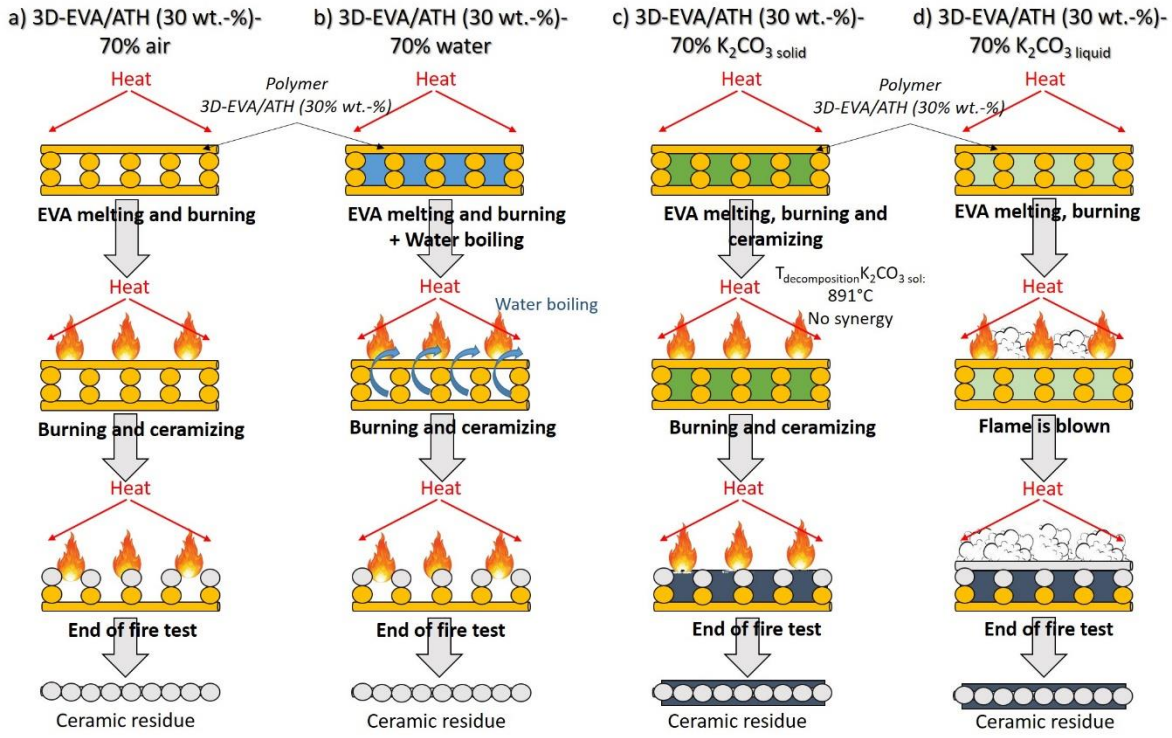

Figure 34. Illustration of fire behavior mechanism of new biphasic sandwich multi-materials (a) 3D-EVA/ATH (30 wt.-%)-70% air, b) 3D-EVA/ATH (30 wt.-%)-70% water, c) 3D-EVA/ATH (30 wt.-%)-70% $K_2CO_{3\ powdered}$, d) 3D-EVA/ATH (30 wt.-%)-70% $K_2CO_{3\ liquid}$).

© 2020 Tous droits réservés.
lilliad.univ-lille.fr

Thèse de Laura Geoffroy, Université de Lille, 2020

4. Conclusion

A new way of thinking was proposed in this chapter. To reach better reaction to fire, the influence of design was tested instead of changing the material formulation as it is usually done. A new design inspired from honeycomb structures was elaborated with voids inside materials to reduce both the weight of the flame retardant materials (3D-EVA/EG (10 wt.-%), 3D-EVA/ATH (30 wt.-%) and 3D-EVA/ATH (65 wt.-%)) and to create versatile systems. Two different plates were printed (such as sandwich materials) and composed of two shells completely filled with 100% polymer, and core with a certain amount of polymer inside (50% or 30%). These designs were evaluated by cone calorimetry and revealed better fire protection performances than standard design. New biphasic sandwich multi-materials were then elaborated with 3D-EVA/ATH (30 wt.-%)-70% air as basic material to improve its flame retardancy. The empty cells created by the design were filled in with water or potassium carbonate in solid or liquid phase. The system with potassium carbonate in the liquid phase revealed fast flame extinguishment (due to H_2O and CO_2 emission and the release of K and KOH into the flame) and hence, this material exhibited extremely low HRR and THR during the heat exposure. This work proves that 3D printing is a promising way to design efficient flame retarded polymers, leading to a new way of thinking for flame retardant community: improve flame retardancy by design modification rather than just by changing materials chemistry.

However, due to the inherent porosity of 3D printed materials and the use of liquid phase, some leakage issues appear during the sample processing. An optimization of design will be done in the next chapter.

© 2020 Tous droits réservés.

lilliad.univ-lille.fr

Key points

- ✓ New design elaboration: Sandwich material with 50 or 70% air inspired from biomimicry.
- ✓ No fire protection improvement for the design with 50% air (except for EVA/EG (10 wt.-%) material), but high improvement for 3D-EVA/ATH (65 wt.-%)-70% air.
- ✓ Combination of various phases (liquid and solid) to improve fire protection performance of 3D-EVA/ATH (30 wt.-%)-70% air: New biphasic sandwich multi-materials.
- ✓ Extremely low HRR for the biphasic sandwich multi-material with K_2CO_3 in liquid phase: full mechanism investigation with a gas and condensed phase action and a fast flame extinguishment.
- ✓ Design modification allows to reach better fire protection performances.
- ✓ **Drawback:** leakage issue coming from the use of liquid phase.

© 2020 Tous droits réservés.
lilliad.univ-lille.fr

Thèse de Laura Geoffroy, Université de Lille, 2020

Chapter 3: 3D Printed Sandwich Materials Filled with Hydrogels for Extremely Low Heat Release Rate

In this chapter, an optimization of the solution developed in the chapter 2 (of this part) is proposed. This optimization consists in filling the core of the previously described EVA/ATH (30 wt.-%) sandwich multi-material (composed of a core of EVA/ATH with square shaped empty cells so that 30% of the resulting core plate is composed of EVA/ATH in the end and two full skins of the sample polymer) with fire retardant hydrogels (Figure 35) rather than water-based solutions. First, from an engineering point of view, this would allow to overcome the leakage issue. Concurrently, the aim is also to take advantage of the hydrogel properties to entrap in a controlled way high amount of water as well as additional fire retardants.

Hydrogels are indeed composed of a polymer network cross-linked in water. The resulting material can be either solid or highly viscous depending on the network, the fabrication process, and the cross-linking system, with water being the major component. Some hydrogels are already used for protection against fire, mainly as active components in extinguishing systems [167], [168]. Illeperuma et al. [169] suggested the idea of using them as fire resistant solution in fabric laminates, since their high water content could limit the temperature rise for a certain time, until water evaporates and dilutes the reactive species in the flame to blow it out.

Despite their high potential, they have only been used as active fire protective solution [170], [171], and never as potential fire retardant material. In the present study, such use of hydrogel is enabled thanks to the use of the 3D-printed hollow polymer core acting as a container for the hydrogel. Three polymers which easily form hydrogels in water through different gelation processes were investigated: alginate, agar and poly(vinyl alcohol) (PVA). The different gelation processes, could provide insights on if and how this has an influence on the fire behavior of the final material.

Fire retardant additives were introduced in the hydrogel. Vermiculite, lamellar clay, filled hydrogels were prepared. Vermiculite was already tested as fire retardant filler in polymer formulation [172], [173] or in thin coatings, such as in layer-by-layer systems [174], [175]. It is believed to act as a char promoting agent and as physical barrier against heat and mass transfer [175]. In a second step, the possibility of including K_2CO_3 in the hydrogel formulation was examined to take advantage of its gas phase action against fire [155]. All samples were tested by mass loss cone calorimetry at an external heat flux of 50 kW/m². Full characterizations by

© 2020 Tous droits réservés.

lilliad.univ-lille.fr

confocal microscope, Electron Probe Micro Analysis (EPMA), and XRD before and after fire tests were also carried out, to investigate the fire protection mechanism.

The work pertaining to this chapter was published in ***Polymer Degradation and Stability*** journal: **https://doi.org/10.1016/j.polymdegradstab.2020.109269** [176].

KEYWORDS: Additive manufacturing, Design, Hydrogel, Sandwich multi-materials, Flame retardancy

Aims

- ✓ Prevent leakage issue from liquid phase: Elaboration of sandwich 3D printed multi-materials, filled with hydrogel phase.
- ✓ Characterization and fire testing of new sandwich 3D printed multi-materials filled with hydrogel and vermiculite hydrogel to see their influence on fire protection performance.
- ✓ Combination of vermiculite hydrogel and potassium carbonate in sandwich 3D printed multi-materials and fire testing.
- ✓ Full mechanism investigation.

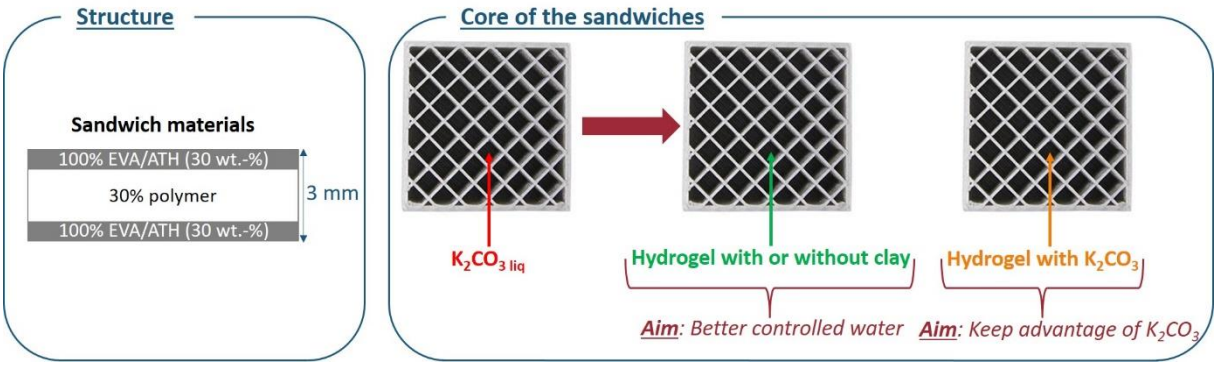

Figure 35. Concepts of sandwich flame retardant 3D printed multi-materials filled with hydrogel.

© 2020 Tous droits réservés.
lilliad.univ-lille.fr

Thèse de Laura Geoffroy, Université de Lille, 2020

1. Samples description

Based on a previous chapter 2 (part 2), the same sandwich design was conceived. The materials, materials' formulations and 3D printing process were fully described in materials & methods part (pages 162 and 164). The sandwich material consists of two skins made of 100% filled layers of EVA/ATH (30 wt.-%), and a partially-filled core (30% of polymer), as illustrated in Figure 36. To be able to fill the empty cells of the core created by the design and thus elaborate the sandwich multi-materials with various phases, the top skin was printed separately from the bottom skin and core.

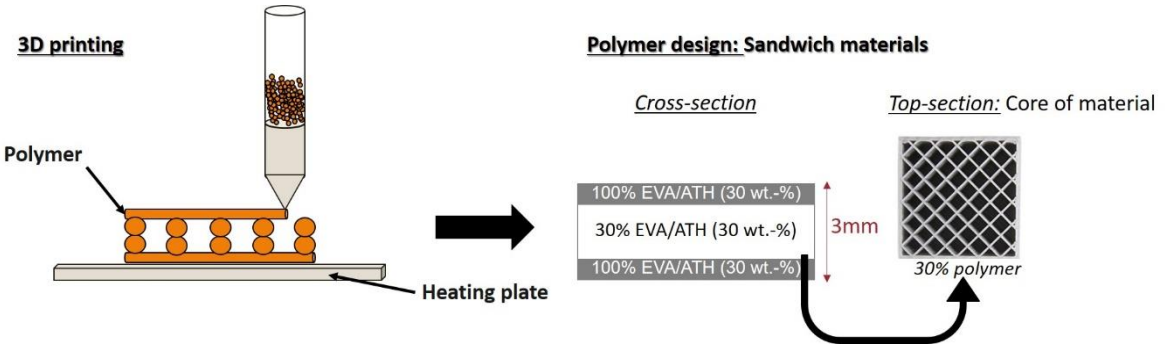

Figure 36. 3D printing process and design elaboration.

At the same time, three hydrogels named hydrogel A, B and C were prepared. They are respectively composed of alginate, agar and PVA borax. To improve their fire retardant performances, four new composite hydrogels containing vermiculite or vermiculite and K_2CO_3 were also elaborated. The hydrogel set-up was fully described in materials & methods part (page 167). Then, a controlled mass (around 2.5 g) of these different hydrogels was incorporated in the empty cells of the core polymer design before (or after for C, C+VMT and A+VMT+K_2CO_3) carrying the cross-linking step as described in materials & methods part (page 167). Indeed, as highlighted in materials & methods part (page 167), the gelation process differs according to the hydrogel: i) a physical cross-linking is performed for hydrogel A by using a gelation bath composed of citric acid and $CaCl_2$, ii) in the case of hydrogel B, the gelation occurs during the cooling down to room temperature of the gel and, iii) for hydrogel C, the addition of borax under stirring and the cooling at room temperature provokes the gelation. It is noteworthy that K_2CO_3 was only incorporated in hydrogel A+VMT using a "cold way" process to obtain a gel (as fully described in materials & methods part (page 168)), because the formation of a hydrogel in presence of K_2CO_3 is not possible with hydrogel B and C. It is assumed that due to the basic pH of K_2CO_3 in water, the formation of gel is very difficult and not achievable in certain cases.

© 2020 Tous droits réservés.

lilliad.univ-lille.fr

Afterwards, the design is sealed by fusing the edges of the polymer top skin to the polymer plate at 200°C, thereby forming the final hydrogel sandwich multi-material. Seven samples were therefore prepared, their name and composition are gathered in Table 15.

To evaluate the efficiency of using hydrogel, instead of air or liquid phase, the results obtained were compared with those obtained in chapter 2 (of this part) [155]. Two additional samples were also prepared to facilitate the comparison: 3D-air, and 3D-$K_2CO_{3\ sat.-liquid}$, where the empty cells in the core created by the design are left empty or filled in with a saturated solution of potassium carbonate, respectively.

Table 15. Name and description of samples prepared.

Name of the samples		3D printed polymer part		Phase incorporated in core	
		Composition	Weight ratio	Composition	Weight ratio
1	3D-H A	EVA/ATH (30 wt.-%)	0.67 ± 0.01	Hydrogel: Alginate	0.33 ± 0.01
2	3D-H A+VMT		0.70 ± 0.02	Hydrogel: Alginate+VMT	0.30 ± 0.02
3	3D-H A+VMT+K_2CO_3		0.72 ± 0.01	Hydrogel: Alginate+VMT+K_2CO_3	0.28 ± 0.01
4	3D-H B		0.75 ± 0.01	Hydrogel: Agar	0.25 ± 0.01
5	3D-H B+VMT		0.73 ± 0.02	Hydrogel: Agar+VMT	0.27 ± 0.02
6	3D-H C		0.73 ± 0.03	Hydrogel: PVA/Borax	0.27 ± 0.03
7	3D-H C+VMT		0.74 ± 0.01	Hydrogel: PVA/Borax+VMT	0.26 ± 0.01
8 ref	3D-air		1	Air	0
9 ref	3D-$K_2CO_{3\ sat.-liquid}$		0.72 ± 0.02	Liquid: Saturated solution of K_2CO_3	0.28 ± 0.02

2. Results

2.1. Characterizations before fire test

Mass, thickness and liquid or hydrogel amount of each system are gathered in Table 16. All hydrogel sandwich multi-materials have almost the same global mass (9.3 g ± 0.7 g) and thickness (3 mm ± 0.1 mm). The hydrogel mass incorporated in the empty cells of the core

© 2020 Tous droits réservés.
lilliad.univ-lille.fr

Thèse de Laura Geoffroy, Université de Lille, 2020

created by the polymer design is very close for all systems and is equal in average to 2.6 g ± 0.3 g.

Table 16. Composition of sandwich multi-materials.

Polymer matrix	Mass (g)	Thickness (mm)	Liquid / hydrogel amount (g)
3D-air	5.82 ± 0.03	3 ± 0	/
3D-K_2CO_3 sat.-liquid	9.4 ± 0.2	3 ± 0.2	2.6 ± 0.2
3D-H A	9.40 ± 0.03	3.1 ± 0.1	3.1 ± 0.1
3D-H A+VMT	9.5 ± 0.3	3 ± 0.2	2.8 ± 0.1
3D-H A+VMT+K_2CO_3	9.9 ± 0.1	3 ± 0.2	2.8 ± 0.2
3D-H B	9.5 ± 0.2	3 ± 0.2	2.33 ± 0.04
3D-H B+VMT	9.2 ± 0.2	3 ± 0.2	2.5 ± 0.2
3D-H C	8.6 ± 0.6	3 ± 0.1	2.3 ± 0.1
3D-H C+VMT	9.0 ± 0.4	3 ± 0.2	2.3 ± 0.2

For VMT containing systems, the dispersion of VMT particles in hydrogel was observed by confocal microscopy (Figure 37). In the case of hydrogel A+VMT (Figure 37 a), the gelation involved the use of an acidic bath (composed of acid citric and $CaCl_2$ as described in materials & methods part (page 167)). However, the fluorescent agent loses its fluorescence properties in acidic environment [177]. Indeed, a low pH reduces the luminescence intensity of the fluorescein, which is the fluorescent agent used in this work (fully described in materials & methods part (page 173)). It is noteworthy that the fluorescence is affected because of the existence of different protolytic reactions in the excited state due to the presence of carboxyl group contained in acidic environment [177]. Therefore, the fluorescence is lost during the hydrogel A+VMT formation preventing its observation. For this reason and only for this case, VMT dispersion observation was done on the liquid dispersion of VMT and alginate before gelation. Moreover, for this kind of hydrogel the gelation starts immediately when the hydrogel is immerged in gelation bath. It is thus reasonable to assume that VMT dispersion in liquid and hydrogel phases is quite similar. Figure 37 a highlights that VMT particles (in black) are well dispersed in liquid phase, without preferential orientation (isotropic distribution of VMT). In hydrogel A+VMT+K_2CO_3, VMT particles show similar dispersion as in hydrogel A+VMT (Figure 37 b). VMT particles have no preferential orientation and are well dispersed. The presence of K_2CO_3 seems to have no influence on the VMT dispersion.

© 2020 Tous droits réservés.

lilliad.univ-lille.fr

Regarding hydrogel B+VMT, VMT particles are oriented in preferential directions as illustrated in Figure 37 c (anisotropic distribution of VMT). After gelation, the structure is frozen, and therefore any organization of the VMT particles wouldn't be possible if there wasn't a primary organization of VMT in the polymer/clay mixture [178], [179]. Evidence of such local ordering in dilute clay suspension was observed for example by Poiron et al. [180]. Therefore, the observed preferential orientation happens before gelation and can be explained by the slow gelation process. For reminder, hydrogel B+VMT is formed when the hot solution of B+VMT is cooled down at room temperature. Therefore, during the cooling, and thanks to the low viscosity of the VMT/agar hot solution, VMT particles have enough time to organize and have an anisotropic distribution before it is frozen by the increase in viscosity as the gel forms.

In the case of hydrogel C+VMT, some VMT particles are oriented, while others form stacks (Figure 37 d). Indeed, as the PVA/VMT dispersion is stirred throughout the hydrogel elaboration (fully described in materials & methods part (page 168)), it is possible that under the shear constraints anisotropic patterns are formed where domains of VMT particles align according to the direction of the stress [181]. Upon borax addition, it is assumed that two mechanisms occur. First, borax cross-linking brings PVA chains closer to each other [182], meaning that vermiculite platelets are brought into tighter aggregates, which explains the VMT stacks observed. Then, the anisotropic structures formed during stirring are frozen by crosslinking, and become more pronounced as the shear stress increase with the viscosity of the medium [183], which justifies the preferential orientation of some VMT particles in Figure 37 d.

These observations thus reveal that VMT particles have different dispersion behaviors depending on the kind of hydrogel and gelation process considered: an isotropic distribution is observed for hydrogel A+VMT and hydrogel A+VMT+K_2CO_3, and an anisotropic distribution is shown for hydrogel B+VMT and C+VMT.

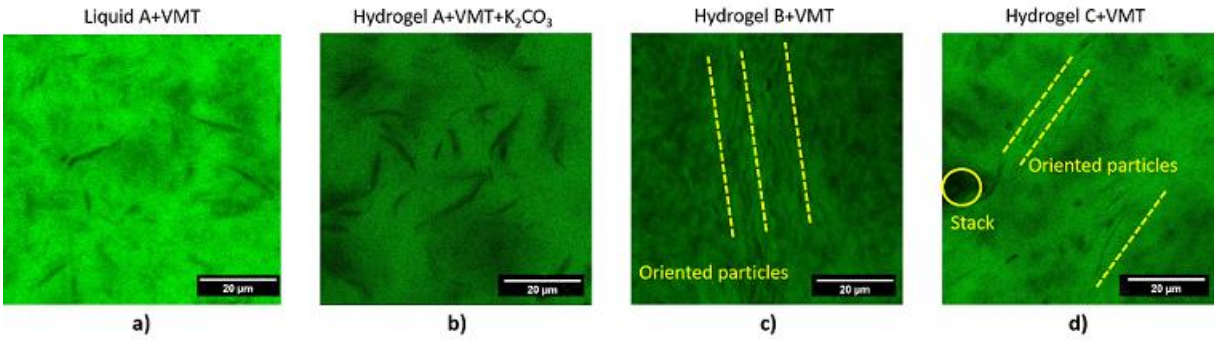

Figure 37. VMT particles dispersion using confocal microscopy (a) Liquid A+VMT, b) Hydrogel A+VMT+K_2CO_3, c) Hydrogel B+VMT, d) Hydrogel C+VMT).

© 2020 Tous droits réservés.
lilliad.univ-lille.fr

Thèse de Laura Geoffroy, Université de Lille, 2020

2.2. Fire behavior

Figure 38, Figure 39 and Table A2 report the Heat Release Rate (HRR) curves versus time and the fire protection characteristics values, i.e. TTI, THR and pHRR of all samples. As illustrated by Figure 38 a, 3D-H A and 3D-H A+VMT both delay the ignition time. Indeed, for these systems, TTI is respectively about 6.5 and 7.5 times longer than the TTI of 3D-air. However, the incorporation of these hydrogels does not improve the THR and pHRR compared to the reference (Figure 38, Figure 39 and Table A2).

On the contrary, for the sandwich multi-materials 3D-H A+VMT+K_2CO_3, the incorporation of K_2CO_3 leads to drastic improvement of THR and HRR (Figure 38 and Figure 39), as it was expected from the behavior of 3D-$K_2CO_{3\ \text{sat-liquid}}$ [155]). It was the reason of the elaboration of this material. The THR of 3D-H A+VMT+K_2CO_3 are reduced by 88%, 66% and 88%, compared to the reference (3D-air), 3D-$K_2CO_{3\ \text{sat-liquid}}$ and sample with hydrogel A+VMT, respectively. A pHRR reduction of 86%, 38% and 84% is also measured for sample with hydrogel A+VMT+K_2CO_3 compared to reference, sample containing K_2CO_3 in liquid phase, and 3D-H A+VMT, respectively (Figure 38 and Table A2). However, the TTI is slightly increased compared to the reference and the sample containing a saturated K_2CO_3 solution (1.9 and 1.5 times longer than 3D-air, 3D-$K_2CO_{3\ \text{sat.-liquid}}$), and considerably decreased (3.9 lower) compared to 3D-H A+VMT. Consequently, K_2CO_3 enables to dramatically reduce the THR and pHRR of the system containing hydrogel A+VMT at the expense of the TTI. However, the gelation process differs from 3D-H A+VMT (where a gelation bath of $CaCl_2$ is used, see materials & methods part (page 168)) to 3D-H A+VMT+K_2CO_3 (where gelation is obtained by a cold way process for 24 h, see materials & methods part (page 168)), what could also be accountable for the variation obtained for TTI measured during MLCC tests. Regarding the second comparison between the system with hydrogel A+VMT+K_2CO_3 and the system with K_2CO_3 in liquid phase, a slight improvement is obtained for the system with hydrogel, compared to the system with K_2CO_3 in liquid phase. However, as shown in Figure 38 and Figure 39, the difference between the two systems is very low and reveals a very low THR and pHRR in both cases.

As it was the case for 3D-H A, the TTI of the system containing hydrogel B (Figure 38 b, Figure 39 and Table A2) is increased by 48 seconds (about 2.8 times longer) than 3D-air, but no reduction of THR and pHRR is obtained (28% and 0.4%, respectively) compared to 3D-air. When VMT is incorporated in hydrogel B, a completely different behavior is observed. Indeed, compared to the reference 3D-air, THR and pHRR of sample containing hydrogel B+VMT are

© 2020 Tous droits réservés.

lilliad.univ-lille.fr

dramatically decreased (by -86% and -64% respectively), whereas the TTI is rather unchanged with an increase of 5 seconds.

Regarding 3D-H C, no improvement is brought in terms of TTI, THR (-2%) and pHRR (-3%) compared to the reference. Figure 38 c shows a quick ignition of sample, with a fast extinction probably due to the water emission from hydrogel, and a second inflammation with a high heat release until the end of the test. However, when VMT is incorporated in hydrogel C, an unexpected fire behavior is observed. The THR and pHRR difference between 3D-H C+VMT and 3D-air corresponds to -82% and -36%, respectively. Regarding the TTI, a slight increase of 12 seconds was measured that is about 1.5 times higher than 3D-air. Therefore, as with 3D-H B+VMT, the incorporation of VMT in hydrogel C provides the formation a very efficient fire barrier exhibiting an extremely low THR value.

Figure 38 d reports the temperature as a function of time measured at the backside of the reference (3D-air), and of the 3D polymer samples with hydrogel inside. First, it was observed that all systems reach a steady state at 500°C after 700 s to 1500 s of fire test. Indeed, the steady state of hydrogel containing systems is reached at longer times than for 3D-air. Moreover, for hydrogel containing systems, a plateau at 100°C is registered whereas it is not obtained for the reference. This plateau is attributed to the water released during the MLCC test. Finally, a slower temperature rise is measured for hydrogel containing systems than for 3D-air and thus the decomposition of the material is delayed.

Therefore, the incorporation of hydrogel A and B in the 3D samples delays the TTI, but has no influence on THR and pHRR. No improvement is observed for hydrogel C. However, when VMT is added in hydrogel B and C an unexpected reduction of THR (> 80%) and pHRR (64% and 36% respectively) is measured, as opposed to hydrogel A where no significant decrease is observed. The incorporation of K_2CO_3 in hydrogel A+VMT allows to reach very low THR and pHRR, at the expense of TTI. To explain these fire behavior differences, visual observations of top and cross-section of residues after MLCC test were carried out and gathered in Figure 40.

© 2020 Tous droits réservés.
lilliad.univ-lille.fr

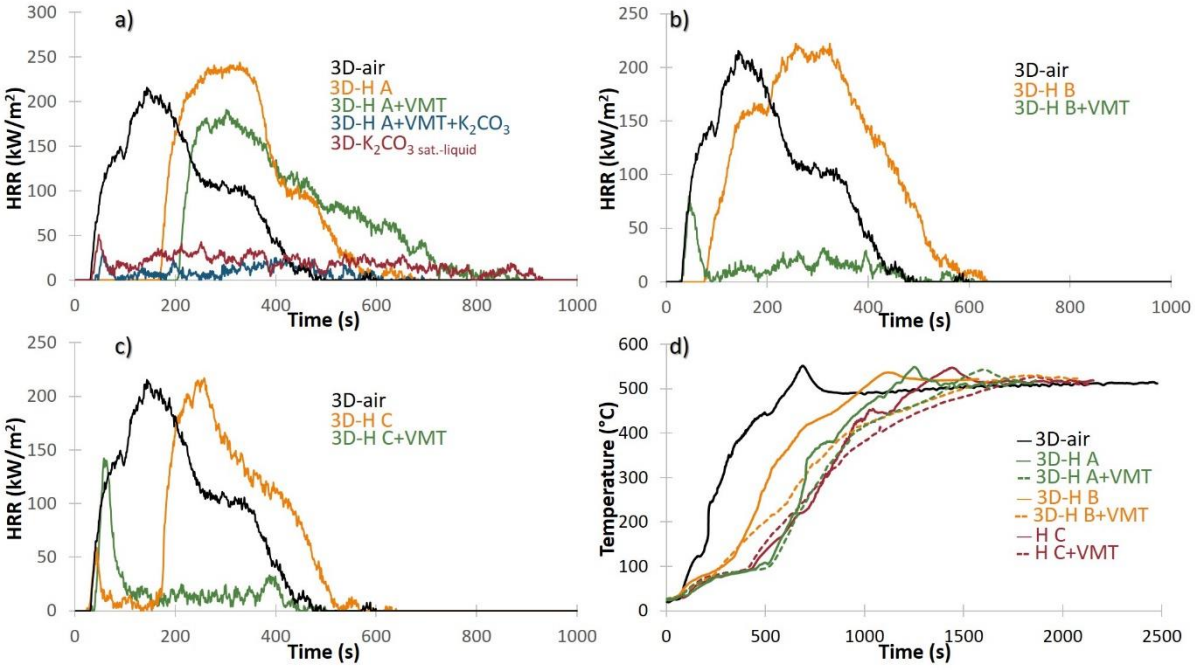

Figure 38. Fire behavior of each system studied (a) for systems with hydrogel A, b) for systems with hydrogel B, c) for systems with hydrogel C, d) evolution of temperature versus time for all systems studied.

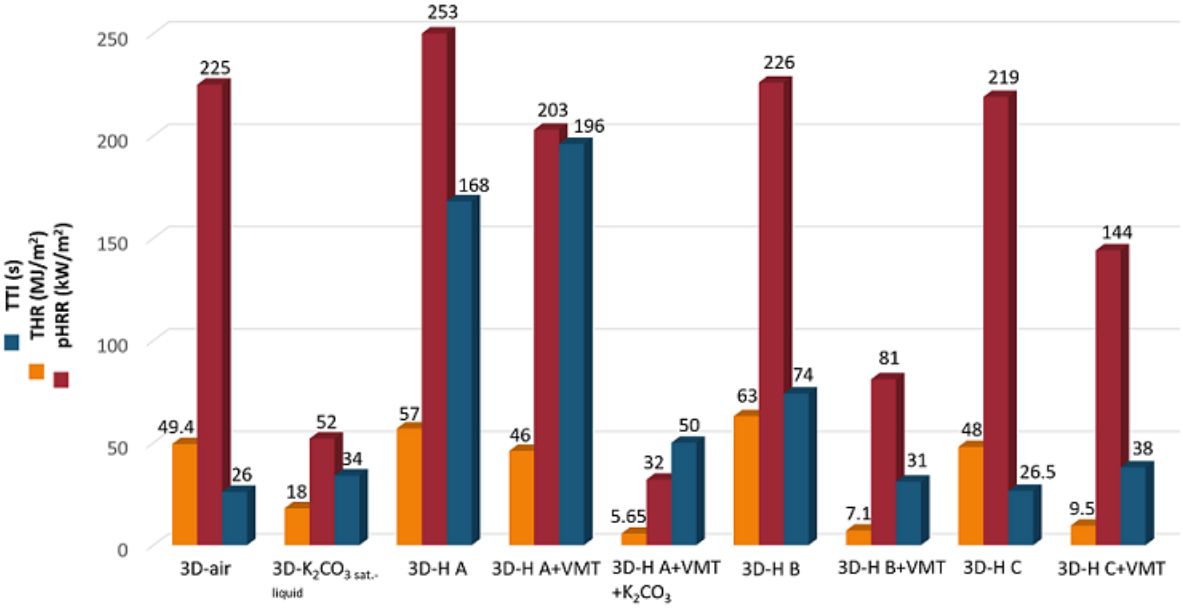

Figure 39. Fire protection performances values of each system studied.

For 3D-air, 3D-H A, 3D-H B, and 3D-H C, similar residues are observed. An agglomerate of white powder (alumina resulting from the dehydration of ATH) is obtained at the end of the MLCC test (Figure 40 a, Figure 40 b, Figure 40 e, Figure 40 g).

© 2020 Tous droits réservés.

lilliad.univ-lille.fr

For 3D-H A+VMT, a grey residue is obtained and the initial structure is partly retained. Additionally, powder agglomerates can once again be seen (Figure 40 c). For 3D-H A+VMT+K_2CO_3 residue, the structure of the residue is maintained but is very brittle. Voids and polymer core can be observed, as illustrated in Figure 40 d. When VMT is added in the two other hydrogels (hydrogel B+VMT (Figure 40 f) and hydrogel C+VMT (Figure 40 h), the initial structure is kept at the end of MLCC test. The two skins and the core with voids inside can be distinguished. A white shell is observed, with a brown polymer core in the center. The brown color is assigned to a mix of alumina residue and VMT network. To understand and explain the difference in terms of fire protection performances between systems with hydrogels containing K_2CO_3 and/or VMT, two type of analysis were made: i) the VMT orientation and distribution in residues obtained after MLCC test were observed using EPMA imaging and ii) XRD analysis were also done to highlight if crystalline network modification occurs during the heat exposure.

© 2020 Tous droits réservés.
lilliad.univ-lille.fr

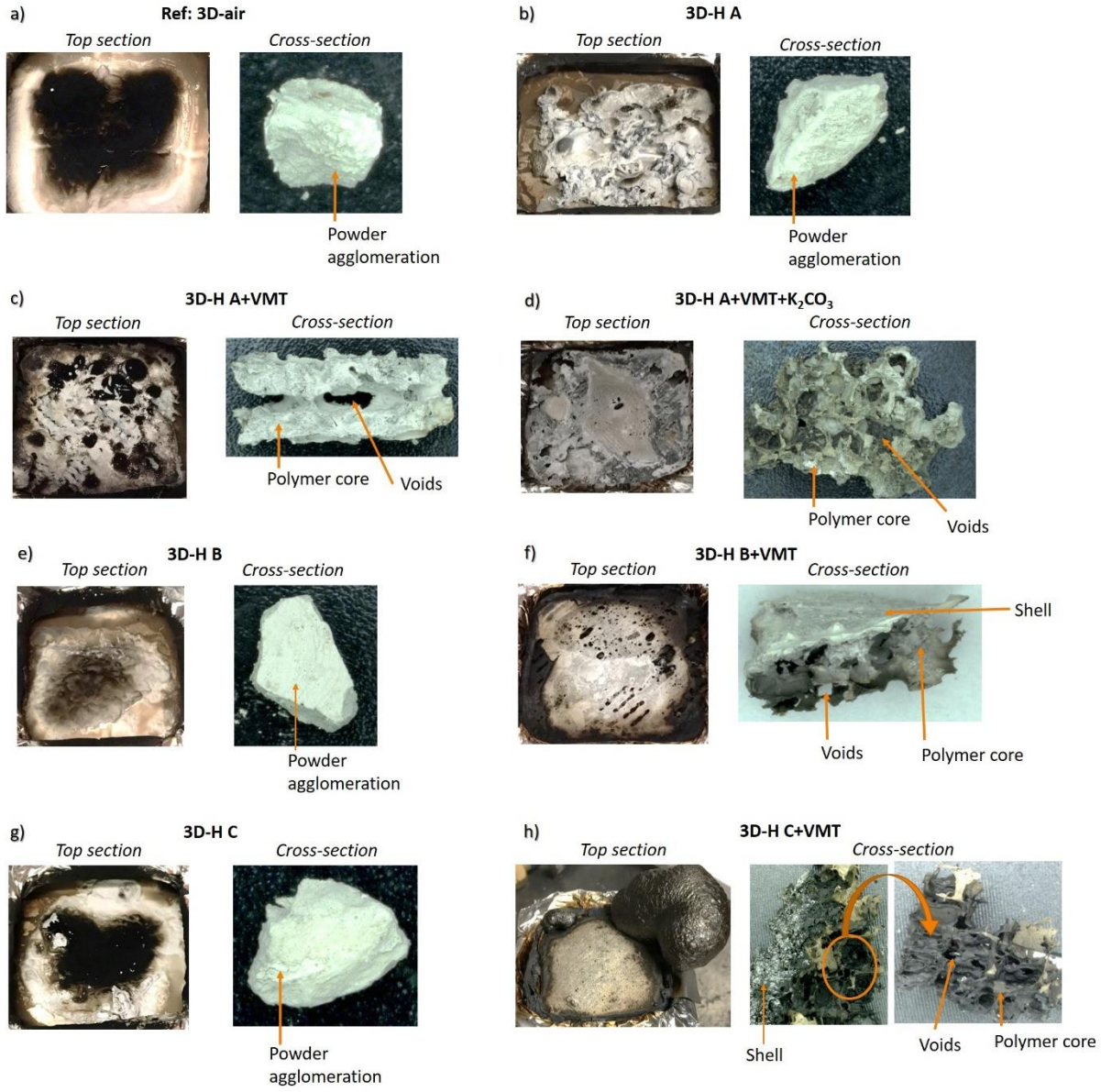

Figure 40. Top and cross-section pictures of residue after MLCC test (a) 3D-air, b) 3D-H A, c) 3D-H A+VMT, d) 3D-H A+VMT+K_2CO_3, e) 3D-H B, f) 3D-H B+VMT, g) 3D-H C, h) 3D-H C+VMT).

2.3. Mechanism investigation

A first investigation is done on the heat release rate difference between samples with hydrogel A+VMT, B+VMT and C+VMT. Then, a particular attention will be paid to the effect of K_2CO_3 in hydrogel A+VMT.

2.3.1. Clay influence investigation on the fireproofing

2.3.1.1. EPMA Observations

Figure 41, Figure 42 and Figure 43 illustrate Al, Mg and Fe distribution for the reference (3D-air) and for the system with hydrogel A and A+VMT, the system with hydrogel B and B+VMT

© 2020 Tous droits réservés.

lilliad.univ-lille.fr

and the hydrogel C and C+VMT, respectively, using EPMA analysis. Al element distribution was observed to identify alumina formed by the 3D printed polymer (EVA/ATH (30 wt.-%)) degradation and Fe and Mg were analyzed to determine the VMT particles distribution after MLCC tests. First, it was observed that the reference and all systems without VMT were only composed of alumina, as Al-mappings illustrated (Figure 41 a_1, Figure 41 a_2, Figure 42 a_1, Figure 42 a_2, Figure 43 a_1 and Figure 43 a_2). No Fe, Mg and K were identified on the mapping, and thus, Fe/Mg and K-mappings of sample with air, hydrogel A, hydrogel B and hydrogel C were not shown. For the samples containing VMT, Mg and Fe-mappings highlight a difference of VMT distribution according to the hydrogel considered. Indeed, for 3D-H A+VMT, VMT particles form clusters with some voids between each particle (Figure 41 b, Figure 41 c and Figure A3- 1 (appendix 3 (page 201))). On the opposite, VMT particles line up and tightly imbricate to form a protective layer for 3D-H B+VMT (Figure 42 b, Figure 42 c and Figure A3- 2 (appendix 3 (page 201))) and 3D-H C+VMT (Figure 43 b, Figure 43 c and Figure A3- 3 (appendix 3 (page 201))). Moreover, Al-mappings and Mg or Fe-mappings reveal that Al surrounds the VMT clusters in the case of 3D-H A+VMT or the tightly imbricated VMT networks in the case of sample with hydrogel B+VMT and C+VMT. It is also noteworthy that the Al, Fe and Mg-mappings of 3D-H B+VMT and 3D-H C+VMT are similar, which makes sense because of the similar initial chemical composition and the similar fire performance.

The distribution difference between VMT particles reveals that VMT particles have a physical effect during MLCC tests, which explains the difference in term of fire protection performances. Indeed, for the system with hydrogel B+VMT, and C+VMT, the VMT particles are organized and tightly imbricated to form a protective layer, which reduces the mass transfer in the system (the gas evolution is limited because of the high tortuosity of the layer), and thus the heat release rate [175]. In comparison, for the system with hydrogel A+VMT, some voids can be distinguished between VMT particles, and therefore mass transfer is not limited and so, the released gases feeds the flame.

To go further in the investigation of the mechanism, a study of the crystalline structure of the residue and thus the crystalline network evolution was carried out using XRD analyses.

© 2020 Tous droits réservés.
lilliad.univ-lille.fr

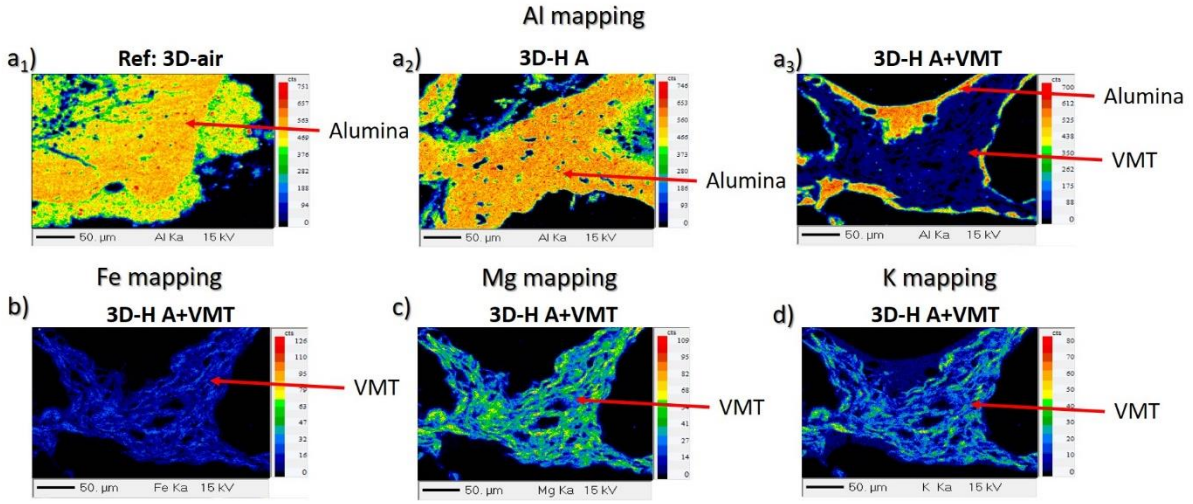

Figure 41. X-rays mappings of (a_1) Al element of 3D-air, a_2) Al element of 3D-H A, a_3) Al element of 3D-H A+VMT, b) Fe element of 3D-H A+VMT, c) Mg element of 3D-H A+VMT, d) K element of 3D-H A+VMT) cross-sections, using EPMA measurements.

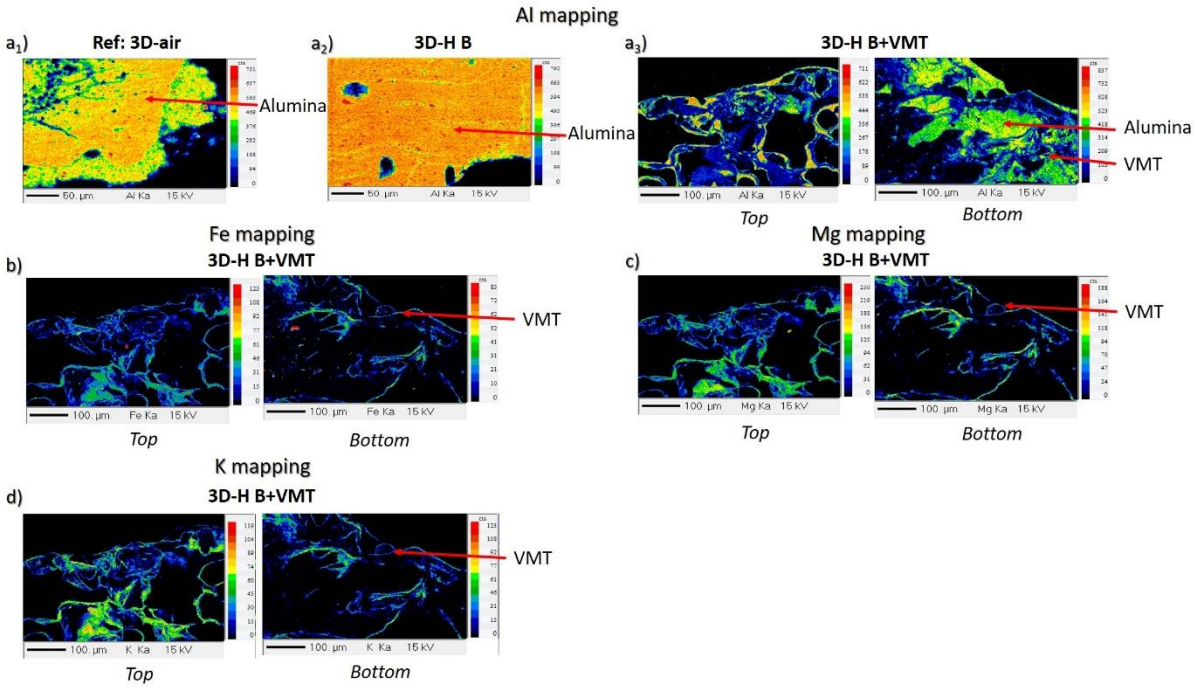

Figure 42. X-rays mappings of (a_1) Al element of 3D-air, a_2) Al element of 3D-H B, a_3) Al element of 3D-H B+VMT, b) Fe element of 3D-H B+VMT, c) Mg element of 3D-H B+VMT, d) K element of 3D-H B+VMT) cross-sections, using EPMA measurements.

© 2020 Tous droits réservés.

lilliad.univ-lille.fr

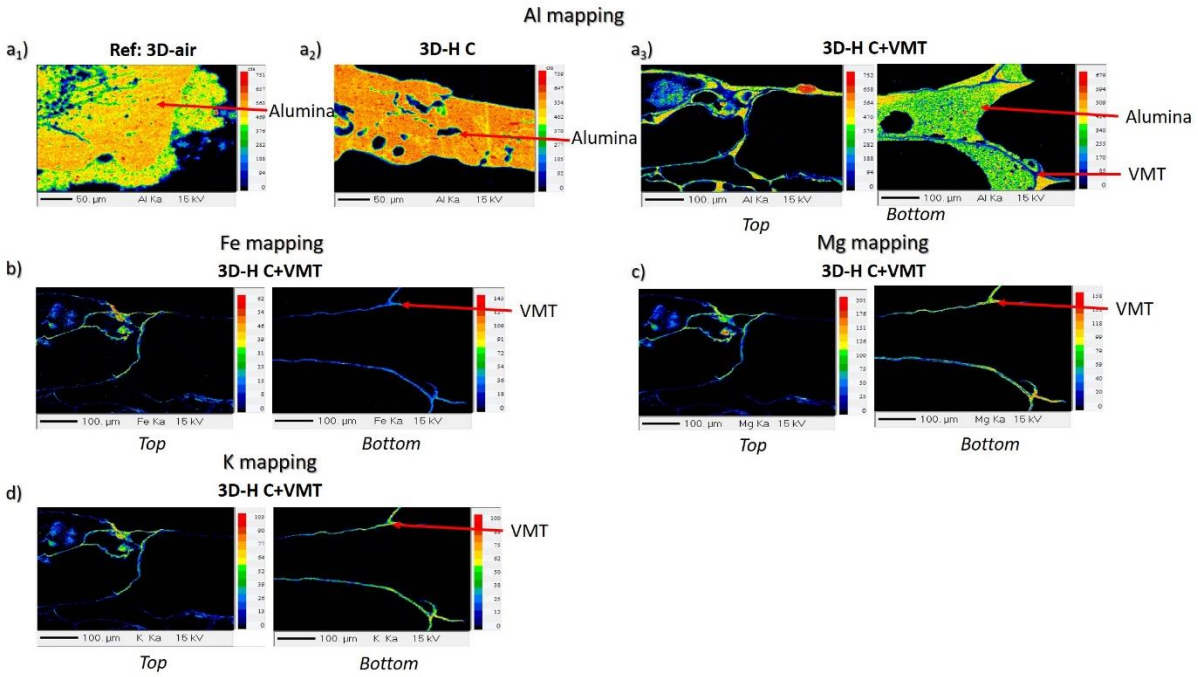

Figure 43. X-rays mappings of (a_1) Al element of 3D-air, a_2) Al element of 3D-H C, a_3) Al element of 3D-H C+VMT, b) Fe element of 3D-H C+VMT, c) Mg element of 3D-H C+VMT, d) K element of 3D-H C+VMT) cross-sections, using EPMA measurements.

2.3.1.2. XRD analysis

Figure 44 gathers the XRD scans of residues 3D-H A+VMT, 3D-H B+VMT, and 3D-H C+VMT. On all XRD patterns, similar peaks can be observed attributed to the presence of alumina and boehmite crystalline phases according to the database used for peaks identification. Indeed, the cubic alumina Al_2O_3 crystalline phase resulting from the ATH decomposition during the fire testing (Figure 44 and Figure A3- 4 (appendix 3 (page 201))) is detected by two peaks at 2θ around 60° to 67°. Moreover, a peak at 2θ value of 14° is attributed to boehmite AlO(OH) crystalline phase (Figure A3- 4 (appendix 3 (page 201))). This peak also results from ATH dehydration during the test.

Then, a peak at 2θ = 30° (Figure 44) is observed for the residue of 3D-H A+VMT, as opposed to other residues where no peak is visible. It corresponds to calcite ($CaCO_3$) crystalline phase, and results from the gelation process of hydrogel A cross-linked using calcium ions. Thus, during the fire test, hydrogel A decompose and $CaCO_3$ is formed.

Finally, other peaks (in the large region at 2θ values between 34° to 50°, from 2θ = 5° to 10° and from 2θ = 26° to 30°) are detected and mainly correspond to VMT and more specifically to the phlogopite $KMg_3(Si_3Al)O_{10}(OH)_2$ crystalline phase (Figure 44 and Figure A3- 4 (appendix 3 (page 201))). Slight differences of position are observed between residues. The

© 2020 Tous droits réservés.
lilliad.univ-lille.fr

peaks identified in two sections of the XRD patterns from 2θ = 5° to 10° and from 2θ = 26° to 30° correspond to the (00l) crystallographic plane of VMT. Their modifications reveal changes in the parameter c of the crystal structure corresponding to the d-spacing between the VMT layers [184], [185]. The peak between 5 and 10° of 3D-H A+VMT residue is detected at a higher 2θ value than the peak obtained for 3D-H B+VMT and 3D-H C+VMT obtained at the same position (Figure 44). The opposite is observed between 26° to 30° where the peak of 3D-H A+VMT residue is detected at lower 2θ value than the one of the two other residues.

To explain the variations of d-spacing, and highlight their influence against temperature, a high temperature X-ray diffraction of VMT was done (Figure 45).

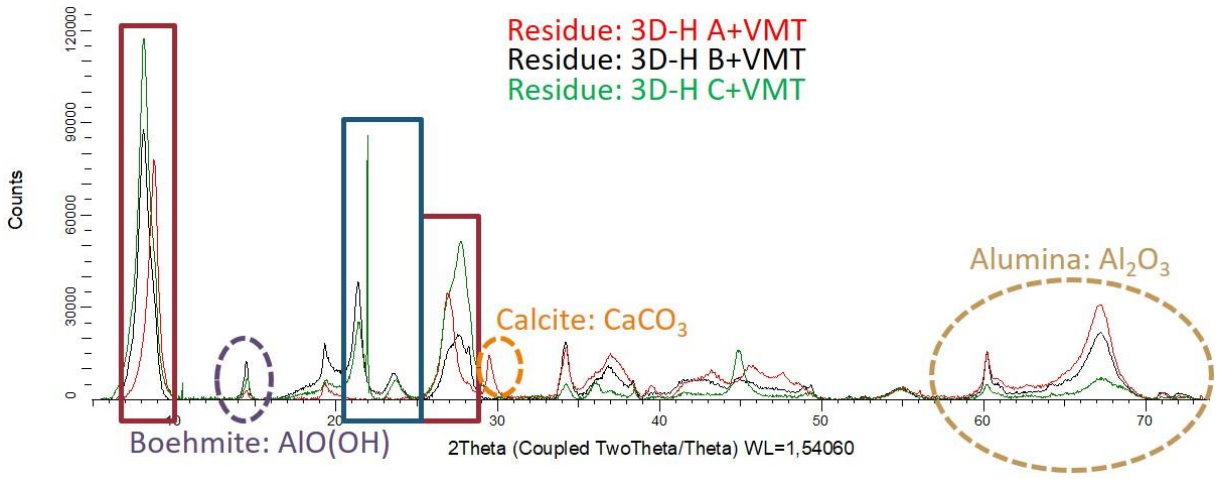

Figure 44. XRD of residues: 3D-H A+VMT, 3D-H B+VMT, and 3D-H C+VMT.

Figure 45 describes the evolution of VMT crystalline phase as a function of temperature (from 50°C to 1000°C). Two phase transitions are clearly observed at 150°C and 900°C. Two 2θ regions (from 5° to 10° and from 26° to 30°) are mainly impacted by these phase transition. The position and the shape of these peaks changes as a function of temperature. These phase transitions are due to the different hydration state of the VMT foils. For the first phase transition at 150°C, the water adsorbed on the surface and the water between interlayer is released, leading to a first crystalline transition, and thus a modification of the interlayer stacking distance [184], [185]. The second transition at 900°C provokes a slight increase of interlayer spacing (Figure 45) not clearly explain in literature. It is assumed that this second transition arises from a structural changed at high temperature [185]. For the residue 3D-H B+VMT and residue 3D-H C+VMT, the same peaks positions (from 5° to 10° and from 26° to 30°) are observed, and are similar to those measured for VMT at 100°C. Furthermore, the same observation (peaks ranging from 5° to 10° and from 26° to 30°) can be done for residue 3D-H A+VMT and for VMT at

© 2020 Tous droits réservés.

lilliad.univ-lille.fr

800°C. These crystalline phase transitions and thus the interlayer stacking distance differences can be explained by the temperature difference reached on the sample surface. Indeed, due to the lower fire protective performances and thus to the presence of flame during MLCC tests, 3D-H A+VMT is submitted to a higher temperature on the top compared to samples with hydrogel B+VMT and C+VMT where the flame is rapidly extinguished.

Moreover, in Figure 44, two peaks at 21.4° and 23.6° are identified for residues 3D-H B+VMT and 3D-H C+VMT, as opposed to the residue of 3D-H A+VMT where no peak is visible. By correlating Figure 44 and Figure 45, it is possible to suppose that both peaks do not come from VMT. Indeed, no peak is observed in Figure 45. Therefore, it is assumed that this phase corresponds to an organic phase from the polymer decomposition during the heat exposure. Indeed, a carbonaceous phase is observed in XRD diagram between 20° to 25°, fully discussed in some previous papers as for example [186]. Based on Figure 44 and the fire protective performances, this assumption makes sense because of the low heat release rate of 3D-H B+VMT and 3D-H C+VMT, compared to 3D-H A+VMT. It suggests that the carbonaceous phase has time to organize for systems with hydrogel B+VMT and C+VMT compared to system with hydrogel A+VMT, which is exposed to flame and higher temperature.

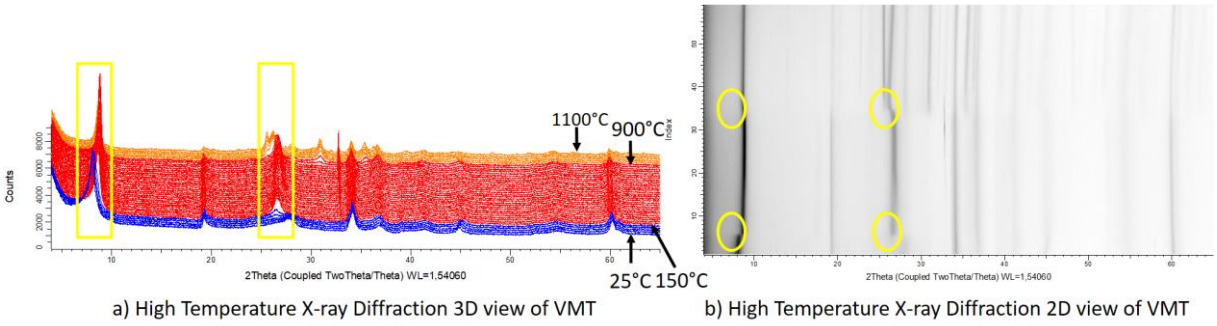

a) High Temperature X-ray Diffraction 3D view of VMT b) High Temperature X-ray Diffraction 2D view of VMT

Figure 45. High Temperature X-ray Diffraction of VMT.

XRD results pointed out the absence of chemical interaction between the components of the systems. The variation of peaks attributed to VMT is due to dehydration processes related to the difference in heat exposure time between the different samples, which have a consequence on the interlayer distance. As a conclusion, VMT has seemingly no influence on the degradation of other constituents. Therefore, its action is purely a physical process rather than a chemical one, which confirms the previous EPMA observations.

© 2020 Tous droits réservés.
lilliad.univ-lille.fr

2.3.2. K_2CO_3 influence on fireproofing

2.3.2.1. Gas phase mechanism

K_2CO_3 has been reported to act both in condensed and gas phase as shown in [155] and in the previous chapter. Figure 46 clearly highlights the presence of potassium into the flame (purple color) for the system containing hydrogel A+VMT+K_2CO_3 compared to the classical yellowish flame obtained for the system containing only hydrogel A+VMT [155]. Indeed, the coloration of flame is caused by the de-excitation of thermally excited electrons, which provokes the emission of a photon (light) with a precise wavelength depending on the electronic structure of the chemical element (K^+ leads to a purple flame coloration).

Therefore, before fire testing, K_2CO_3 is dissociated in the water of hydrogel according to this reaction: $K_2CO_{3\,(s)} + H_2O \rightarrow KOH + KHCO_3$. During MLCC tests, when the sample ignites, the solution reaches its boiling temperature and the solution is vaporized into the flame, leading to a purple flame observation because of the presence of potassium (Figure 46). As flame temperature is higher than $KHCO_3$ decomposition temperature, $KHCO_3$ decarbonizes according to the following reaction: $KHCO_3 \rightarrow CO_{2\,(g)} + H_2O_{\,(g)} + K_2CO_{3\,(s)}$. CO_2 and H_2O, two nonflammable gases, are produced, which dilute the flame and provoke its fast extinguishment, thus reducing the heat release rate during the MLCC test. Therefore, the gas phase mechanism in hydrogel phase is similar to those observed in liquid phase (solution of K_2CO_3) [155].

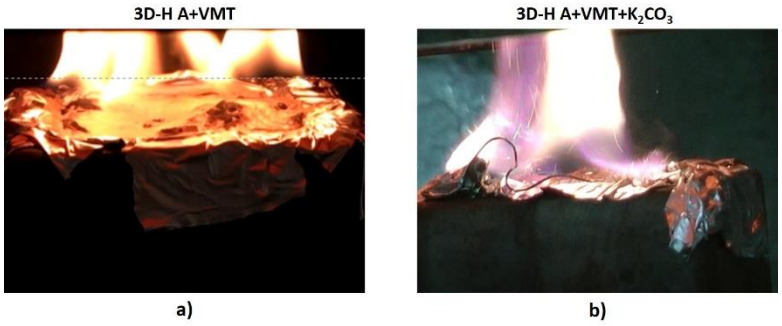

Figure 46. Visual observation of flame color (a) for 3D-H A+VMT, b) 3D-H A+VMT+K_2CO_3).

2.3.2.2. Condensed phase mechanism

The condensed phase mechanism in presence of K_2CO_3 was also investigated. XRD analyses were carried out on the 3D-H A+VMT+K_2CO_3 residue and compared to those of 3D-$K_2CO_{3\,\text{sat.-liquid}}$ residue (Figure A3- 5 (appendix 3 (page 201))). As illustrated by Figure 47, the same ($KAl(CO_3)(OH)_2$) crystalline phase was identified. Additionally, other crystalline phases attributed to VMT (phlogopite) and alumina (Al_2O_3) were observed on the XRD diagram.

© 2020 Tous droits réservés.

lilliad.univ-lille.fr

Therefore, as previously described, when the hydrogel A+VMT+K_2CO_3 is vaporized into the flame, the following reaction occurs: 2 $KHCO_3$ → $K_2CO_{3\,(s)}$ + $CO_{2\,(g)}$ + $H_2O_{\,(g)}$. The K_2CO_3 formed reacts with the ATH contained in EVA during the degradation, which leads to the formation of the crystalline phase $KAl(CO_3)(OH)_2$ identified using XRD analysis.

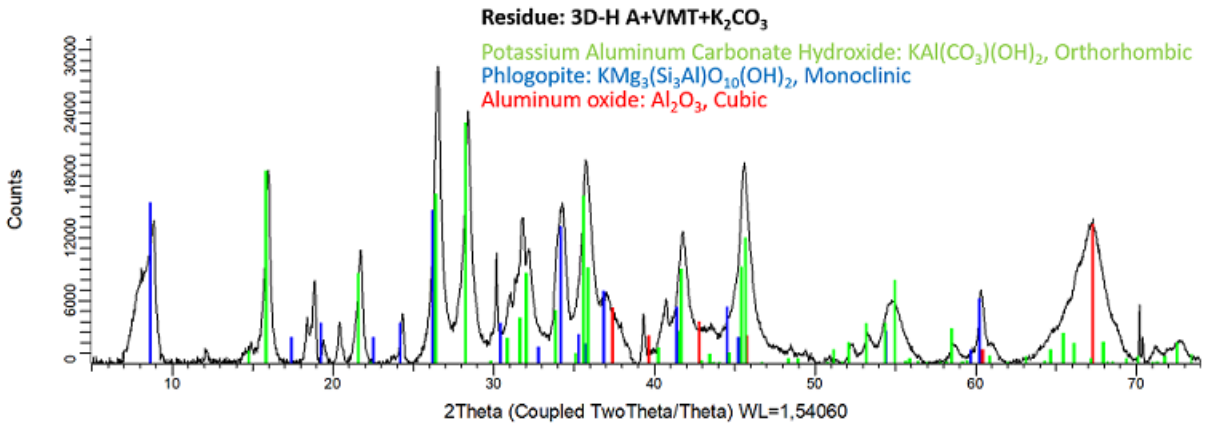

Figure 47. XRD of residue 3D-H A+VMT+K_2CO_3.

To determine the action of the VMT in the fire protective mechanism of the system containing hydrogel A+VMT+K_2CO_3, Al, Fe and Mg mappings were carried out using EPMA. As for the system with hydrogel A+VMT, no stack of VMT is observed. VMT particles form clusters with some voids between VMT particles (Figure 48 and Figure A3- 6 (appendix 3 (page 201))). Therefore, the efficiency of the VMT barrier is not as high as those formed by the systems containing hydrogel B+VMT or hydrogel C+VMT. However, VMT particles organize anyway and form a physical thermal barrier (less efficient than for system with hydrogel B+VMT and C+VMT, but still performant) which is added to K_2CO_3 thermal insulation action. Moreover, the crystalline phase composed of K and Al is confirmed on K and Al mappings. Indeed, a predominant phase (in yellow and green on Al (Figure 48 a_2) and K (Figure 48 d_2) mappings, respectively) is observed and located in the same part of the mapping.

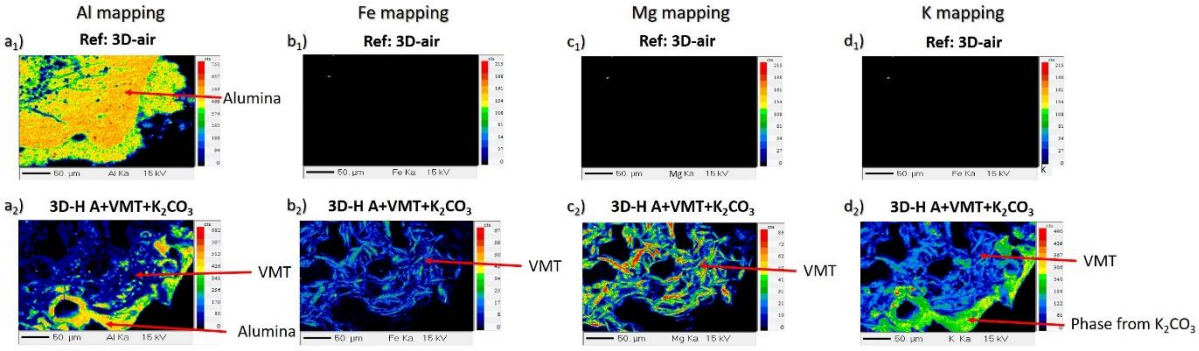

Figure 48. Cross-section X ray mapping in a) Al element, b) Fe element, c) Mg element, d) K element, using EPMA measurements of (1) 3D-air, 2) 3D-H A+VMT+K_2CO_3).

© 2020 Tous droits réservés.
lilliad.univ-lille.fr

Therefore, the efficient fire protective performance of 3D-H A+VMT+K_2CO_3 is explained by the combination of two phenomena: i) mostly due to the action of K_2CO_3 in gas and condensed phase (fully described in paper [155]]), and also with ii) the physical action of VMT particles contained in hydrogel.

3. General discussion

The mechanisms of action of the various systems studied in this work are summarized in Figure 49 and Figure 50. When 3D-H A (Figure 50 a), 3D-H B (Figure 49 a) and 3D-H C (Figure 49 c) are exposed under a radiative heat flux, the top section of the materials (a 0.6 mm-thick plate of EVA/ATH) starts to decompose as the hydrogel slowly releases water. As a consequence, a long TTI is measured compared to the reference (3D-air). However, when all water is released, the material burns and decomposes, with a high heat release rate. In comparison with system using water as sole liquid phase [155], the use of hydrogel phase allows to reach longer TTI. Therefore, it is assumed that hydrogel phase allows to better control the water releasing during the MLCC test by spreading its release over a longer time [155]. Moreover, as previously mentioned, the only difference between hydrogel A, hydrogel B and hydrogel C is the gelation process: hydrogel C contains borax which provokes a swelling phenomenon, as it is illustrated in Figure 49 c, hydrogel A is formed using a cross-linking gelation bath, and hydrogel B is obtained by cooling at room temperature. Nevertheless, these different gelation processes have no influence on the heat release rate. They only influence the water release rate, which is different according to the system studied, thus leading to a short-to-long TTI value. The water release rate is slower for hydrogel A (which is an ionically cross-linked hydrogel) than for hydrogel C and hydrogel B. It is assumed that the rate of water release from a hydrogel depends on the degree of chemical bonding of water with the network and the ease to break these bonds (which is easily in the case of hydrogel B and C compared to hydrogel A) [187], [188].

When VMT is added in the hydrogel, a completely different behavior is observed: a very low HRR is measured for samples containing hydrogel B+VMT and C+VMT compared to samples with hydrogel A+VMT. The VMT organization and its link with thermal insulating mechanism was investigated using different techniques namely confocal microscope, EPMA and XRD analysis. It is noteworthy that under temperature VMT particles organize themselves and form a network which act as a physical barrier to delay the heat propagation. The efficiency of the physical barrier formed depends on i) the initial VMT distribution in hydrogel phase, and ii) the VMT organization and orientation during the heat exposure. On the one hand, the initial VMT distribution in hydrogel phase is a significant factor to provide an efficient thermal barrier

© 2020 Tous droits réservés.

lilliad.univ-lille.fr

because it influences the formation of VMT network upon heating. On the other hand, the VMT network formed during fire testing is very important. The tighter and more organized VMT network is, the less gas can be released to feed to the flame (as it was previously described with EPMA observations). For hydrogel B (Figure 49 a) and hydrogel C (Figure 49 c) VMT particles have an anisotropic distribution, with preferential orientation (confocal microscopy observations – see Figure 37). When these samples are exposed to heat, the water contained in the hydrogel phase boils and the VMT particles migrate through to the top section. Due to their initial anisotropic distribution the VMT particles rapidly form an efficient physical barrier of high tortuosity constituted by aligned and stacked VMT platelets, which limits the gas emission, causing fast extinguishment. Therefore, a very low THR and pHRR are measured, due to this physical barrier. At the end of the fire test, the initial design is retained, which explains the efficient fire protective performances.

In comparison, VMT particles in hydrogel A+VMT (Figure 50 b) have an isotropic distribution. When 3D-H A+VMT is exposed to heat, the water contained in the hydrogel boils, and all the VMT particles migrate towards the surface without preferential orientation. The VMT particles organize in clusters, surrounded by polymer (EPMA observations – see Figure 41). The physical barrier formed in that case is not gas proof. Voids are observed between the VMT particles, allowing gases to circulate, and thus feeding the flame. Therefore, a high rate of heat release is measured. At the end, only some parts of the design are retained.

Finally, depending on the fast (for systems with hydrogel B+VMT and C+VMT) or slow (for system with hydrogel A+VMT) flame extinguishment, the crystalline structure of the VMT network is modified (XRD analysis). For the systems with hydrogel B+VMT or hydrogel C+VMT, a fast flame extinguishment is observed. The high temperature exposure time is thus less important compared to that reached for the system with hydrogel A+VMT. As a consequence, for system with hydrogel B+VMT and C+VMT, a crystalline transition similar to that obtained for VMT at 100°C is observed. It highlights a higher interlayer stacking distance. In comparison, Clusters of VMT located on surface are submitted to a high temperature due to the flame. As a consequence, the system with hydrogel A+VMT have a crystalline transition similar to that obtained for VMT at 800°C (XRD analysis – see Figure 45), which means the interlayer stacking distance is lower [184], [185]. XRD analysis thus highlight that no chemical interactions occur between the VMT particles and the polymer, and that different hydration levels and interlayer stacking distance between VMT particles are observed between the hydrogels. These analyses confirm that VMT has only a physical action.

© 2020 Tous droits réservés.
lilliad.univ-lille.fr

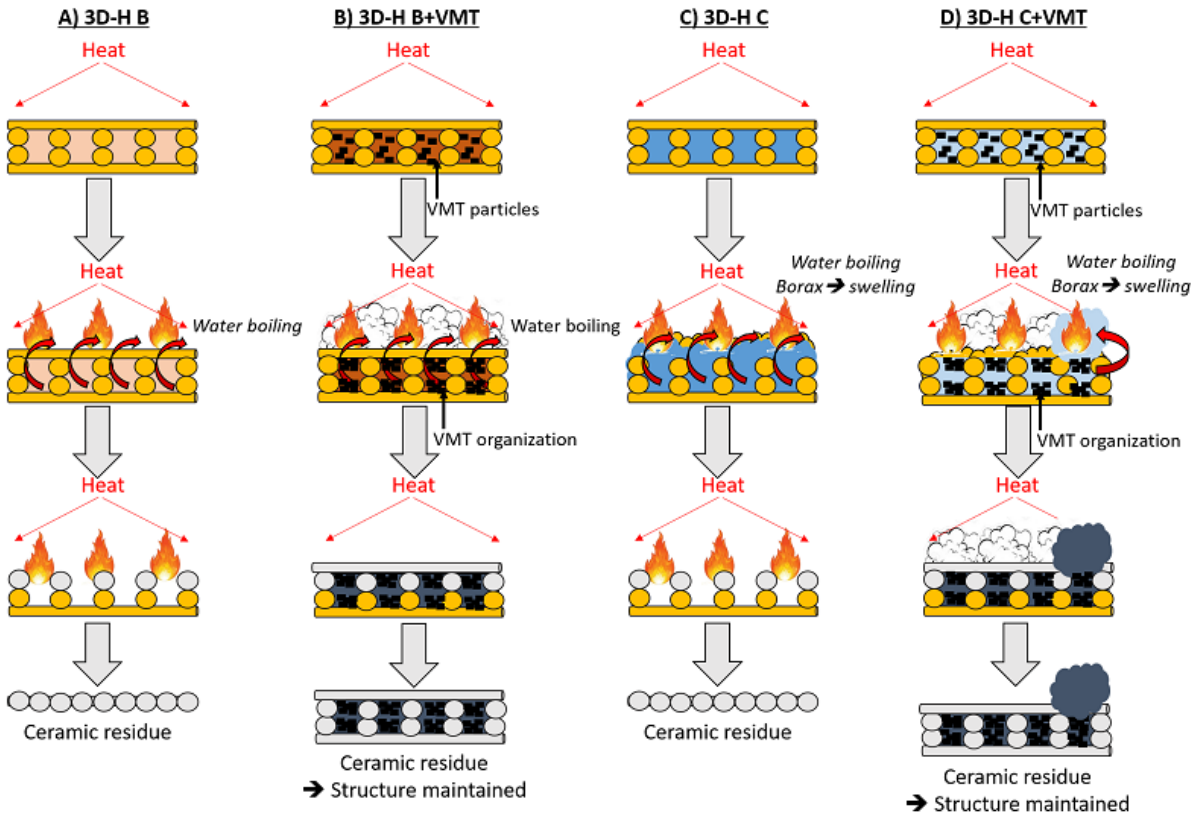

Figure 49. Illustration of fire behavior mechanism of new hydrogel sandwich multi-materials (a) 3D-H B, b) 3D-H B+VMT, c) 3D-H C, d) 3D-H C+VMT).

When VMT particles are isotropically distributed, as it is the case in hydrogel A+VMT, the physical barrier is not as efficient as previously, and thus no significant improvement is measured in terms of THR and pHRR. To improve that, K_2CO_3 was incorporated in this system. Efficient fire protection performances are measured for 3D-H A+VMT+K_2CO_3, with a very low THR and pHRR during MLCC tests. These low values can be explained by the combination of two phenomena, as illustrated in Figure 50 c. On one hand, K_2CO_3 acts in gas and condensed phase [155]. When the sample is exposed under a radiative heat flux, the water contained in the hydrogel starts to boil and vaporizes into the flame (as confirmed by the purple flame coloration). Therefore, the solution of K_2CO_3 is dissociated. With the high flame temperature, the decarbonation of $KHCO_3$ occurs and produces two nonflammable gases (CO_2 and H_2O), provoking a fast flame extinguishment. This dramatically reduces the heat release rate and consequently improves the fire protective performance of the material. In parallel, the K_2CO_3 formed reacts with the ATH contained in the polymer matrix, which leads to the formation of another ceramic composed of Al and K (as demonstrated using XRD analysis). On the other hand, a physical action occurs with VMT particles contained in the hydrogel. Under heat exposure, the VMT particles have a preferential orientation around the polymer wall, allowing

© 2020 Tous droits réservés.

lilliad.univ-lille.fr

to retain the initial design. With these two phenomena, significant fireproof properties are achieved.

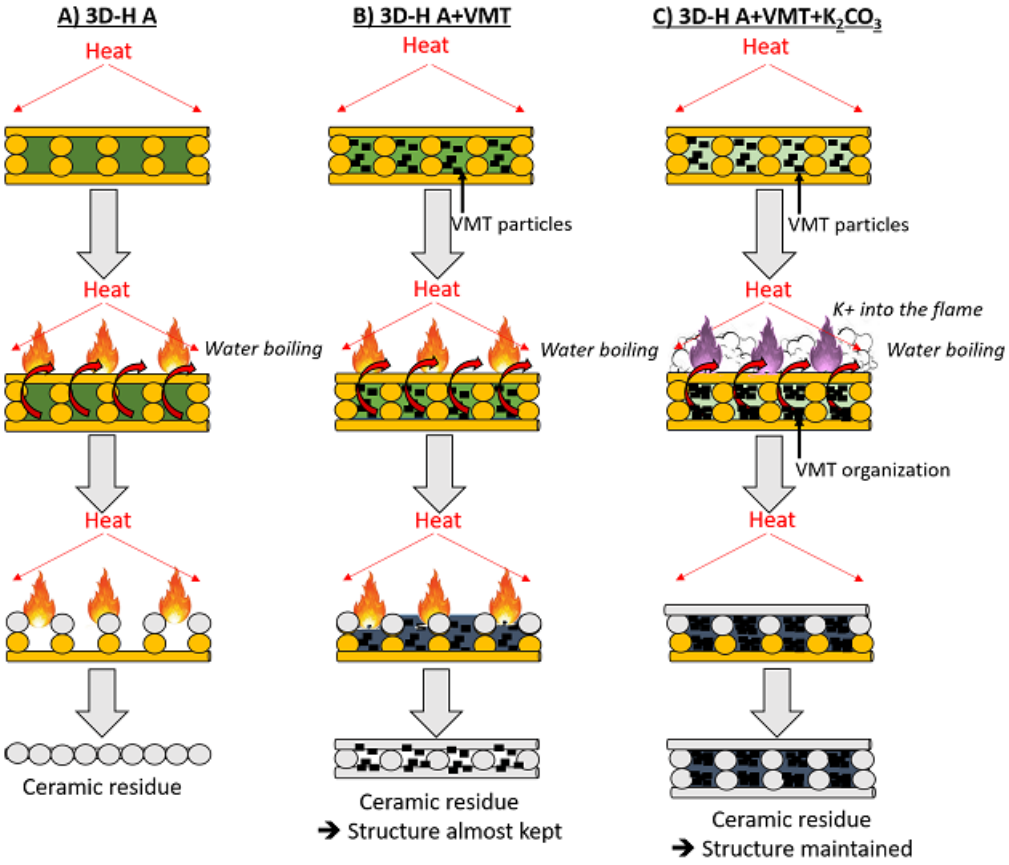

Figure 50. Illustration of fire behavior mechanism of new hydrogel sandwich multi-materials (a) 3D-H A, b) 3D-H A+VMT, c) 3D-H A+VMT+K_2CO_3).

4. Conclusion

The design developed in chapter 2 (of this part), composed of two shells completely filled in with 100% polymer, and a core with 30% of polymer inside, was retained. However, the empty cells created by the design were not filled with a standard liquid or solid phase, but with a hydrogel phase to simplify the process and find a solution to leaking issues due to the porosity of the material. Three waterborne hydrogels, with various gelation processes were thus elaborated. Vermiculite was incorporated to improve their fire protective performances. Hydrogels improve the TTI of systems, and VMT can in certain cases (e.g. for hydrogel B and C) dramatically reduce the heat release rate during heat exposure. These results were correlated with EPMA measurements and XRD analyses, that highlight the influence of VMT particles orientation and organization under temperature, and their influence on crystalline structure. To

© 2020 Tous droits réservés.
lilliad.univ-lille.fr

try to improve fire performances, K_2CO_3 was incorporated in the hydrogel phase. When K_2CO_3 is dissociated in water, it acts in gas (by diluting flame with CO_2 and H_2O released) and condensed phases (by forming a thermal protective ceramic residue). Therefore, by combining K_2CO_3 and VMT in a 3D printed system, a design with excellent fireproof performances is conceived.

The interest of using hydrogel as flame-retardant constituent to design new multi-materials systems was thus established. However, even if a fast flame-extinguishment occurs for the systems with very low heat release rate, the TTI remains very short. Therefore, an improvement of the design is proposed in the next chapter to reach superior fire protection performances.

Key points

- ✓ Hydrogels A, B and C improve TTI of system but have no influence on THR and pHRR.
- ✓ Hydrogels B+VMT and C+VMT improve THR and pHRR (but not TTI): VMT acts as a physical barrier and slows down the gas emission from the polymer decomposition, which extinguishes the flame and explains the HRR reduction.
- ✓ K_2CO_3 in hydrogel A+VMT dramatically decreases the THR and pHRR (but no influence on TTI): K_2CO_3 acts in gas phase by diluting flame and in condensed phase by forming thermal protective residue, which is combined to VMT effect and thus reduce HRR.
- ✓ **Perspective**: improve the TTI of sandwich 3D printed multi-materials filled with hydrogel phase to reach superior fire protective performances.

© 2020 Tous droits réservés.

lilliad.univ-lille.fr

Chapter 4: Combining low emissivity thin coating and 3D printed original designs for superior fire protective performance

According to chapter 3 (part 2) [176], a hydrogel phase composed of agar and vermiculite (VMT) revealed an extremely low heat release rate (with a reduction of 86% and 64% as regards peak of heat release rate and total of heat release, respectively, compared to reference (3D-air)) while being easily processed. Nevertheless, the time to ignition (TTI) of material is short, even if the extinguishment occurs rapidly after ignition.

The objective of this chapter was to improve the TTI via a surface treatment in order to maintain the very low heat release rate of this sandwich multi-material. To reach this goal, the use of highly heat reflective coatings was considered. These coatings exhibit a low emissivity and as they reflect infrared rays responsible for radiative heat transfer, the surface temperature is much lower, reducing the heat conduction through the material thickness and thus preventing its decomposition. The first study on such systems was performed by Schartel et al. in 2011 on polycarbonate and polyamine 6,6. A trilayer composed of chrome, copper and silicon dioxide ($Cr/Cu/SiO_2$) reduced the flammability indexes on both substrates [189]. Then, in 2014, Försth et al. took over this method using indium tin oxide (ITO) on poly(methyl methacrylate) (PMMA) and vanadium dioxide (VO_2) on steel. However, these systems did not reach the low emissivity obtained with copper [190]. Recently, Davesne et al. studied the combination of a thin layer of metal such as aluminum, protected by a dielectric such as alumina on polypropylene and polyamine 6, which revealed an interesting behavior upon heating [191].

Therefore, based on that literature, the influence of such low emissivity coating (composed of aluminum protected by alumina and deposed by pulsed DC magnetron sputtering) on the exposed skin surface of sandwich 3D printed materials was firstly determined (Figure 51). Then, this coating was deposited on hydrogel sandwich 3D printed multi-materials to examine its potential influence on TTI of the material. A full characterization of samples (emissivity, mass, and hydrogel amount) was carried out, and all samples were then tested by mass loss cone calorimetry under a 50 kW/m^2 external heat flux. Finally, the fire protection mechanism was investigated.

The results and discussion of this chapter were published for publication in ***ACS Omega*** journal: **https://doi.org/10.1021/acsomega.0c02902**.

© 2020 Tous droits réservés.
lilliad.univ-lille.fr

Thèse de Laura Geoffroy, Université de Lille, 2020

KEYWORDS: 3D printing, Design, Hydrogel, sandwich multi-materials, low emissivity coating, Flame retardancy

Aims

- ✓ Improve TTI of hydrogel sandwich 3D printed multi-materials: low emissivity coating deposition.
- ✓ Fire testing and characterization of new design.
- ✓ Full mechanism investigation.

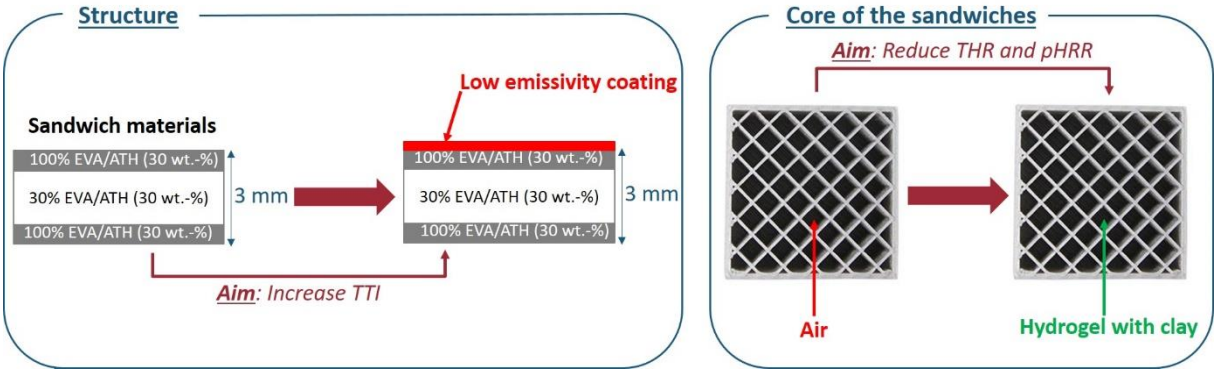

Figure 51. Concept of low emissivity hydrogel sandwich flame retardant design using additive manufacturing.

1. 3D printed sandwich multi-materials description

In this chapter, four samples were prepared and their name and composition are gathered in Table 17.

The materials, materials' formulations and 3D printing process were previously described in materials & methods part (pages 162 and 164). Based on the work of chapter 2 (of this part), a sandwich design was conceived and composed of two skins completely filled with EVA/ATH (30 wt.-%) polymer, and a core partially fill with 30% of EVA/ATH (30 wt.-%) material and thus 70% of empty cells, as illustrated in Figure 51. According to samples studied (Table 17), (i) the empty cells created by the design are filled with hydrogel composed of agar and vermiculite hereafter named H B+VMT (hydrogel B+VMT preparation fully described in materials & methods part (page 168)), as it is the case for IR-3D-H B+VMT and for 3D-H B+VMT (Figure 52), and (ii) a low emissivity coating is deposed on the top skin of the design using a Physical Vapor Deposition (PVD) process, more specifically by pulsed DC magnetron

© 2020 Tous droits réservés.

lilliad.univ-lille.fr

sputtering (fully described in materials & methods part (page 169)), as it is the case for IR-3D-air and for IR-3D-H B+VMT (Figure 52). Therefore, it is important to notice that to be able to depose the low emissivity coating by PVD and also fill the cells of the core created by the design with hydrogel B+VMT, the top skin and the core and bottom skin have to be printed separately. Only 3D-air sample can be printed in one step.

Finally, to design the sandwich materials, the top section (with or without low emissivity coating, depending on the samples studied) is deposited on the core (filled with hydrogel B+VMT and kept empty, depending on the samples studied) and sealed by fusing it at 200°C to the edges of the bottom shell of 3D printed polymer plate (Figure 52).

Table 17. Description and composition of materials studied.

Name of the samples		Top section		Core composition
		Material	Low emissivity coating	
1	3D-air	EVA/ATH (30 wt.-%)	No	air
2	IR-3D-air		Yes	air
3	3D-H B+VMT		No	Hydrogel: Agar+VMT
4	IR-3D-H B+VMT		Yes	Hydrogel: Agar+VMT

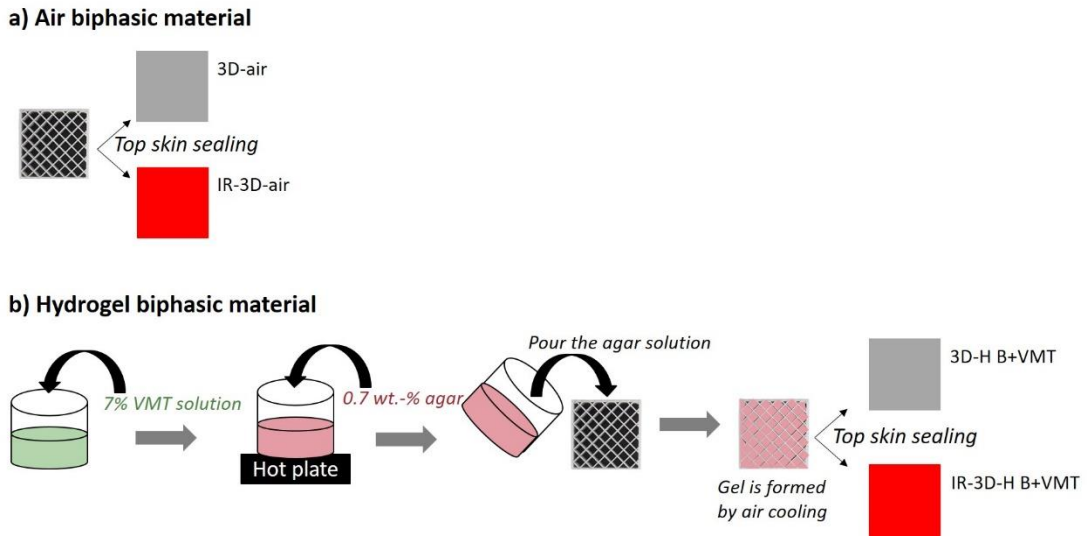

Figure 52. Description of (a) air, b) hydrogel) sandwich multi-materials elaboration.

© 2020 Tous droits réservés.
lilliad.univ-lille.fr

2. Results

2.1. Characterization before fire testing

All samples studied were characterized before fire testing (Table 18 and Figure 53). As illustrated in Figure 53, the top section of sample 3D-air and 3D-H B+VMT, looks the same. The only difference is the presence of hydrogel B+VMT in the cells present in the sandwich core. Considering the coated samples (i.e. IR-3D-air (Figure 53 b) and IR-3D-H B+VMT (Figure 53 d)), homogeneous deposits presenting mirror aspect are observed on both surfaces.

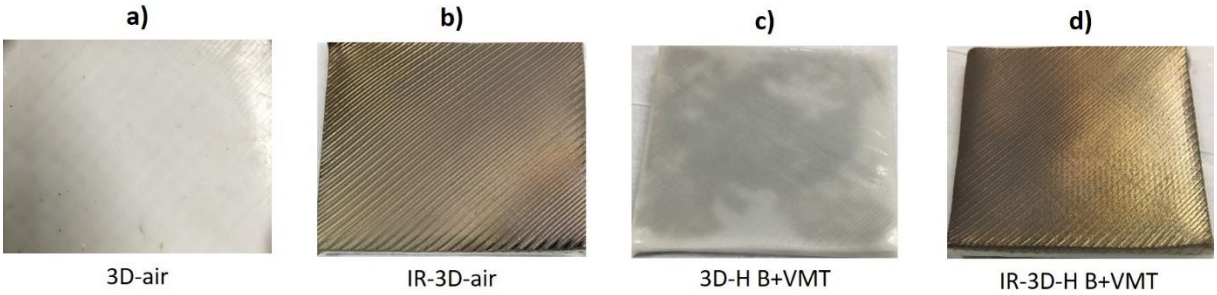

Figure 53. Top section pictures of each sandwich multi-material studied (a) 3D-air, b) IR-3D-air, c) 3D-H B+VMT, d) IR-3D-H B+VMT).

According to Table 18, the thickness and mass of the materials with air, i.e. 3D-air and IR-3D-air is identical and equal at 3 mm and 7.2 g, respectively. For the hydrogel sandwich multi-materials, i.e. 3D-H B+VMT and IR-3D-H B+VMT, the same observation is done as the thickness, mass and hydrogel mass of the design is the same and equal at 3 mm, 11.3 g, and 4.1 g, respectively. Meanwhile, the top section emissivity of coated samples was measured (Table 18) and compared (following the set-up described in materials & methods part (page 175)). It is possible to point out the significant emissivity decrease between the samples without surface treatment, and the samples with a metallic coating. Hence, the reflection of infrared rays is enhanced and it can be expected that the heat absorption during exposure to a radiative thermal constraint should be decreased.

Table 18. Quantitative values of each sandwich multi-material studied.

Polymer matrix	Mass (g)	Thickness (mm)	Hydrogel amount (g)	Emissivity
3D-air	6.5 ± 0.9	3 ± 0	/	0.96 ± 0.00
IR-3D-air	7.89 ± 0.08	3.1 ± 0.2	/	0.21 ± 0.03
3D-H B+VMT	11.2 ± 0.8	3 ± 0.2	4.1 ± 0.3	0.96 ± 0.00
IR-3D-H B+VMT	11.5 ± 0.1	3.1 ± 0.1	4.17 ± 0.08	0.19 ± 0.04

© 2020 Tous droits réservés.

lilliad.univ-lille.fr

Finally, the composition of the low emissivity coating and its thickness were checked using SEM-EDS analysis (described in materials & methods part (page 174)) (Figure 54). Al, O and Si-mappings were done on the cross-section of low emissivity coating deposed on glass slide as illustrated in Figure 54. O element distribution were analyzed to distinguish the Al_2O_3 layer from the Al which composed the low emissivity coating (Figure 54 a). Al element repartition was observed to identify the coating and its thickness (Figure 54 b). Si element was also analyzed to locate the glass slide on which the low emissivity coating is deposed (Figure 54 c). These analyses firstly revealed that the low emissivity coating is well composed of aluminum and alumina layers. Indeed, during the PVD process, a homogeneous layer of Al was firstly deposed on glass slide with a thickness equal at 0.490 µm on which a homogeneous layer of Al_2O_3 having a thickness of 0.093 µm is applied. No delamination or bubbles are observed between both layers. However, it is important to note that the thickness of coating strongly depends on the substrate [191]. Therefore, a slight variation between Al and Al_2O_3 thicknesses can occur on the EVA/ATH (30 wt.-%) 3D printed samples deposition.

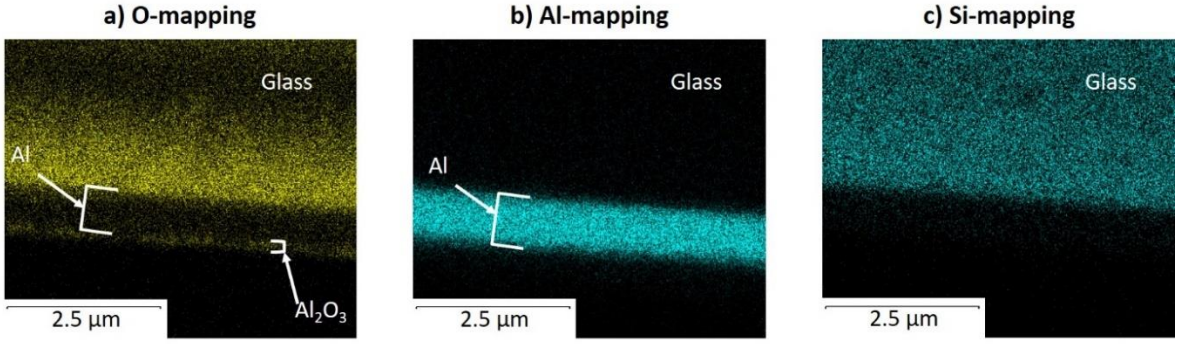

Figure 54. Cross-section X-rays mapping of (a) O element, b) Al element, c) Si element) or the low emissivity coating deposed on a glass slide using SEM-EDS analysis.

2.2. Fire testing

Figure 55 illustrates the comparison of heat release rate (HRR) as a function of time (Figure 55 a), and the temperature rise versus time (Figure 55 b) for each material (fire testing description fully presented in materials & methods part (page 170)). Table 19 gathers the three main parameters determined from the HRR versus time curve illustrated in Figure 55 a.

First of all, it is observed that the incorporation of hydrogel B+VMT dramatically reduces the THR and the pHRR of materials. Indeed, for 3D-H B+VMT, the THR and pHRR are reduced by 85 % and 51 %, respectively, compared to 3D-air. As regards the TTI, a slight improvement by 8 seconds (about 1.36 times longer) is observed when compared to the sample with air (3D-air). The addition of a low emissivity coating allows to considerably delay the TTI. Indeed, the

© 2020 Tous droits réservés.
lilliad.univ-lille.fr

Thèse de Laura Geoffroy, Université de Lille, 2020

TTI jumps from 22 s for 3D-air to almost 6 min for IR-3D-air. However, in terms of THR (11%) and pHRR (14%) no improvement is measured compared to 3D-air.

By combining the low emissivity coating and hydrogel in the core cells, the fire behavior is dramatically enhanced. The THR and pHRR differences between IR-3D-H B+VMT and 3D-air are -91% and -64%, respectively, with a high increase of TTI by 162 seconds (about 8.36 times longer, which corresponds to a jump from 22 s up to 3 min). This increase of TTI is not as huge as observed for the coated sandwich without hydrogel (IR-3D-air). For both samples, ignition occurs when combustible gases are released. The low emissivity coating acts as a reflective barrier against infra-red by reflecting heat and thus slowing down the heat propagation in the sample. However, when the EVA/ATH decomposition temperature is reached, gases are released, that create a pressure at the interface coating/polymer, which damage the low emissivity coating and lead to cracks. As a consequence, the coating loses its protective property, and ignition occurs. In the presence of hydrogel (IR-3D-H B+VMT), water vapor is released in addition to decomposition gases from EVA/ATH. Therefore, higher pressure is reached and an earlier failure of coating is observed, which explains the lower TTI measured for this system compared to IR-3D-air. However, thanks to the hydrogel B+VMT and especially due to VMT orientation, the flame quickly extinguishes, which explains the low THR and pHRR recorded during the MLCC test.

During the MLCC tests, the temperature rise was measured using a thermocouple at the backside of the material (Figure 55 b). When the reference, 3D-air is exposed to heat, the backside temperature increases quickly, with a slope equal to 1.7°C/s, and reaches a steady-state temperature of 500°C. For IR-3D-air, the increase in temperature is slowed down more than 4 times, with a slope of 0.4°C/s. Before sample ignition, the temperature is never higher than 200°C. This slow temperature rise is explained by the low emissivity coating, which limits the heat absorption, leading to a delayed ignition. After 500 s, ignition occurs and the temperature increases rapidly, with a slope of 2.4°C/s, and reaches 500°C after 700 s of heat exposure. Regarding 3D-H B+VMT, a slow temperature rise, with a slope equal at 0.5°C/s (3.4 times lower than slope obtained for 3D-air), is observed during the whole MLCC test. It can be explained by the presence of hydrogel B+VMT. According to chapter 3 (of this part) [155], VMT particles present in the hydrogel phase have a preferential orientation. When the sample with hydrogel B+VMT is exposed to heat, the water contained in hydrogel boils. The VMT particles form quickly a gradient of tight stack of VMT. This tight layer of VMT acts as an efficient physical barrier, which slows down the gas emission from polymer decomposition that

© 2020 Tous droits réservés.

lilliad.univ-lille.fr

feeds the flame. As a consequence, the flame is fast extinguished and low THR and pHRR are measured, which justifies the slow temperature rise, compared to the reference 3D-air. Finally, by the combination of low emissivity coating and hydrogel B+VMT, an even slower increase in temperature is observed during MLCC test. Indeed, from 200 s to 400 s, a plateau at 100°C is observed for IR-3D-H B+VMT. After 400 s, temperature goes up, with a low slope equal at 0.6°C/s. Therefore, the low emissivity sandwich multi-material designed in this work allows to obtain i) a very low heat release (fast flame extinguishment), ii) a longer time to ignition, and iii) a high thermal gradient between the top and backside of sample, with a very slow temperature rise.

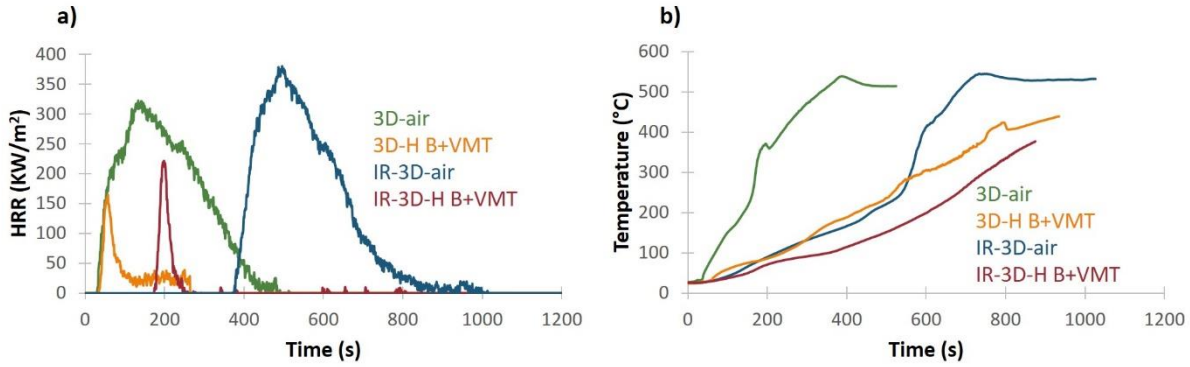

Figure 55. Fire behavior of each material studied (a) Heat release rate versus time, b) Temperature rise versus time).

Table 19. Fire protection performances values of each material studied.

Polymer matrix	TTI (s)	THR (MJ/m²)	pHRR (kW/m²)
3D-air	22	55	249
IR-3D-air	340 (x15.5)	61 (11%)	283 (14%)
3D-H B+VMT	30 (x1.36)	8 (-85%)	122 (-51%)
IR-3D-H B+VMT	184 (x8.36)	5 (-91%)	152 (-64%)

After heat exposure, the top sections of the residues of each material were observed (Figure 56). On one hand, only agglomerated powder remains after the fire test for 3D-air and IR-3D-air. Both residues contain alumina from ATH dehydration and for the coated sample, additional alumina with aluminum (mainly oxidized [191]) from the low emissivity coating. On the other hand, Figure 56 shows that the design initially created is retained for the samples containing hydrogel B, both coated and uncoated: the top section is visibly kept for both samples. This point can be explained by the presence of VMT in hydrogel, which agglomerates on the polymer walls, and thus maintains the initial structure (formation of an exoskeleton), as it was

© 2020 Tous droits réservés.
lilliad.univ-lille.fr

Thèse de Laura Geoffroy, Université de Lille, 2020

demonstrated in a previous paper [191]. The only difference between these samples is the color of the top residue surface. A grey color is observed for IR-3D-H B+VMT, compared to a yellowish color for 3D-H B+VMT. This observation makes sense and results from the presence of the low emissivity coating, which remains in place during the test and is mostly composed of aluminum and aluminum oxides at this point.

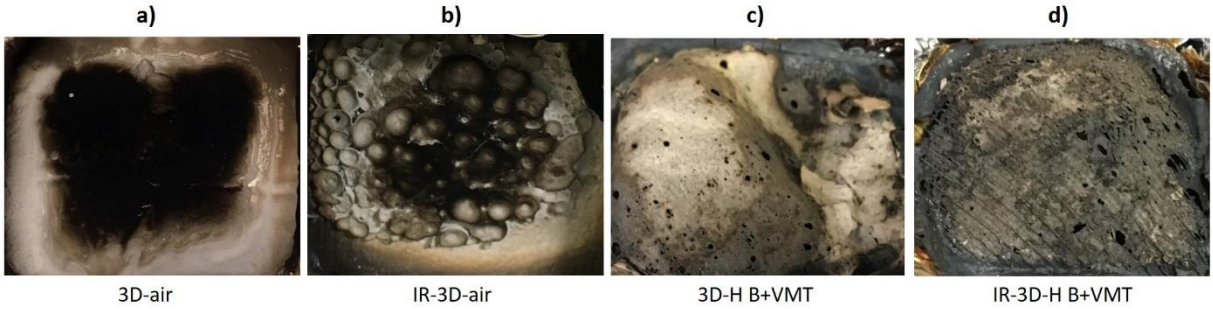

Figure 56. Top residue surface pictures of each material studied (a) 3D-air, b) IR-3D-air, c) 3D-H B+VMT, d) IR-3D-H B+VMT).

2.3. Mechanism of action

The fire behavior of each material is illustrated in Figure 57. For the reference 3D-air, when the material is exposed to a radiative thermal constraint, the sample ignites, starts to melt and decomposes: all empty cells then collapse (Figure 57 a). Therefore, the design is not retained and no improvement in terms of TTI, THR or pHRR is measured. When a low emissivity coating is deposited on the top surface on the sample (IR-3D-air), it reflects the infrared rays, which significantly delay the TTI (Figure 57 b). However, when the backside of the sample reaches 200°C, the polymer starts to melt and decompose, releasing gases. On one hand, the polymer melting damages the design initially elaborated. On the other hand, the gases released by the polymer decomposition weaken the coating (creation of an internal pressure at the interface coating – decomposing polymer), which leads to the ignition and the decomposition of the whole sample. Therefore, the only effect of the low emissivity coating is to longer the TTI, but when the sample ignites, no reduction of THR of pHRR is recorded. For 3D-H B+VMT, as it was previously explained in chapter 3 (part 2) [176], when the sandwich multi-material is exposed to heat, ignition occurs rapidly, but due to the water and VMT particles contained in hydrogel, the flame extinguishes rapidly (Figure 57 c). Indeed, the water in hydrogel phase is released slowly. At the same time, VMT particles organize upon heating and form a protective barrier constituted by the accumulation of VMT platelets that prevents the gases coming from polymer decomposition to feed the flame. Therefore, very low THR and pHRR are measured during the MLCC test, and the design initially elaborated is maintained.

© 2020 Tous droits réservés.

lilliad.univ-lille.fr

However, the TTI of this sandwich multi-material is not improved. Finally, when IR-3D-H B+VMT is exposed to heat, the low emissivity coating reflects most of infrared rays (Figure 57 d). Simultaneously, the water contained in the hydrogel phase starts to boil when 100°C is reached, which causes the top section of the material to swell, and this swelling creates cracks in the coating, ultimately leading to ignition. However, as for 3D-H B+VMT, the flame extinguishes rapidly with the combined action of water and VMT particles contained in the hydrogel. Therefore, by combining both concepts, i.e. low emissivity coating and sandwich multi-materials design, fire protective performances are dramatically enhanced, characterized by a very low THR and pHRR and a longer TTI.

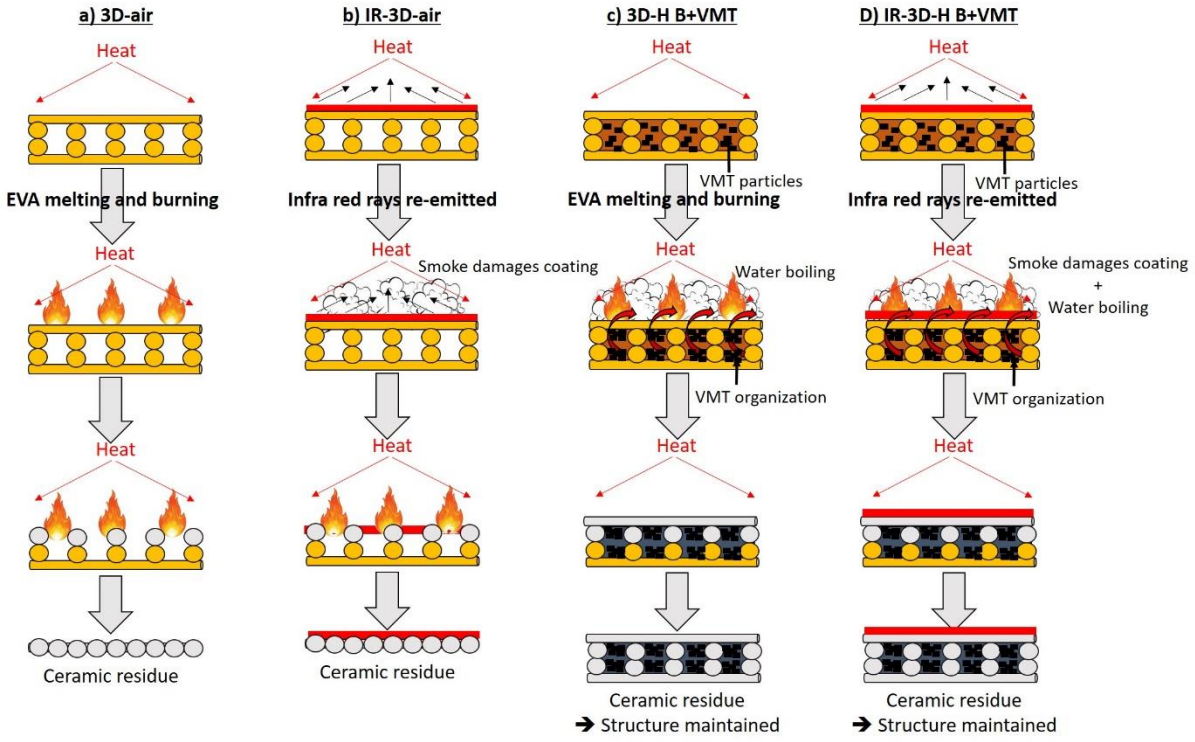

Figure 57. Illustration of fire behavior mechanism of each sandwich multi-material studied (a) 3D-air, b) IR-3D-air, c) 3D-H B+VMT, d) IR-3D-H B+VMT).

3. Conclusions

Two concepts were combined in this chapter: i) the reduction of the surface emissivity through the use of a thin metal/dielectric coating, which significantly improves the TTI of materials by reflecting infrared rays to limit radiative heat transfer, and ii) the sandwich multi-material design, which decreases the heat of release rate by combining various phases using an original 3D printed design. This novel work allows reaching superior fire retardancy through the elaboration of a new design and combination of various materials instead of only modifying the material formulation and chemistry.

© 2020 Tous droits réservés.
lilliad.univ-lille.fr

Thèse de Laura Geoffroy, Université de Lille, 2020

Key points

- ✓ TTI is improved using low emissivity coating.
- ✓ Low emissivity coating reflects most of the infrared rays responsible for heat absorption.
- ✓ However, TTI is quicker in presence of hydrogel due to water emission which causes the coating cracking early.
- ✓ New design of flame-retardant multi-material with very low THR and pHRR and TTI higher than 2 min.

© 2020 Tous droits réservés.

lilliad.univ-lille.fr

General conclusion & Outlook part 2

In this part, a novel bio-inspired design (honeycomb like structure) was created, and fire tested to evaluate the influence of the design modification on flame retardant properties. The advantage of this original design was taken to incorporate various phases (liquid and solid) to reduce the heat release rate of materials. Finally, two optimizations were done: (i) on the process to simplify it and find a solution to leaking issue caused by the inherent porosity related to the 3D printing process and (ii) on the time to ignition of sample to reach superior fire protective performances. Therefore, a new 3D printed design of flame-retardant multi-materials with very low heat release rate against high temperature environment was conceived. This work proves that design modification and the combination of various materials (polymer, liquid, hydrogel, and metal) offer a new way of thinking to improve the fire protective properties of materials.

The present study could be completed following different ways that could be realized thanks to short term or long term projects.

In the short term and as direct perspective of this work, the problematic of the ageing of the optimized solution could be investigated. Indeed, this work highlights that the use of hydrogel as fire retardant constituents of sandwich multi-materials designing allows to obtain a very low heat release rate. The multi-materials developed could be for example used in buildings, such as floor or wall covers. However, it is important to point out that a hydrogel will eventually dry out after a certain period of time, losing its flame retardant properties. Therefore, the durability of hydrogel-containing materials is an important point to be addressed in further studies, by using hygroscopic species, or by designing some kind of barrier to prevent the water from evaporating. The use a silicon polymer to act as a water barrier could be interesting for this purpose.

In the long term, other designs could be considered. Indeed, 3D printing process allows to be really free in terms of design thinking. Among all of them, design with a fractal geometry (Figure 58) could be conceived. Indeed, according to paper [192], carbonaceous structure formed by the intumescent coating decomposition (passive fire protections) has a fractal structure. Therefore, this particular structure acts in fireproofing. Thus, it could be interesting to create such designs to see their influence. In addition, many works were done on biomimetic structures [193]–[195] and have led to new performance in several fields, like the honeycomb-inspired design that was done in this work. To pursue that approach, another design of system

© 2020 Tous droits réservés.
lilliad.univ-lille.fr

from nature or a bio-design could be imitated and elaborated for improving fire protective properties.

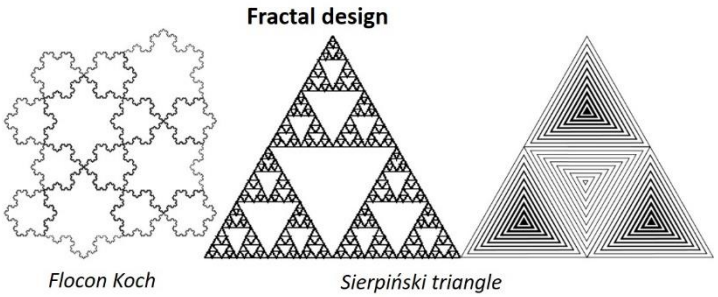

Figure 58. Other 3D printed design thinking: Fractal design.

Furthermore, in this work, EVA polymeric matrix was used as model material to prove the concept. It could be worthwhile to apply similar scientific approach on other polymeric materials and see if the strategies proposed in this work could be widespread to other materials such as polypropylene or polyamide.

Finally, it could be interesting to use the principle of 4D printing to create a smart fire barrier, which adapt over the time, which means find a polymer able to change its shape and thus its fire protection performances over the time and according to the undergone thermal constraint.

Based on these perspectives, this work is a step forward opening new possibilities in flame retardancy field.

© 2020 Tous droits réservés.
lilliad.univ-lille.fr

Thèse de Laura Geoffroy, Université de Lille, 2020

Part 3: Design of fire resistant multi-materials

Within the framework of passive fire protection (described in part 1), the objective of this part is to conceive a fire barrier that protects a substrate for a predetermined time against fire impingement and high temperature environment. The purpose is to have the highest possible thermal gradient between the side exposed to the fire and the substrate to be protected. Many passive fire resistant protections were already developed and formulated to insulate the substrate from fire. However, with the development of science and technology, the need of increasingly efficient fire barrier is required. The standard approach consists in changing the materials formulation, but it becomes harder and harder to find new synergies or molecules and thus elaborate new fire barriers. Therefore, in this part, new approaches based on the modification of design and the combination of materials (detailed in part 1) were attempted (Figure 59). Two concepts were selected, based on the state of the art on fire proofing solution, namely intumescence and delamination induced in polymer metal laminates structure (presented in chapter 1). The elaboration of new fire barriers based on these two already existing technologies was envisioned via two different designs, as detailed in chapter 2 and 3. Finally, in the last and fourth chapter, the optimized fire barrier was applied on another substrate to highlight its versatility and potential use in other application fields. All materials and methods used are described at the end of manuscript on a special section (beginning on page 176), easily spotted on colored pages.

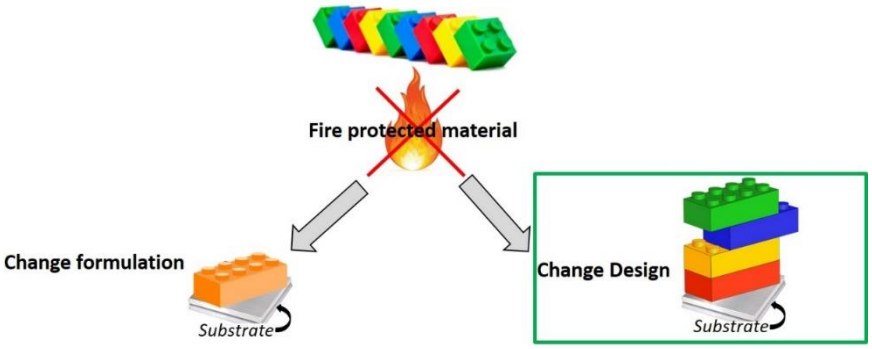

Figure 59. Design of fire protective barrier.

© 2020 Tous droits réservés.
lilliad.univ-lille.fr

Thèse de Laura Geoffroy, Université de Lille, 2020

Table of Content part 3

PART 3: DESIGN OF FIRE RESISTANT MULTI-MATERIALS **99**

CHAPTER 1: INTUMESCENCE AND POLYMER METAL LAMINATE AS FIRE PROOFING LAYERS: STATE OF THE ART **101**
1. INTUMESCENT MATERIALS AND COATINGS 102
1.1. Intumescence background 102
1.2. Intumescence process and key factors 102
1.3. Novels ingredients developed for intumescent coatings 104
2. LAMINATED COMPOSITES 106
3. CONCLUSION 109
CHAPTER 2: INTUMESCENT POLYMER METAL LAMINATE FOR FIRE PROTECTION **110**
1. SAMPLES DESCRIPTION 111
2. RESULTS 112
2.1. IPML characterizations before fire test 112
2.2. Fire performances 112
2.3. Expansion measurements 116
2.4. Char morphology analysis 117
2.5. Thermal and carbonization gradients 118
3. DISCUSSION 122
4. CONCLUSIONS 124
CHAPTER 3: BI-LAYER INTUMESCENT PAINT METAL LAMINATE: A NOVEL DESIGN FOR A HIGH PERFORMANCE FIRE BARRIER **126**
1. SAMPLES DESCRIPTION 127
2. RESULTS 128
2.1. Intumescent bilayer metal laminate characterizations before fire test 128
2.2. Fire behavior 130
2.3. Mechanism investigation 135
3. CONCLUSIONS 139
CHAPTER 4: EXTENSION TO OTHER APPLICATIONS: SUBSTRATE CHANGING **141**
1. SAMPLES DESCRIPTION 142
2. RESULTS 143
2.1. Characterizations before fire testing 143
2.2. Fire testing 144
3. CONCLUSION 149
GENERAL CONCLUSION & OUTLOOK PART 3 ..... **151**

© 2020 Tous droits réservés.

lilliad.univ-lille.fr

Chapter 1: Intumescence and Polymer metal laminate as fire proofing layers: State of the art

Nowadays, in transportation and building applications, fire safety is crucial, and materials must meet stringent regulations. Indeed, materials such as steel, aluminum or polymer based composite materials have to be protected against fire to avoid losing their mechanical and structural properties. For example, when an unprotected steel structure is exposed to fire, due to its high heat conductivity, the temperature at the backside of the steel increases rapidly and depends on the section factor and the severity of the fire itself. With the increase in temperature, the mechanical properties of steel change, and thus steel begins to loose most of its structural properties between 470 and 550°C, with a deformation which occurs above 500°C [24]–[28]. As a consequence, to improve the fire resistance of steel columns, solid concrete protection is usually used. However, the major disadvantage of this technique is the increase in weight of the structure. Moreover, in the case of polymer-based composite materials, their compressive and flexural load-bearing capacity decreases above their glass transition temperature. In addition, decomposition starts at 300 - 350°C or even earlier (depending on the composite materials considered) with flammable volatiles released, which feeds the fire [196], [197]. Therefore, to comply with more demanding standards, other passive fireproofing solutions, i.e. insulating systems designed to decrease heat transfer from a fire to the structure being protected, have been developed (as it was previously described in part 1). Among all passive fireproofing materials, cementitious products [23], fibrous materials [29], [30], composites or fire protective panels [31], [198], ceramic coatings [23], or intumescent materials [24]–[28] can be cited as examples.

In this chapter, two passive fireproofing solutions used to protect a substrate, i.e. intumescent paints and composite laminate (especially polymer metal laminate), are particularly detailed (Figure 60) as both concepts will be combined in this thesis to design a new type of fire protective barrier.

KEYWORDS: Intumescent coatings, Polymer Metal Laminates

Aim

- ✓ Provide general information about two ways to fire protect a substrate: intumescent coating and composites laminate (polymer metal laminate).

© 2020 Tous droits réservés.
lilliad.univ-lille.fr

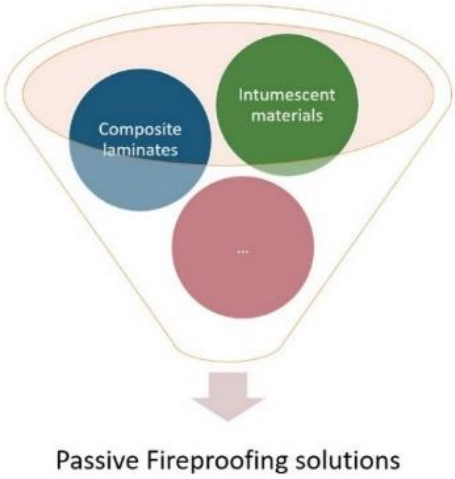

Figure 60. Some passive fireproofing solutions.

1. Intumescent materials and coatings

Several passive fireproof materials exist to protect a substrate against fire. Among them, intumescent coatings appear as an interesting approach.

1.1. Intumescence background

Intumescent phenomenon was firstly reported by J.L. Gay-Lussac in 1821 with reference to the flame retardancy of textiles [24]–[28], but the word 'intumescence' was not mentioned. In 1934, a German patent claimed the fire protection of wood, and the formation of a swollen char layer upon heating was reported, but again the word 'intumescence' was not used in the text. In 1967, an aircraft carrier fire happened on the flight deck of the USS Forrestal (CVA-59) [199], [200]. To prevent this accident from happening again, the navy established a committee for firefighting and initiated an Aircraft and Ordnance Safety program to extinguish flight deck fires and develop methods to protect explosives and munitions from the heat. From this program, intumescent paints were developed and evaluated as a solution [199], [200]. In 1971, Vandersall published a paper [63] which describes the history and the critical elements of intumescent coatings. Then, it was only in the 1980s that Camino successfully applied this concept to bulk polymers (mainly thermoplastics) [64].

1.2. Intumescence process and key factors

Among intumescent materials, intumescent coatings (IC) are known as an efficient, economical and widely used solution to preserve the bulk material properties [23]. Moreover, these coatings are convenient as they can be applied in a simple way by spray, brush or roller onto several substrates including metallic materials, polymers, textiles and wood. Intumescent coatings are

© 2020 Tous droits réservés.

lilliad.univ-lille.fr

classified as either thin or thick film coatings. Thin film (1 – 3 mm thick) is used for cellulosic fire scenario (ISO834), compared to thick film (3 – 5mm thick), usually used for hydrocarbon fire scenario (UL1709). When the surface temperature of the coating reaches a critical temperature upon heating, the film begins to melt or soften, and is converted into a highly viscous liquid. Simultaneously, endothermic reactions are initiated that result in the release of inert gases with low thermal conductivity. These gases are trapped inside the viscous fluid (formation of bubbles) (Figure 61). At higher temperatures, the porosity of the intumescent char increases as well as its volume. Finally, intumescent char slowly degrades and its expansion remains constant. The result is the expansion or foaming of the coating, to form a protective multicellular carbonaceous char that acts as an insulated barrier between the fire and the substrate (Figure 61). This char layer absorbs a large part of the heat generated by the fire, thus maintaining the protected structure's temperature above the critical temperature of the substrate. It is noteworthy that the coating continues to react until all its components are used up and consequently the protection rating is determined by the thickness applied. Indeed, for a same intumescent coating, the thicker the intumescent coating, the higher the thermal protection, to a certain extent, where the thickness no longer has any influence [24]–[28].

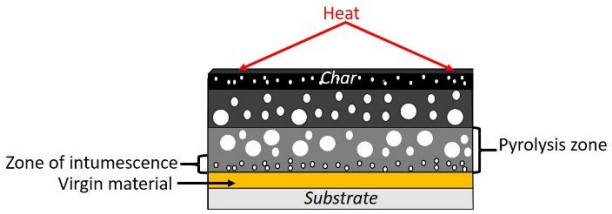

Figure 61. Illustration of an intumescent material behavior against fire exposure.

Jones and al [62] focused on intumescent coatings and tried to identify the combination of ingredients leading to the formation of a controlled volume of cohesive, insulated char when the intumescent coating is exposed to a fire. They defined as 'carbonific" the compounds in intumescent formulation that act as a carbon source for char formation and as 'spumific" those which evolve gaseous products and induce foaming [62]. However, it was Vandersall [63] who classified the chemical compounds of intumescent systems. Three main ingredients are thus needed for intumescence: i) a carbonization agent influencing the amount of char formed; ii) an acid source, either free or formed acting as a precursor of reaction upon heating; iii) a blowing agent releasing high quantities of non-flammable gases to form a porous insulating barrier. Examples of these compounds are given in Table 20. Therefore, many combinations of components (acid, carbon and blowing sources) are possible to elaborate intumescent organic

© 2020 Tous droits réservés.
lilliad.univ-lille.fr

Thèse de Laura Geoffroy, Université de Lille, 2020

(epoxy or acrylic) and/or inorganic (silicone) based coatings, which are gathered in a recent review [24].

Table 20. Examples of carbonization agent, acid source, blowing agent and catalyst used in intumescent material.

Carbonization agent	Acid source	Blowing agent
Polyol including pentaerythritol (PER), mannitol, starch, …	Ammonium Poly-Phosphate (APP), boric acid, melamine phosphate, …	Melamine, urea, dicyandiamide, …

Combining these compounds do not guarantee the intumescent phenomenon. In addition, chemical and physical processes have to occur at the right time (kinetics) during the temperature rise. First, during heating, acid source has to be released when intumescent material starts to melt or soften. This acid source esterifies the carbon source at a temperature above decomposition temperature. After esterification, the ester decomposes via dehydration, yielding a carbonaceous residue. Then, the blowing agent has to decompose at the proper temperature (i.e. after the intumescent material melting or softening, and before the char hardening), releasing gases which are trapped and diffuse slowly in the highly viscous melt degraded material. The char layer finally solidifies through crosslinking and condensation reactions, in order to create a stable, low-thermal-conductivity shell, with an appropriate morphology, on the surface of the flammable materials. The viscosity of the degraded matrix in the blowing phase is, as a consequence, a critical factor to form an efficient carbonaceous porous barrier. Indeed, the size and size distribution of cells are active factors in the performance coating, and generally, the closed cells that form during the blowing agent decomposition improve the heat insulation properties. Therefore, the construction of the intumescent structure is controlled by several critical aspects which have to be taken into account such as rheology (expansion phase, viscoelasticity of char), chemistry (charring) and thermophysics (limitation of heat and mass transfers) [24]–[28].

1.3. Novels ingredients developed for intumescent coatings

Due to these physical and chemical processes, the level of fire protection performance greatly depends on the coatings used. Indeed, some of them provide quickly a high efficiency which only lasts for a short period, while others are less efficient at the beginning but then provide longer fire protection [27], [201]. As a consequence, the formulation of the coating must be optimized, and for these reasons, considerable efforts have been devoted to improve the

© 2020 Tous droits réservés.

lilliad.univ-lille.fr

performance of intumescent coatings using various binders [202], [203], active ingredients [204], [205] and fillers [206]–[208].

Commercial intumescent coatings based on epoxy (Figure 62 a) and polyacrylate (Figure 62 b) resins have been widely investigated [209], [210]. The traditional system used is composed of phosphoric and inorganic acid (such as ammonium polyphosphate, melamine polyphosphate, …), pentaerythritol as char precursor and melamine as blowing agent [211]. These coatings have a bubbling (chemical) expansion when exposed to fire.

Some novel active ingredients such as expandable graphite (EG) and metal oxides were used to improve the performances of intumescent coatings [212]–[217], thank to another expansion way: a physical way. EG is a graphite intercalation compound in which sulfuric acid and/or nitric acid is inserted between the carbon layers. Upon heating, due to graphite expansion, an entangled network build of graphite "worms" is created and leads to an efficient heat barrier (Figure 62 c).

Nanotechnology involving nanoparticles has also been considered as a means to enhance the fire resistant performance of intumescent coating [218], [219]. Indeed, nano-silica [220], [221], clay [222], [223] and layered double hydroxide [224] were reported to promote the formation of carbonaceous char, increasing the strength of the intumescent char, the thermal stability and the shielding performance of the char barrier.

Fibers or meshes were also incorporated to improve thermal protective properties and mechanical resistance of char. Indeed, the loss of cohesion of char structure and poor adhesion to the substrate at high temperatures do not always guarantee the performance of this intumescent systems, and fibers or meshes can be a great solution to prevent that.

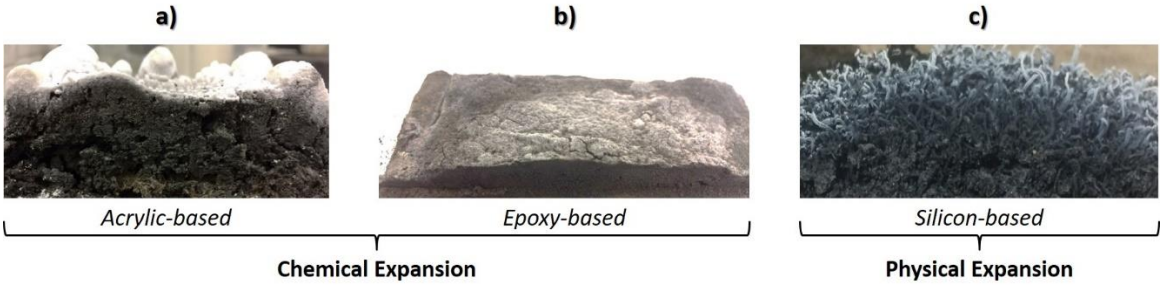

Figure 62. Residue obtained after fire testing (a) for acrylic-based intumescent coating, b) for epoxy-based intumescent coating, c) for silicon-based intumescent coating).

Even though novel chemistries and additives are still under investigation to increase coatings efficiency and to reduce thickness and weight, it becomes harder and harder to improve the fire

© 2020 Tous droits réservés.
lilliad.univ-lille.fr

Thèse de Laura Geoffroy, Université de Lille, 2020

protective performances. Figure 63 gathers the number of scientific papers and patents dealing with intumescence and intumescent coatings, which were published since 1970s. It revealed that, from 1970s to 1997, the number of papers remains constant, and quite low. From 1997 to 2010 an exponential increase is observed, and could partly be explained by the development of new intumescent coating formulations including the use of nanotechnology. However, since 2010, a stabilization of the number of papers dealing with intumescent coating is noted compared to those referring to intumescent, where an increase is observed. This stabilization reveals the complexity to improve the fireproof properties of intumescent coatings. This confirms that the development and improvement of intumescent coatings have some limits and for this reason, other strategies must be investigated, as for example the modification of design and the combination of materials. As previously described in part 1, materials combination leads to new products (e.g. composite materials) with new properties.

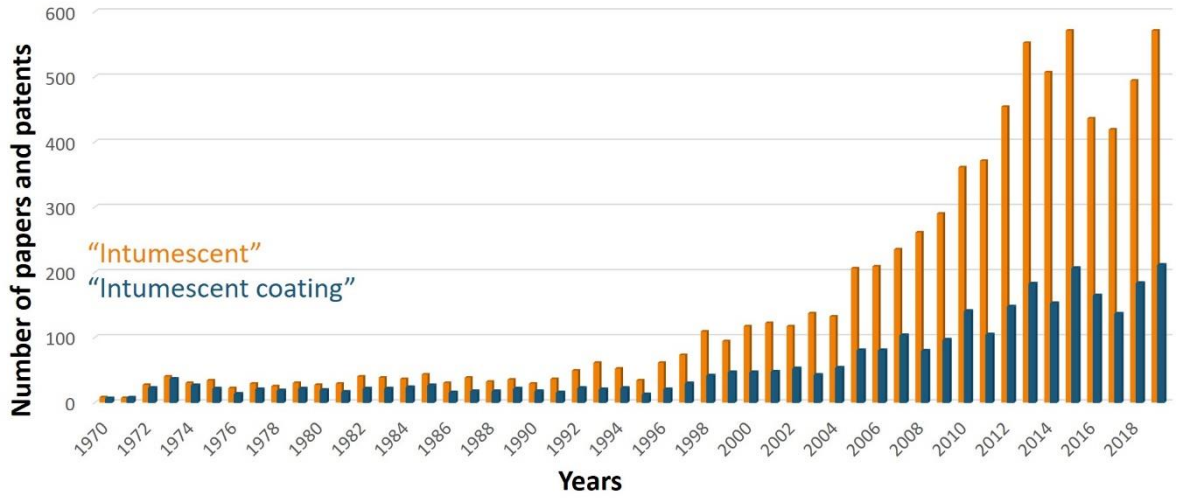

Figure 63. Number of scientific papers and patents from 1970 to 2019 related to the term "intumescent" and "intumescent coating" (based on the SciFinder database).

2. Laminated composites

A composite material is composed of two or more constituents of different physical or chemical properties, which have different characteristics than those obtained for individual components [31], [197]. Driven by the demand for high-performance lightweight structures, different kinds of composite were developed, among which laminated composites that are particularly used in aircraft industry [225]–[227]. A multitude of laminate build up can be made by alternating layers of different materials: fibers [227]–[229], polymers (thermosets [225] or thermoplastics [230]), metals (Al [231], Ti [230] or Mg [232] alloys), …These laminated structures are generally primarily aiming to provide suitable mechanical properties. For example, it was

© 2020 Tous droits réservés.

lilliad.univ-lille.fr

revealed that the fatigue crack growth rates in adhesive bonded sheet materials can be reduced by using a laminated structure instead of using a one thick monolithic sheet [227]. Moreover, in the more specific case of metal laminated structures, additional performances are obtained at the same time.

The metal laminates structures can be used as protection for substrates, when they are bonded to them. It is a hybrid composite structure composed of alternating thin sheets of metal alloys and polymeric material reinforced with fiber (called Fiber Metal Laminates (FMLs)), or with no reinforcement (named Polymer Metal Laminates (PMLs)). Metallic layers and polymeric material can be bonded by classical techniques, i.e. mechanically or adhesively. These hybrid materials combine advantages from their two key constituents: metals (mostly aluminum) and polymeric materials (fiber reinforced or not). Indeed, metal laminated materials have for example a higher bearing strength and impact resistance than the only use of polymeric materials [226], [233] and a better thermal insulation property than the only use of metallic materials. Indeed, the rate of heat conduction through composites is much slower than through metals [227]–[229]. FML design, i.e. several interlacing layers of very thin metal layers and fiber reinforced adhesives (Figure 64), was primarily elaborated to achieve better mechanical performances (such as fatigue and damage tolerance) but it also improved burn-through characteristics of aircraft fuselages compared to aluminum skins alone [227]–[229], [231], [234]. The most well-known FML are: i) Aramid Reinforced Aluminum Laminate (ARALL) (alternating of thin aluminum alloy layers / uniaxial or biaxial aramid fibers), ii) Glass Reinforced Aluminum Laminate (GLARE) (alternating of thin aluminum alloy layers / glass fibers), iii) CentrAL (alternating of thicker aluminum alloy layers (than GLARE) / glass fibers), iv) Carbon Reinforces Aluminum Laminate (CARALL) (alternating of thin aluminum alloy layers / carbon fibers).

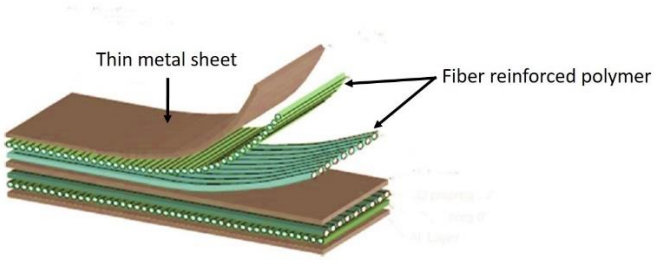

Figure 64. Illustration of Fiber Metal Laminate (FML).

PML (Figure 65), i.e. alternating thin metallic foils (such as aluminum or titanium) and thin organic resin layers without reinforcement (such as epoxy or acrylic resin or polyethylene) glued on substrates, was principally developed for fire resistance [231]. Indeed, the main

© 2020 Tous droits réservés.
lilliad.univ-lille.fr

advantage of this design is to improve the thermal performances owing to the delamination of the structure. Upon fire exposure, the polymer part decomposes, evolving gases which create a delamination (Figure 65). This delamination effectively decreases the heat conductivity of the material, reducing heat transfer in the materials (creation of an additional thermal resistance). The number of plies of the protection influences the overall performances of the fire barrier. If PML contains many interfaces susceptible to delaminate, the fireproof property of the substrate is improved. In addition to the fire protection provided by this design, such laminated layers also contribute to improve the mechanical failure time of the substrate, due to the use of aluminum foils. For these reasons, the fire barrier developed in this part was inspired from the PML structure.

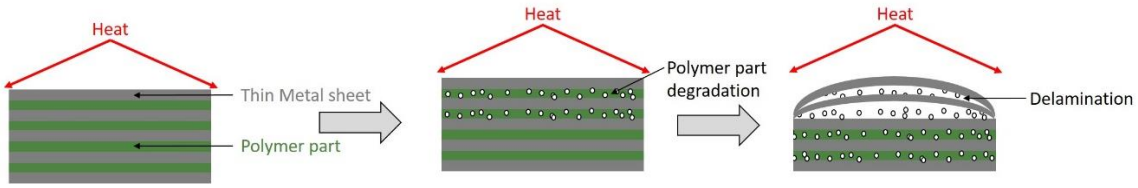

Figure 65. Fire behavior of Polymer Metal Laminate.

Most of studies were focused on mechanical advantages [235]–[237] of metal laminated materials, but few of them investigated fire protection performances [230], [231]. Figure 66 shows that the number of papers and patents for polymer metal laminate starts to rise around 1990, but is still very low, with few papers and patents published per year, especially compared to those published for composite materials (Figure 66). The scarcity of studies on that kind of composite design highlights the new aspect of the work undertaken in this part.

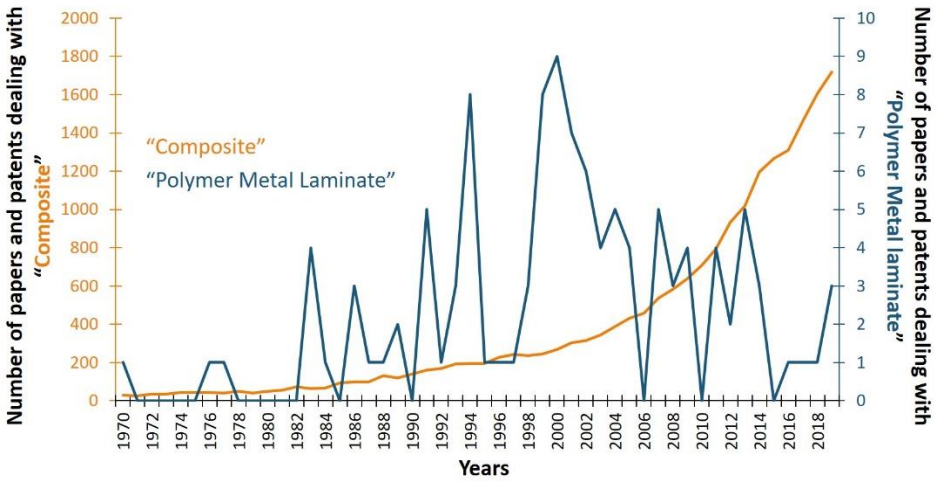

Figure 66. Number of scientific papers and patents from 1970 to 2019 related to the therm "composite and Polymer Metal Laminate" (based on the SciFinder databased).

© 2020 Tous droits réservés.

lilliad.univ-lille.fr

3. Conclusion

Several techniques were developed to fire protect a substrate. This chapter highlights the interest of intumescent paints to fire protect different kinds of substrates. These paints form a porous carbonaceous residue, which act as a fire barrier to protect a substrate. However, even if intumescent paint is a mature and well-controlled technology, it becomes harder and harder to improve their fire protective performances. Our strategy, previously presented in part 1, consists in modifying the design and combining various materials to reach better fire protection properties. Polymer Metal Laminates, hybrid composite materials composed of a metallic and polymeric part and offering versatility in their design answer this strategy. These materials were developed to obtain lightweight structures in many fields, notably in aeronautical field, and revealed great mechanical and fire protective properties. Indeed, delamination creates gas filled cavity, delaying the heat propagation in the material and thus protecting it. Combining both concepts, i.e. intumescence and delamination, novel fireproof multi-materials were developed in this work to reach better fire protection performances, capable of responding to aeronautical constraints. The influence of the number of layers, the type or combination of paints were investigated, leading to two different types of design (Figure 67): 10 layers Intumescent Polymer Metal Laminate (IPML) and bilayers intumescent paint metal laminate that will be fully described in the next chapters.

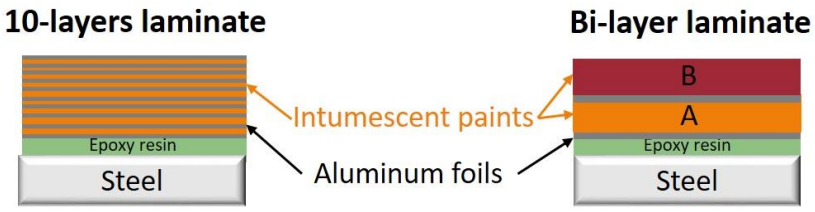

Figure 67. Illustration of different types of design elaborated.

Key points

- ✓ Intumescent paints swell, expand and form a porous carbonaceous residue against heat, which protect substrate.
- ✓ Great fire protective performance of composite laminate (Polymer Metal Laminate) are explained by the delamination between layers which occurs when polymer degrades.
- ✓ **Main observation:** Hard to develop new chemistries to elaborate innovative fire barriers.

© 2020 Tous droits réservés.
lilliad.univ-lille.fr

Thèse de Laura Geoffroy, Université de Lille, 2020

Chapter 2: Intumescent Polymer Metal Laminate for fire protection

In this chapter, the main idea was to set up an original concept, by gathering two technologies described previously (i.e. intumescent paint (Figure 68 a) and PML (Figure 68 b)). As a consequence, a novel thermal barrier was designed, called "Intumescent Polymer Metal Laminate" (IPML) (Figure 68 c), consisting in alternating thin layers of aluminum foils and intumescent coatings. Three different intumescent coatings were selected to prepare ten-plies IPML glued onto steel substrates. The IPMLs were characterized using optical microscopy, and their efficiency towards fire was evaluated using a burn-through test. Thermal profiles obtained were compared to those obtained for a monolayer of intumescent paint. Characterizations (expansion measurements, microscopic analyses, in situ temperature, and thermal measurements) were carried out on the different samples to explain the IPML mode of action against fire.

The results and discussion of this chapter were published in ***Polymers*** journal: **https://doi.org/10.3390/polym10090995** [238]**.**

KEYWORDS: Polymer Metal Laminate (PML), Fire protection, Intumescent paints

Aims

- ✓ Design a new fire protective barrier against fire: Intumescent Polymer Metal Laminate (IPML) elaboration.
- ✓ Fire behavior comparison between intumescent paint and IPML.
- ✓ Investigation of IPML mechanism against fire exposure.

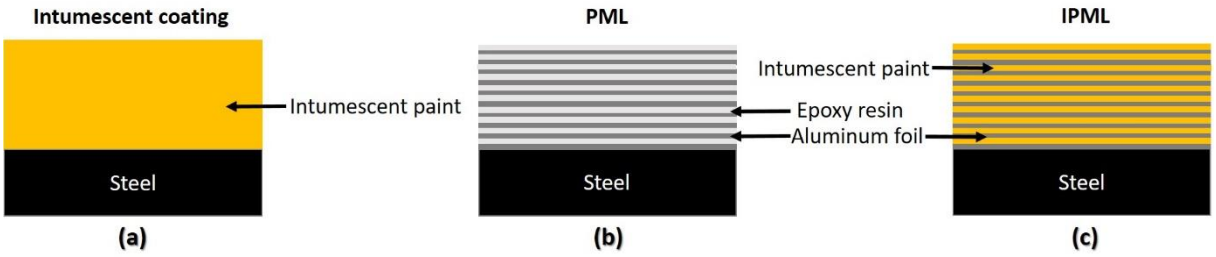

Figure 68. Illustration of (a) intumescent coatings, (b) polymer metal laminate (PML), and (c) intumescent polymer metal laminate (IPML) systems.

© 2020 Tous droits réservés.

lilliad.univ-lille.fr

1. Samples description

Using the process fully described in materials & methods part (page 177), IPMLs made of 10 aluminum foils with layers of commercial intumescent paints A (epoxy-based), B (acrylic-based), or C (silicone-based) (described in materials & methods part (page 176)) were prepared and glued onto steel plates (Figure 69). They were named S-IPML-A, S-IPML-B, and S-IPML-C, and their total thicknesses were 8, 5.5, and 5 mm, respectively (Table 21).

To demonstrate the benefit of IPML over monolayers of intumescent coatings, additional samples were prepared using a film applicator to coat steel plates with respectively paint A (S-A), B (S-B), and C (S-C) (Figure 69). Their total thicknesses were 8, 5, and 4.8 mm, respectively (Table 21). Uncoated steel plate (S) was also used as a reference for each fire test.

Table 21. Monolayer of intumescent coating and IPML characterization.

Samples	Type of paint	Type of intumescence	Thickness (mm)	Weight (g)
S-A	Epoxy, bi-component [201], [239]–[242]	Chemical	8.0	288
S-IPML-A			8.0	291
S-B	Acrylic, mono-component	Chemical	5.0	257
S-IPML-B			5.5	249
S-C	Silicone, bi-component [212]–[215], [217], [222]	Physical	4.8	272
S-IPML-C			5.0	269

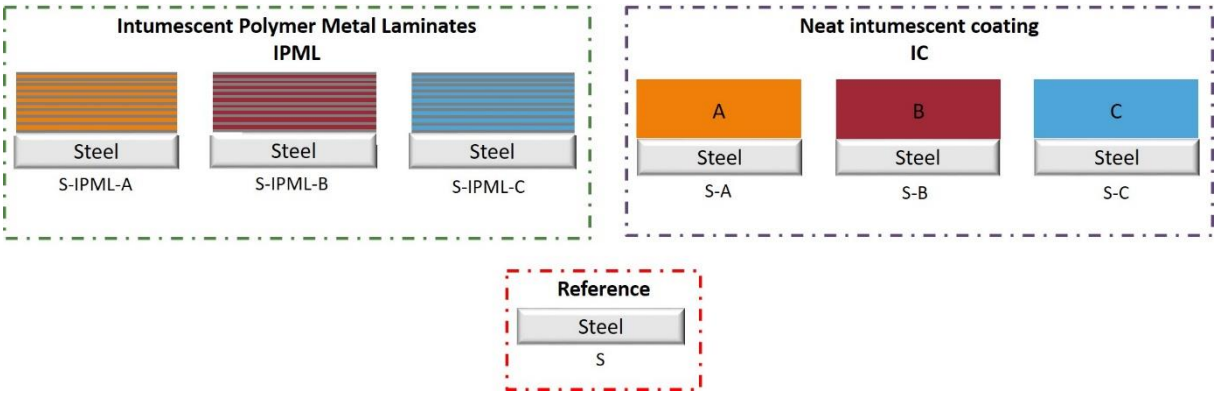

Figure 69. Illustration of studied samples.

© 2020 Tous droits réservés.
lilliad.univ-lille.fr

Thèse de Laura Geoffroy, Université de Lille, 2020

2. Results

2.1. IPML characterizations before fire test

Before fire testing, a cross-section of each IPML not glued onto substrate, and thus respectively named IPML-A, IPML-B, and IPML-C, was observed using an optical microscope (following the set-up described in materials & methods part (page 181)). The resulting pictures are gathered in Figure 70. All IPMLs seem quite homogeneous, with no voids observed between aluminum foils. Moreover, the IPMLs have almost the same thickness of intumescent paint between each aluminum foil. The mean thickness gap between each aluminum foil was calculated for each IPML and corresponded to 70, 105 and 77 µm, for IPML-A, B and C, respectively. The thickness of the upper coating layer (applied after press step) was different and dependent on the coating applied: 300 µm for IPML-A, 160 and 170 µm for IPML-B and IPML-C, respectively. It was observed that intumescent layers in IPML-B and C were thinner compared to IPML-A. This was explained by the difference in terms of coating viscosity: Coating A is very viscous and difficult to apply because it contains many fillers and fibers, preventing to get very smooth layers. However, even if thicknesses of the IPML-A, B, and C are different, they can be considered as acceptable as (i) results were repeatable (repeatability measurements were made in triplicate), and (ii) the IPMLs are not compared to each other in the following, but are compared to single intumescent layers of similar thicknesses, i.e., S-A, S-B, and S-C.

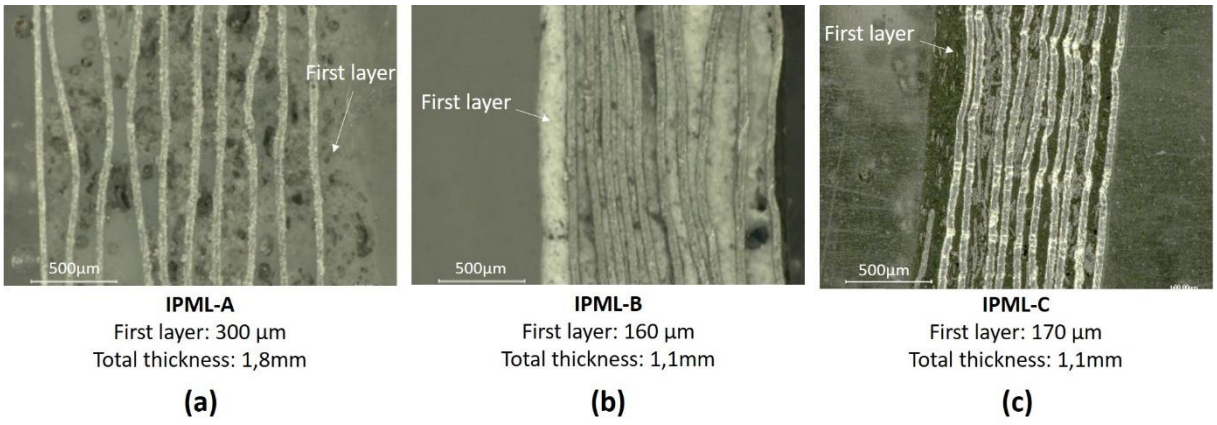

Figure 70. Cross section pictures obtained by microscopic analyses of (a) IPML A, (b) IPML-B, and (c) IPML-C, before burn-through test.

2.2. Fire performances

Fire protection performances of S-IPML-A, B, and C were compared to those of S-A, B, and C of almost similar total thickness using burn-through test (fully described in materials & methods

© 2020 Tous droits réservés.

lilliad.univ-lille.fr

part (page 179)). Figure 71 and Table 22 report the temperature versus time curves and values measured at the backside of the uncoated (S) and coated steel plates, for the different systems.

First, it was observed that all coated systems, whatever monolayers of intumescent coatings or IPML systems, were very efficient in protecting steel against fire. The backside of the reference plate reached about 550°C in a few minutes, whereas monolayers of intumescent coatings and IPML systems allowed limiting backside temperature increase to maximum 300°C.

Table 22. Temperature reached after 2, 10, and 15 min burning, for each sample studied.

Samples	Thickness (mm)	T Reached after 2 min Burning (°C)	T Reached after 10 min Burning (°C)	T Reached after 15 min Burning (°C)
S	3.0	437	561	567
S-A	8.0	110	236	254
S-IPML-A	8.0	67	189	232
S-B	5.5	191	241	234
S-IPML-B	5.0	96	225	253
S-C	5.0	147	255	256
S-IPM-C	4.8	147	291	326

The S-IPML-A design (Figure 71 a, Table 22) is more advantageous than a monolayer of intumescent coating A. Indeed, during the first minutes of the test, the slope of the curve of S-IPML-A is 2.6 times lower than that of the S-A system (Figure 72), leading to a maximum temperature difference of about 65°C after 5 min 50 s. In addition, at the end of the test, the temperature reached by S-IPML-A is still slightly lower (22°C difference, corresponding to 9%) than that measured for S-A, but this difference is not considered to be significant based on the incertitude range of the measurements. In that case, the IPML design clearly allows improving the fire protection performance of the system, especially at the beginning of the fire testing. For the S-IPML-B system (Figure 71 b, Table 22), similar observations were done but, at the beginning of the test, the benefit of using IPML was even higher than for the previous system. The slope of the curve was strongly reduced (factor 4) (Figure 72), and a maximum temperature difference between both systems of about 102°C was observed after 2 min 50 s. At the end of the test, the temperature reached by S-IPML-B was 19°C (8%) higher than the

© 2020 Tous droits réservés.
lilliad.univ-lille.fr

Thèse de Laura Geoffroy, Université de Lille, 2020

temperature reached by the S-B system, which was not significant (incertitude range of the measurements).

Therefore, both S-IPML-A and S-IPML-B systems provide a real benefit in terms of fire protection, compared to single coating layers (S-A and S-B). It is of high interest to manage to reduce the temperature at the beginning of the test. This is usually achieved, for a short time, by using additives dehydrating for the first minutes of the test, but here, through the IPML design, the effect lasted for more than 10 min.

S-IPML-C system (Figure 71 c, Table 22*)*, on the contrary, does not exhibit any improvement compared to the S-C system. The thermal protection was better without IPML design. Indeed, at the beginning of the fire test, the slope of the S-IPML-C system increased by 2.6 compared to the S-C system (Figure 72*)*. At the end of the fire test, the temperature reached by the S-IPML-C system was also higher than the one reached by S-C (difference of 70°C, corresponding to 27% after 15 min, Table 22). Based on this result, the IPML design seemed not to be working for coating C system.

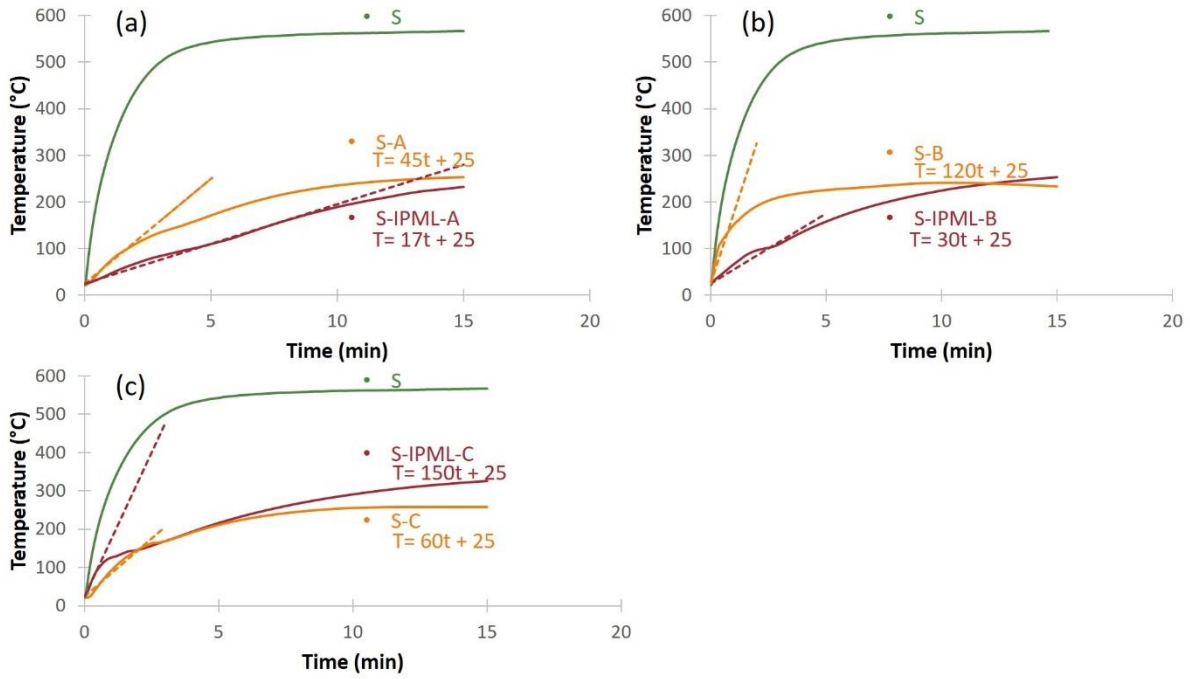

Figure 71. Evolution of temperature versus time for each system ((a) Temperature vs. time for A system, (b) Temperature vs. time for B system, (c) Temperature vs. time for C system).

© 2020 Tous droits réservés.

lilliad.univ-lille.fr

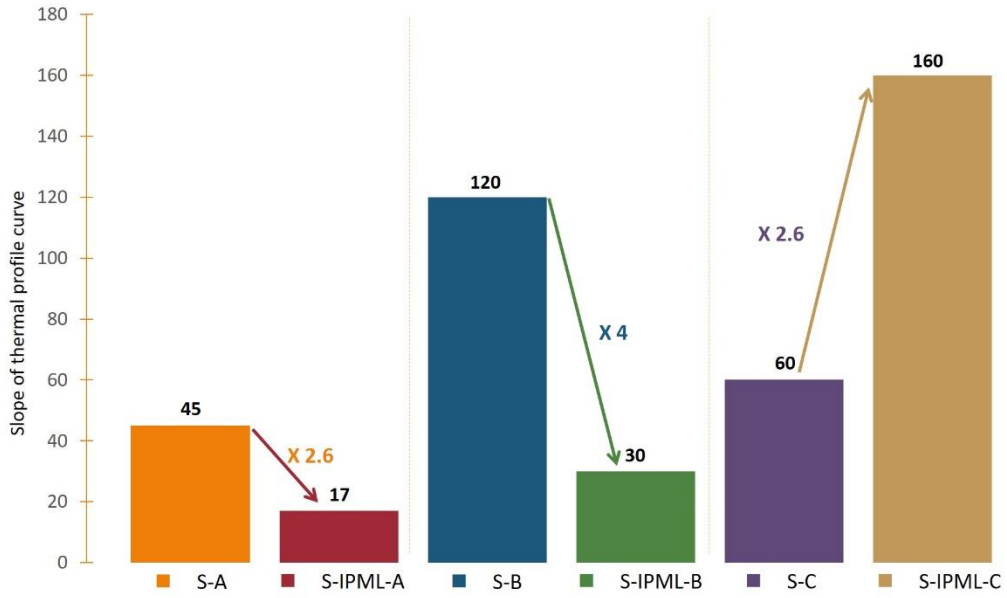

Figure 72. Slope comparison of thermal profile curve at the beginning of burn-through test.

To try to understand and explain the results obtained, cross-section pictures of IPML residues obtained after the 15 min burn-through test are presented in Figure 73. In cases A and B, swelling and delamination were observed, due to some carbonaceous and cohesive residue formation between aluminum foils. In addition to the swelling of intumescent paints, the delamination phenomenon could also be explained by the thermal dilatation coefficient difference between aluminum and intumescent coating. Therefore, these observations confirmed all expectations triggered by the PML design itself (delamination phenomenon). These phenomena might explain the good fire protection properties of the A and B systems, previously reported (creation of an additional thermal resistance by delamination).

However, the case of the C coating was different. In that system, some swelling was also observed, as well as delamination. However, as reported previously, coating C is a silicon-based system containing expandable graphite, and its efficiency is mainly based on a "physical expansion": the entangled network between the graphite "worms" creates an efficient heat barrier. However, due to the IPML design, the intumescent layers were not in direct contact: the thin swelled layers containing expandable graphite were not thick enough to lead to the formation of an entangled network. "Worms" of expandable graphite grow perpendicularly to aluminum foils, which form thermal bridges between aluminum and graphite. Thus, S-IPML-C was not able to yield a similar protection than the single 5 mm thick S-C layer (which formed an entangled network with holes reducing thermal propagation), explaining the relatively poor fire protective properties.

© 2020 Tous droits réservés.
lilliad.univ-lille.fr

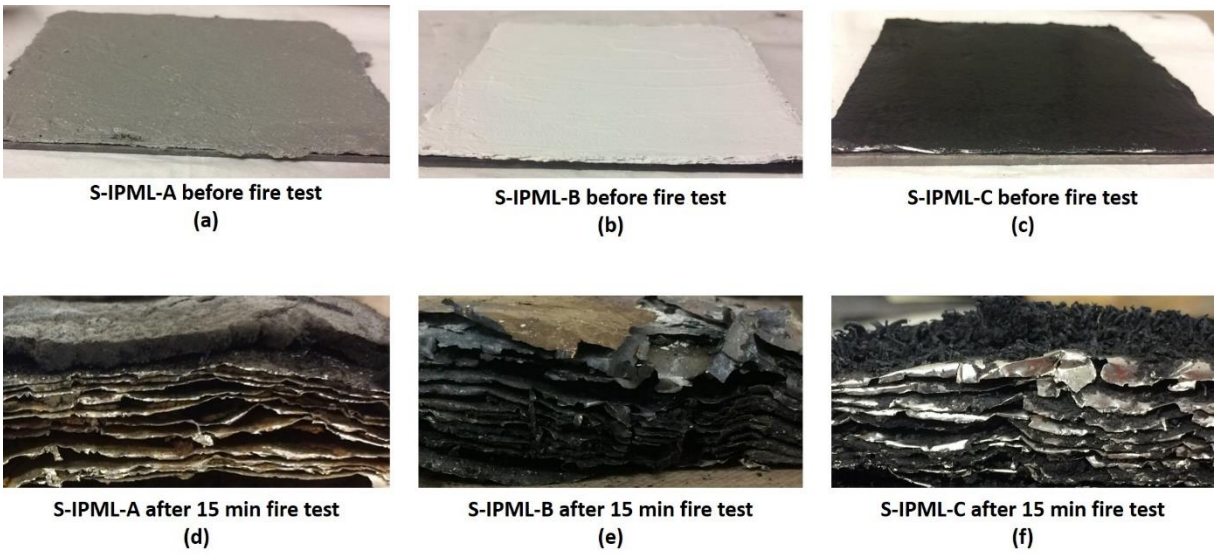

Figure 73. Cross-section of IPML after 15 min burn-through test exposition ((a) S-IPML-A before fire test, (b) S-IPML-B before fire test, (c) S-IPML-C before fire test, (d) S-IPML-A after 15 min fire test, (e) S-IPML-B after 15 fire test, and (f) S-IPML-C after 15 min fire test).

As S-IPML-C exhibited poor performance compared to the two other systems, the rest of the study will focus on S-IPML-A and B, to try to understand why and how both these systems work.

It is well known that expansion plays a crucial role in the efficiency of intumescent coatings, especially if it is combined with the right char porosity and morphology [24]. Therefore, expansion and morphological analyses were carried out and are described in the following sections.

2.3. Expansion measurements

The objective here was first to evaluate expansion during the fire test (measurement described in materials & methods part (page 181)), by stopping the test at characteristic times, depending on the thermal profiles obtained in the previous section. Three characteristic times were selected: 2 min 50 s, 5 min 50 s, and 15 min (end of the test). Based on the thermal profiles, at 2 min 50 s the gap between the S-B and the S-IPML-B was the highest (102°C), and at 5 min 50 s the gap between S-A and S-IPML-A was the highest (65°C). Expansions were measured after 2 min 50 s, 5 min 50 s, and 15 min, and the expansion versus time curves obtained are plotted in Figure 74. These curves revealed that, after 2 min of testing, the expansion of S-IPML-A was higher than that of S-A, whereas for the other system, from the beginning of the test, the expansion of S-IPML-B was lower than that of S-B. S-A and S-IPML-A reach in a few minutes a “plateau” corresponding to about 180% and 250% expansion, respectively. Whereas S-B and S-IPML-B still expanded after the 15 min test, and expanded much more than the A

© 2020 Tous droits réservés.

lilliad.univ-lille.fr

system, with final expansions between 600 and 700%. No clear conclusion could be drawn from these measurements, as both systems were efficient but clearly worked in a different manner.

Based on these experiments, it is well known that expansion must be correlated to a morphological analysis [24] to confirm the good fire barrier phenomenon, because it is at least as important as the expansion study. Thus, a morphological analysis was undertaken to try to clarify the results obtained.

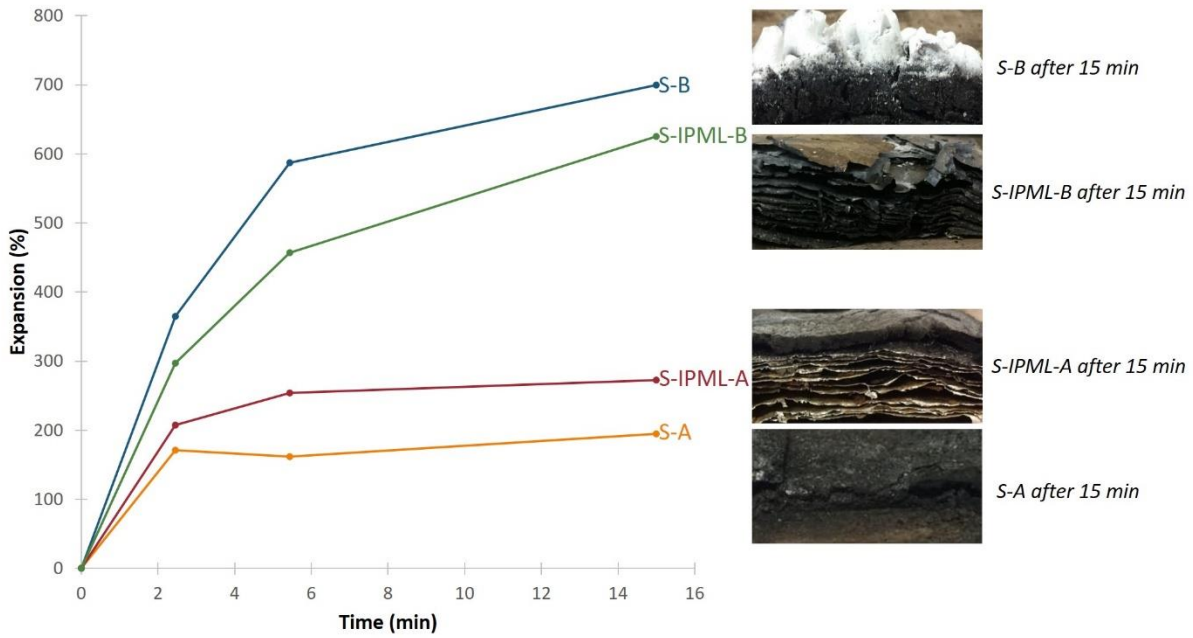

Figure 74. Expansion versus time curves for S-A, S-B, S-IPML-A and S-IPML-B systems.

2.4. Char morphology analysis

The S-IPML-A and S-IPML-B chars obtained at the end of the fire test were analyzed by SEM (fully described in materials &methods part (page 182)) and compared to S-A and S-B final chars, respectively (Figure A4- 1 and Figure A4- 2 in appendix 4 (page 205)). For IPML systems, chars taken from the layer 10 (surface) to layer 6 were analyzed.

Unfortunately, for both systems, due to the very thin layers of intumescent coating between aluminum foils, leading to a low amount of carbonaceous residue, observations were difficult. Looking at the SEM pictures, it was rather hard to conclude on a modification of the char structure. Sole interesting observation was that from layer 6 to layer 1, in both IPML systems, no porosity was observed, as if no intumescent char had developed, whereas on the contrary, the upper layers were where porosity could be observed. This might probably mean that there was a high thermal and carbonization gradient inside the IPML, which could explain the good

© 2020 Tous droits réservés.
lilliad.univ-lille.fr

Thèse de Laura Geoffroy, Université de Lille, 2020

fire protective effect observed. Thus, based on these observations, there are some differences, which will be studied in the next section.

2.5. Thermal and carbonization gradients

To better understand the fire protective behavior of S-IPML-A and S-IPML-B, the thermal gradient inside these systems was measured during the fire test, following the set-up described in the materials & methods section (page 180). Figure 75 highlights the evolution of the temperature versus time in the layers 2, 6, and 9, in which thermocouples were incorporated. The curves obtained clearly showed a thermal gradient in both cases. For S-IPML-A, after a 15 min fire test, the temperature reached 232, 350, 428, and 562°C, for the steel backside, and for the layers 2, 6, and 9, respectively. For S-IPML -B, the temperature reached 253, 279, 316, and 482°C, for the steel backside, and the layers 2, 6, and 9, respectively. The thermal gradient between the backside of the plate and layer 9 of the IPML, was about 330°C for S-IPML-A (initial thickness 8 mm) and 229°C for S-IPML-B (initial thickness 5.5 mm).

Related to this thermal gradient, a carbonization gradient is also observed (Figure 76). The color of each residual layer appears different, involving different carbonization degrees: the top layer exposed to fire is much darker, and thus more carbonized than the last layer. In addition, this carbonization gradient was much clearer with the IPML design than with monolayers of intumescent coatings systems. Moreover, using the thermal gradient measurement, the carbonization gradient was highlighted. The layer 9 reached a temperature above 560 and 480°C, for S-IPML-A and S-IPML-B, respectively, which confirmed intumescent coating degradation, and the visual aspect of the residue. For layer 2, the temperature was under 350 and 280°C, for S-IPML-A and S-IPML-B, respectively. Using TGA measurement (fully described in materials & methods part (page 182)) in Figure 77 and Figure 78, the thermal degradation of the coating occurs at around 400 and 300°C, for S-A and S-B, respectively. Therefore, thermal degradation had just started in this layer after 15 min fire exposition. These observations confirmed better fire protection performance.

© 2020 Tous droits réservés.

lilliad.univ-lille.fr

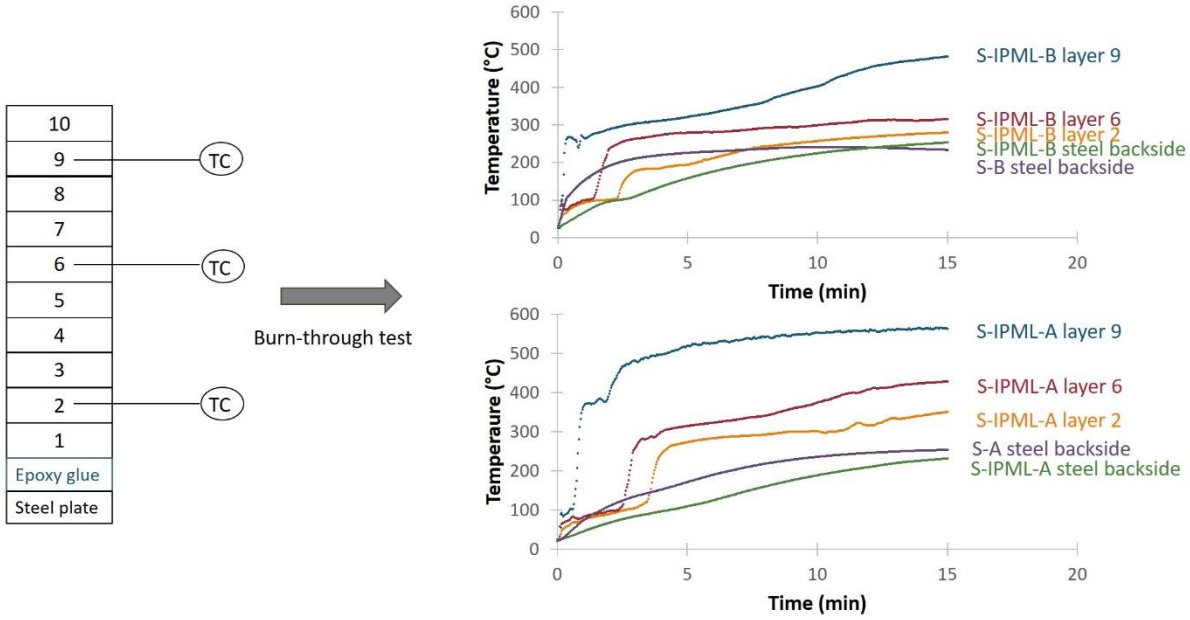

Figure 75. Thermal gradient evolution in S-IPML-A and S-IPML-B.

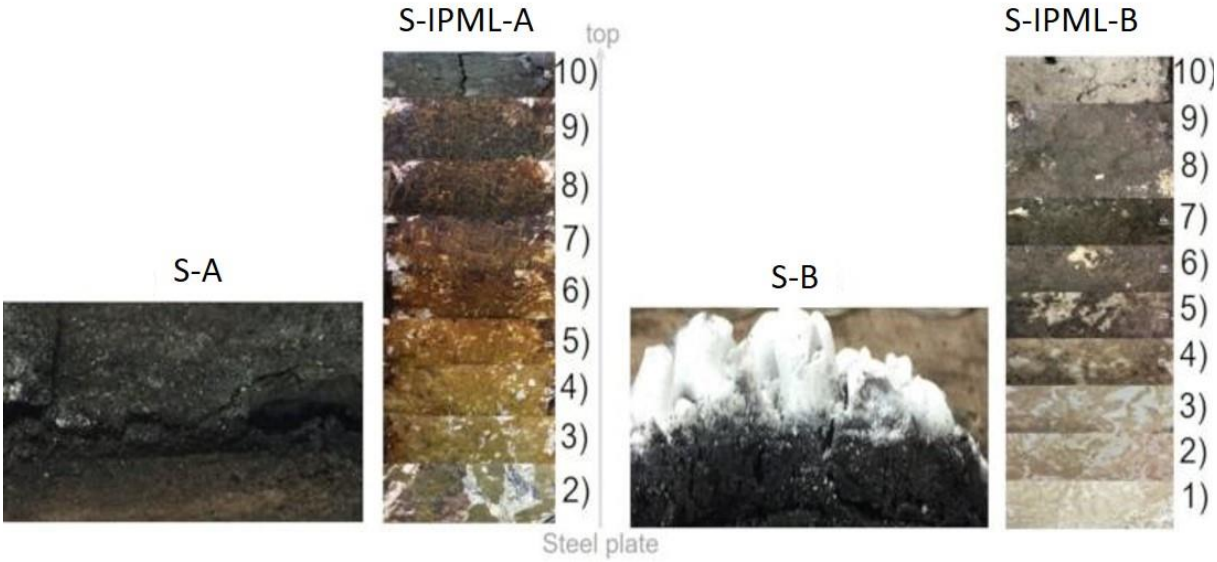

Figure 76. Carbonization gradient evolution in S-IPML-A and B, compared to S-A and S-B chars (Layer 10 is the top layer (directly exposed to fire) for S-IPML-A and S-IPML-B).

To obtain quantitative information on this carbonization gradient, char retrieved from each layer of S-IPML-A and S-IPML-B was submitted to thermogravimetric analyses (TGA) to estimate its residual organic degree at the end of the fire test, compared to the TGAs of the top and bottom parts of the S-A and S-B systems (Figure 77, Figure 78 and Table 23). Therefore, most residues were further analyzed by TGA. It is important to notice that no TGA measurements were done for residues of layers 1 and 2 of S-IPML B, because aluminum foils were too strongly glued, and no residue could be extracted.

© 2020 Tous droits réservés.
lilliad.univ-lille.fr

Thèse de Laura Geoffroy, Université de Lille, 2020

For both IPML systems, the carbonization gradient was obvious. S-IPML-A showed a gradient ranging from 25% organic content (top-layer 10) to 63% (bottom-layer 1), corresponding to a 38% difference between the top and bottom layers. For the S-A char, a difference of only 8% of organic content was reached between the top and bottom layers. It was also observed that from layer 7, the coating was less degraded than in the monolayers of intumescent coatings system. Similar observations were done for the S-IPML-B system. S-IPML-B showed a gradient from 7% (top-layer 10) to 34% (layer 4), corresponding to a difference of 27%. The same difference (27%) is registered between the top and bottom layers of the S-B char. These differences were quite similar, but one must not forget that it was not possible to analyze layers 1, 2, and 3, which were obviously less degraded than the other ones.

The evolution of the organic degree for S-IPML-A and S-IPML-B was plotted versus the IPML layer numbers (Figure 79), and curves were fitted with polynomial equations ($y = -0.4143x^2 + 0.3656x + 62.581$, $R^2 = 0.9993$ for S-IPMLA; and $y = 0.2548x^2 - 6.748x + 56.194$, $R^2 = 0.9883$ for S-IPML-B). This fitting was done to estimate the organic degree in layer 1, 2, and 3 in S-IPML-B (note that no theory supports the choice of polynomial equations and so, they are only valid in the range of measurement). Moreover, the organic degree of S-A top and bottom, and S-B top and bottom, is indicated in Figure 79. For both systems with coatings A and B, it is clear that the organic degree is higher for the IPML design than for the monolayers of intumescent coatings design.

Table 23. Organic residue of S-IPML-A and S-IPML-B for each layer.

IPML Layers	Organic Residue of S-IPML-A (%)	Organic Residue of S-IPML-B (%)
1	63	Cannot be measured
2	61	Cannot be measured
3	60	Cannot be measured
4	57	34
5	54	29
6	50	23
7	46	20
8	39	19
9	32	17
10	25	7
Intumescent coating-top	35	2
Intumescent coating-bottom	43	29

© 2020 Tous droits réservés.

lilliad.univ-lille.fr

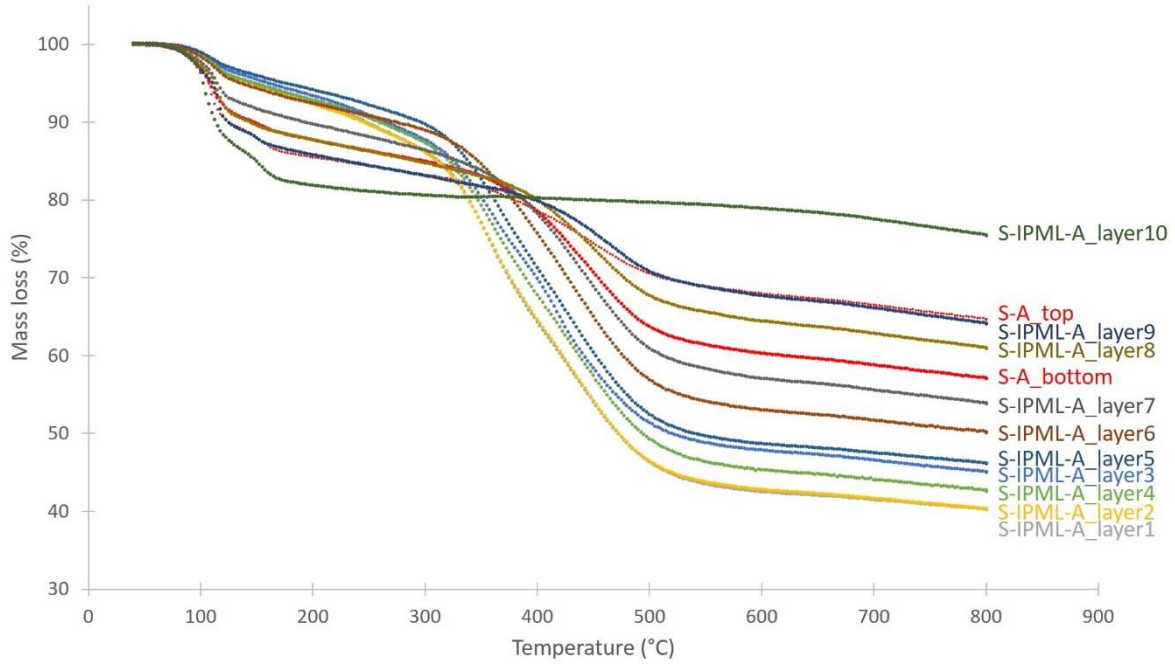

Figure 77. TG curves for each char layer of S-IPML-A and for S-A char layer, obtained after 15 min burn-through test exposure.

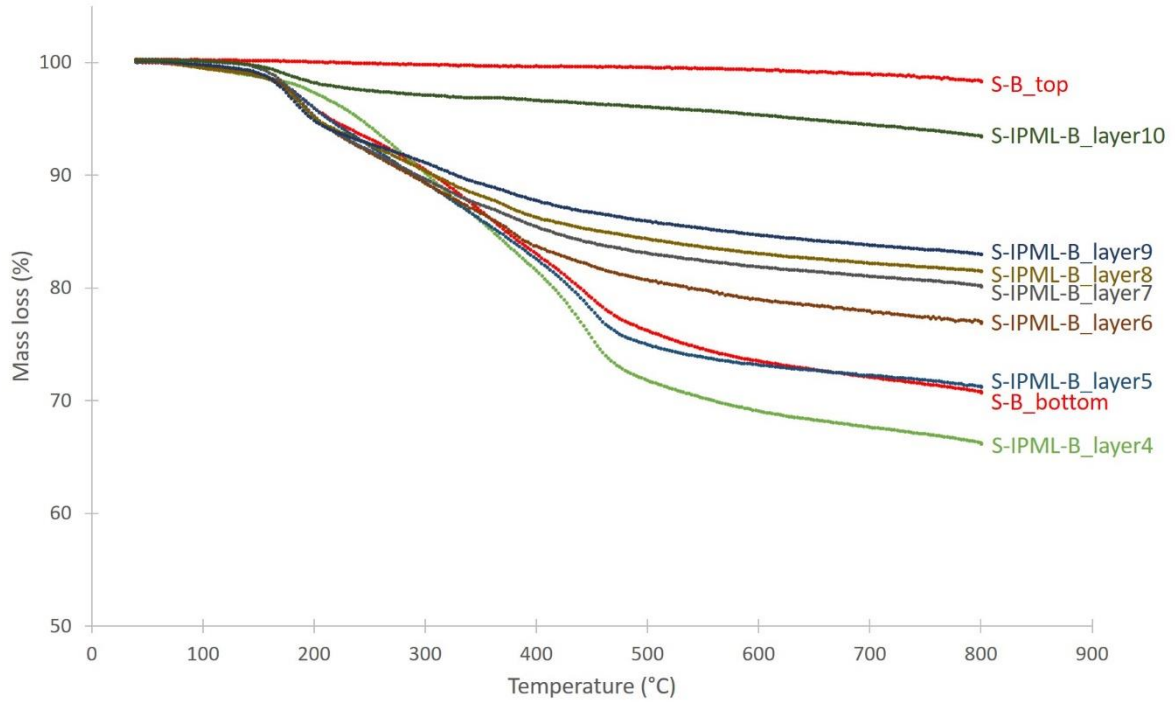

Figure 78. TG curves for each char layer of S-IPML-B and for S-B char layer, obtained after 15 min burn-through test.

© 2020 Tous droits réservés.
lilliad.univ-lille.fr

Thèse de Laura Geoffroy, Université de Lille, 2020

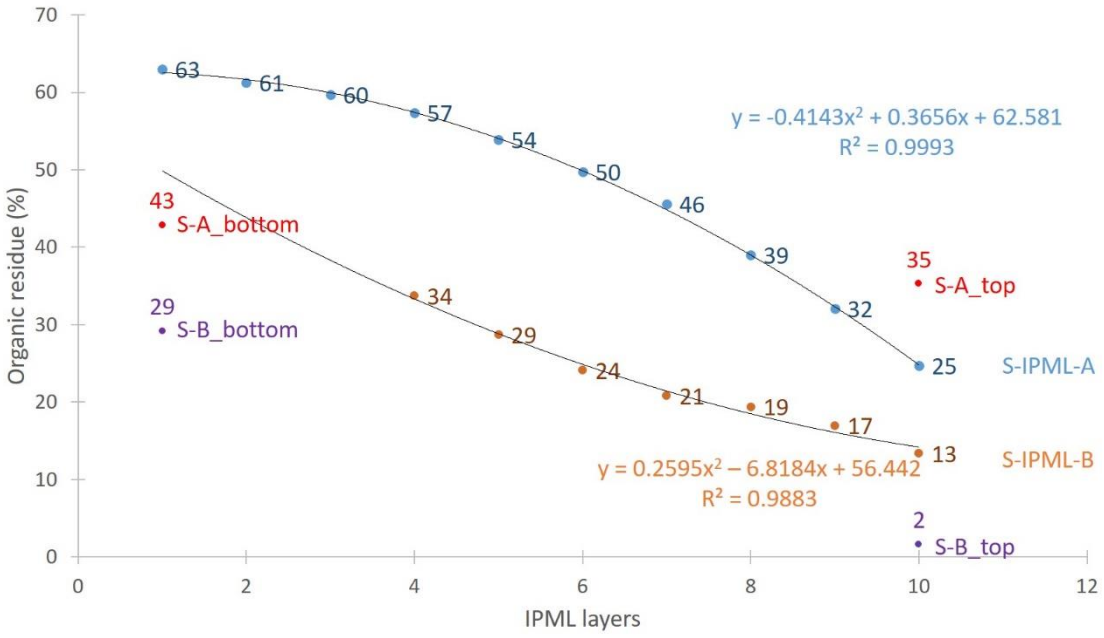

Figure 79. Evolution of carbonization gradient depending on the IPML layer number.

3. Discussion

In this chapter, a new concept was evaluated, namely Intumescent Polymer Metal Laminate, which was compared to neat intumescent coatings to estimate the PML design advantage. Three intumescent coatings based on three different chemistries (epoxy, acrylic, and silicone) were tested. In the case of a physical expansion (silicon-based resin containing expandable graphite), IPML design did not improve the fire protection of the steel substrate. On the contrary, the steel backside reached higher temperatures quicker. As explained previously, no entangled network is formed between expandable graphite "worms" and aluminum foils due to too thin layers applied in-between the aluminum foils, and the higher constraint that multi-layer design triggers. In the S-IPML-C system, "worms" of graphite were oriented perpendicularly to aluminum foils. Owing to this "worms" orientation, some thermal bridges were created between aluminum foils and "worms" of graphite, increasing the heat propagation. On the opposite, when S-C was exposed to fire, physical "worms" expansion occurred, and an entangled network (through graphite entanglement) with holes was formed. As a result, an efficient heat barrier, leading to good fire protective properties, was ensured. S-A and S-B are classical intumescent coatings relying on the chemical intumescent process based on degradation of the carbon source, dehydration of the acid source, and release of gases from the swelling agents. For these systems, using the PML design allowed improved thermal protection properties, particularly

© 2020 Tous droits réservés.

lilliad.univ-lille.fr

for the first ten minutes of the test. Thermal analyses and instrumentation of the IPML with thermocouples showed that high temperature and carbonization gradients are obtained, much higher than those obtained in the intumescent chars without foils. Differences in terms of expansion and char morphologies, not being obvious between the IPML and the monolayers of intumescent coatings samples, the explanation of this fire protection improvement could be (i) the delamination effect observed between layers, and (ii) the chemical intumescent phenomenon. It created a heat gradient, and hence a large carbonization gradient. Therefore, when the IPML design is exposed to fire, the first intumescent layer starts to swell and decompose. This phenomenon protects other layers from heat propagation for a certain time. Then, the heat slowly spreads through the aluminum foil to the second intumescent layer. After a certain temperature is reached, the second intumescent layer starts to decompose and swell. This swelling combined with the thermal dilatation coefficient difference between aluminum and intumescent coating create a delamination between aluminum foils. In addition to the intumescent phenomenon, it improved the fire protection performance of the IPML system, because of air heat insulation properties, arising from delamination. Afterwards, the heat is spread to other intumescent layers, and the same mechanism occurs in each layer. Thus, it is the combination of successive intumescence and delamination, that the material can reach better thermal protection properties. The thermal gradient between layers is consequently more important, leading to a higher carbonization gradient.

To conclude Figure 80 summarizes the different mechanisms of action of the intumescent coating, the PML, and IPML. In the intumescent coating case (Figure 80 a), only intumescence occurs to protect the steel substrate from the heat. With PML design (Figure 80 b), fire protection is brought by delamination (epoxy resin decomposes and produces gas). With the new IPML design (Figure 80 c), as it was previously explained, both phenomena were combined (chemical intumescence and delamination), which led to good heat protection performance.

© 2020 Tous droits réservés.
lilliad.univ-lille.fr

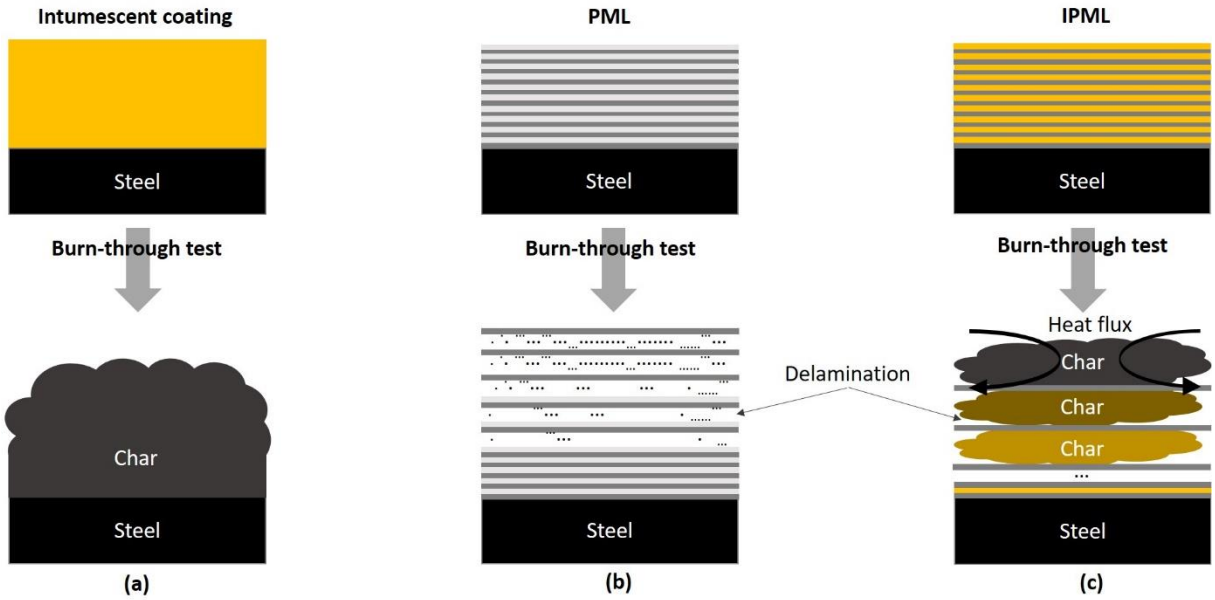

Figure 80. Illustration of the thermal behavior when ((a) intumescent coating, (b) PML, and (c) IPML) are exposed to a high heat flux fire test.

4. Conclusions

In this chapter, a new design was elaborated and tested: PML systems combined with intumescent paints, namely IPML. Three kinds of fireproof paints were studied, exhibiting different mechanisms of action. It was evidenced that when using an intumescent coating relying on physical intumescence (due to expandable graphite), the IPML system does not bring any advantage compared to a sole intumescent coating layer. Indeed, fire protective properties are not improved in that case, which can be explained by the fact that aluminum foils probably disturb the physical expansion of the coating. However, the IPML concept shows strong interest, compared to a monolayer of paint, when intumescent coatings relying on chemical intumescence processes are used. These IPML systems clearly improve fire protection, particularly for the first ten minutes of the fire tests. After 10 min, the temperature still increases, and the benefits are lost. The significant temperature reduction at the beginning of fire exposure is explained by the combination of the chemical intumescent process and delamination observed in between the aluminum foils. Both these phenomena increase the thermal and carbonization gradient in the IPML system, and thus improve heat protection performance on the steel substrate.

Current development of novel intumescent coatings is reaching a limit due to the limit in “novel chemistries”. Thanks to these first series of experiments, IPML design was proven as an efficient concept and a unique opportunity to improve fire protection without changing the

© 2020 Tous droits réservés.
lilliad.univ-lille.fr

formulation chemistry. However, further optimizations can be done to improve the fire protection performances on longer fire exposure time that will be presented in the next chapter.

Key points

- ✓ Development of new fire resistant barrier composed of aluminum foils and intumescent coatings: IPML.
- ✓ Depending on the intumescent coating: IPMLs reveal better fire protection properties than a sole intumescent coating or PML, from the beginning of the fire exposure to 10 min fire exposure.
- ✓ Fire protection mechanism of IPML is explained by the combination of intumescence and delamination phenomena.
- ✓ **Perspective**: Minimize the steady-state temperature reached at the end of fire exposure.

© 2020 Tous droits réservés.
lilliad.univ-lille.fr

Thèse de Laura Geoffroy, Université de Lille, 2020

Chapter 3: Bi-layer intumescent paint metal laminate: a novel design for a high performance fire barrier

In chapter 2 (of this part), Intumescent Polymer Metal Laminate (IPML) composed of ten plies were developed, by replacing the epoxy of PML by an intumescent paint between the aluminum foils [238]. It was demonstrated that, when glued on steel substrate, a dramatic reduction of the temperature rise at the beginning of the fire test for the systems based on chemical intumescence is obtained. Indeed, due to the delamination and the small residue formation between aluminum foils, the carbonization and thus the heat diffusion were delayed. Unfortunately, after 15 min of fire exposure, the temperature reaches the same value or is higher than the temperature measured for a sample simply coated with an intumescent coating. If carbonization is observed between aluminum foils, there is however no intumescence, most probably because of the too thin paint layers used between the aluminum foils.

In this context, the purpose of this chapter is to propose a new design inspired of previous IPML with higher thermal insulating performances. Our strategy to reach this goal is to take advantage of the use of two intumescent paints targeting different fire scenarios, applied at higher thicknesses than in the IPML system and to benefit from the use of metal foils to also initiate delamination. Bilayer paint structures are proposed instead of the 10 layers of IPML, and a metal foil is placed at the interface between the two paints, and/or between the paint and the substrate (Figure 81). In the last case, the metal foil is glued on the substrate (Figure 81). After characterizing these new fire barrier designs, fire protective performances were evaluated and compared to reference materials, i.e. the neat intumescent coatings applied on steel plate, with the same global mass and thickness. Tests were stopped after different exposure times. Then, visual residue observations, expansion measurements and pull-off tests were carried out to investigate the mechanism of action.

The work pertaining to this chapter was published in ***Industrial & Engineering Chemistry Research*** journal: **https://doi.org/10.1021/acs.iecr.9b06345** [243]**.**

KEYWORDS: Bilayer Intumescent Polymer Metal laminate, Fire protective performances, Intumescent paints

© 2020 Tous droits réservés.

lilliad.univ-lille.fr

Aims

- ✓ During the fire test: retain the slow temperature rise at the beginning, and lower the steady state temperature.
- ✓ Elaboration of new fire barriers for steel protection, combining the use of two different intumescent paints and a metal laminate structure, named Intumescent Bi-layer Polymer Metal Laminate (IBPML).
- ✓ Evaluation of IBPML fire protection performances.
- ✓ Full mechanism investigation to understand the behavior of IBPML against fire.

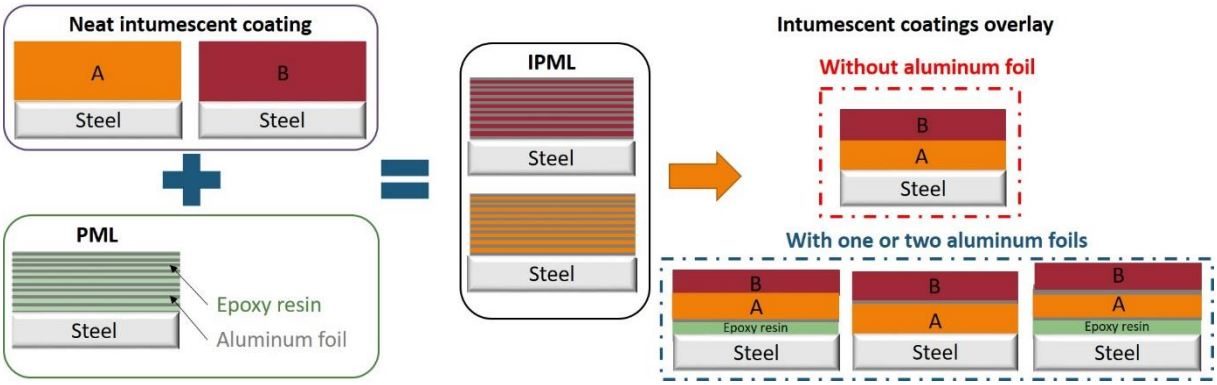

Figure 81. Development of Intumescent Bilayer Polymer Metal Laminate materials.

1. Samples description

In this chapter, eleven samples presented in Figure 82 were prepared, following the set-up described in materials & methods part (page 177)). The name of the sample indicates its composition from the substrate to the top layer (S for steel, A and B for paint type, Al for the aluminum foil). As Figure 82 shown, different structures and designs are studied in this work. To see if the addition of the metallic layers is efficient, some additional samples were prepared, namely S-A, S-B, S A+B and S-B+A, which were taken as reference. In that case, steel plates were covered using a film applicator, with coating A (S-A), or coating B (S-B), or both (S-A+B and S-B+A: with a 24h curing step at room temperature between the first and the second intumescent coating deposition). All paints were cured for 48 h at room temperature before fire testing. All samples were prepared in triplicate to check repeatability of results.

© 2020 Tous droits réservés.
lilliad.univ-lille.fr

Thèse de Laura Geoffroy, Université de Lille, 2020

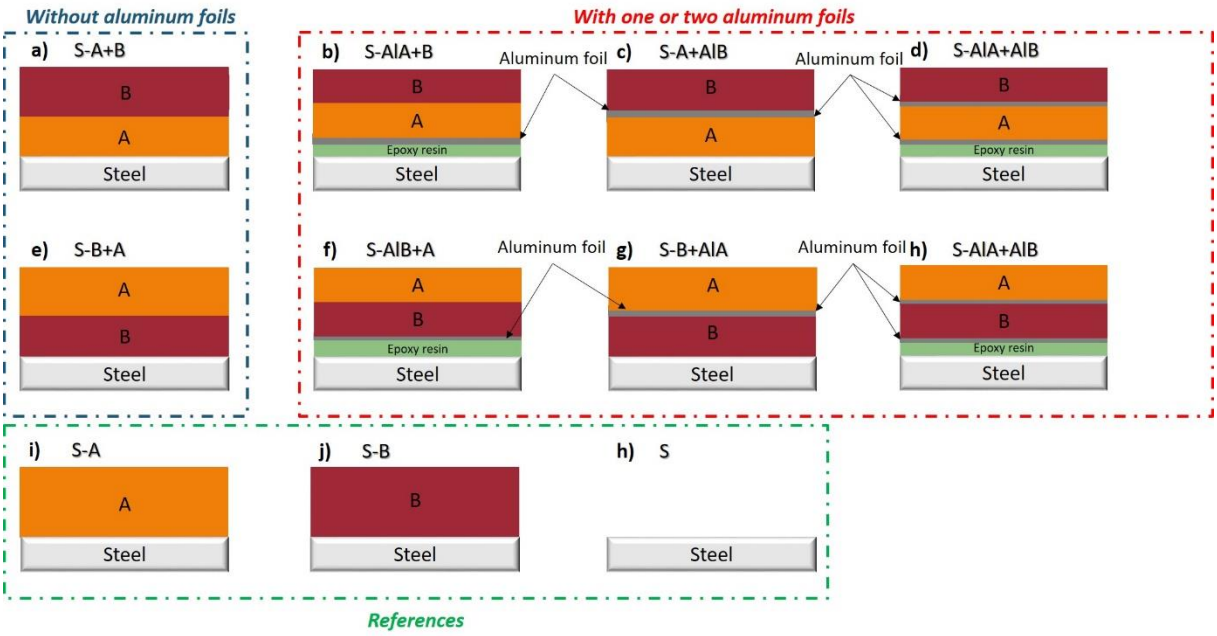

Figure 82. Intumescent bilayer metal laminate: Samples studied.

2. Results

2.1. Intumescent bilayer metal laminate characterizations before fire test

The bilayers morphology of the materials has been characterized using optical microscopy (fully described in materials & methods part (page 181)). Cross section pictures of the different coatings (without substrate) are gathered in Figure 83. It should be noticed that, for cross section analyses, the coatings were not applied on steel substrates. This explains why the cross sections of S-A+B and S-B+A are not presented, but it is assumed that their aspect is similar to the cross sections of S-AlA+B and S-AlB+A, respectively, as the only difference is the presence of the aluminum foil. From these cross section pictures (Figure 83), it is noticed that the adhesion between layers is homogeneous. In addition to this, the thickness of each layer has been estimated, and average values of each layer and total sample thicknesses and masses are reported in Table 24. It can be observed that when 10 g of coating is deposited, thicknesses of around 700 µm and 600 µm for coatings A and B, respectively. Some bubbles are observed in paint layers (which correspond to the removal of large particles during polishing), but not at the interfaces coating/coating or coating/aluminum (Figure 83). All samples look homogeneous (Table 24), and exhibit similar thicknesses (between 4.7 and 4.9 mm) and total coating masses (around 15.8 g). The relative gaps of 4% for the thickness and 6% for the total mass are indeed considered as negligible.

© 2020 Tous droits réservés.

lilliad.univ-lille.fr

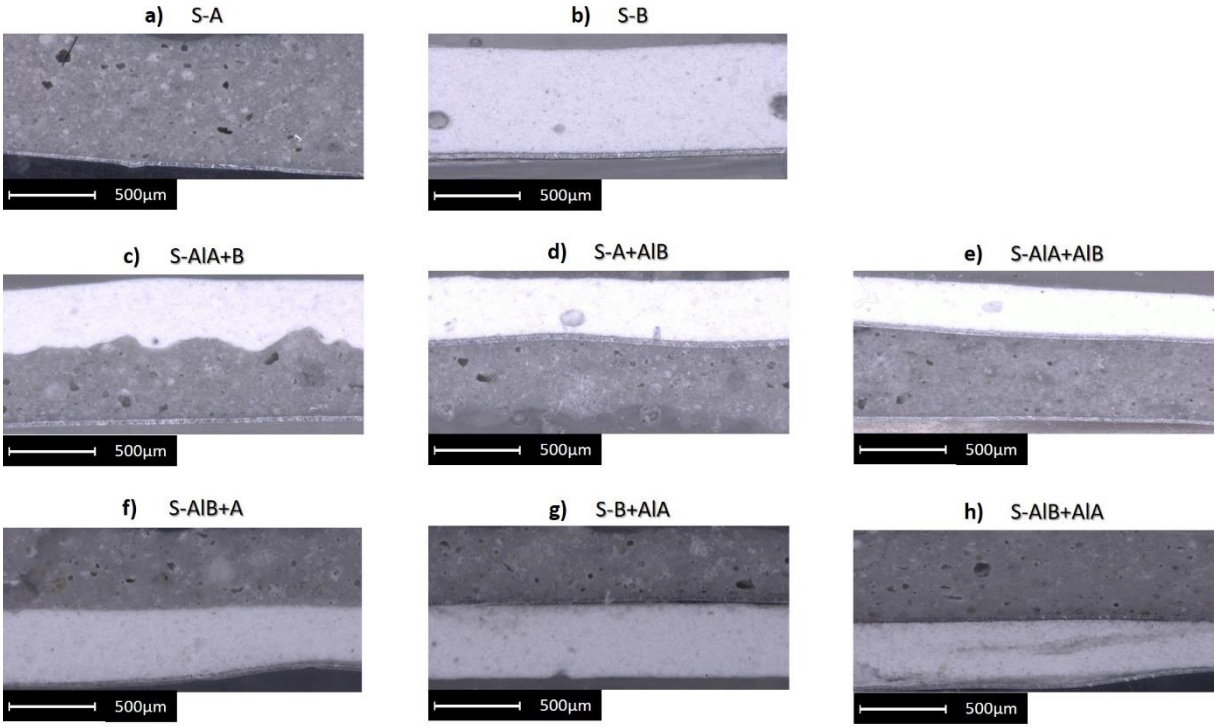

Figure 83. Optical microscopy observation in cross-section of the studied samples.

Table 24. Quantitative characterization of each sample studied.

Samples	Mass of coating A (g)	Mass of coating B (g)	Total mass (g)	A thickness layer (µm)	B thickness layer (µm)	Total thickness (mm)
S-A	19.5 ± 0.6		256.5 ± 0.4	~ 1300		4.85 ± 0.07
S-B		19.6 ± 0.1	260.4 ± 0.2		~ 1200	4.7 ± 0
S-A+B	10.2 ± 0.1	10.23 ± 0.03	251.2 ± 0.1	~ 700	~ 600	4.8 ± 0
S-A+AlB	10.2 ± 0.1	10.23 ± 0.03	251.2 ± 0.5	~ 670	~ 620	4.8 ± 0.01
S-AlA+B	10.21 ± 0.04	10.2 ± 0.2	258 ± 1	~ 700	~ 600	4.7 ± 0
S-AlA+AlB	9.96 ± 0.02	10.4 ± 0.2	257 ± 3	~ 700	~ 620	4.9 ± 0.1
S-B+A	10.88 ± 0.03	11.36 ± 0.01	255 ± 2	~ 780	~ 700	4.7 ± 0
S-B+AlA	10.0 ± 0.7	9.91 ± 0.04	266 ± 3	~ 670	~ 620	4.8 ± 0
S-AlB+A	10.6 ± 0.5	10.6 ± 0.3	267 ± 2	~ 780	~ 700	4.9 ± 0.1
S-AlB+AlA	10.2 ± 0.5	10.0 ± 0.5	254 ± 1	~ 700	~ 600	4.8 ± 0.1

© 2020 Tous droits réservés.
lilliad.univ-lille.fr

Thèse de Laura Geoffroy, Université de Lille, 2020

2.2. Fire behavior

Fire protective performance of steel coated with intumescent coatings (A, B and the overlay of A+B and B+A) were compared to the raw steel plate. Figure 84 shows the evolution of the temperature versus time at the backside of the systems, and Table 25 gathers temperatures reached at the end of fire test (steady state) and reports the slope of the curves at different time intervals of fire test (measurements fully described in materials & methods part (page 179)). The temperature at the backside of the raw steel plate dramatically increases from the beginning of the fire test (with 300°C/min as a slope) and reaches its steady state temperature at 620°C after 10 min fire test (Figure 84 a and Table 25). For the steel plate coated with intumescent paint A, the temperature increases until 4 min, with a slope (102°C/min) 2.94 times lower than the slope of the reference at the beginning of the fire exposure. Then the slope of S-A dramatically decreases and temperature reaches 345°C (leading to a temperature difference of 275°C, which corresponds to 44% lower than the temperature reached for the raw steel). For S-B, similar observations can be done: from the beginning of the fire test until 2 min, the slope of S-B is 2.24 times lower than the slope of S (Figure 84 a and Table 25). Then, it decreases and temperature reaches a plateau at 270°C. Both intumescent coatings protect steel against fire, however coating B seems to show a better resistance to fire at the end of the test while coating A is more efficient at the beginning of the test (with a slope reduction of 1.31 compared to the slope of S-B). For this reason, the resistance to fire of the overlay of coatings A and B was evaluated (S-A+B and S-B+A), to try to combine the advantages of the two coatings. S-A+B and S-B+A exhibit similar fire protection. From the beginning to 1 min fire test, the slopes of S-A+B and S-B+A are respectively 3.16 and 1.34 times lower than the slopes of S and S-B and similar than the slope of S-A (Figure 84 a and Table 25). After 30 min fire test, the temperature reaches 320°C (48% lower than temperature reached for S and 19% higher than temperature reached for S-B). Therefore, the temperature profiles of the simple overlay of coatings A and B do not allow to improve the fire protection performance. Other designs (bilayer metal laminate) were considered afterward to take advantage of the aluminum foil in the system with an intumescent coating combination.

© 2020 Tous droits réservés.

lilliad.univ-lille.fr

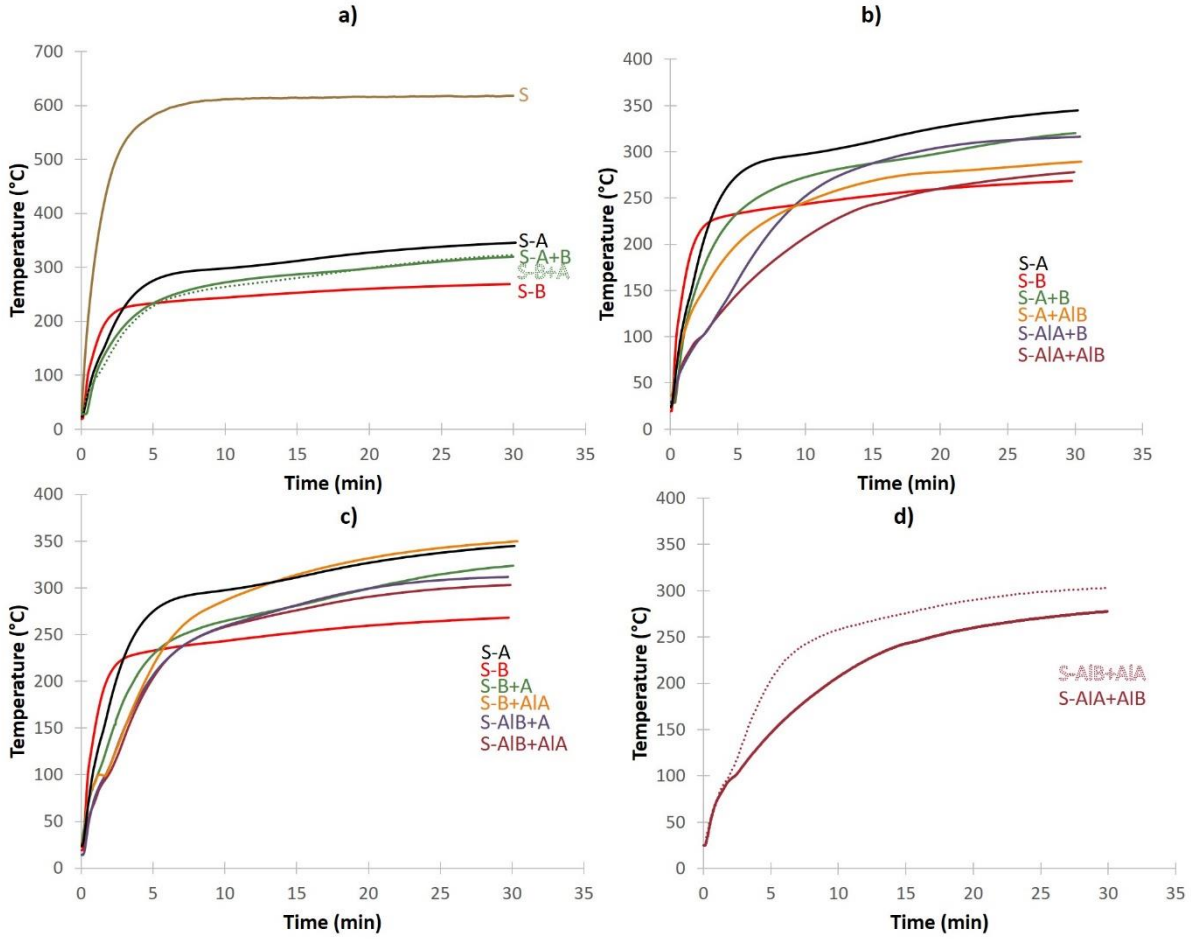

Figure 84. Fire protection performance comparison of each system studied (a) for the standard overlay without aluminum foils, b) for the overlay A (steel side) and B (A side), c) for the overlay B (steel side) and A (B side), d) for the two best systems).

The fire performance of laminated samples (S-A+AlB, S-B+AlA, S-AlA+B, S-AlB+A, S-AlA+AlB, S-AlB+AlA) were then compared to those of samples simply coated with the paints (S-A, S-B, S-A+B and S-B+A). The resulting curves are gathered in Figure 84 b and Figure 84 c. Figure 84 b shows temperature versus time curves for the bilayers with A as bottom layer (steel side) and B as top layer. On the contrary, in Figure 84 c, B is the bottom layer and A is the top layer. In both cases, better resistance to fire performance is obtained at the beginning of the test for the systems with aluminum foils and the designs with two aluminum foils (S-AlA+AlB and S-AlB+AlA) show the best results. Moreover, the S-AlA+AlB design reveals better fire protection performance compared to S-AlB+AlA (Figure 84 d).

In the case of the overlay B (bottom)/A (top), all systems with one or two aluminum foils exhibit almost the same fire behavior with a lower temperature rise from the beginning to 5 min of test compared to S-B+A. But after 5 min fire exposure, no stabilization of the temperature is observed, and temperature still increases to reach between 270 and 350°C at the end of the test.

© 2020 Tous droits réservés.
lilliad.univ-lille.fr

Thèse de Laura Geoffroy, Université de Lille, 2020

The temperatures reached after 30 min fire exposure are similar to those obtained with S-A+B and S-A. These samples do not provide the same fire protection properties compared to S-B, particularly after 5 min of flame exposure. It is assumed that the expansion of coating B is modified and lower, because of coating A on the top, and the presence (for some systems) of aluminum foil. Figure 85 reveals the less expansion of coating B in the case of S-B+AlA (Figure 85 a), which has a global expansion of 308%, and S-A+AlB residues (Figure 85 b), which has a global expansion of 602%. These expansion measurements confirm that the expansion of coating B is hindered by coating A and aluminum foil in the case of the overlay B (bottom)/A (top) with or without aluminum foil, and thus can explain their lower fire protection properties, compared to the overlay A (bottom)/B (top) with or without aluminum foil systems. Indeed, the residue created by coating B is not very well developed, and thus cannot properly ensure the thermal protection of the system. Subsequently, S-A+B was selected as the reference for the beginning of the test due to its best fire protection performance, and S-B was chosen at the end of the fire test because this system exhibits the lowest temperature after 30 min fire exposure.

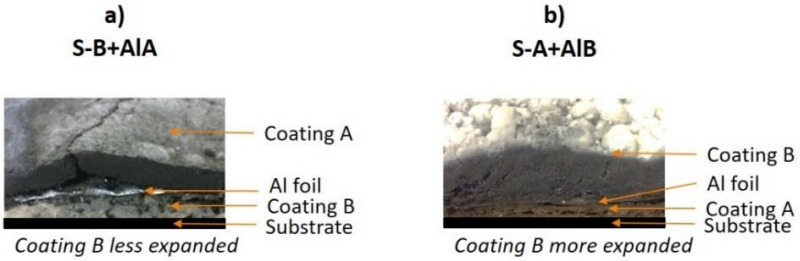

Figure 85. Comparison of coating B expansion between a) S-B+AlA and b) S-A+AlB.

Having the coating B in the top layer leads to more differentiated behaviors of the samples and better performances compared to samples with B in the bottom layer. Indeed, the final temperatures of the different designs are between 250 and 300°C, consequently the systems remain at least as efficient as the S-A+B design. However, because of an additional fire resistance (commented in the next part), the increase of temperature during the fire testing, is better for the system with aluminum foils. For S-A+AlB a change of slope is observed at 1 min and is 1.37 times lower than S-A+B. Then, after 30 min fire test, the temperature reaches 290°C, 20°C higher than temperature reached for S-B (Table 25). Aluminum foil between A and B allows to delay the thermal diffusion into the system at the beginning of the test, but after 9 min of fire exposure, the benefit of the design is lost compared to S-B. For S-AlA+B, at the beginning of the test, the slope is 2.32 lower than the slope of S-A+B, and an inflexion point at 2.5 min, are observed, which improves the resistance to fire of the system. But similarly to S-A+AlB, for longer time, higher than 9 min, the improvement is lost, leading to a maximum

© 2020 Tous droits réservés.

lilliad.univ-lille.fr

temperature of 316°C after 30 min fire test. For S-AlA+AlB, an inflexion point is observed at almost 2.5 min, with a slope reduction of 2.5 compared to the slope of S-A+B. This system exhibits better resistance to fire performances than S-B up to 20 min. Indeed, S-AlA+AlB reaches 250°C after 17 min fire exposure compared to 13.5 min of fire test for S-B. At the end of the test, a temperature of 280°C is recorded which is only 10°C higher than the temperature of S-B.

© 2020 Tous droits réservés.
lilliad.univ-lille.fr

Table 25. Rates of change of temperature according to different times, and temperatures reach after 30 min fire exposure.

Samples	Rate of change of Temperature (°C/min): from 0 s to 1 min	Reduction		Rate of change of Temperature (°C/min): from 1 to 2 min	Reduction		Time to reach 250°C (min)	Temperature after 30 min fire test (°C)	% Reduction of Temperature after 30 min fire test	
		Against S	Against S-A+B		Against S	Against S-A+B			Against S	Against S-B
S	300			129			0.7	620		
S-A	102	÷ 2.94		59	÷ 2.19		3.7	345	- 44%	
S-B	134	÷ 2.24		48	÷ 2.69		13.5	270	- 56%	
S-B+A	95	÷ 3.16		44	÷ 2.93		7	320	- 48%	
S-A+B	100	÷ 3		45	÷ 2.87		6.5	320	- 48%	+ 19%
S-AlA+B	43		÷ 2.32	24		÷ 1.87	9.9	320		+ 19%
S-A+AlB	73		÷ 1.37	34		÷ 1.32	10.8	290		+ 7%
S-AlA+AlB	40		÷ 2.50	22		÷ 2.04	17	280		+ 4%
S-AlB+A	76		÷ 1.31	31		÷ 1.45	8.5	312		+ 16%
S-B+AlA	83		÷ 1.20				6.5	345		+ 28%
S-AlB+AlA	55		÷ 1.82	30		÷ 1.50	8.5	303		+ 12%

2.3. Mechanism investigation

To understand the differences in term of fire performance between the laminated samples (S-A+AlB, S-AlA+B, S-AlA+AlB) and the references S-A, S-B and S-A+B, some additional experiments were done. Each sample was exposed to fire for different durations (40 s, 2 min, 10 min and 30 min). At each time, the cross-section of the residue was visually observed (Figure 87 and Figure 88), and the expansion was measured (Figure 86) (following the set-up described in materials & methods part (page 181)).

For sample without aluminum foils (S-A, S-B and S-A+B), coatings degrade during the fire exposure, a residue is formed, and no delamination is observed (Figure 87). S-A residue looks very dense and cohesive, with an expansion of 165% after 30 min fire test, as illustrated in Figure 86 and Figure 87. In comparison, S-B residue is brittle with a high expansion of 983% (Figure 86 and Figure 87), 6 times higher than that of S-A expansion. The residue obtained for S-A+B is dense and less expanded than S-B residue (twice lower). Figure 86 reports that S-A+AlB and S-AlA+AlB have almost the same expansion (around 600%) over fire exposure time. Same observation was done for S-A+B and S-AlA+B expansion (around 350%) (Figure 86). Therefore, it is possible to consider that aluminum foil (glued onto steel plate) has no influence on the residue expansion, on the contrary to coating A which clearly influences expansion of the B paint and thus its fire protective properties.

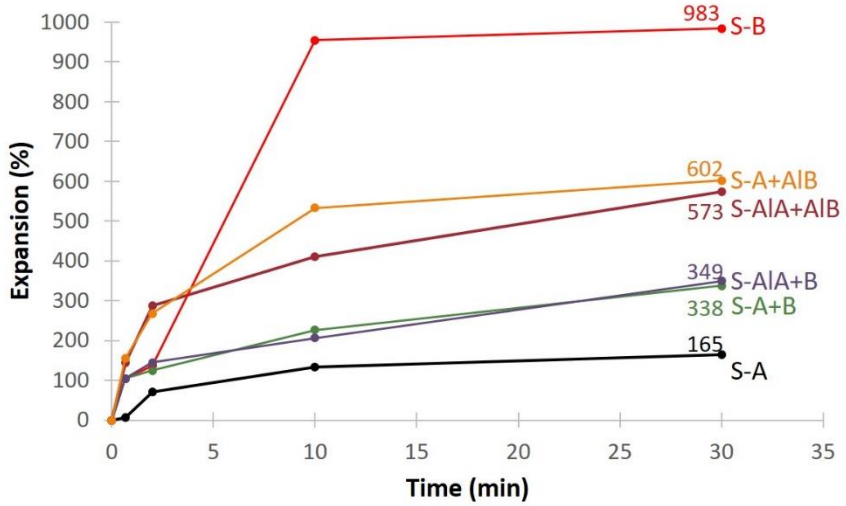

Figure 86. Expansion evolution versus time for each sample studied.

When aluminum foil is added in the systems, different behaviors occur (Figure 88): for S-AlA+B, at 40 s, the residue starts to decompose to the top, coating A remains intact. At 2 min fire test, a delamination between coating and aluminum foil occurs (Figure 88 c). This delamination is maintained throughout the test up to 30 minutes of exposure to fire. S-AlA+B

© 2020 Tous droits réservés.
lilliad.univ-lille.fr

Thèse de Laura Geoffroy, Université de Lille, 2020

and S-A+B residues have the same aspect, except for the delamination observed in the case of S-AlA+B. For S-A+AlB, the B-residue on the top starts to form (contrary to coating A which seems apparently unaffected) and no delamination is observed at 2 min. However, a delamination between the aluminum foil and the coating A appears after 10 min of fire test (Figure 88 b) and is maintained until 30 min of fire exposure. This delamination which occurs at different times (2 min for S-AlA+B and 10 min for S-A+AlB) could explain the different temperature versus time curves obtained and illustrated in Figure 88 b. Indeed, the delamination at 2 min could cause the inflexion point observed at 2.5 min for S-AlA+B that is not observed for S-A+AlB.

For S-AlA+AlB, after 40 s fire exposure, coating B on the top starts to decompose. At 2 min, coating A starts to decompose, and two delaminations between (i) aluminum foil (glued onto steel plate) and coating A and (ii) coating A and aluminum foil (between coating A and coating B) occur (Figure 88 a). These two delaminations remain until the end of the test, creating an additional thermal resistance, and could justify the better resistance to fire of S-AlA+AlB compared to the other systems.

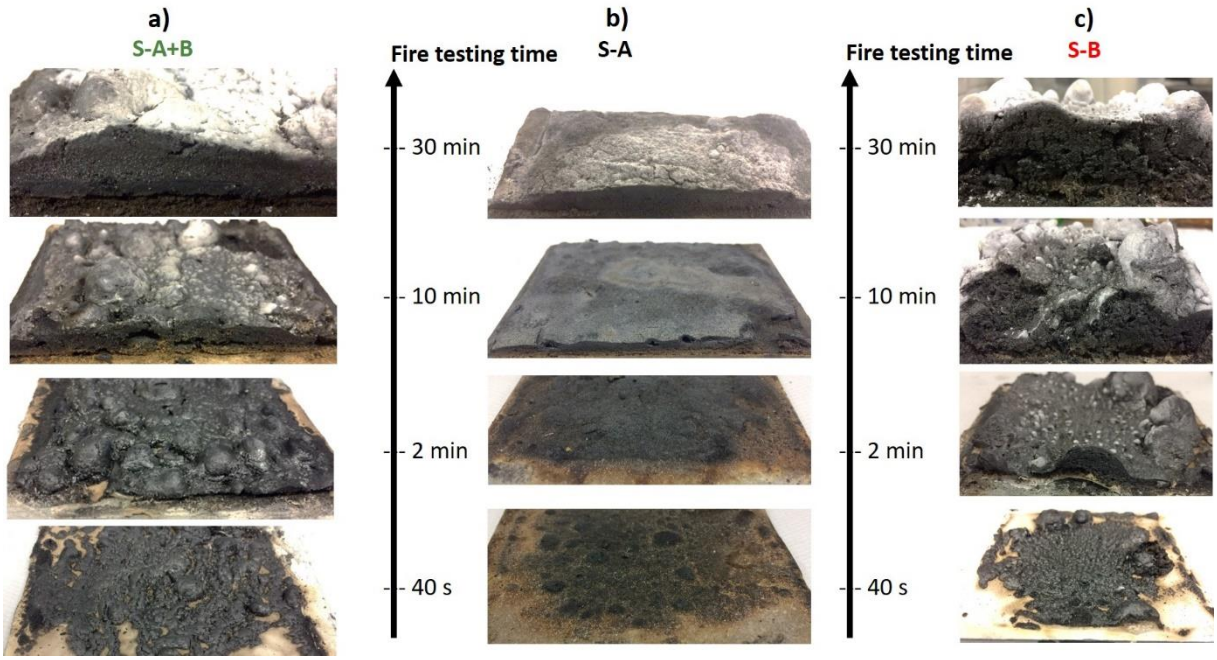

Figure 87. Fire tests stopped at different exposure times for the systems (a) S-A+B, b) S-A, c) S-B).

© 2020 Tous droits réservés.

lilliad.univ-lille.fr

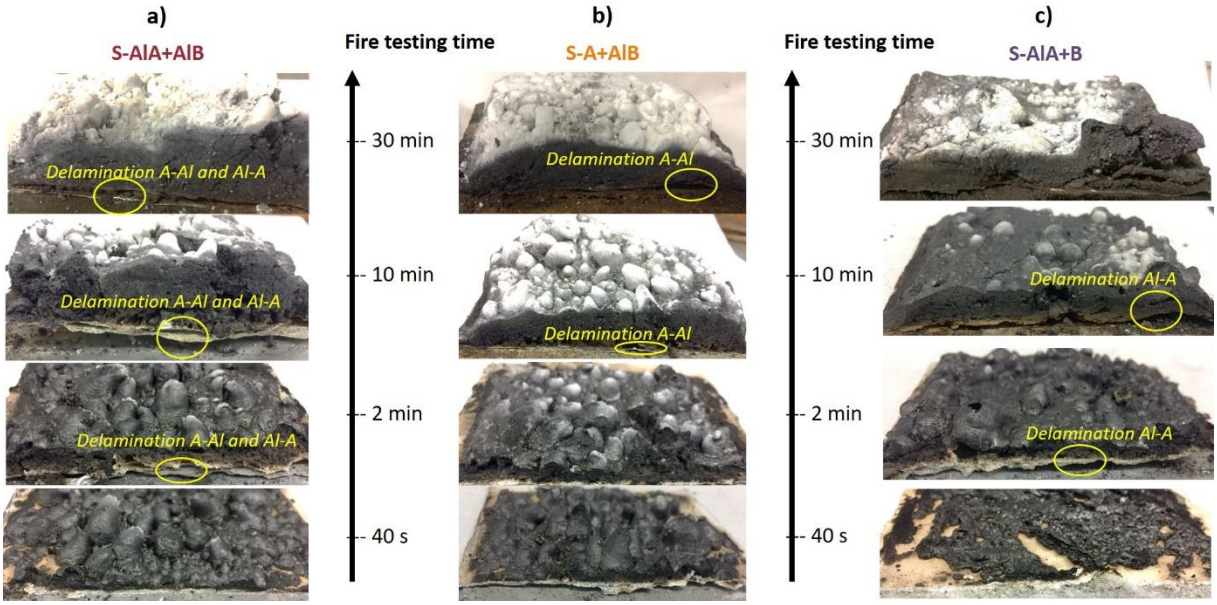

Figure 88. Fire tests stopped at different exposure times for the designs (a) S-AlA+AlB, b) S-A+AlB, c) S-AlA+B).

Based on the previously presented analyses, Figure 89 summarizes the mechanisms of action of the fire barriers S-A+B, S-AlA+B, S-A+AlB, S-AlA+AlB. Two main conclusions can be drawn. On one hand, delamination only occurs when aluminum foils are used and preferentially at the interface with coating A. Indeed, no delamination is visible for S-A+B (Figure 89 d) unlike to S-AlA+B.

The fact that delamination is only visible at the interface of aluminum foils and coating A could be explained by: i) the release of gases during the decomposition of the coating, ii) the dilatation coefficient difference between coating and aluminum foil and iii) the lower adhesion between coating A and aluminum foil compared to the adhesion between coating A and sandblasted steel. Indeed, when the coating is exposed to fire and decomposed, gases are released (assumption i) [27], [28], [201], [239], [240] and thus the coating A softens and takes a wavy shape (Figure 89 a and Figure 90). These gases are trapped between aluminum foil and provoke a delamination. Moreover, to confirm assumption iii), pull-off tests (fully described in materials & methods part (page 182)) were carried out on S-AlA and S-A to quantify the adhesion difference between aluminum foil/coating A and sandblasted steel/coating A, respectively. These tests reveal that coating A has a significantly stronger adhesion with sandblasted steel than with aluminum foils. For this reason, when coating A is in contact with aluminum foil, delamination occurs when coating A starts to decompose.

On the other hand, delamination occurs earlier on the aluminum foil glued onto steel plate (for S-AlA+AlB and S-AlA+B) compared to the aluminum foil placed between coating A and B

© 2020 Tous droits réservés.
lilliad.univ-lille.fr

(for S-A+AlB). It is assumed that aluminum foils glued onto steel plate are more constrained (and so, they cannot accommodate the stresses) (Figure 89 c) than aluminum foil between both coatings. Indeed, the delamination of S-A+AlB (Figure 89 b) occurs later due to the higher degree of freedom of aluminum (accommodation of stresses is possible), and thus can easily adapt to the deformation and decomposition of coating A compared to aluminum foils glued onto steel plate. To verify this assumption, the fire test of AlA+B without steel plate was carried out to remove the constraint imposed by the substrate. The aim of this test reveal whether delamination takes place at the same time with and without applied constraint by steel plate. As expected, a delamination was observed for AlA+B, after 2 min of fire exposure compared to 10 min for S-AlA+B, which confirms the previous assumption. Therefore, the constraint applied by the steel plate, and thus the localization of aluminum foil in the system have an influence on the delamination and consequently on the fire protective properties.

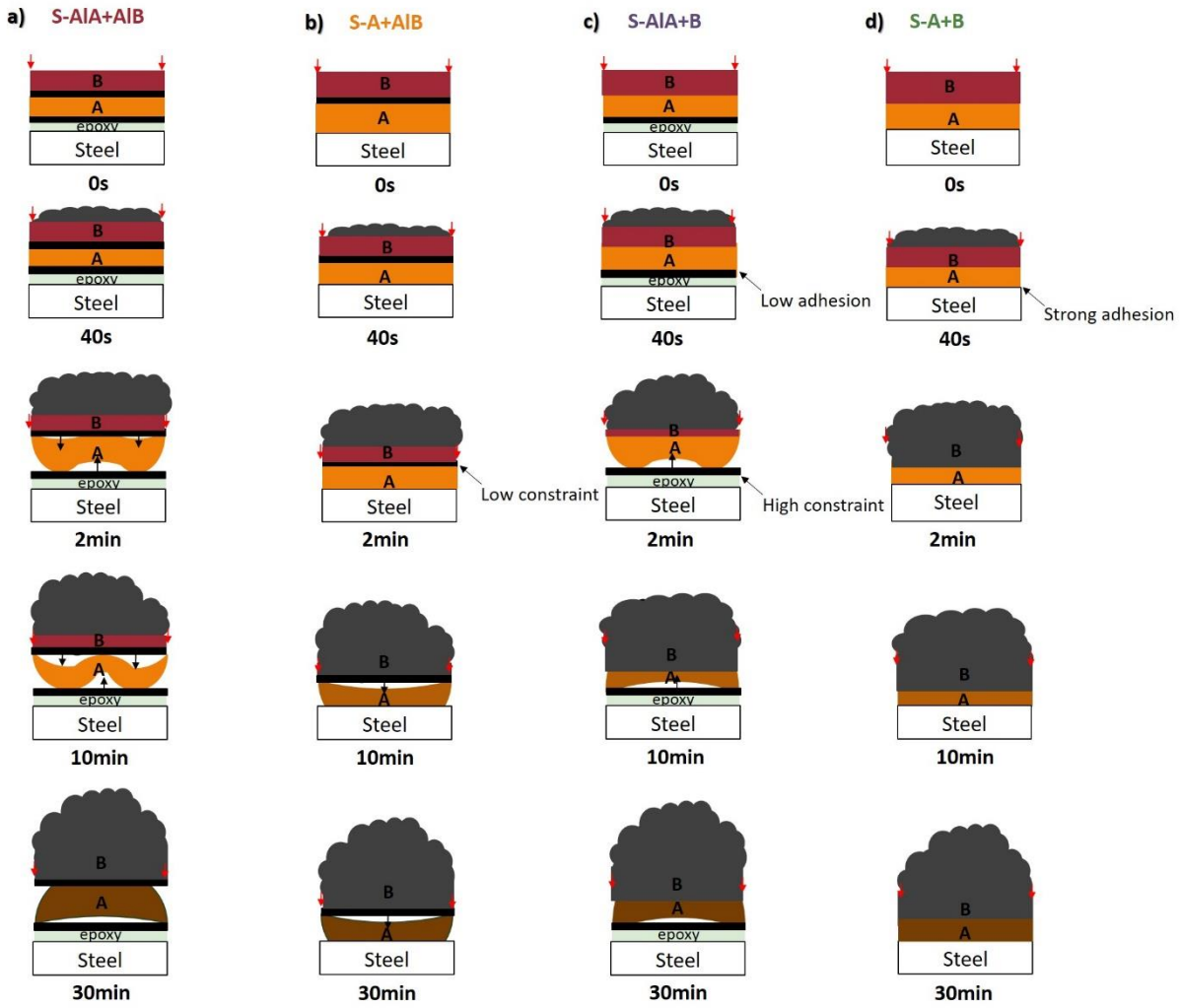

Figure 89. Mechanism of protection during the fire test for a) S-AlA+AlB, b) S-A+AlB, c) S-AlA+B, d) S-A+B.

© 2020 Tous droits réservés.

lilliad.univ-lille.fr

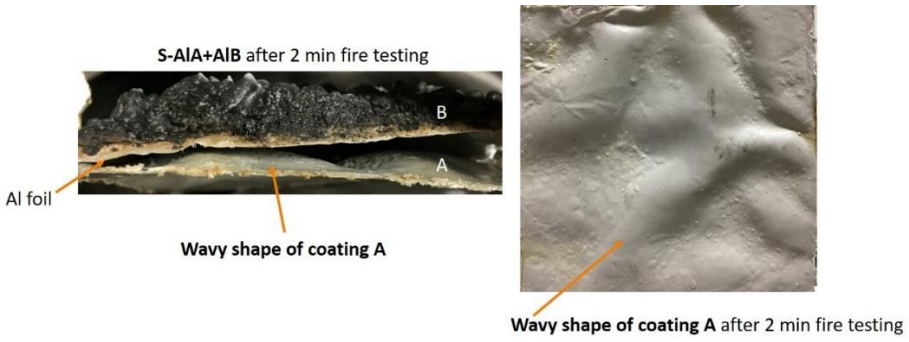

Figure 90. Observation of the wavy shape of coating A after 2 min fire testing.

3. Conclusions

In this work, novel designs of fire barriers based on a combination of two different intumescent coatings (A and B) laminated or not using aluminum foils were evaluated in term of fire protection and their mechanism of action were elucidated. With a simple overlay, no improvement in terms of fire protection is achieved. However, with a laminated design inspired from PML, fire protective properties are improved. In particular, a drastic reduction of the temperature at the backside of the protected steel plate is observed at early stage of the fire exposure for all laminated samples, which answers one of the main challenges in the intumescent coating industry. Combining two different intumescent coatings showing different chemistries and expansion behavior with the metal foils is the key innovation of this work. The order of the coatings has to be chosen wisely: depending on their fire behavior, one shows better performances when placed on the top whereas the second one is more effective when placed in between aluminum foils. The best fire performances are obtained with the two aluminum foils design. This configuration allows (i) to drastically decrease the slope of the time-temperature curve up to 20 minutes and (ii) to then reach a plateau barely above the reference up to the end of the test. These excellent fire protective properties are mainly due to two delaminations occurring during fire test. This work highlights that by changing the design of a fire barrier combining different coatings instead of the chemistry of it components, its fire protection properties can be enhanced.

However, the temperature reached after 30 min fire test is similar or a slightly higher than that obtained for a monolayer of intumescent coating. To reduce this temperature even further, an optimization was tested by replacing the interlayer materials (aluminum foils) by heat conductor (copper foils) or heat insulator (mica foils) (appendix 5 (page 206)). However, the results

© 2020 Tous droits réservés.
lilliad.univ-lille.fr

obtained did not improve the fire protection performances. More details are given in the appendix 5 (page 206).

Therefore, having developed a new fire barrier that is effective under severe conditions until 20 min, its use to protect another substrate for another application will be discussed in the next chapter.

Key points

- ✓ Different designs combining two different intumescent coatings, with various chemistries and expansion were tested to fire.
- ✓ The design and particularly the order of the coatings allow to reach completely different fire protection properties.
- ✓ Drastic decrease of temperature rise up to 20 min fire exposure is obtained with two aluminum foils designs with coating A (with a less expansion) on the bottom and coating B (with a high expansion) on the top.
- ✓ The best fire protection performances of this design are explained by two delaminations and both intumescent phenomena occurring during the fire exposure.
- ✓ The fire protective properties are improved by just changing the design of a fire barrier combining different coatings instead of changing their formulations.
- ✓ **Perspective**: Development of this concept for other fields.

© 2020 Tous droits réservés.

lilliad.univ-lille.fr

Chapter 4: Extension to other applications: substrate changing

Based on chapter 3 (of this part), it was demonstrated that, glued on steel substrate, two layers composed of two aluminum foils and two intumescent paints with various chemistries and expansion lead to a dramatic decrease of temperature up to 20 min fire exposure. Indeed, due to two delaminations occurring during the fire exposure, and the intumescent phenomena from the two intumescent paints, heat diffusion was slowed down and revealed superior fire protection performances.

In this context, the purpose of this chapter is to evaluate if the best fire barrier (i.e. two aluminum foils with coating A on the bottom and coating B on the top) developed in this part can protect other substrate, and thus be used for other fields (Figure 91). Indeed, the substrate depends on the intended application. Therefore, instead of using steel as a substrate, composites (epoxy resin with carbon fiber) were tested to have a lighter material, which is a real benefit for some specific industrial applications. After characterization, the fire protection performances of the fire barrier were evaluated on the new composite substrate. Cross-section of residue observations, expansion and mass loss measurements were carried out to investigate the mechanism of action.

KEYWORDS: Bilayer Intumescent Polymer Metal laminate, Fire protective performances, Composite

Aim

- ✓ Test the efficiency of the best fire resistant system developed on another substrate, for others applications: Steel plate substituted by composite (composed of epoxy resin and carbon fiber).

© 2020 Tous droits réservés.
lilliad.univ-lille.fr

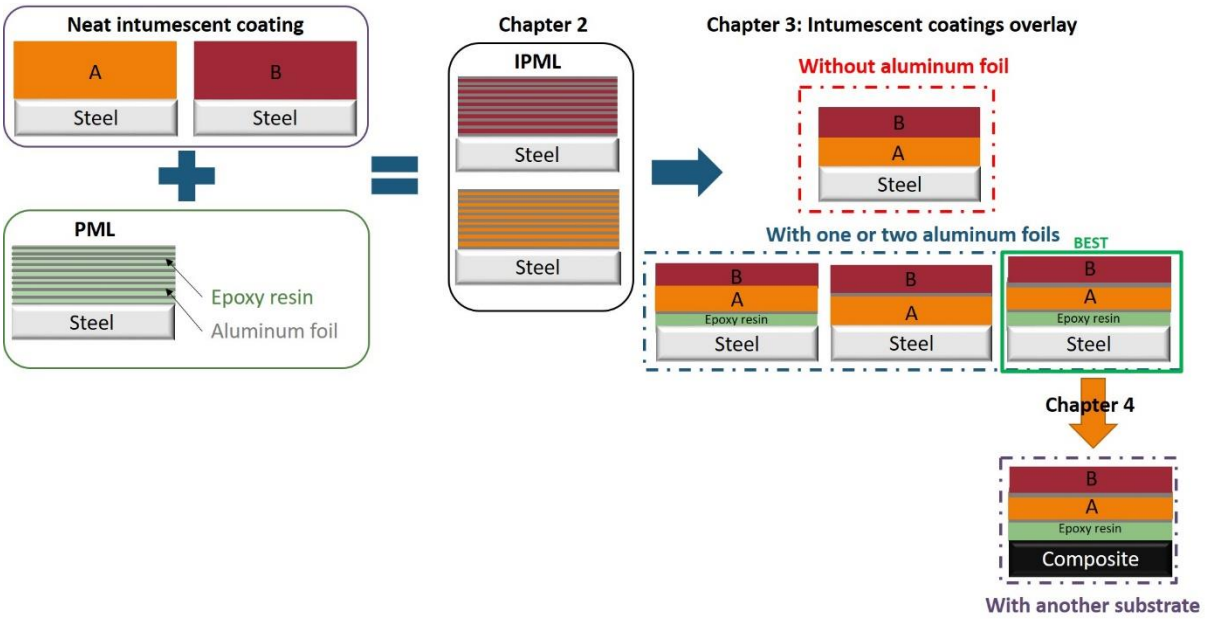

Figure 91. Optimization of the concept by changing metal foils or substrate.

1. Samples description

Table 26 describes the name and composition of all samples studied in this chapter (materials used fully described in materials & methods part (page 176)). It is important to notice that, the elaboration process was the same as that described in chapter 3 (part 3), and following the set-up described in materials & methods part (page 177). The only difference is that steel plate using as substrate was replaced by composite plate supplied by Goodfellow and composed of an epoxy resin and carbon fibers (with a volume fraction of fibers equal to 55%).

Table 26. Name and composition of sample studied.

Samples	Substrate	Epoxy glued	Metal foil	Coating A	Metal foil	Coating B
S-AlA+AlB	Steel	Yes	Aluminum	Yes	Aluminum	Yes
Composite	Composite	/	/	/	/	/
Composite-A	Composite	/	/	Yes	/	/
Composite-B	Composite	/	/	/	/	Yes
Composite AlA+AlB	Composite	Yes	Aluminum	Yes	Aluminum	Yes

© 2020 Tous droits réservés.

lilliad.univ-lille.fr

2. Results

2.1. Characterizations before fire testing

Cross-section picture of Composite-AlA+AlB, was observed using optical microscopy, following the set-up described in materials & methods part (page 181) (Figure 92). To examine the cross-section, it is important to notice that, as well as for samples described in chapter 3 (of this part), the coatings were not applied on substrate because of the optical microscopy sample preparation. Moreover, it is noteworthy that the cross-section pictures of S-AlA+AlB is exactly similar than Composite-AlA+AlB, the only difference is the substrate on which AlA+AlB is bonded. Figure 92 reveals that no bubble or void is observed between coating A, coating B and aluminum foils. The adhesion between layers is homogeneous. Moreover, the coating A and coating B thicknesses are globally the same for each sample observed and the average corresponds to 740 µm and 650 µm, respectively.

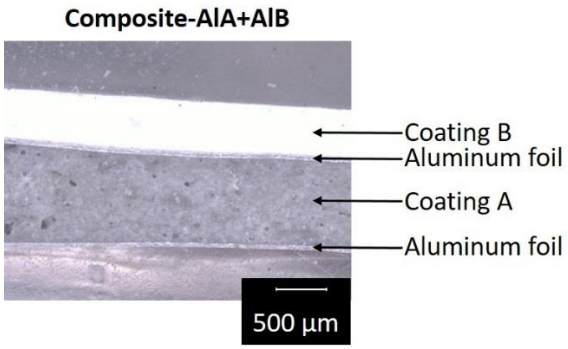

Figure 92. Cross section optical microscopy analysis before fire testing of Composite-AlA+AlB.

Table 27 gathers the quantitative values of all samples studied. For each sample, same mass of coating, 19 g, was deposed on substrate, and thus same total thickness is obtained, around 5 mm. All samples look homogeneous, the only difference between them is the substrate mass, which is divided per 4.3 between steel and composite plate having the same initial thickness. Therefore, using composite as substrate, lighter materials are elaborated.

© 2020 Tous droits réservés.
lilliad.univ-lille.fr

Thèse de Laura Geoffroy, Université de Lille, 2020

Table 27. Quantitative characterization of all samples studied before fire testing.

Samples	Mass of coating A (g)	Mass of coating B (g)	Mass of substrate (g)	Total mass (g)	Total thickness (mm)
S-AlA+AlB	9.39	10.22	233.81	253.15	5.08
Composite	/	/	55.5	55.5	3
Composite-A	18.55	/	54.86	68.73	5
Composite-B	/	20.27	53.19	73.1	5.1
Composite AlA+AlB	9.24	10.41	56.89	76.1	5

2.2. Fire testing

Temperature as a function of time was shown on Figure 93 and illustrates the influence of the substrate modification (with the substitution of steel by composite plate). In addition, the temperature reached after 30 min fire testing (see in materials & methods part (pages 179 and 180)) and the slope of the curves at different time intervals during fire test were gathered in Table 28. The temperature at the backside of the raw composite plate dramatically increases from the beginning of the fire test (with 234°C/min as a slope until 1 min), and reaches its steady state temperature at 328°C, after 5 min fire test (Figure 93 and Table 28). For the composite plate coated with intumescent paint A (Composite-A), the temperature rapidly increases until 2 min, with a slope of 90°C/min (which is 2.60 times lower than raw composite plate) from 0 min to 2 min, raises slower until 5 min, with a slope of 32°C/min and finally reaches its steady state temperature at 288°C (12% lower than for raw composite plate), after 5 min fire exposure. Same fire evolution was observed for Composite-B until 2 min fire test. Indeed, a fast temperature rise occurs from the beginning to 2 min fire test, with a slope of 106°C/min (which is 2.21 times lower than slope obtained for Composite). Then, a stabilization after 2 min fire exposure is observed and temperature reaches 217°C, -34%, and -22% lower than the temperature reached for the raw composite plate and S-AlA+S-AlB, respectively. Based on the temperature evolution of Composite-A and Composite-B, the deposition of neat intumescent coating on composite plate allows to reduce the temperature reached at the end of the fire test and to improve the stabilization of the temperature. Moreover, a slight reduction in temperature evolution is observed at the beginning of the fire test, but it remains very low. Regarding Composite-AlA+AlB, the same temperature rise as for S-AlA+AlB is observed from

© 2020 Tous droits réservés.

lilliad.univ-lille.fr

the beginning to 6 min fire exposure. Indeed, similar slopes (59°C/min from the beginning to 1 min, and 10°C/min from 2 min to 4 min) are obtained, that are 3.90 and 2.90 times lower than the slope measured for the raw composite, respectively. After 6 min of fire test, the temperature measured at the backside of S-AlA+AlB still increases whereas a temperature stabilization for Composite-AlA+AlB is observed. As a consequence, after 30 min fire test, the temperature reached for Composite-AlA+AlB is 203°C, 38% and 27% lower than temperature reached for neat Composite plate and S-AlA+AlB, respectively. Based on these results, the modification of substrate reveals benefits. It allows to have a better stabilization of temperature after 30 fire test, by retaining the low temperature evolution performance at the beginning of the fire test.

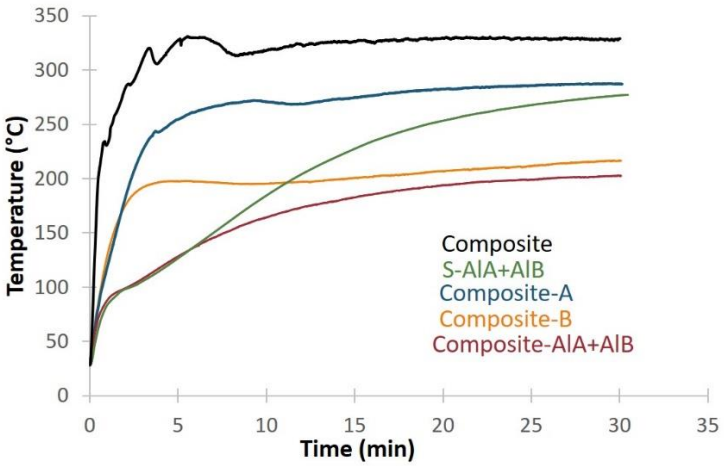

Figure 93. Fire behavior of S-AlA+AlB and of systems deposited on composite substrate.

© 2020 Tous droits réservés.
lilliad.univ-lille.fr

Table 28. Rate of temperature and temperature reached during fire test for each sample studied.

Samples	Rate of change of Temperature (°C/min): from 0 s to 1 min	Reduction		Rate of change of Temperature (°C/min): from 2 to 4 min	Reduction		Temperature after 30 min fire test (°C)	% Reduction of Temperature after 30 min fire test	
		Against Composite	Against S-AlA+AlB		Against Composite	Against S-AlA+AlB		Against Composite	Against S-AlA+AlB
S-AlA+AlB	**62**	÷ 3.77		**9**	÷ 3.22		**278**	-15	
Composite	**234**		x 3.77	**29**		x 3.22	**328**		18
Composite-A	**90**	÷ 2.60	x 1.47	**32**	x 1.10	x 3.56	**288**	-12	4
Composite-B	**106**	÷ 2.21	x 1.71	**8**	÷ 3.625	÷ 1.12	**217**	-34	-22
Composite-AlA+AlB	**59**	÷ 3.97	÷ 1.05	**10**	÷ 2.90	x 1.11	**203**	-38	-27

The residues collected after 30 min fire test of all samples detailed in Table 26 were observed in Figure 94. Table 29 gathers the mass loss and the expansion of samples after 30 min fire exposure (both measurements are fully described in materials & methods part (page 181)). As it was previously shown in chapter 3 (of this part), two delaminations are observed between coating A and both aluminum foils for S-AlA+AlB (Figure 94 b). These delaminations explain the better fire protection performances obtained especially at the beginning of the fire test, for this design compared to others presented in chapter 3 (of this part). Due to these delaminations and also to the intumescent coatings swelling, the expansion of S-AlA+AlB reaches 610%, with a low mass loss equal at -3% (Table 29).

For the raw composite plate, delamination of the substrate was observed at the end of the fire exposure (Figure 94 a). The lower fire protective performance recorded in Figure 93 is thus explained by the degradation of the epoxy resin from the composite plate itself. This degradation leads to a 32% mass loss (confirmed by TGA in appendix 6 (Figure A6- 1)) and an expansion of 132% after fire testing (Table 29).

Figure 94 c and Figure 94 d show the aspect of residue obtained for Composite-A and Composite-B, respectively. No delamination between substrate and intumescent residue occurs for both samples. However, in the case of Composite-A, carbon fibers from the substrate start delaminate, while they remain intact in the case of Composite-B. This difference can be explained by the temperature reached after 30 min fire exposure which is 70°C higher for Composite-A (288°C) compared to Composite-B (217°C). Moreover, it is noteworthy that the temperature reached at the backside of Composite-A (288°C) is below the epoxy resin decomposition temperature (360°C) measured by TGA (in appendix 6 (Figure A6- 1)). This observation can be explained by two aspects. On one hand, due to the low thermal conductivity of composite (axial and radial thermal conductivity of composite equal at 0.61 W/(m.K) ± 0.03 W/(m.K) and 2.12 W/(m.K) ± 0.09 W/(m.K), respectively (set-up fully described in materials & methods part (page 175))), it is important to note that the backside temperature of composite plate is lower than the temperature reached at the topside. Therefore, even if the backside temperature of the Composite-A (288°C) is lower than the decomposition temperature of the composite measured by TGA (360°C see in appendix), a carbon fibers delamination can be observed, as it is the case. On the other hand, according to Tranchard et al. [244] and Mouritz et al. [198], the delamination effects can appear in the virgin part of material, before the beginning of the degradation of the material. Indeed, as mentioned in the first aspect, composite plate is anisotropic (axial thermal conductivity is 4 times lower than radial thermal

© 2020 Tous droits réservés.
lilliad.univ-lille.fr

Thèse de Laura Geoffroy, Université de Lille, 2020

conductivity). Due to this anisotropy of the carbon fibers, a thermal expansion is created by the material heating. It is assumed that from this phenomenon, a small amount of energy is released and created some cracks in resin. Therefore, the lack of cohesion between fibers and the resin can lead to a delamination in the first plies. Furthermore, for both residues, a char (carbonaceous residue) is observed with an expansion equal at 170% and 529%, respectively. This expansion difference is due to the swelling difference of the two intumescent paints used. As previously shown in chapter 3 (part 3) – 2.3. Mechanism investigation, coating A has a lower expansion than coating B. In addition, a mass loss of 11% and 26% was measured for Composite-A and Composite-B respectively and can be explained by the composite substrate delamination of the loss of the residue during the fire test (as a reminder the residue from Composite-B is brittle compared to the residue from Composite-A).

Regarding Composite-AlA+AlB, two delaminations occur between coating A and aluminum foils, similar to those observed for S-AlA+AlB. This observation could explain the same temperature evolution at the beginning of the fire testing. Moreover, the expansion measured after 30 min fire test reaches 640%, closely equivalent to the expansion obtained for S-AlA+AlB. Furthermore, the substrate is intact, no delamination or epoxy degradation occur during the fire exposure. It is confirmed by the low temperature reached (203°C) and a low mass loss (-6%) measured (Table 29), after 30 min fire testing.

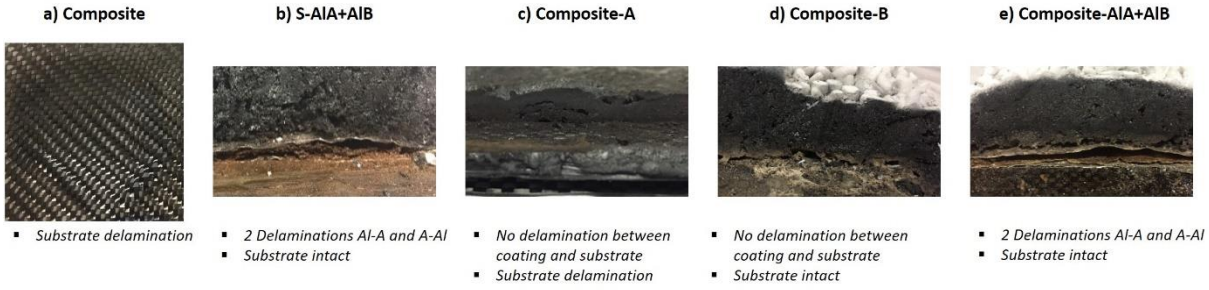

Figure 94. Residues aspect after 30 min fire exposure for a) Composite, b) S-AlA+AlB, c) Composite-A, d) Composite-B, e) Composite-AlA+AlB.

© 2020 Tous droits réservés.

lilliad.univ-lille.fr

Table 29. Mass loss and expansion after 30 min fire exposure for each sample studied.

Samples	Mass loss after 30 fire exposure (%)	Expansion after 30 min fire exposure (%)
Composite	-32	132
S-AlA+AlB	-3	610
Composite-A	-11	170
Composite-B	-26	529
Composite AlA+AlB	-6	640

To summarize, at the beginning of fire test, the similar fire behavior between S-AlA+AlB and Composite-AlA+AlB can be explained by the same design and coating (two aluminum foils with coatings A and B), and thus the same phenomenon (two delaminations between both aluminum foils and coating A and intumescence of coating A and B). Then, the heat diffuses through the system to the substrate and differs according to the thermal conductivity of the substrate. Indeed, for Composite-AlA+AlB and S-AlA+AlB, the temperature reached is below the decomposition temperature of the composite and steel (as illustrated in Figure 93), respectively. Consequently, the temperature evolution will be governed by the thermal conductivity of the composite which is almost 100 lower than for steel (ratio about 0.6 [245] to 68 W/(m.K) [246], respectively). The temperature in the stationary state will therefore be much lower than in the case of steel. The fire resistant barrier created in this work can thus be used to protect another substrate, and provide a fireproofing protection for other applications.

3. Conclusion

In chapter 3 (of this part), bilayer metal laminate with the overlay of two different intumescent coatings revealed very good fire protection performances, especially at the beginning of the fire testing. The aim of this work was to evaluate if the best fire resistant barrier developed on steel can be applied on another substrate to be used for other applications. Steel plate was thus substituted by a composite (carbon fiber in epoxy resin) plate. By changing the substrate, a benefit has been identified: the total mass of the sample was reduced per 4.3 and thus lighter materials were elaborated. Moreover, better fire protection was reached, especially at the end of fire testing. After 30 min fire exposure, the temperature at the backside of composite plate does not exceed 200°C. These excellent fire protective properties can be explained by i) the two delaminations located between coating A and both aluminum foils, which delay the heat spread

© 2020 Tous droits réservés.
lilliad.univ-lille.fr

Thèse de Laura Geoffroy, Université de Lille, 2020

in the system at the beginning of the test, ii) the swelling resulting from the intumescent phenomena, iii) the higher protective performance of composite compared to steel, composites having a lower heat conductivity. This work highlights that the fire barrier developed is very efficient, flexible and can protect other substrates against fire for various others applications such as aeronautic or structural engineering fields.

Key points

- ✓ Using composite instead of steel plate as substrate allows to have a very low temperature evolution at the beginning of fire test, and a fast temperature stabilization with a steady-state temperature under 200°C.
- ✓ The fire protective performances of this design is explained by the combination of two delaminations, two intumescence phenomena and the lower heat conductivity of composite compared to steel.
- ✓ The fire barrier elaborated in this work can protect other substrates such as composite, to be used in many fields.

© 2020 Tous droits réservés.

lilliad.univ-lille.fr

General conclusion & Outlook part 3

This part reports the elaboration of a new fire barrier, which allows to dramatically reduce the temperature rise at the backside of different substrates throughout severe fire testing conditions. This fire barrier was designed based on two concepts i) intumescence, which is an efficient heat insulating layer by forming a porous carbonaceous residue, ii) the delamination, which delays the heat diffusion in the material by creating an additional thermal resistance. The main advantage of this design is its flexibility, which allows it to easily adapt to different environments by some design optimizations. In the last chapter, the best fire barrier obtained on steel was tested on another substrate (a carbon fiber epoxy composite) to evaluate if it can protect other materials, and thus be used for other applications. This last test proves the versatility and the efficiency on multi-substrate of the fire barrier created in this work.

To go further in this work, other optimizations could be considered:

- Test other intumescent coatings with other chemistries working with a chemical expansion. Indeed, based on chapter 2 (of this part), intumescent coating with physical expansion did not allow to reduce the heat propagation.
- Apply this design on other substrates (such as ceramic, or high performance polymer (PEEK, PEI)) (Figure 95 a), to confirm the flexibility and versatility of this system and to extend to other possible application fields.
- Substitute intumescent paints with geopolymers [247]–[251] (Figure 95 b). Geopolymers indeed revealed efficient fire protection performances in recent works [250], [251]. It could be interesting to combine it in our concept. However, a special attention should be done on the thickness (it is hard to depose as thin layer) and weight (because of the high geopolymer density: twice as much as a conventional polymer).
- Add a very thin layer of PEEK or PEI in coating A to even more improve the thermal insulation properties (Figure 95 c) due to their very high thermal decomposition temperature. Moreover, PEEK has the ability to delaminate under high temperature exposure, as fully demonstrated by Uematsu et al. [252]. Therefore, an additional layer of PEEK could create another delamination interface, which delays even more the temperature rise. The incorporation of PEEK or PEI is preferentially done in coating A because of its lower expansion, to not prevent the expansion of coating B and/or its morphology. Indeed, the expansion of coating B is related to it fireproofing efficiency, and as it was previously demonstrated, the expansion of coating B is much higher than

© 2020 Tous droits réservés.
lilliad.univ-lille.fr

Thèse de Laura Geoffroy, Université de Lille, 2020

that of coating A. As a consequence, the expansion of coating A will probably not be affected by the incorporation of other materials.

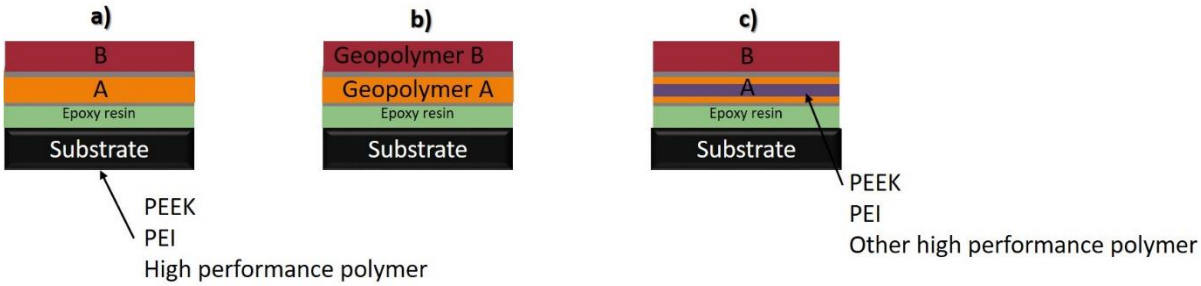

Figure 95. Illustration of perspectives which could be considered.

Moreover, to complement this work, it could be interesting to simulate numerically this design to predict which material could be used to achieve the best and optimal fireproof system. This numerical model could provide some additional information. For example, if delamination is easily obtained with a rigid or brittle material or if a soft material is better because it could easily adapt to the deformation. Another point could be to determine through simulation the best expansion that intumescent coating needs to reach to achieve the best fire protective performances.

Furthermore, it may be worthwhile to assess the ageing over time of this new fire barrier and evaluate whether the fire protection performances are retained.

Finally, it could also be interesting to test the fireproofing efficiency of the fire barrier created under other fire scenarios. In the FireBar-Concept project, a jet fire bench at the reduced scale has been developed, involving heat fluxes up to 400 kW/m^2. This very versatile test could give additional information on the maximum heat flux under which the fireproofing properties of the fire barrier are maintained, and if this barrier can be used for a higher heat flux for extreme environment. Following the same idea, the fire barrier developed in this work could also be tested in furnace test, according to standards ISO834 and UL1709. By these additional tests, fire barrier could be used for others fields such as building.

To conclude, this concept highlights that changing the design allows to dramatically improve the fire protection performances. It is a new and promising way of thinking.

© 2020 Tous droits réservés.

lilliad.univ-lille.fr

Thèse de Laura Geoffroy, Université de Lille, 2020

General conclusion & Outlook

This PhD aimed at developing innovative fire protective multi-materials to reduce the reaction to fire and increase the fire resistance. To achieve these goals, an innovative approach was considered: it consisted in changing the material design and combining various concepts and materials, instead of changing the materials chemistry as it is usually the case. Two novel fireproofing protections were thus developed and exposed to different fire scenarios.

The great flexibility offered by 3D printing process to prepare sophisticated shapes was firstly used to develop a new biomimetic sandwich design inspired from honeycomb structures, enabling to reach superior flame retardancy by design changing. In that case, a radiative fire scenario was considered. The cells created by this design were then used to elaborate new biphasic multi-materials containing liquid or solid phases. This combination acting chemically in both gas and condensed phases led to a multi-material with extremely low rate of heat release. An optimization was then undertaken to prevent the leakage issue resulting from the porosity induced by the printing process and the subsequent use of a liquid phase. Incorporation of a hydrogel as a substituent for the liquid phase was studied. In addition, clays were incorporated into hydrogel, as they act physically, creating an additional physical fire barrier. The gas emission from the material degradation was thus slowed down, leading to self-extinguishment and a very low heat release rate. In spite of self-extinguishment, ignition of the material occurred very quickly, after a few seconds. Therefore, a last optimization was done to delay the time to ignition. An additional concept was integrated into the previous design and consisted in reflecting the infrared rays by depositing a low emissivity coating on the surface exposed to radiative heat flux. The combination of all these concepts and materials allowed to lengthen the time to ignition from few seconds to 3 minutes, while retaining the very low heat release rate properties. Therefore, by changing the design and combining various concepts, an innovative flame-retardant 3D printed multi-material acting chemically (using potassium carbonate in liquid phase, which acts both in gas and condensed phases), physically (by forming a physical barrier due to the use of clay) and optically (with the low emissivity coating) was elaborated, leading to extremely low reaction to fire. This work opens up new ways of thinking to elaborate flame-retardant materials.

© 2020 Tous droits réservés.
lilliad.univ-lille.fr

Thèse de Laura Geoffroy, Université de Lille, 2020

A similar approach based on combination of concepts and design changing was also assessed for fire resistance, in order to protect substrates such as steel plates. Based on the concepts of intumescence and delamination used separately in existing passive fire protective systems, a multi-material called Intumescent Polymer Metal Laminate (IPML) was developed. The creation of 10 interfaces between an intumescent paint and aluminum foils led to a dramatic reduction of heat propagation, especially at the beginning of the fire exposure, compared to the use of a paint monolayer in severe fire testing conditions (i.e. a burn-through test with a high heat flux). Consequently, the thermal and carbonization gradients were considerably increased up to 10 min of fire exposure. To improve resistance to fire at longer exposure times, another design inspired from the previous one was elaborated. Three modifications were proposed for the novel fire barrier: (i) the use of thicker paint layers to increase intumescence, (ii) the use of two intumescent paints with different chemistries to combine their respective advantages and (iii) the limitation of the number of delamination foils to one or two to reduce processing time. The fire results revealed that the coating with the highest expansion have to be on the top (i.e. fire exposed surface) to ensure an optimal fire protection. Furthermore, the configuration with two aluminum foils, creating delamination, allows to drastically reduce the heat propagation up to 20 minutes and to reach a relatively low steady-state temperature. As a consequence, to conceive an efficient intumescent paint laminated fire barrier, a specific configuration is required: i) an appropriate thickness of intumescent layer to ensure a low steady-state temperature, ii) a particular intumescent layer stack, which depends on the expansion of paint and iii) an adequate number of delaminations (at least two) to reduce the heat propagation at the beginning of fire test. Finally, the new efficient fire barrier designed was tested on another substrate in order to confirm its versatility and its potential use for other applications. It was thus highlighted that the fire barrier developed can fire protect composites as well as steel plates.

In summary, changing the design and combining concepts led to two new fire protective multi-materials for lowering reaction to fire and improving fire resistance. All in all, this work has been the first step towards a novel approach based on design and is a really promising way to create new fireproofing systems.

Looking at the final perspective, it is legitimate to wonder if a universal system, able to provide at the same time flame retardancy and flame resistance against different thermal constraints (burn-trough test and MLCC test for example) could be developed. In order to answer this question, it is necessary to expose the designed materials to various fire scenarios and evaluate their fire protection. A preliminary work was done on IPML design to assess whether this design

© 2020 Tous droits réservés.

lilliad.univ-lille.fr

could be also efficient in the case of reaction to fire. Therefore, IPMLs were tested by MLCC test under a 50 kW/m^2 external radiative heat flux. However, no delamination was observed, only intumescence phenomenon occurred. As a consequence, IPML design provided no improvement or benefit compared to the only use of neat intumescent paint. It was assumed that the thermal constraint was not high enough to initiate delamination. Indeed, heating conditions can have an influence on the fire protective system, as it was recently demonstrated by Lucherini et al on a thin intumescent coating [253]. To confirm this assumption, it could be relevant to test IPML design under a higher radiative heat flux, such as 100 kW/m^2 (conception of high heat flux MLCC is in progress in the laboratory). Nevertheless, by this preliminary test, an important point is raised. It seems that IPML design adapts to the thermal constraint. For radiative heat flux equal to 50 kW/m^2, only intumescence is triggered to protect the substrate and prevent ignition of material. In case of burn-through test at 116 kW/m^2, intumescence phenomenon coupled with delamination occurs to ensure the fire protection. Additional tests could be done to complete this study. For example, it could be relevant to expose IPML design to other fire scenarios, such as furnace tests, to assess their fire protective performances. Moreover, same investigations could be undertaken with the 3D printed design inspired from honeycomb structure. The fire resistance properties of this design could for example be tested under burn-through test or another fire resistance test.

Finally, in an attempt to find a universal system, another design gathering the fireproofing concepts of IPML design and 3D printed design could also be developed. Indeed, from IPML design, it was highlighted that the combination of a sufficient number of delamination interfaces in addition to a sufficient thickness of insulating layer provides significant fire resistance. In addition, the final concept of the 3D printed bio-inspired structure was (i) to reflect the infra-red rays to delay the materials ignition using a low emissivity coating on the exposed surface and (ii) to then use the cells as flame retardant carrier. Therefore, a design combining all of these concepts could be considered. An example is proposed in Figure 96. A metal laminated structure, composed of two metal layers, could be retained to delay the heat propagation. In addition, a low emissivity coating could also be deposited on the top to delay ignition as long as possible. However, it is important to note that this coating is mainly efficient in the case of a high radiative heat flux. Therefore, the effect of this coating may be minimized for the burn-through test for example, where the radiative flux is estimated between 15% to 20%. However, the objective is to find a universal system providing fire protection whatever the fire scenario considered. In this aim, a low emissivity coating could be a clear advantage. Moreover, it is

© 2020 Tous droits réservés.
lilliad.univ-lille.fr

Thèse de Laura Geoffroy, Université de Lille, 2020

noteworthy that this coating should be deposited on a material with low expansion to prevent it from cracking in the early stage of fire exposure, and thus ensure its efficiency. The middle of the design could be an intumescent layer to initiate the delamination phenomenon. Finally, clays may be considered to form a physical barrier and thus delay the material degradation by reducing the gas release to the flame. Another study could be done to find out the optimal position of clays in the system: at the top within the polymer matrix or at the bottom. In parallel with this work, a numerical approach simulating the assembly could be attempted to quantify the effect of each material and so, to optimize the assembly.

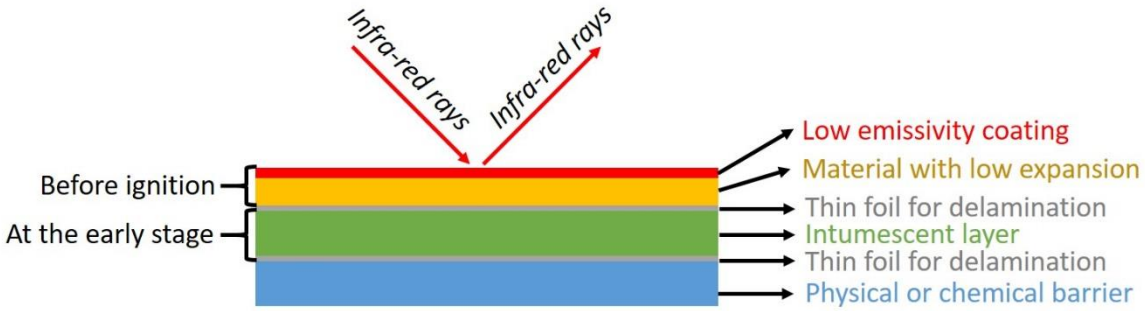

Figure 96. Example of the development of a multi-fireproofing concept.

To conclude, it is a challenge to develop a design that is able to adapt to all thermal constraints. However, based on this work, several routes remain to explore in order to produce an optimal design that could meet the expectations of various fire scenarios. Design adaptation and combination of existing concepts could be one potential solution.

© 2020 Tous droits réservés.

lilliad.univ-lille.fr

PhD Communications

Written communications

Peer-reviewed scientific articles

[1] L. Geoffroy, F. Samyn, M. Jimenez, and S. Bourbigot, "Intumescent Polymer Metal Laminates for Fire Protection," *Polymers (Basel).*, vol. 10, no. 9, pp. 1–16, 2018.

[2] L. Geoffroy, F. Samyn, M. Jimenez, and S. Bourbigot, "Additive manufacturing of fire-retardant ethylene-vinyl acetate," *Polym. Adv. Technol.*, vol. 30, no. 7, pp. 1878–1890, 2019.

[3] L. Geoffroy, F. Samyn, M. Jimenez, and S. Bourbigot, "Innovative 3D printed design to conceive highly fire-retardant multi-material," *Polym. Degrad. Stab.*, vol. 169, pp. 1 – 17, 2019.

[4] L. Geoffroy, F. Samyn, M. Jimenez, and S. Bourbigot, "Bi-layer intumescent paint metal laminate: a novel design for a high performance fire barrier," *Ind. Eng. Chem. Res.*, vol. 59, no. 7, pp. 2988 – 2997, 2020.

[5] L. Geoffroy, A. Davesne, S. Bellayer, F. Blanchard, F. Samyn, M. Jimenez and S. Bourbigot "3D printed sandwich materials filled with hydrogels for extremely low heat release rate," *Polym. Degrad. Stab.*, vol. 179, pp. 1 – 15, 2020.

[6] L. Geoffroy, A. Davesne, F. Parent, F. Sanchette, F. Samyn, M. Jimenez and S; Bourbigot, "Combining low emissivity thin coating and 3D printed original design for superior fire protective performance," *ACS Omega*, vol. 5, no.43, pp. 27857 – 27863, 2020.

Oral communications

International congress

L. Geoffroy, F. Samyn, M. Jimenez, and S. Bourbigot, "3D printed original design to conceive highly flame retardant multi materials", GDR Feux, 27ème edition, February 13th and 14th 2020, Lille (France)

L. Geoffroy, F. Samyn, M. Jimenez, and S. Bourbigot, "Playing with 3D printed designs to conceive highly flame retardant multi-materials", Journées des Jeunes Chercheurs 2019,

© 2020 Tous droits réservés.
lilliad.univ-lille.fr

UGéPE – GEPROC, 6ème edition Wallonie/Nord de France/, November 7th, Mons (Belgium): **Best price**

L. Geoffroy, F. Samyn, M. Jimenez, and S. Bourbigot, "Design of new multi-material using additive manufacturing for extreme temperature environment", IUPAC, July 5th – 12th 2019, Paris (France)

S. Bourbigot, L. Geoffroy, F. Samyn and M. Jimenez, "3D printing and Fire Retardancy: Conventional way or new opportunities?", European Meeting on Fire Retardant Polymeric Materials (FRPM 2019), June 26th – 28th 2018, Turku (Finland)

L. Geoffroy, F. Samyn, M. Jimenez, and S. Bourbigot, "3D Printing Fire Retarded Ethylene-Vinyl Acetate Copolymer: Design of New Fire Protection Multi Material", Flame 30, BCC Research, Mai 19th – 22th 2019, San Antonio Texas (United-States)

F. Samyn, L. Geoffroy, M. Jimenez, and S. Bourbigot, "Intumescent Polymer Metal Laminates (PML): new concept for fire protection?", Matériaux 2018, November 19th – 23th 2018, Strasbourg (France)

Seminar

L. Geoffroy, F. Samyn, M. Jimenez, and S. Bourbigot, "Design of new multi-material using additive manufacturing for extreme temperature environment", seminar in Texas A&M university, Mai 23th – 25th 2019, College Station Texas (United States)

L. Geoffroy, F. Samyn, M. Jimenez, and S. Bourbigot, "Design of fire protective multi-materials", GDR French/German, June 23th – 26th 2018, Flamièrge (Belgium)

Poster

L. Geoffroy, F. Samyn, M. Jimenez, and S. Bourbigot, "Playing with 3D prited designs to conceive higly flame retardant multi-materials", MIPOL, 2020, Milan (Italy)

L. Geoffroy, F. Samyn, M. Jimenez, and S. Bourbigot, "Fire retarded ethylene-vinyl acetate copolymer: Thermoforming versus 3D printing", Journées des Jeunes Chercheurs 2018, UGéPE – GEPROC, 5ème édition Nord de France/Wallonie, November 20th and 21th 2018, Villeneuve d'Ascq (France): **Best price**

© 2020 Tous droits réservés.

lilliad.univ-lille.fr

Materials & Methods

This part is divided into two chapters and described the materials and methods used to design the new flame retardant materials using 3D printing and the new intumescent metal laminate fire barrier, respectively. Therefore, materials, polymer processing, fire testing and characterizations (Figure 97) are fully presented.

KEYWORDS: Materials, Processing, Fire testing, Characterizations

Aims

- ✓ Description of materials and methods used to design a flame retardant materials using 3D printing.
- ✓ Description of materials and methods used to design a new fire resistant materials.

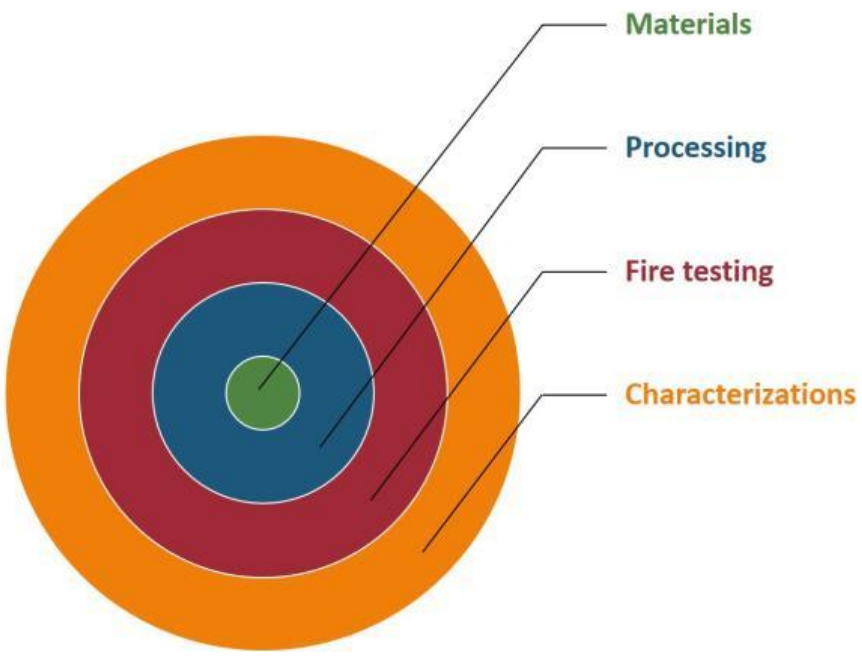

Figure 97. Illustration of Material, methods and characterizations.

© 2020 Tous droits réservés.
lilliad.univ-lille.fr

Thèse de Laura Geoffroy, Université de Lille, 2020

Table of content Materials & Methods

MATERIALS & METHODS 159

CHAPTER 1: MATERIALS & METHODS OF PART 2 FOR DESIGNING THE NEW 3D PRINTED FLAME-RETARDANT MULTI-MATERIAL **162**
1. MATERIALS 162
2. MATERIAL ELABORATION: EXTRUSION PROCESS 163
3. SHAPING PROCESSES 164
3.1. Thermocompression 164
3.2. Additive manufacturing / 3D printing 164
4. SAMPLE PROCESSING 166
4.1. Biphasic sandwich multi-materials elaboration process 167
4.2. Hydrogel and sandwich multi-materials elaboration process 167
4.2.1. Reference hydrogels 167
4.2.2. Hydrogels containing vermiculite and vermiculite/K_2CO_3 168
4.3. Low emissivity coating deposition 169
5. FIRE TESTING 170
5.1. Mass Loss Cone Calorimeter 170
5.2. Temperature versus time measurement 171
5.3. Gas phase analysis 171
5.4. Soot picking in the flame 172
6. CHARACTERIZATIONS 172
6.1. Weight, thickness and apparent density measurements 172
6.2. Optical microscopy 172
6.3. Confocal microscopy 173
6.4. Electron Probe Micro-Analysis 173
6.5. Scanning Electron Microscopy 174
6.5.1. Scanning Electron Microscopy for observation 174
6.5.2. Scanning Electron Microscopy for EDS analysis and X-ray mappings 174
6.6. X-Ray Diffraction and/or High Temperature X-ray Diffraction 174
6.7. Thermal conductivity measurements 175
6.8. Emissivity measurements 175
CHAPTER 2: MATERIALS & METHODS OF PART 3 FOR DESIGNING THE NEW INTUMESCENT METAL LAMINATE FIRE BARRIER **176**
1. PROCESSING OF SAMPLES 176
1.1. Materials 176
1.2. Intumescent Polymer Metal Laminate (IPML) samples elaboration 177
1.3. Bilayer Metal Laminate samples elaboration 177
2. FIRE TESTING 179
2.1. Burn-Through test 179
2.2. Temperature versus time measurements 180
2.2.1. For steel plate as substrate 180
2.2.2. For composite plate as substrate 180
2.3. Thermal gradient measurement 180
3. CHARACTERIZATIONS 181

© 2020 Tous droits réservés.

lilliad.univ-lille.fr

3.1. Mass loss measurements 181
3.2. Expansion measurements 181
3.3. Optical microscopy 181
3.4. Scanning Electron Microscopy observations 182
3.5. Thermal analyses 182
3.6. Pull-off test 182

© 2020 Tous droits réservés.
lilliad.univ-lille.fr

Thèse de Laura Geoffroy, Université de Lille, 2020

Chapter 1: Materials & methods of part 2 for designing the new 3D printed flame-retardant multi-material

1. Materials

A copolymer of Ethylene and Vinyl Acetate hereafter call EVA (Evatane 28-05 batch A70760804, molar mass: 114.142 g/mol, melt index between 5 – 8 g/10 min (at 190°C, 2.16 kg) [254], Arkema, Colombes, France) was used as polymeric matrix because of its softness, flexibility and polarity, which makes it easy to extrude. This widely used polyolefin was extensively studied in our laboratory, and was thus chosen as a model material [150]–[153]. Two flame-retardants were separately incorporated in this matrix namely Aluminum Tri-Hydroxide named ATH (Apyral 40CD, D_{50} of 1.5µm, Nabaltec, Schwandorf, Germany), and Expandable Graphite hereafter call EG (ES 350F5, 80% of particles ≥ 300 µm, AMG graphite, Hauzenberg, Germany). These flame-retardants were chosen because of their two different modes of action under heat flux exposure. On the one side, ATH acts in condensed phase to protect material with the formation of protective ceramic-like residue (alumina) according to an endothermic decomposition reaction ($2\ Al(OH)_3 \rightarrow Al_2O_3 + 3H_2O$, ΔH=280 cal/g) coupled with a dilution effect due to water emission into gas phase [150]–[153]. On the other side, EG has an intumescent behavior due to the physical expansion of the graphite worms caused by the sublimation of inserted compounds trapped between the layers [154]. An entangled network ensures a protective barrier formation.

Liquid solutions (part 2: chapters 2 and 3) and hydrogels (part 2: chapters 3 and 4) were prepared using the hereafter presented chemicals. Sodium alginate (molar mass: 216.12 g/mol, viscosity: 5 – 40 cps for 1 wt.-% water at 25°C [255]), PVA (molar mass: 86.09 g/mol, viscosity: 24 – 32 cps for 4 wt.-% water at 20°C [256]), calcium chloride ($CaCl_2$), citric acid and potassium carbonate (K_2CO_3, 98% purity) were supplied by Sigma Aldrich (St Louis, Missouri, United States). In addition, anhydrous sodium carbonate was used and purchased from Carlo Erba Reagenti (Barcelona, Spain). Agar (molar mass: 336.33 g/mol, viscosity: 10 – 100 cps for 1.5 wt.-% water at 60°C [257]) from Mc Cormick (Baltimore, Maryland, United States), was used as well as borax from Borax Europe Ltd (Kolding, Denmark) and a solution of dispersed vermiculite (VMT) (Microlite 963, 7.8 wt.-% in water, Specialty Vermiculite Corp., Enoree, South California, United States).

© 2020 Tous droits réservés.

lilliad.univ-lille.fr

2. Material elaboration: Extrusion process

Four polymeric materials were prepared (Table 30) using a twin-screw extruder (Haake Rheomex OS PTW16, Thermo Scientific (Waltham, Massachusetts, United States of America)) (Figure 98). This twin-screw extruder was composed of ten heating chambers, with the following set temperature profile: T_1: 150°C, T_2: 160°C, T_3: 160°C, T_4: 160°C, T_5: 170°C, T_6: 170°C, T_7: 170°C, T_8: 160°C, T_9: 160°C, T_{10}: 150°C, from the EVA polymeric matrix pellets and flame-retardants additives (ATH or EG depending on the material elaborated) feed area to the material die (Figure 98). In the fourth zone (at 160°C), another part of the flame-retardants additives was added in a second additives insertion area and mixed with the EVA matrix. The polymer and flame-retardants additives incorporation was done using gravimetric feeder. The extrusion speed was 100 and 250 rpm for EVA/ATH and EVA/EG materials, respectively. After extrusion, the filaments of EVA/ATH or EVA/EG were cooled down under air at room temperature and cut into pellets with a pelletizer (Thermo Scientific (Waltham, Massachusetts, United States of America)).

Table 30. Materials' formulation.

Name of polymer material	Amount of additives (%)	Thermal behavior
EVA	0	Reference: melting and burning
EVA/ATH (30 wt.-%)	30	Endothermic decomposition and dilution effect: ceramic residue
EVA/ATH (65 wt.-%)	65	Endothermic decomposition and dilution effect: ceramic residue
EVA/EG (10 wt.-%)	10	Physical expansion [154]

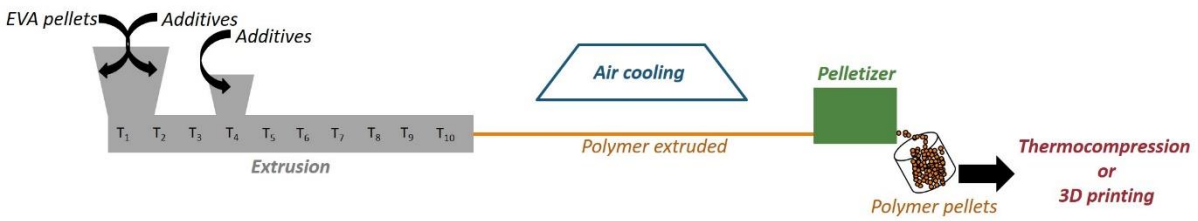

Figure 98. Extrusion process.

The pellets of EVA/ATH or EVA/EG were then used to produce plates by two processes: thermocompression and 3D printing. These two processes are described in the next sections.

© 2020 Tous droits réservés.
lilliad.univ-lille.fr

Thèse de Laura Geoffroy, Université de Lille, 2020

3. Shaping processes

3.1. Thermocompression

100x100x3 mm^3 plates were produced by thermocompression process, using Fontune presses (Fontijne Grotnes B.V., Niles, Michigan, United States) (Figure 99). A defined mass of polymer pellets was put in a mold, allowing to obtain homogeneous plate. The following simultaneous temperature and pressure cycles were applied: the pellets were heated at 140°C for 14 min then cooled at 30°C for 1 min meanwhile a force was set to 20 kN for 3 min, then 40 kN for 12 min.

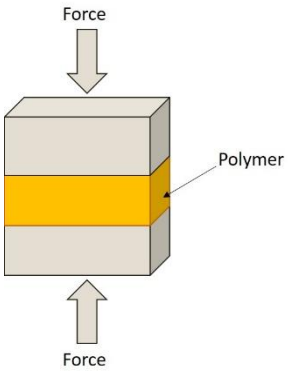

Figure 99. Thermocompression process.

3.2. Additive manufacturing / 3D printing

The pellets prepared in section 2. *Material elaboration: extrusion process*, were used to elaborate 100x100x3 mm^3 (in appendix 2) or 50x50x3 mm^3 (in part 2 chapters 2, 3 and 4) samples by 3D printing process using Polymer Additive Manufacturing (PAM) Series P (Pollen, Ivry-sur-Seine, France), capable of printing materials as pellets (Figure 100). This technique is a fused polymer deposition and consists in feeding polymers pellets from polymer container to a heater printer extruder, and depositing a fused polymer on a heating plate according to a computed pattern (Figure 100), as it was described in part 2 chapter 1. The numerical 3D model was elaborated using Catia V5 (Computer-Aided Three-Dimensional Interactive Application) software, then the 3D model was sliced in many sections using Ultimaker Cura software, and finally, the file was exported on a last software: Pollen to start or stop the printing. Before starting the printing, the polymer cartridge has to be filled in with polymer pellets.

The 3D printer used has twelve temperature control points located in the printer head, which ensure that the polymers are exposed to negligible shear forces and residence time. Moreover, this 3D printer has 4 extruders, enabling to print a multi-material up to 4 on a single part.

© 2020 Tous droits réservés.

lilliad.univ-lille.fr

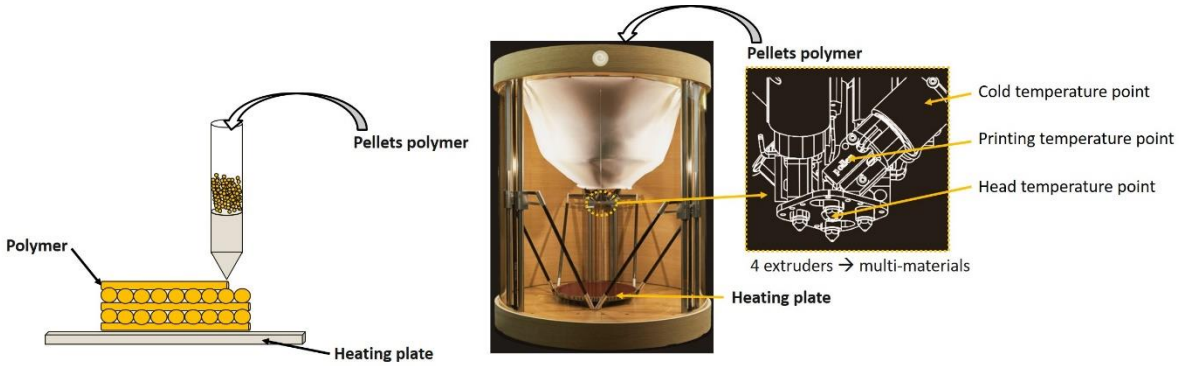

Figure 100. 3D printing process.

The main parameters which were used to print the four materials are defined in Table 31. These parameters were obtained after many tests and optimizations to reach the best printed materials as possible. Nozzle diameter was higher for EVA containing 10% of expandable graphite because of the higher EG particle size (300 µm) than ATH particle (1.5 µm). Moreover, three temperature points (Figure 100) are really important to define: (i) cold temperature which corresponds to a polymer pellets temperature before extrusion, (ii) printing temperature which is the temperature in extruder, and (iii) head temperature which corresponds to a nozzle temperature (polymer output). The head temperature of EVA/EG (10 wt.-%) is lower than other materials to avoid the graphite expansion during 3D printing process. Furthermore, the bed temperature of the EVA with 65 wt-% of ATH were higher than the other materials due to its poor adhesion onto the heating plate. The percentage of the infill (Table 31) corresponds to the amount of polymer in 3D object designed. In this work, the percentage changes from 100, 50 to 30 according to design studied.

© 2020 Tous droits réservés.
lilliad.univ-lille.fr

Thèse de Laura Geoffroy, Université de Lille, 2020

Table 31. Printing parameters.

Polymer materials	EVA	EVA/ATH (30 wt.-%)	EVA/ATH (65 wt.-%)	EVA/EG (10 wt.-%)
Cold temperature (°C)	65	65	65	65
Printing temperature (°C)	130	130	130	130
Head temperature (°C)	225	225	225	200
Printing speed (mm/s)	20	20	20	20
Nozzle diameter (mm)	0.4 or 0.8 [(2)]	0.4 or 0.8 [(2)]	0.4 or 0.8 [(2)]	1
Bed Temperature (°C)	45	65	80	65
Infill (%)	100	100 or 50 or 30	100 or 50 or 30	100 or 50 or 30
Layer height	0.3	0.3	0.3	0.3

4. Sample processing

Different designs were elaborated in this work: a standard design (3D printed polymer plates composed of EVA, EVA/ATH (30 wt.-%), EVA/ATH (65 wt.-%) and EVA/EG (10 wt.-%)) in appendix 2 and a honeycomb-inspired sandwich design in part 2 chapters 2, 3 and 4. This latter design is composed of two skins completely filled with flame retardant EVA polymer, and a core partially fill with 30% (or 50%) of flame-retardant EVA material and thus 70% (or 50%) of empty cells, as illustrated in part 2 chapter 2. These samples were design using the 3D printing parameters previously defined in section 3.2. Additive manufacturing / 3D printing. For sandwich design, the empty cells created by the design are left empty or filled with liquid or hydrogel, depending on the samples studied (part 2: chapters 2, 3 and 4). It is important to notice that to be able to fill the cells of the core created by the design, the top skin and the core and bottom skin have to be printed separately. The elaboration of these samples filled with liquid or hydrogel phases will fully describe in next section.

[(2)] Nozzle diameter of 0.8 mm was used in part 2 (chapters 2, 3, 4). In appendix 2 (comparison between thermocompression and 3D printing process), nozzle diameter of 3D printer was equal at 0.4 mm.

© 2020 Tous droits réservés.

lilliad.univ-lille.fr

4.1. Biphasic sandwich multi-materials elaboration process

To elaborate biphasic sandwich multi-materials (part 2 chapter 2), potassium carbonate used as a powder and diluted in water (as saturated solution and as a solution with 0.05 g/ml mass concentration) and anhydrous sodium carbonate diluted in water (as a solution with 0.05 g/ml mass concentration) were employed. These solutions were respectively poured in the empty cells created by the design with a control mass. Finally, to design the sandwich materials, the top section is then deposited on the core and sealed by fusing it at 200°C to the edges of the polymer plate.

4.2. Hydrogel and sandwich multi-materials elaboration process

This section fully describes the steps to elaborate sandwich multi-materials filled with hydrogels (part 2: Chapters 3 and 4).

4.2.1. Reference hydrogels

Hydrogel A was prepared by dissolving 3 wt.-% of sodium alginate in hot distilled water (at 70°C), under magnetic stirring. A controlled mass of alginate solution (around 2.7 g) is then poured in the core polymer design and directly plunged overnight into a water based gelation bath containing 2 wt.-% of $CaCl_2$ and 0.5 M of citric acid monohydrate (Figure 101 a). Citric acid was used in addition to $CaCl_2$ to avoid the retraction of alginate-gel [258]. A physical cross-linking thus occurs to ensure the formation of the hydrogel phase (Figure 101 a).

Hydrogel B is formed by dissolving 0.7 wt.-% of agar in boiling water (at 100°C) under magnetic stirring (Figure 101 c). The hot agar solution is then poured (with a controlled mass around 2.7 g) in the core, and leaved to cool down at room temperature. The gelation process occurs when the agar solution reaches room temperature.

For hydrogel C, 3 wt.-% PVA is dissolved and stirred in hot distilled water (at 75°C). Then, cross-linking in hydrogel C occurs by adding 0.6 wt.-% of borax in the stirred solution of PVA (Figure 101 d) [259]. The stirring is maintained until the solution cooled-down at room temperature and the gel is formed. Afterwards, the gel is incorporated in the empty cells of the core directly, with a controlled mass around of 2.7 g. Due to the constant stirring during the gel formation to ensure its homogeneity, hydrogel C has to be applied in the empty cells of the core polymer design after gelation. However, thanks to its soft texture, hydrogel C is easily applied (Figure 101 d).

© 2020 Tous droits réservés.
lilliad.univ-lille.fr

Thèse de Laura Geoffroy, Université de Lille, 2020

4.2.2. Hydrogels containing vermiculite and vermiculite/K_2CO_3

Hydrogels containing vermiculite or vermiculite and K_2CO_3 were then prepared in order to improve the fire retardant performances of the hydrogels A, B, C.

Three new composite hydrogels containing vermiculite named A+VMT, B+VMT and C+VMT were elaborated. A commercial solution of dispersed vermiculite at 7.8 wt.-% in water was diluted to 7 wt.-% using distilled water and heated to the appropriate temperature (70°C for A+VMT, 100°C for B+VMT and 75°C for C+VMT). Then the gels A+VMT, B+VMT and C+VMT were prepared by respectively adding sodium alginate, agar and PVA directly into the solution, then pouring it in the empty cells of the core polymer design before (or after for C+VMT) carrying the cross-linking step as previously mentioned (Figure 101 a, Figure 101 c and Figure 101 d).

Finally, the incorporation of K_2CO_3 in the previously prepared gels containing VMT was not straightforward. Indeed, its addition in B+VMT and C+VMT causes VMT particles to agglomerate and thus prevent the gel formation whereas it disrupts the crosslinking process of A+VMT as it reacted with $CaCl_2$ and the citric acid to yield $CaCO_3$ and CO_2 (Figure 101 b). Likewise, alginate and K_2CO_3, agar with K_2CO_3 or PVA/Borax with K_2CO_3 alone (without VMT) did not form a gel. Nevertheless, a gel containing alginate, VMT and K_2CO_3 (hereafter called A+VMT+K_2CO_3) was prepared with a modified gelation process. Based on a part 2 chapter 2 (and paper [155]), 0.2 g/10 ml of K_2CO_3 was added in a solution containing 3 wt.-% of alginate and 7 wt.-% VMT (preparation previously described). The solution was then cooled down in a refrigerator for 48 h [260]. Then, the hydrogel is taken out of the fridge and deposited in the empty cells of the core polymer design, with a controlled mass around 2.7g (Figure 101 b).

© 2020 Tous droits réservés.

lilliad.univ-lille.fr

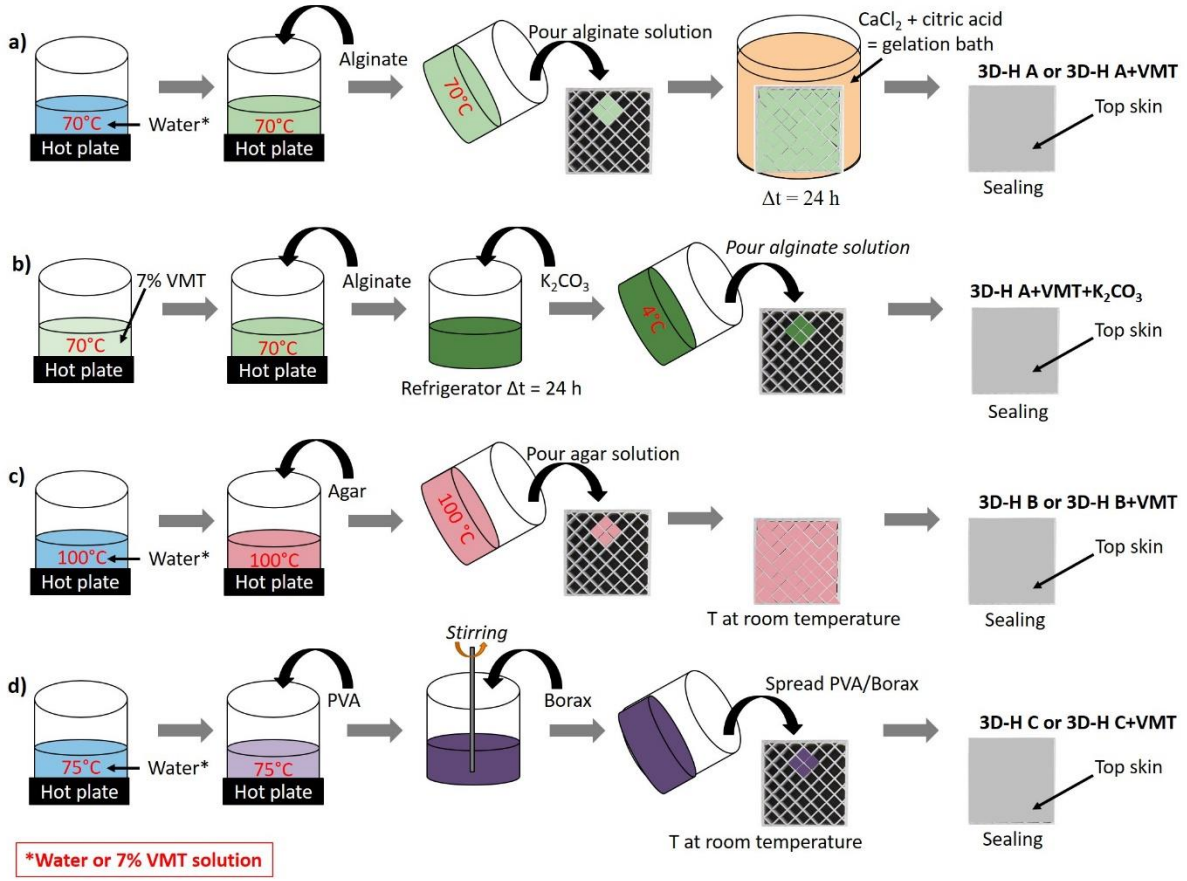

Figure 101. Hydrogel sandwich multi-materials elaboration (a) 3D-H A or 3D-H A+VMT, b) 3D-H A+VMT+K_2CO_3, c) 3D-H B or 3D-H B+VMT, d) 3D-H C or 3D-H C+VMT).

Afterwards, the design is sealed by fusing the edges of the polymer top skin to the polymer plate at 200°C, thereby forming the final hydrogel sandwich multi-material.

4.3. Low emissivity coating deposition

Prior to coating deposition (on samples in part 2 chapter 4), the substrates were cleaned with an ultrasonic bath for 5 min in ethanol, then fixed in the chamber on the sample holder in front of the target using Kapton adhesive, and sputter-cleaned in the argon plasma for 20 min. During this step, the pressure was set at 0.3 Pa, and the RF power at 200 W. This step is meant to enhance the adhesion of the metal to the polymer. Then for samples in part 2 chapter 4 (IR-3D air ad IR-3D-H B+VMT), the low emissivity coating composed of a layer of aluminum protected by a thin layer of alumina (Al_2O_3) on top was deposited sequentially on the top skin using a DEPHIS4 (DEPHIS, Etupes, France) pulsed DC magnetron sputtering machine. Aluminum was deposited in metallic mode by sputtering a pure aluminum target with a diameter of 20 cm (A.M.P.E.R.E. industry, Saint-Ouen-l'Aumône, France) in an atmosphere of pure argon. The argon flow rate was set at 100 sccm, and the Al discharge current was 1 A. After 30 min, oxygen was introduced in the chamber with a flow rate of 20 sccm to deposit

© 2020 Tous droits réservés.
lilliad.univ-lille.fr

Thèse de Laura Geoffroy, Université de Lille, 2020

Al_2O_3 via reactive sputtering for 60min. No bias is performed during deposition. A whole cycle lasts for about 3h. Deposition was also carried out simultaneously on glass for visual control.

5. Fire testing

5.1. Mass Loss Cone Calorimeter

The reaction to fire performance of the prepared materials was evaluated using a Mass Loss Cone Calorimeter (MLCC) (Fire Testing Technology (FTT), West Sussex, UK) according to standards ISO 13927 or ASTM E906 [261]–[263]. The equipment is similar to that used in cone calorimetry (ASTME-1354-90), except that the Heat Release Rate (HRR) is measured, after a calibration step with methane, using a thermopile (constituted of four thermocouples) located at the top of a chimney instead of employing the oxygen consumption principle (Figure 102). The 100x100x3 mm^3 (in appendix 2) or 50x50 mm^3 (in part 2: chapters 2, 3, 4) samples placed on a ceramic backing board at a distance of 35 mm from a conical radiant heater were exposed in a horizontal orientation to an external heat flux 50 kW/m^2 , which corresponds to the late stage of a developing fire scenario [261]–[263]. All experiments were done using a piloted ignition and by submitting samples to an electric arc (32 nA). When the ignition occurs, the electric arc is removed. During the heat exposure, HRR was recorded as a function of time via a data acquisition system using (MLC Calc software, Radcal, Monrovia, California, United States of America). Three main parameters were determined from this curve (HRR versus time): (i) the peak of Heat Release Rate (pHRR), which is one of the critical factors in predicting the growth rate of fire, (ii) the Total of Heat Release (THR), which corresponds to the area under the HRR versus time curves and (iii) the Time To Ignition (TTI), which is the time until sample is ignited. Each prepared sample was subjected to at least three measurements, in order to ensure repeatability within the error margins of ±10% for pHRR and THR and ±15% for TTI. The average values were chosen for the comparison between samples afterward.

© 2020 Tous droits réservés.

lilliad.univ-lille.fr

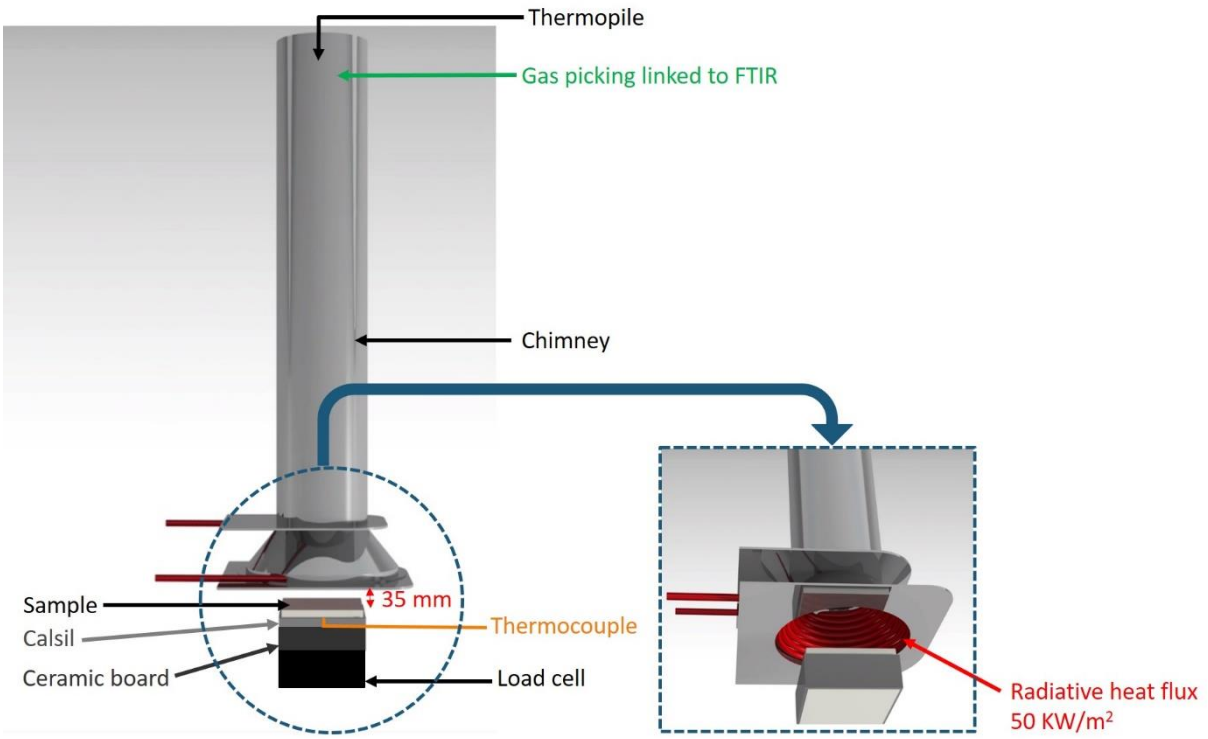

Figure 102. Fire testing: Mass Loss Cone calorimeter test.

To obtain further information, MLCC test was in certain studies on this work instrumented with thermocouple to measure the temperature versus time profiles (more details in section 4.2. Temperature versus time measurement), with Fourier Transform InfraRed to analyze gas phase during fire testing (more information in section 4.3. Gas phase analysis) or with soot picking to examine the composition of soot (fully described in section 4.4. Soot picking in the flame).

5.2. Temperature versus time measurement

The temperature versus time profiles were measured in the middle of the backside of the polymer plates using a K-type thermocouple (TC SA, Dardilly, France) fixed in a calsil plate to ensure its steadiness during the test (Figure 102). Data were recorded using a graphtec 34970A data logger (Keysight Technologies, Santa Rosa, CA, USA).

5.3. Gas phase analysis

Concurrently to MLCC test, gas phase analysis was done using a Fourier Transform InfraRed (FTIR) spectrometer (Antaris TM Industrial Gas System (Thermofisher, Waltham, Massachusetts, United States)). A gas picking and transfer line (M&C Tech Group, Ratingen, Germany), were put on the top of chimney. The 2 m long transfer line between MLCC and FTIR is heated up at 200°C. To assure constant temperature of the transfer line, two temperature controllers are installed. Before analyzing the gases by FTIR, soot particles are filtered by two

© 2020 Tous droits réservés.
lilliad.univ-lille.fr

Thèse de Laura Geoffroy, Université de Lille, 2020

different filters (2 and 0.1µm). These filters are composed of glass fibers and ceramic respectively. The FTIR gas cell is set at 185°C and 652 Torr. The optical pathway is 2 m long and the chamber of the spectrometer is filled with dry air. FTIR spectra obtained using MLCC-FTIR are treated using OMNIC software. The spectrometer is calibrated to quantify water, carbon monoxide, and carbon dioxide. Quantification is reproducible within 10%.

5.4. Soot picking in the flame

Soot samples were collected (in part 2 chapter 2) by applying a 45x15x0.9 mm^3 mirror polished stainless-steel plate (Goodfellow, Cambridge, United Kingdom) inside the flame. The mirror polished stainless-steel plate was beforehand cleaned for 10 min in 1:1 acetone and ethanol solution (Sigma Aldrich, St. Louis, Missouri, Unites States), then put for 10 min at 65°C in a solution of water and 2% of RBST105 (Chemical products R. Borghgraef. S.A., Brussels, Belgium) which is a liquid alkaline and foaming cleaner, and finally put in water solution at room temperature for 5 min before being dried. Then, the mirror polished stainless-steel plate was applied in the flame at the pHRR [158].

6. Characterizations

6.1. Weight, thickness and apparent density measurements

The weight and the thicknesses (using a ruler placed vertically) of all samples were measured before fire testing to compare samples with each other. Moreover, samples volume and apparent density were calculated using formula 1: length (mm) x width (mm) x thickness (mm)) and formula 2: weight (kg) divided by volume (m^3), respectively.

6.2. Optical microscopy

Optical microscopy observations were carried out on samples before and after fire test on top and cross-section using a microscope VHX-1000 HDR (High Dynamic Range, Keyence, Osaka, Japan).

For the top section, sample was simply observed under the microscope.

For the cross-section observation:

- before fire test: each sample was put in liquid nitrogen for 5 min and then cut using a blade and a hammer. Using this protocol, a brittle fracture was obtained without affecting the integrity of the sample. The cross-cut samples obtained were then embedded in an epoxy resin, dried for 48h at room temperature, and polished (up to ¼

© 2020 Tous droits réservés.

lilliad.univ-lille.fr

µm) using silicon carbide disks (ESCIL, Chassieu, France) to obtain the smoothest surface as possible to facilitate observations.

- after fire testing: residues obtained were cut using a blade, and the cross-sections were observed using the optical microscope, without embedding into epoxy resin.

6.3. Confocal microscopy

The dispersion of VMT particles in liquid or hydrogel phase (part 2 chapter 3) before MLCC tests was observed using an inverted confocal microscope (ZEISS LSM 780, Carl Zeiss MicroImaging GmbH, Jena, Germany). Fluorescence was obtained by using fluorescein (Sigma Aldrich, St Louis, Missouri, United States). When hydrogels containing VMT (H A+VMT, H B+VMT, H C+VMT) were prepared (as described in section 4. Hydrogel and sandwich multi-materials elaboration process), a 10^{-5} mol/L solution of fluorescein was used instead of pure distilled water. Then, a drop of each hydrogel formed containing fluorescein was deposed on a thin glass slide for observation. The fluorescent aqueous probe was excited at 488 nm and emitted light was observed in the range 493 - 624 nm. In these experiments, water appears in green due to fluorescein coloration, whereas VMT particles, not colored with fluorescein, appear in black. Observations were done using an immersion oil objective 40x, with numerical aperture of 1.3. Z stack were acquired on each sample. Finally, ImageJ software was used for image processing. Among Z stack pictures acquired, a representative image of sample was chosen.

6.4. Electron Probe Micro-Analysis

X-ray mappings of the cross-section of the samples before and after MLCC tests were carried out to figure out the elemental repartition and dispersion (in appendix 2 and part 2 chapter 3). To perform these mappings, all samples were initially embedded into an epoxy resin. After 48h of curing at room temperature, samples were polished (up to 0.25 µm) using silicon carbide disks (ESCIL, Chassieu, France), followed by a carbon coating with a Bal-Tec SCD005 sputter coater (Bal-Tec, Los Angeles, California, United States). Cross-section back scattered electron (BSE) image and X-ray mappings were carried out at 15 KV, 40 nA using a Camera SX100 electron probe microanalyser (Electron Probe Micro-Analysis: EPMA) (Cameca, Gennevilliers, France). On the mappings, a color-coded legend characterizes the concentration of the element (black color: absence of the element to red color: highest concentration).

Moreover, for mappings: (1) a PC2 (a multilayer of Ni/C), was used to detect Kα of C, (2) a Thallium Acid Phtalate (TAP) crystal was used to detect Al and Mg, (3) a Pentaerythritol (PET)

© 2020 Tous droits réservés.
lilliad.univ-lille.fr

Thèse de Laura Geoffroy, Université de Lille, 2020

crystal was used to detect S and K and (4) a Lithium Fluoride (LIF) crystal was used to detect Fe.

6.5. Scanning Electron Microscopy

JEOL JSM 7800F LV (JEOL ltd, Tokyo, Japan), a scanning Electron Microscopy were used for observations, EDS analysis and X-ray mappings.

6.5.1. Scanning Electron Microscopy for observation

Scanning Electron Microscopy (SEM) observations of the cross-section of the residues obtained after MLCC tests were carried out to analyze their aspect. The cross-cut samples (previously described) were embedded into epoxy resin, polished and carbon coated with the same process details in materials & methods part – 6. Characterizations – 6.4. Electron Probe Micro-Analysis (page 173).

6.5.2. Scanning Electron Microscopy for EDS analysis and X-ray mappings

In part 2 chapters 2 and 4, EDS analysis and X-ray mapping were done for some samples and residues in cross-section (which were previously embedded into epoxy resin, polished and carbon coated with the same process described in materials & methods part – 6. Characterizations – 6.4. Electron Probe Micro-Analysis (page 173)) and for soot collected samples (which were previously carbon coated with a Bal-Tec SCD005 sputter coater (Bal-Tec, Los Angeles, California, United States)). X-ray mappings were performed using an Oxford Instruments SDD EDS detector (Abingdon, United Kingdom), coupled with Aztec software. K, Al, C, O, Ni, Fe, Cr, Si and Mo elements were studied (developed in 2.3). All EDS spectra, EDS mappings and images obtained were treated using Aztec software afterward.

6.6. X-Ray Diffraction and/or High Temperature X-ray Diffraction

In part 2 chapter 2, the crystalline structure of the residues after MLCC test were determined using XRD analyses. XRD scans were recorded in the 5° - 60° range using a Bruker AXS D8 diffractometer (Massachusetts, United States), equipped with a Cu Kα (λ = 0.154 nm) radiation in configuration $\theta/2\theta$.

In part 2 chapter 3, both Room-Temperature (RT-XRD) and High Temperature X-ray Diffraction (HT-XRD) experiments were done using a SmartLab© Rigaku diffractometer (Rigaku, Tokyo, Japan) equipped with a 9 kW rotating anode X-ray generator (Cu Kα=1.5418 A), fitted with a DTEX one-dimensional silicon-strip detector, in Bragg-Brentano reflection geometry. For RT, the θ-2θ scans were performed in the range 5°-75°, with a step size of 0.03°

© 2020 Tous droits réservés.

lilliad.univ-lille.fr

and a speed of 2°/min, while for HT-XRD, patterns were recorded in the range 4°-65°, with a step size of 0.01° and a speed of 4°/min. The experiment was conducted under a static air atmosphere in an Anton Paar DHS1100 heating attachment, with a temperature range 25 - 1000°C, using, on heating, 25°C plateau (heating rate 5°C/min between each plateau) and 50°C plateau at cooling. Scans were recorded after a one-minute temperature stabilization plateau.

All spectra obtained were analyzed using DIFFRAC.EVA software (Bruker, Massachusetts, United States).

6.7. Thermal conductivity measurements

Thermal conductivity was measured at room temperature by a hot disk thermal constant analyser (Hot Disk TPS 2500S, Thermoconcept, Bordeaux, France), which is a transient plane source technique [264]. The sensor (warmth emitter) is mould in the middle of two samples (25 x 25 x 6 mm^3) to ensure a good contact during the experiment. The conductivity measurements were carried out by applying a power of 0.06 and 0.065 W for 10s for T-EVA/EG (10 wt.-%) and 3D-EVA/EG (10 wt.-%) (in appendix 2), respectively. The experiment was repeated four times to check the repeatability of the measurement. The presented results are the average of the obtained values.

6.8. Emissivity measurements

Directional hemispherical emissivity of the surfaces was measured by infrared diffuse reflectance. The measurements were performed at 20°C on a Vertex 70v spectrophotometer (Bruker, Bellerica, MA, USA) equipped with a 75 mm-large, gold-coated integrating sphere (Bruker A562). 128 scans from 350 to 7500 cm^{-1} were performed with a resolution of 4cm^{-1}, and the results were integrated between 7.5 and 13 µm. The beam comes from a SiC light source, going through a KBr beam splitter and an aperture of 6 mm, and impacts the sample with an angle of 13°. The results were interpreted on the Bruker OPUS software (black body emission calculated at 20°C), also used to run the spectrophotometer. The emissivity values are presented as the average of 4 measures on different places of the samples to check for repeatability.

© 2020 Tous droits réservés.
lilliad.univ-lille.fr

Thèse de Laura Geoffroy, Université de Lille, 2020

Chapter 2: Materials & methods of part 3 for designing the new intumescent metal laminate fire barrier

1. Processing of samples

1.1. Materials

100x100x3 mm^3 steel plates (grade XC40, Couzon Aciers Service, Saint Chamond, France) were used as substrates. All of the plates were sandblasted (Normfinish, Jean Brel SA, Stains, France) to improve the coating adhesion, using a white aluminum oxide (Guyson, Chambly, France) (particle size around 355 - 500 µm), at a 5 bars pressure. Acetone (VWR, Radnor, Pennsylania, United States), was used to clean substrates prior to use. 30 µm thick aluminum foils (Carl Roth, Karlsruhe, Germany) with 99% of purity were applied to elaborate metal laminate samples. Three fireproofing coatings hereafter called A, B and C (proprietary formulation) were studied, and described in Table 32. They were all designed for cellulosic (ISO834) or hydrocarbon (UL1709) fire scenarios. A and B are conventional commercial epoxy and acrylic based coatings, respectively, containing classical intumescent agents and designed to pass UL 1709 and ISO 834, respectively. A bubbling (chemical) expansion occurs when these coatings are exposed to fire. Coating C is a silicone-based coating designed by our team, as described in reference [214], containing expandable graphite as the main additive. Physical expansion was thus observed upon heating, due to expansion of the graphite. Mechanical cohesion was reported to be obtained through the formation of Si-C bonds [212]–[215], [217], [222].

Table 32. Intumescent coatings characteristics.

Paint	Targeted fire Scenario	Type of Paint	Type of Intumescence
A	UL 1709	Epoxy, bi-component [201], [239]–[241]	Chemical
B	ISO 834	Acrylic, mono-component	Chemical
C	UL 1709, ISO 834	Silicone, bi-component [212]–[215], [217], [222]	Physical

In addition of that, composite plates with a thickness of 3 mm and composed of carbon fibers and epoxy resin, were used as other substrate, and were purchased from Goodfellow (Huntingdon, Cambridge, United Kingdom). From the same supplier (Goodfellow, Huntingdon, Cambridge, United Kingdom), copper foils with 99.9% of Cu purity and a thickness of 25 µm, and potassium aluminosilicate sheets, hereafter named mica, with a

© 2020 Tous droits réservés.

lilliad.univ-lille.fr

thickness of 25 µm, were used to prepare other bi-layer metal laminates presented in the next section.

1.2. Intumescent Polymer Metal Laminate (IPML) samples elaboration

IPML (samples in part 3 chapter 2) processing occurred in several steps, illustrated in Figure 103. Aluminum foils were first cut into 100 mm × 100 mm squares. Then, intumescent coatings (respectively A, B, and C coatings) were manually deposited onto the aluminum foils. Three stacks of ten aluminum foils and nine intumescent coating layers were prepared and pressed using a press supplied by Fontijne Grotnes B.V. (Vlaardingen, Netherlands), to reduce the void content due to air entrapment. For coatings A and C, a force was applied, starting at 10 to 20 kN, with a ramp of 0.9 kN/min at 50°C. Then, the load was set at 20 kN for 1 min. For paint B, due to the different chemistry and viscosity of the coating (acrylic based), a 10 kN load was applied for 12 min at 50°C.

After that, a last thin layer of coating (A, B, and C, respectively equal at 300, 160, and 170 µm (measured using an optical microscope)) was applied to the top of the aluminum foils to form the final IPML, which was then cured for 48 h at room temperature. Finally, it was glued onto a steel plate, using an epoxy resin (DGEBA, purchased from Sigma-Aldrich, St louis, Missouri, United States, reference 31185) cross-linked with Diethylenetriamine, (purchased from Sigma-Aldrich, St louis, Missouri, United States, reference D93856) with a ratio of 100:11.7. The whole system (plate + IPML) was cured again, for 48 h at room temperature.

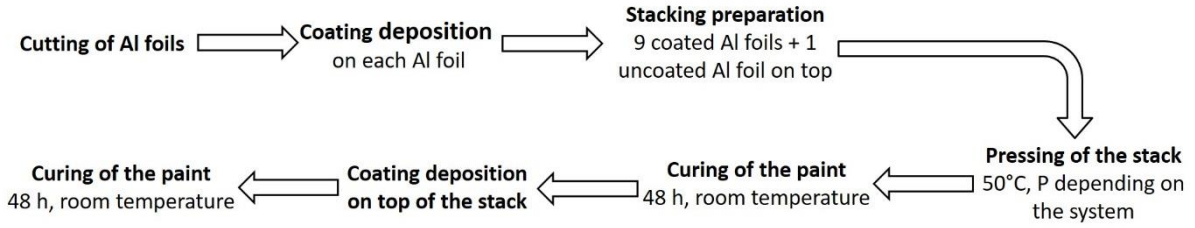

Figure 103. IPML elaboration process.

1.3. Bilayer Metal Laminate samples elaboration

Bilayer Metal Laminate structures processing is carried out in several steps (Figure 104) and depends on the structure of the bilayer laminate. The global intumescent coating mass deposited on the substrate is kept constant and corresponds to 20 g (total mass around 260 g substrate and aluminum foils potentially present included) in order to be able to compare the different designs.

For the first layer:

© 2020 Tous droits réservés.
lilliad.univ-lille.fr

Thèse de Laura Geoffroy, Université de Lille, 2020

i) Aluminum foils are cut into 100x100 mm^2 squares.

ii) Aluminum foil is glued onto sandblasted steel plate using almost 1 g of an epoxy resin (DGEBA, purchased form Sigma-Aldrich, St louis, Missouri, United Stated, reference 31185) cross-linked with Diethylenetriamine, (purchased from Sigma-Aldrich, St louis, Missouri, United States, reference D93856) with a ratio of 100:11.7.

iii) Curing step is performed for 48h at room temperature, to fix the first aluminum foil onto steel plate.

iv) A controlled mass of intumescent coatings (A or B, according to the system studied) is manually applied onto aluminum foil glued onto steel plate, using a film applicator.
For the second layer:

v) A second aluminum foil is added on top of the first paint layer.
vi) The system is cured for 24h at room temperature.
vii) A second intumescent coating (A or B according to the system elaborated) is applied on the aluminum layer.

viii) Finally, for the whole system is cured for 48h at room temperature. Therefore, using this process, different intumescent bilayer metal laminates were prepared with one or two aluminum foils and two layers of coating A and B (Figure 104).

It is important to note that, according to the system studied, some steps could be removed (Table 33). Indeed, if no aluminum foil is put between the substrate and the first coating as S-A+AlB or S-B+AlA, steps ii) and iii) are suppressed and coating is directly applied on the substrate according to step iv).

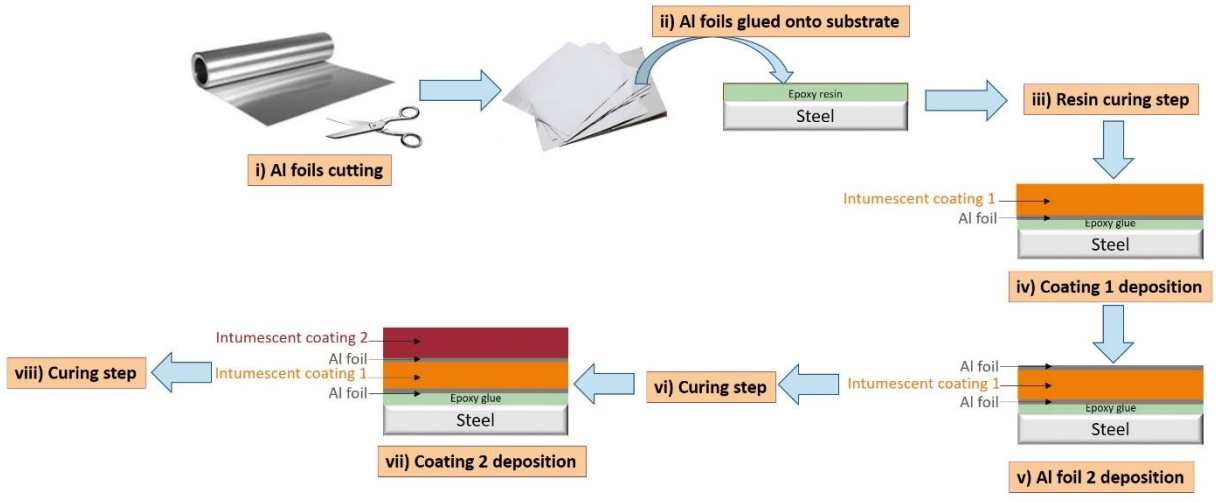

Figure 104. Elaboration process of intumescent bilayer metal laminate.

© 2020 Tous droits réservés.

lilliad.univ-lille.fr

Table 33. The steps of the process according to the intumescent bilayer metal laminate samples.

Samples	S	S-A and S-B	S-A+B and S-B+A	S-AlA+B and S-AlB+A	S-A+AlB and S-B+AlA	S-AlA+AlB and S-AlB+AlA
Process steps	/	(iv), (vii)	(iv), (vi),(vii)	(i), (ii), (iii), (iv), (vi), (vii)	(i), (iv), (v), (vi), (vii)	(i), (ii), (iii), (iv), (v), (vi), (vii)

2. Fire testing

2.1. Burn-Through test

The selected bench scale fire test (fully described elsewhere, in reference [244]), consists in exposing the samples to a 116 kW/m^2 heat flux, using a propane torch, as illustrated in Figure 105. This test bench was compliant with two aeronautical certification fire tests: ISO2685:1998(E) and FAR25.856(b):2003.

At the beginning of the test, each sample was maintained between two 10 mm thick insulating panels from FINAL Advanced Materials (Calsil) and attached using four screws. The test was carried out without any ventilation, to avoid the influence of convection. Before exposing the samples to fire, a calibration of the propane flame was done for 5 min to check that the heat flux was constant and equal to 116 kW/m^2, (corresponding to a flame temperature of ~1100°C) (Figure 105 a). Then, the samples were directly subjected to the flame for 15 min (in part 3 chapter 2) or for 30 min (in part 3 chapters 3 and 4) and cooled down to room temperature (Figure 105 b). Moreover, the weight and thickness (using a ruler placed vertically) of all samples are measured before and after the torch test to calculate mass loss and intumescent expansion, respectively.

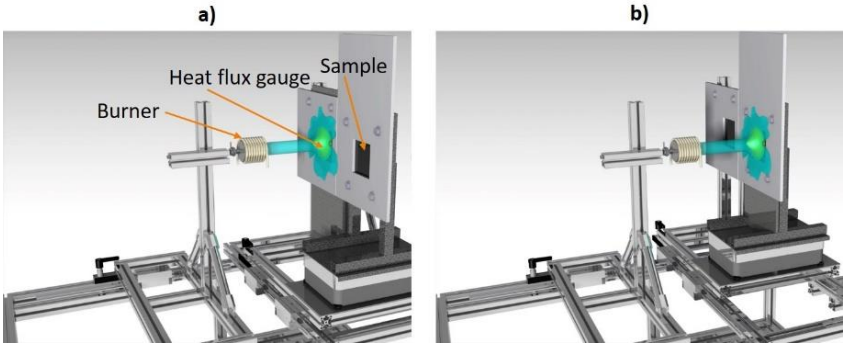

Figure 105. Burn-through test bench illustration [244] (a) Flame calibration, (b) Switch between calibration to sample: fire testing.

© 2020 Tous droits réservés.
lilliad.univ-lille.fr

Thèse de Laura Geoffroy, Université de Lille, 2020

2.2. Temperature versus time measurements

2.2.1. For steel plate as substrate

To compare the resistance to fire of the designed samples deposited on steel plate, temperature versus time profiles were measured during the fire test. K-type thermocouples (TC SA, Dardilly, France) welded onto the middle of the backside of the steel plates were used. Data were recorded using an Agilent 34970A data logger (Keysight Technologies, Santa Rosa, California, United States). Each experiment was repeated at least 3 times, to check the repeatability of the fire test results.

2.2.2. For composite plate as substrate

For sample using composite plates as substrate, the temperature versus time profiles cannot be registered using a K-type thermocouple as it cannot be welded onto the plate. Therefore, during the fire testing, the temperature evolution of these samples was measured using an infrared camera (FLIR thermovision A40, Wilsonville, Oregon, United States), placed at a fixed distance from the backside of the steel plate. All sample backsides were previously spray-coated with a heat resistant mat black paint (Jelt noir mat 700°C supplied by ITWPC Spraytec, Asnières-sur-Seine, France), ensuring that they all had the same surface emissivity (close to 0.9). All the IR measurements were recorded using Thermacam research professional 2.0. software (FLIR system, Wilsonville, Oregon, United States), and computed using Research IR software (FLIR system, Wilsonville, Oregon, United States). Each experiment was repeated at least 3 times, to check the repeatability of the fire test results.

2.3. Thermal gradient measurement

Thermal gradient of some Intumescent Polymer Metal Laminate (IPML) samples in part 3 chapter 2 was measured. Three thermocouples were inserted perpendicularly to the heat flux (according to the work [265], [266]) and between aluminum foils (before press step), as Figure 106 shown. Then, the IPML was pressed, cured, and coated, following the set-up described in the materials & methods section – 1. Processing of samples – 1.2. Intumescent Polymer Metal Laminate (IPML) samples elaboration (page 177). Finally, IPML containing thermocouples were exposed to fire for 15 min.

© 2020 Tous droits réservés.

lilliad.univ-lille.fr

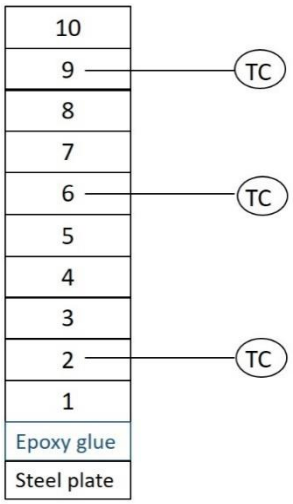

Figure 106. Illustration of thermal gradient measurement in IPML.

3. Characterizations

3.1. Mass loss measurements

The mass of the samples before (m_{before}) and after x min of fire exposure ($m_{after\ x}$) were measured using a scale. The mass loss (ML) is calculated as the ratio between the difference of mass loss after and before fire testing to mass before fire testing, as illustrated by this equation: ($ML = (m_{after\ x} - m_{before}) / m_{before}$).

3.2. Expansion measurements

The thicknesses of the samples before (e_{before}) and after x min of fire exposure ($e_{after\ x}$) were measured using a numerical caliper and a thickness gauge. The expansion (E) is calculated as the ratio between the difference of thicknesses after and before fire testing to thickness before fire testing, as illustrated by this equation: ($E = (e_{after\ x} - e_{before}) / e_{before}$).

3.3. Optical microscopy

Before fire testing, optical microscopy observations were carried out on cross sections using a microscope VHX-1000 HDR (High Dynamic Range), Keyence (Osaka, Japan). Preparation of the cross sections was as follows: each sample was put in liquid nitrogen for 5 min, and then cut using a blade and a hammer. Using this protocol, a brittle fracture was obtained without affecting the integrity of the sample. Samples obtained were then embedded in an epoxy resin, dried for 48h at room temperature, and polished (up to 1/4 µm) using silicon carbide disks (ESCIL, Chassieu, France) to obtain the smoothest surface as possible to facilitate observations.

After fire testing, residues were also cut in cross-section using a thin cutter blade. The possible delamination of the coating was then observed visually.

© 2020 Tous droits réservés.
lilliad.univ-lille.fr

Thèse de Laura Geoffroy, Université de Lille, 2020

3.4. Scanning Electron Microscopy observations

Scanning Electron Microscopy (SEM) observations were performed on residues obtained after fire testing, using a Hitachi S4700 (Tokyo, Japan). The residues were cut and fixed on the SEM holder using carbon conductive double-face adhesive tape, supplied by Nisshin EM Co., Ltd. (Tokyo, Japan). Then, samples were carbon coated using a Bal-Tec SCD005 sputter coater (BAL-TEC, Pläffikon, Switzerland).

3.5. Thermal analyses

Thermogravimetric analyses (TGA) were carried out on residues obtained after fire testing, using a TG 209 F1 Libra supplied by Netzsch (Selb, Germany). When possible, residues were collected between each aluminum foils. They were then ground in a mortar and for each experiment: 10 mg samples were positioned in aluminum open pans, on a gold sheet to avoid possible reactions of the phosphorus species of the coating with the alumina pans.

The thermograms were recorded in the 40–800°C temperature range, with a heating rate of 10°C/min under nitrogen flow, Air Liquide grade (40 mL·min^{-1}).

3.6. Pull-off test

Adhesion tests were carried out using a pull-off test (Erichsen, Hemer, Germany) (Figure 107 e). This test procedure is divided into four main steps. First, the sample is cut down to the substrate in a circle which is the size of the dolly used for the test (Figure 107 a). Then, the dolly is glued on the delimited area using a cyanoacrylate adhesive (Henkel, Düsseldorf, Germany) dried for 48 hours at room temperature (Figure 107 b). The dolly is tightened up on the loading gauge (Figure 107 c). The gauge is reset before applying the load. Finally, the load is manually smoothly increased using a crank handle. The pull-off force is measured when failure occurs using a manometer (Figure 107 d).

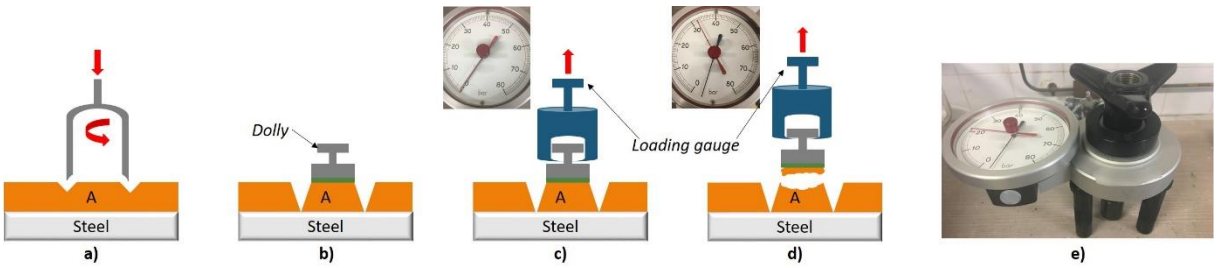

Figure 107. Description of pull-off test

© 2020 Tous droits réservés.

lilliad.univ-lille.fr

Appendix

Appendix 1 – Part 2, chapter 1

In this appendix some standard polymer shaping process to elaborate complex design are described.

1. Plastic extrusion

Extrusion is the most widespread processing method for thermoplastics, fully described in paper [91]. Polymer pellets are fed into the hopper (Figure A1- 1). Extruder is composed of singled or twin screw. By rotating the extrusion screw, polymer is dragged along the extruder. The polymer pellets are thus melted by the heat from friction with barrel walls and also by the external heat source. The turning screw compacts polymer and mixes the melt. The molten polymer leaves the extruder through a shaped die which defines the geometry of the product (sheet, pipe, rod, or more complex sections). With this process, two or more polymers can be extruded together (co-extrusion) to produce a multi-layer structure. In that case, separate extruder for each polymer is required. Then, extrusion of one or more polymers can be followed by quenching using air or water to retain the shape. Finally, part is cut off.

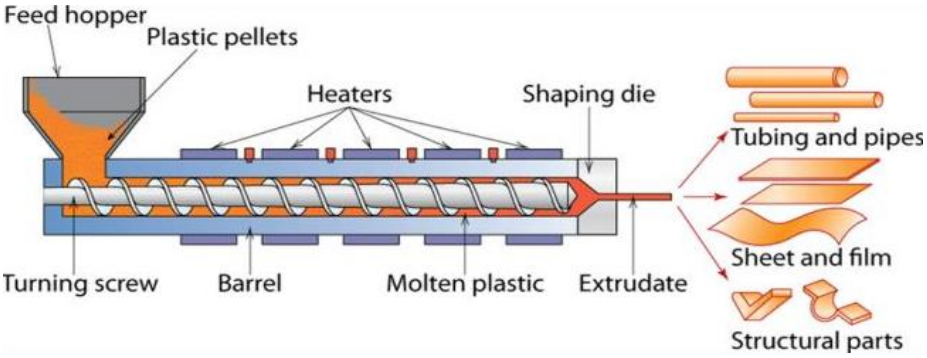

Figure A1- 1. Illustration of polymer extrusion process [267].

2. Injection molding

Injection molding is a very versatile process for metals and polymers, described in paper [75]. It can produce large variety of polymers and wide range of part sizes. This process is divided into four main steps. Polymer pellets or powder are first of all melted using an extruder (fully described in part 1.1.). The molten polymer accumulates in a chamber in front of the screw (Figure A1- 2 a). When the chamber is full, molten polymer is forced into a shape metal mold

© 2020 Tous droits réservés.
lilliad.univ-lille.fr

Thèse de Laura Geoffroy, Université de Lille, 2020

at high pressure (Figure A1- 2 b). This step is achieved by the whole screw moving, acting as a hydraulic ram. Once the polymer is in the mold, the screw can be drawn back so that the molten polymer can be collected again. During polymer injection molding, the melt path into the mold starts with a sprue and splits off into individual melt tubes (called runners), each feeding one of the multiple mold cavities through flow entrances. The polymer injected in the mold is then cooled and solidified rapidly (Figure A1- 2 c). Finally, the mold is opened to eject the finished product (Figure A1- 2 d). This process has a very short cycle time which mainly depends on the cooling step. As a consequence, the production rate of this process is very high. However, to design a complex shape (when it is still possible), the use of complex mold is necessary and often very expensive.

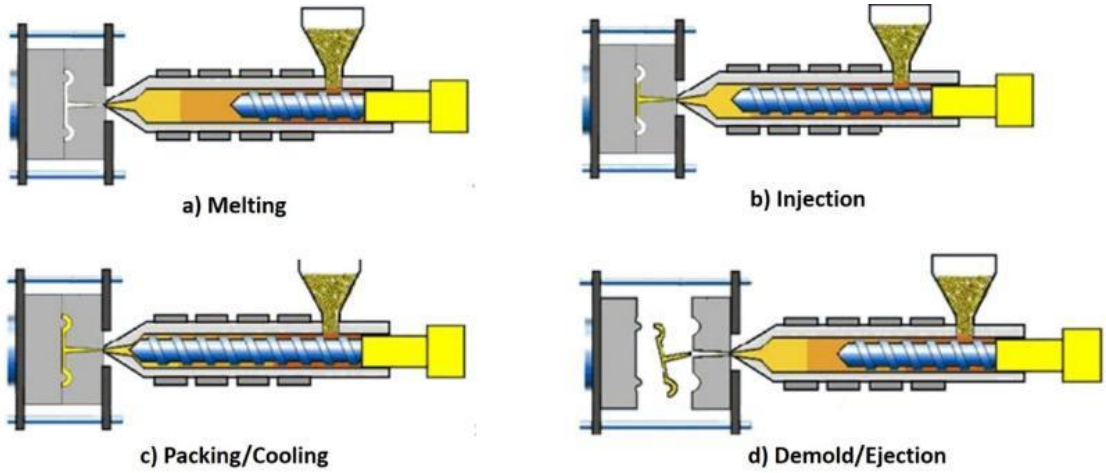

Figure A1- 2. Illustration of injection molding process [75].

3. Blow molding

Blow molding is the process by which products are formed by inflation of a molten polymer to fill in a mold cavity having the desired shape and dimensions [76]–[79]. This process is divided into three main steps. Polymer pellets or powder are melted using extrusion process described in part 1.1. An annular die is used to extrude a molten vertical tube of polymer named parison (Figure A1- 3 a). The parison with well-defined and control dimension is then clamped between the two mold halves, and is inflected by internal air pressure to take the shape of the mold cavity (Figure A1- 3 b). In this step, the polymer is at same time air-cooled down to solidify the finished product. Finally, the mold is opened to remove the product and cut form the remaining tube (Figure A1- 3 c). Using this process, multilayer can be deposed and thus complex design can be elaborated.

© 2020 Tous droits réservés.

lilliad.univ-lille.fr

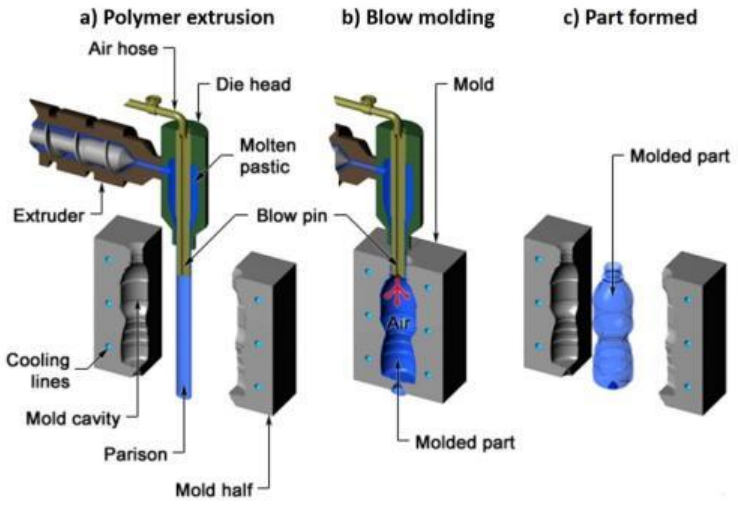

Figure A1- 3. Illustration of blow molding process [268].

4. Thermoforming and compression molding

Thermoforming process involves the softening of the polymer by heat, followed by forming by the application of vacuum or pressure, hereafter named thermoforming under vacuum and thermocompression, respectively [76]–[79].

Thermoforming under vacuum consists in heating a polymer sheet previously attached by clamps (Figure A1- 4 a_1). When polymer sheet is softened (Figure A1- 4 a_2), vacuum is applied and polymer is drawn into the mold (Figure A1- 4 a_3). At the same time, the polymer is cooled-down under vacuum to retain the shape of the mold. Finally, the vacuum is turned off and finished part is demolded (Figure A1- 4 a_4).

Instead of using vacuum, pressure is involved in thermocompression process. A pre-weighed amount of polymer pellets or powder is deposed on bottom mold (Figure A1- 4 b_1). Polymer is pressed in the mold by heated plates of a hydraulic press (Figure A1- 4 b_2). Heat and pressure cause the material to melt and to ensure the finished shape of the part, respectively. The polymer is then cooled to retain the finished shape, still under pressure. Finally, the finished part is removed.

The main advantage of this process is the relatively low cost of thermoforming machines. However, with this process, finished part shape is quite limited.

© 2020 Tous droits réservés.
lilliad.univ-lille.fr

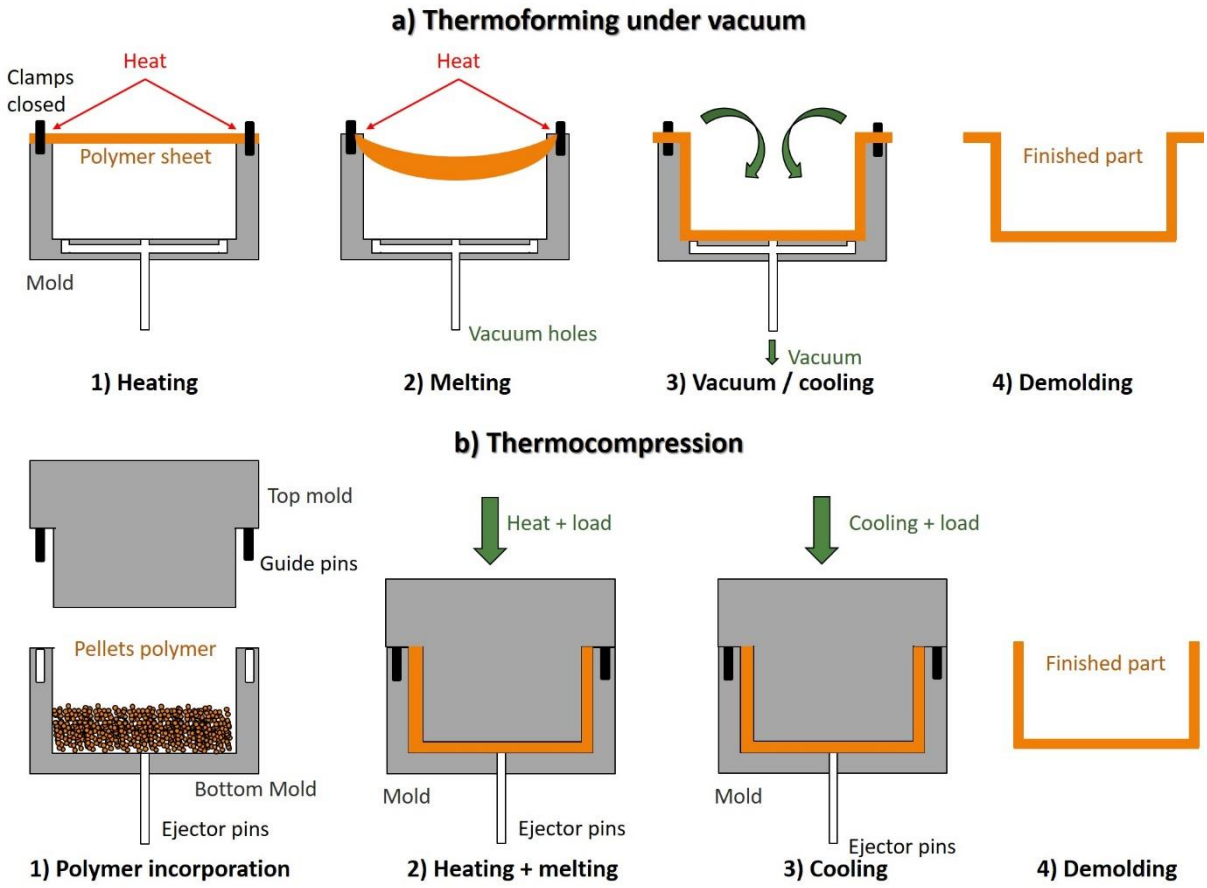

Figure A1- 4. Illustration of a) thermoforming under vacuum and b) thermocompression processes.

5. Rotational molding

Rotational molding process consists in forming a product by heating and cooling the mold containing product while turning it [76]–[79]. No pressure is needed to form a product, and thus no stress is applied on finished product. This process is divided into four main steps. Polymer pellets or polymer powder are first incorporated into a mold with a mass equivalent to the mass required for the finished product (Figure A1- 5 a). The mold is then closed, heated to a set temperature to melt the polymer and rotated around both vertical and horizontal axes (Figure A1- 5 b). By the mold rotating and heating, polymer starts to melt and adhere to the inner surface of the mold. More and more polymer is thus melted and deposed to produce an even layer over the surface of the mold. After that, the mold is cooled down (using air and in some cases water) whilst still rotating to retain the shape (Figure A1- 5 c). When the polymer inside is completely solidified, finished product can be removed from the mold (Figure A1- 5 d). Finally, a last cooling process is done to ensure that the finished product is well solidified. The cycle length of this process depends on the material used, the wall thickness ant the machinery involved.

© 2020 Tous droits réservés.

lilliad.univ-lille.fr

Rotational molding process has some advantages. It can be used for any size of product: large product such as boat hulls or automotive bodies, or small part like syringes. Moreover, this process allows to elaborate complex geometries by incorporating into a one-pot product. However, to elaborate such complex design, a complex mold has to be created.

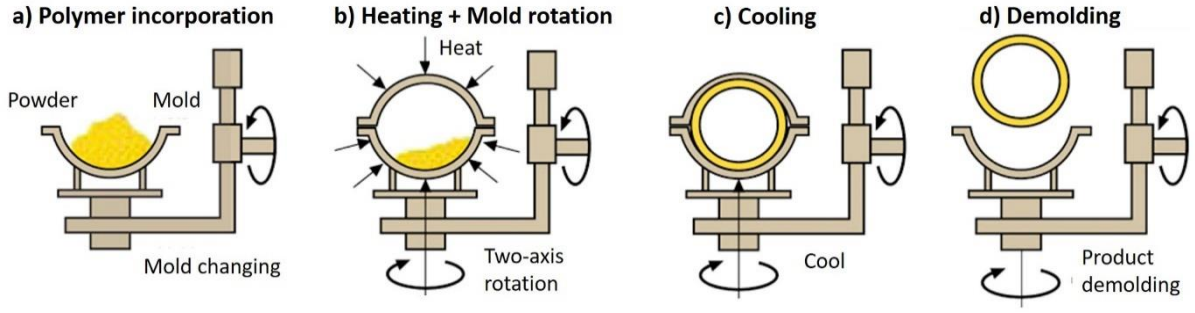

Figure A1- 5. Illustration of rotational molding process [269].

© 2020 Tous droits réservés.
lilliad.univ-lille.fr

Appendix 2 – Part 2, chapter 1

A preliminary study, aims to print flame retarded EVA materials and to compare them with thermocompressed ones (a conventional manufacturing process) (Figure A2- 1) is fully described in this appendix. As mentioned in part 2 chapter 1, EVA polymeric materials was chosen and considered as a model material to prove a concept. The objective of this work was to investigate if disadvantages resulting of 3D printing process (such as higher porosity and anisotropy as part 2 chapter 1 shown) have an influence on the fire protection performance of materials studied.

Four polymers matrices were elaborated, that are composed of neat EVA, or EVA flame retarded with Aluminum TriHydroxyde (ATH) (at different loading: 30 wt.-% and 65 wt.-%) or expandable graphite (EG) (at 10 wt.-%), and shaped using both thermocompression and fused polymer deposition 3D printing processes. All plates were characterized and compared quantitatively (mass, thickness and apparent density) and qualitatively by optical microscopy and Electron Microprobe analyses (EPMA). Comparison of flame retardant properties of 3D printed and thermocompressed plates were carried out by mass loss cone calorimeter test (MLCC) using an external heat flux of 50 kW/m².

The results and discussion of this appendix were published in ***Polymer Advanced Technologies*** journal: **https://doi.org/10.1002/pat.4620** [148].

KEYWORDS: Thermocompression, 3D printing, Flame-retardancy

Aims

- ✓ Elaboration of flame retardant EVA materials using 3D printing process.
- ✓ Quantitative and qualitative characterization and comparison between thermocompressed and 3D printed materials.
- ✓ Fire behavior comparison between thermocompressed and 3D printed materials.

© 2020 Tous droits réservés.

lilliad.univ-lille.fr

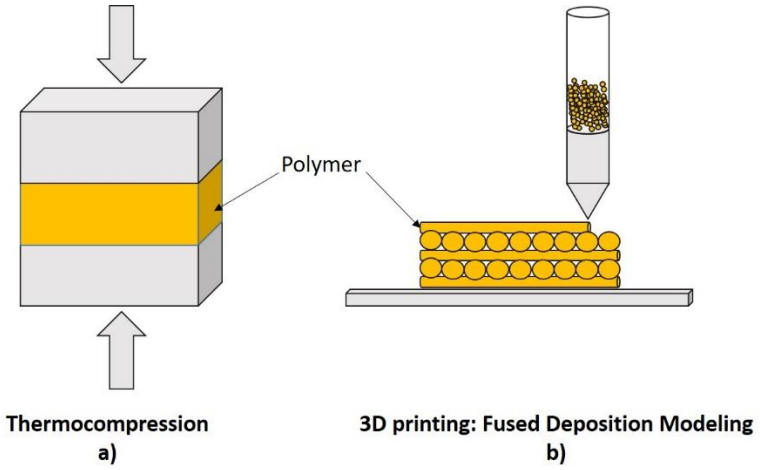

Figure A2- 1. Illustration of a) thermocompression vs b) 3D printing by fused polymer deposition.

1. Samples description

The materials' formulations of EVA, EVA/ATH (30 wt.-%), EVA/ATH (65 wt.-%) and EVA/EG (10 wt.-%) are described in materials & methods part (pages 162 and 163). Thermocompressed and 3D printed plates were elaborated using the processes described in materials & methods part, page 164. Their name and composition are gathered in Table A2- 1.

Table A2- 1. Name and composition of samples.

	Name of the samples	Polymer formulation	Shaping process
1	T-EVA	EVA polymeric matrix	Thermocompression
2	T-EVA/ATH (30 wt.-%)	EVA polymeric matrix containing 30 wt.-% of ATH additives	Thermocompression
3	T-EVA/ATH (65 wt.-%)	EVA polymeric matrix containing 65 wt.-% of ATH additives	Thermocompression
4	T-EVA/EG (10 wt.-%)	EVA polymeric matrix containing 10 wt.-% of EG additives	Thermocompression
5	3D-EVA	EVA polymeric matrix	3D printing (fused polymer deposition)
6	3D-EVA/ATH (30 wt.-%)	EVA polymeric matrix containing 30 wt.-% of ATH additives	3D printing (fused polymer deposition)
7	3D-EVA/ATH (65 wt.-%)	EVA polymeric matrix containing 65 wt.-% of ATH additives	3D printing (fused polymer deposition)
8	3D-EVA/EG (10 wt.-%)	EVA polymeric matrix containing 10 wt.-% of EG additives	3D printing (fused polymer deposition)

© 2020 Tous droits réservés.
lilliad.univ-lille.fr

2. Results

2.1. Thermocompressed and 3D-materials before fire testing

A quantitative comparison between thermocompressed and 3D printed plates was firstly carried out in terms of mass, thickness, volume and apparent density (Table A2- 2) (following the set-up described in materials & methods part (page 172)). According to Table A2- 2, whatever the material, standard deviation between each sample is very small (lower than 5 g, 0.3 mm, 154 kg/m^3 for weight, thickness and apparent density respectively). Therefore, the three samples are comparable for each material studied. Moreover, the thickness and mass differences between thermocompressed and 3D printed plates were calculated for each material and correspond to 5%, - 7%, 14%, and 1%, and 1%, - 14%, 7%, and - 8% for EVA, EVA/ATH (30 wt.-%), EVA/ATH (65 wt.-%), and EVA/EG (10 wt.-%) respectively. Considering the only slight differences between values (relative error is lower than 15%), the thermocompressed and 3D printed plates can therefore be considered as similar in size. In addition to that, the apparent density difference between thermocompressed and 3D printed plates was estimated for each material studied and corresponds to - 5%, - 11%, - 4%, and - 9% for EVA, EVA/ATH (30 wt.-%), EVA/ATH (65 wt.-%) and EVA/EG (10 wt.-%) respectively. As it was shown above, relative error between thermocompressed and 3D printed plate is lower than 15%, which is considered as acceptable. Therefore, thermocompressed and 3D printed plates are considered quantitatively comparable, whatever the polymeric material studied.

Table A2- 2. Thermocompression vs 3D printing: samples comparison before fire test.

Samples	Mass (g)			Thickness (mm)			Apparent density (kg/m^3)		
	T	3D	Δ%	T	3D	Δ%	T	3D	Δ%
EVA	27.5±0.1	27.9±0.9	1	2.94±0.02	3.1±0.1	5	938±3	890±1	-5
EVA/ATH (30 wt.-%)	35±1	30±5	-14	3.15±0.09	3.02±0.07	-7	1151±43	1026±154	-11
EVA/ATH (65 wt.-%)	44±2	47±4	7	2.9±0.1	3.3±0.3	14	1517±4	1449±14	-4
EVA/EG (10 wt.-%)	30.85±0.01	28.3±0.4	-8	3.099±0.005	3.12±0.01	1	996±1	906±10	-9

© 2020 Tous droits réservés.

lilliad.univ-lille.fr

Based on these results, a morphological analysis was carried out and is presented in the next section.

2.2. Morphological analysis before fire test

Surface and cross section microscopic analyses were carried out on thermocompressed and 3D printed plates using optical microscopy and EPMA observations, following the set-up described in materials & methods part, pages 172 and 173, respectively. The aim of these analyses were to evaluate the morphology differences and examine the flame-retardant repartition and dispersion between the two processes, depending on the materials studied.

2.2.1. Surface characterizations

Thermocompressed and 3D printed plate surfaces were compared by optical microscopy, the resulting pictures are gathered in Figure A2- 2. In each case, the top surfaces of the material look different depending on the formulations and on the process. It is noteworthy the 3D printed plate surfaces are rougher than the thermocompressed ones. This difference is due to the juxtaposition of the filaments deposited at each nozzle passage during 3D printing. The polymer filament diameter was measured for each material studied using optical microscopy (Figure A2- 2) and it is directly linked to the nozzle diameter used for printing. The filaments have indeed diameters of 400 µm, 400 µm and 1000 µm for 3D-EVA, 3D-EVA/ATH (with 30 wt.-% and 65 wt.-%), and 3D-EVA/EG (10 wt.-%) respectively corresponding to the nozzle diameters (see materials & methods part (page 164), Table 31).

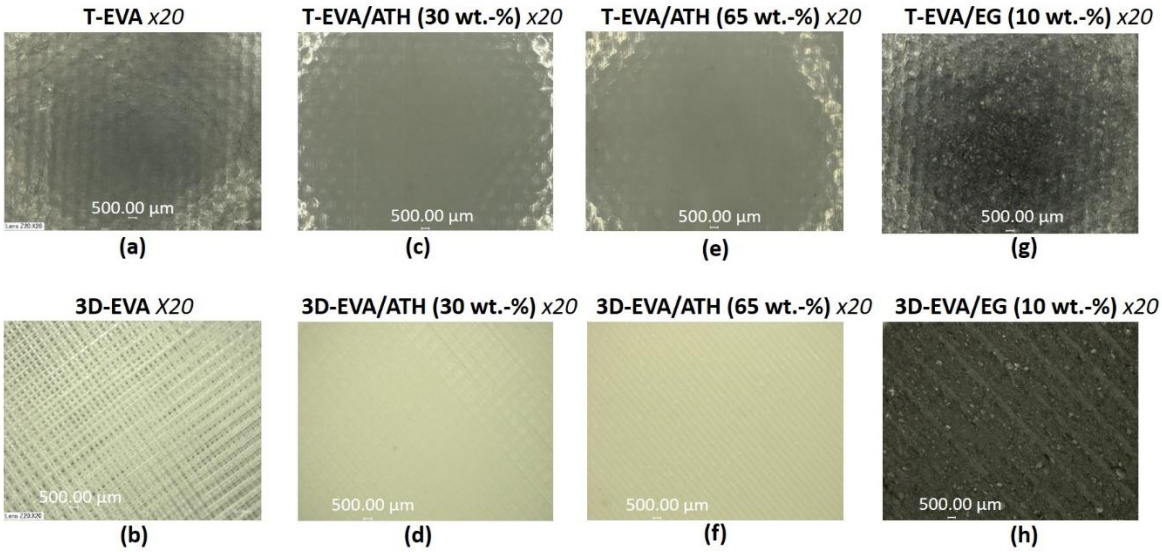

Figure A2- 2. Surface observations of thermocompressed and 3D printed samples using optical microscopy x20 (a) T-EVA, b) 3D-EVA, c) T-EVA/ATH (30 wt.-%), d) 3D-EVA/ATH (30 wt.-%), e) T-EVA/ATH (65 wt.-%), f) 3D-EVA/ATH (65 wt.-%), g) T-EVA/EG (10 wt.-%), h) 3D-EVA/EG (10 wt.-%)).

© 2020 Tous droits réservés.
lilliad.univ-lille.fr

2.2.2. Cross-section analyses

Cross-section observations using optical microscopy and EPMA were carried out on all thermocompressed and 3D printed samples studied (Figure A2- 3, Figure A2- 4, Figure A2- 5, Figure A2- A 1 and Figure A2- A 2), to evaluate and compare the porosity and fillers dispersion. For neat EVA, some small pores are clearly detected in 3D-EVA plates with diameters between 115 and 500 µm, compared to T-EVA, in which no pore can be distinguished (Figure A2- 3 a, Figure A2- 3 b and Figure A2- A 1). For 3D-EVA/ATH (30 wt.-%), small pores with diameters approximatively between 35 and 115 µm are observed (Figure A2- 3 d and Figure A2- A 2), whereas no pores are noticed for T-EVA/ATH (30 wt.-%) (Figure A2- 3 c). With a higher ATH ratio (65 wt.-%), no pores are detected, whatever the shaping process used (T or 3D), as observed in Figure A2- 3 e, Figure A2- 3 f and Figure A2- A 2. This difference between 30 wt.-% and 65 wt.-% filled samples could be explained by the higher density of the material containing the higher ATH amount. Indeed, it is possible to assume that ATH particles (with a quite low diameter (1.5 µm)) collapse pores. Finally, cross section X-Ray mappings in Al element (Figure A2- 4) show that no difference is observed between thermocompressed and 3D printed materials, whatever the ATH ratio used.

Regarding 3D-EVA/EG (10 wt.-%), some small pores with diameters approximatively between 100 and 200 µm are observed (Figure A2- 3 h), whereas no pores are noticed for T-EVA/EG (10 wt.-%) (Figure A2- 3 g). Therefore, in most cases, and as already reported in the literature [270], 3D plates show higher porosity compared to those obtained with the thermocompression process (Figure A2- 3 and Figure A2- A 1 and Figure A2- A 2). This porosity caused with 3D printing shaping process is explained by the thin melting polymer filaments which are deposed successively to form a 3D model.

Moreover, for 3D-EVA/EG (10 wt.-%), 3D-EG particles appear smaller than T-EG particles. Indeed, average length of 3D-EG particles is 116 µm compared to 263 µm for T-EG. This length difference between both shaping process (T vs 3D) could be explained by the second extrusion run. It causes that particles could be cut by shear stresses during extrusion. Moreover, the small nozzle diameter in 3D printing process (1 mm for EVA/EG (10 wt.-%)) could also justify this length difference. On top of that, 3D-EG particles seem to be aligned (Figure A2- 3 h) while to T-EG particles exhibit a random distribution (Figure A2- 3 g). These observations are confirmed by the cross section X-ray mapping of S element in Figure A2- 5. S element was chosen as element to detect in EVA/EG (10 wt.-%) because of the presence of H_2SO_4 and HNO_3 as insertion compounds in expandable graphite. This preferential orientation can be explained

© 2020 Tous droits réservés.

lilliad.univ-lille.fr

by the nozzle moving and the juxtaposition of the filaments deposited at each nozzle passage during the 3D printing.

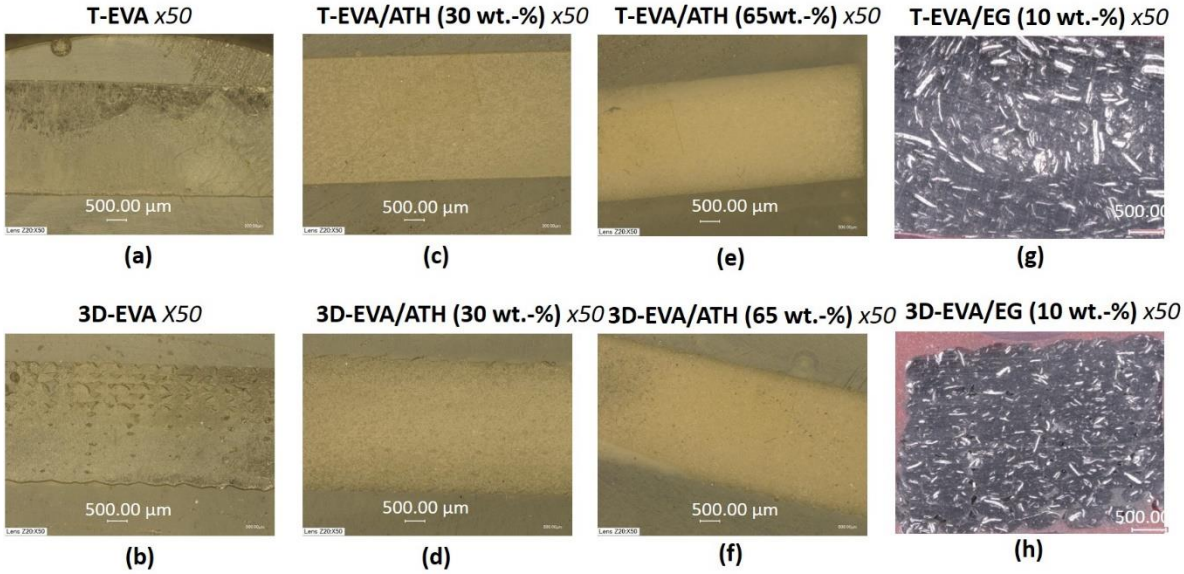

Figure A2- 3. Cross-section observations of thermocompressed and 3D printed samples using optical microscopy x50 (a) T-EVA, b) 3D-EVA, c) T-EVA/ATH (30 wt.-%), d) 3D-EVA/ATH (30 wt.-%), e) T-EVA/ATH (65 wt.-%), f) 3D-EVA/ATH (65 wt.-%), g) T-EVA/EG (10 wt.-%), h) 3D-EVA/EG (10 wt.-%)).

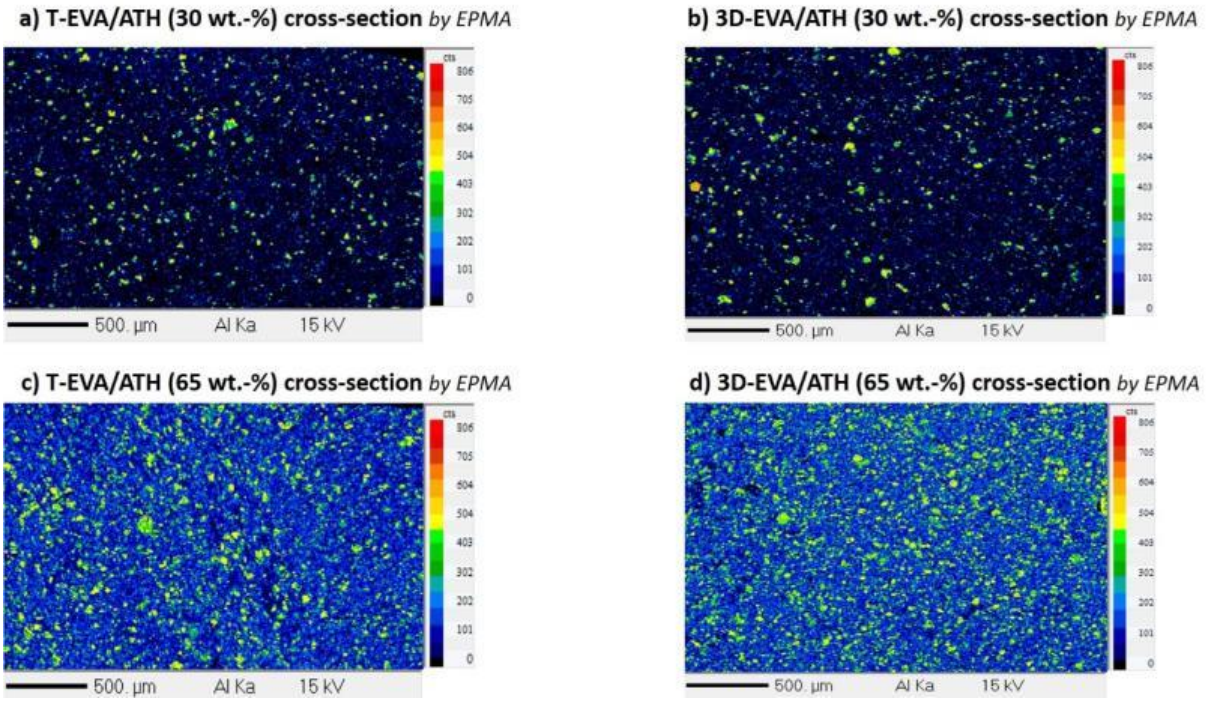

Figure A2- 4. Cross-section X-ray mapping in Al element using EPMA measurements of (a) T-EVA/ATH (30 wt.-%), b) 3D-EVA/ATH (30 wt.-%), c) T-EVA/ATH (65 wt.-%), d) 3D-EVA/ATH (65 wt.-%).

© 2020 Tous droits réservés.
lilliad.univ-lille.fr

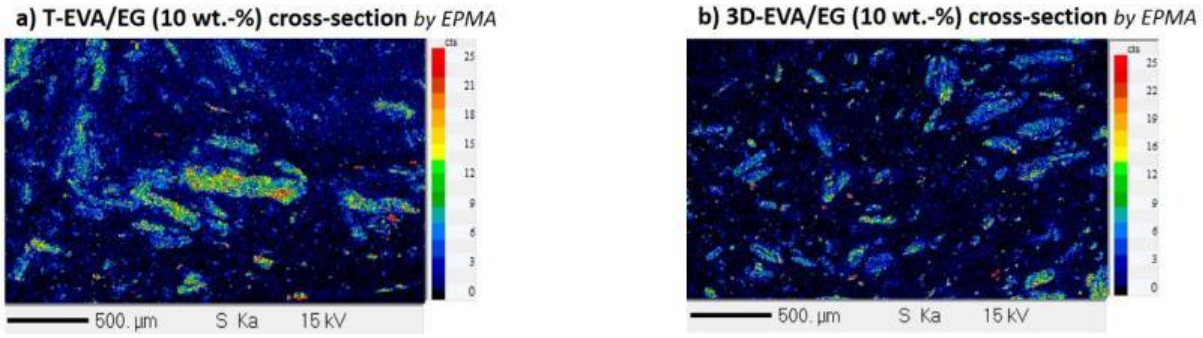

Figure A2- 5. Cross-section X-ray mapping in S element using EPMA measurements of (a) T-EVA/EG (10 wt.-%), b) 3D-EVA/EG (10 wt.-%)).

In the next section the flame retardant properties of 3D printed and thermocompressed samples will be compared.

2.3. Fire behavior

Fire retardant performances of 3D-EVA, 3D-EVA/ATH (30 wt.-%), 3D-EVA/ATH (65 wt.-%), and 3D-EVA/EG (10 wt.-%) were compared to those of T-EVA, T-EVA/ATH (30 wt%), T-EVA/ATH (65 wt.-%), and T-EVA/EG (10 wt.-%)) (Fire testing fully described in materials & methods part (page 170)). Figure A2- 6 and Table A2- 3 report the heat release rate (HRR) curves and the main values measured during the test (TTI, THR, and pHRR) respectively. In all cases, the pHRR and THR are dramatically reduced by the addition of ATH and EG (Figure A2- 6). The highest fire retardant performances are observed with EVA/ATH (65%) (THR and pHRR are reduced by 49 % and 78 % respectively and the TTI is increased by 25 seconds (about 1.6 times longer than neat EVA) compared to neat EVA) and EVA/EG (10 wt.-%) (THR and pHRR are decreased by 17 % and 70 % respectively, in comparison with neat EVA). As regards EVA/ATH (30 wt.-%), a slightly reduction of pHRR (23%) is noticed compared to neat EVA, but no improvement of THR and TTI are observed. For EVA/EG (10 wt.-%), the flame-retardant properties are explained by a physical “worm” expansion, due to the expansion of graphite, as it was expected. Regarding EVA/ATH material, an endothermal dehydration occurs upon heating, leading to the formation of a ceramic-like residue (alumina). A critical amount of ATH is needed to obtain an efficient homogenous residue, which then acts as a fire barrier. This explains why EVA/ATH (65 wt.-%) shows higher fire retardant performances than EVA/ATH (30 wt.-%).

Moreover, whatever the shaping process (thermocompression or 3D printing), EVA (Figure A2- 6 a), EVA/ATH (30 wt.-%) (Figure A2- 6 b) and EVA/ATH (65 wt.-%) (Figure A2- 6 c) have similar fire behavior. The THR difference between thermocompressed and 3D printed

© 2020 Tous droits réservés.

lilliad.univ-lille.fr

plates corresponds to only 3 %, - 12 % and 8 % (2 MJ/m^2, 9 MJ/m^2 and 3 MJ/m^2), for EVA, EVA/ATH (30 wt.-%) and EVA/ATH (65 wt.-%) respectively: it lies in the margin of errors and they cannot be considered as significant. In the same manner, pHRR differences between thermocompressed and 3D printed plates are quite small (37 kW/m² for EVA, 38 kW/m^2 for EVA/ATH (30 wt.-%) and 12 kW/m² for EVA-ATH (65 wt.-%) (also in the margin of error: - 7 % - 9 % and - 11%). Therefore, it can be concluded that shaping process has no particular influence on fire behavior for these two matrices. However, for EVA/EG (10 wt.-%), differences are noticeable: thermocompressed plates show improved flame retardant properties compared to the 3D shaped ones. THR difference between thermocompressed and 3D printed plates is indeed 12 MJ/m^2, corresponding to 19 % difference. Moreover, the pHRR difference for the same formulation is 61 kW/m^2 (i.e. 39 %). Regarding the ignition time, it is quite similar between thermocompressed and 3D printed plates, whatever the materials studied (Table A2-3).

To sum up the fire behavior, the TTI is roughly equivalent between samples studied. However, even if the TTI difference is negligible, it noteworthy that the TTI of 3D printed plates is always shorter than for thermocompressed plates (as noted in other studies in part 2 chapter 1 [146], [147]). THR and pHRR are similar between thermocompressed and 3D printed plates except for EVA/EG (10 wt.-%). Indeed, in this case, 3D printing process impairs fire properties, as pHRR and THR both increase (+ 39 % and + 19 %) for the 3D printed samples.

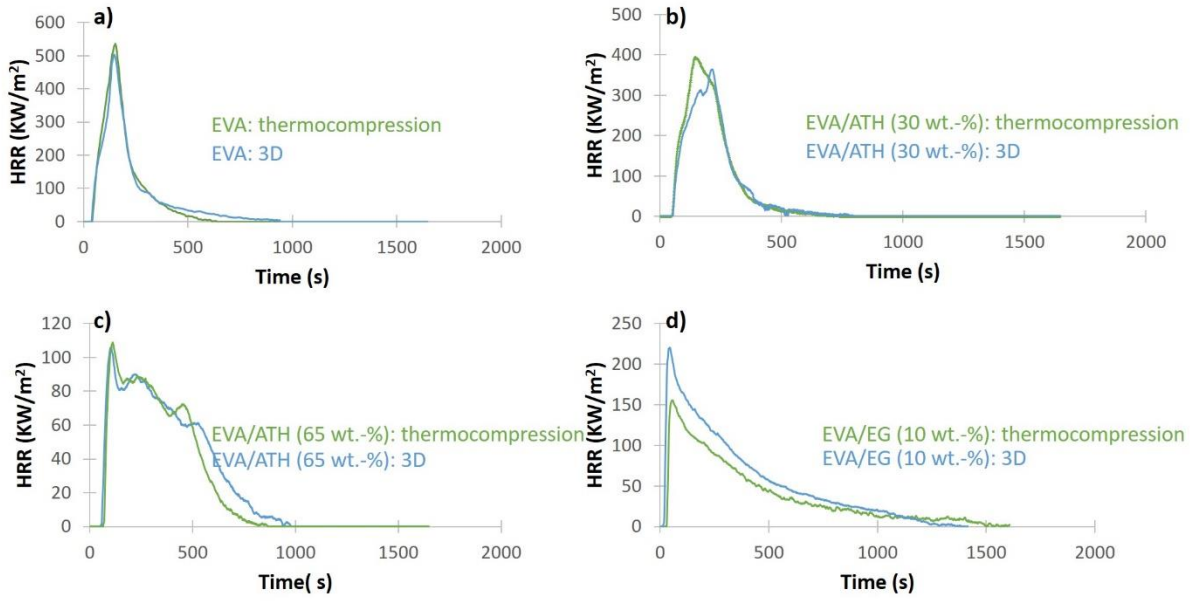

Figure A2- 6. Fire behavior comparison between thermocompression and 3D printing process (a) EVA, b) EVA/ATH (30 wt.-%), EVA/ATH (65 wt.-%), d) EVA/EG (10 wt.-%)).

© 2020 Tous droits réservés.
lilliad.univ-lille.fr

Table A2- 3. Comparison of MLCC results between thermocompression and 3D printing depending on the polymer materials' studied.

Samples	Ignition time (s)			THR (MJ/m²)			pHRR (kW/m²)		
	T	3D	Δ%	T	3D	Δ%	T	3D	Δ%
EVA	40 ± 0	35 ± 4	-13	76 ± 6	78 ± 5	3	519 ± 26	482 ± 31	-7
EVA/ATH (30 wt.-%)	37 ± 4	31 ± 5	-16	77 ± 4	68 ± 12	-12	401 ± 15	363 ± 18	-9
EVA/ATH (65 wt.-%)	65 ± 5	58 ± 4	-11	39 ± 0.1	42 ± 2	8	113 ± 5	101 ± 10	-11
EVA/EG (10 wt.-%)	21 ± 2	18 ± 1	-14	63 ± 5	75 ± 2	19	156.0 ± 0.2	217 ± 4	39

Pictures of the residues obtained after MLC testing are gathered in Figure A2- 7. For each system, and whatever the shaping process, residues have the same visual aspect. EVA burns completely and does not yield any residue. For EVA/ATH (30 wt.-%) and EVA/ATH (65 wt.-%) samples, a ceramised residue is obtained with similar visual aspect (Figure A2- 7), regardless the shaping process. Same conclusion can be made regarding the visual aspect of EVA/EG (10 wt.-%) residues. Indeed, a "worm-like" expansion occurs in both cases. Therefore, shaping process (thermocompression vs 3D printing) has no influence on the visual aspect of the residue for each polymer matrix studied.

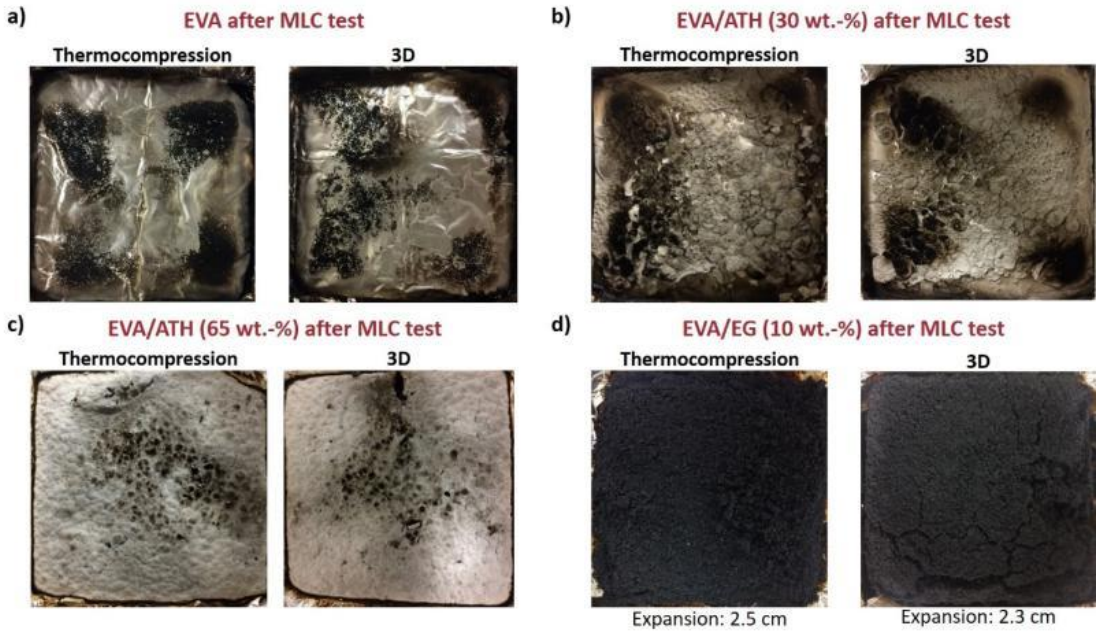

Figure A2- 7. Visual aspect of residues after MLCC test for (a) EVA, b) EVA/ATH (30 wt.-%), c) EVA/ATH (65 wt.-%), and d) EVA/EG (10 wt.-%)).

© 2020 Tous droits réservés.

lilliad.univ-lille.fr

During MLC experiment, the residual weight after fire test was also measured for each sample and results are presented in Table A2- 4. For EVA and EVA/ATH (30 wt.-%), the same residual weight is obtained, whatever the shaping process used. But, for EVA/ATH (65 wt.-%) and EVA/EG (10 wt.-%) a difference is measured between thermocompressed and 3D printed plates. This difference reaches 4 % between T-EVA/ATH (65 wt.-%) and 3D-EVA/ATH (65 wt.-%) (which is considered as negligible) and 42 % between T-EVA/EG (10 wt.-%) and 3D-EVA/EG (10 wt.-%). This residual mass difference after fire test is related to the difference observed in term of fire retardant performance between 3D and thermocompressed plates, as previously highlighted.

Table A2- 4. Comparison of residual mass after MLCC test for thermocompressed and 3D printed plates.

Samples	Residual weight (g)	Residual weight/initial weight (%)	Δ Residual mass (thermocompressed vs 3D) (%)
T-EVA	0	0	0
3D-EVA	0	0	
T-EVA/ATH (30 wt.-%)	6.8 ± 0.3	19	0
3D-EVA/ATH (30 wt.-%)	6 ± 1	19	
T-EVA/ATH (65 wt.-%)	22.4 ± 0.9	49	4
3D-EVA/ATH (65 wt.-%)	21.2 ± 1.9	47	
T-EVA/EG (10 wt.-%)	7.3 ± 0.09	24	42
3D-EVA/EG (10 wt.-%)	3.9 ± 0.08	14	

Figure A2- 8 summarizes the thermal behavior of the different materials. EVA, EVA/ATH (30 wt.-%) and (65 wt.-%) show the same thermal behavior (and same residual aspect and mass), no matter the shaping process used. When EVA undergoes radiative heating (MLC test), the polymer melts immediately (pores which were created by 3D printing collapse) and burns (Figure A2- 8 a) or ceramizes (if containing ATH) (Figure A2- 8 b). For EVA/EG (10 wt.-%), the fire behavior is worse for 3D printed plates than for thermocompressed ones. The differences between 3D and T-EVA/EG (10 wt.-%) materials could be explained by three-

© 2020 Tous droits réservés.
lilliad.univ-lille.fr

factors: (1) the EG particles size, lower after 3D printing. These smaller EG particles lead to lower graphite expansion [271], to a less cohesive entangled network and thus to lower thermal protective performances (Figure A2- 8 c); (2) the higher porosity observed in the 3D printed materials might also decrease the cohesion of the entangled network, thus damaging the fire protective properties of 3D-materials compared to T-materials; (3) Finally, it was previously reported that 3D-EG particles have a preferential orientation, leading to an anisotropic material (Figure A2- 9 b), compared to an isotropic thermocompressed one (Figure A2- 9 a) [272]. This morphological difference could also partly explain the lower thermal protective performance of 3D-EVA/EG (10 wt.-%). Indeed, when the physical "worm" expansion occurs, it is assumed that graphite expansion differs depending on the EG orientation. Moreover, influence of the first factor (higher porosity of 3D sample) on the thermal behavior is confirmed by the thermal conductivities (following the set-up described in materials & methods part (page 175)) of T-EVA/EG (10 wt.-%) and 3D-EVA/EG (10 wt.-%) equal to 0.451 ± 0.002 W/mK and to 0.241 ± 0.001 W/mK respectively. Thus, the thermal conductivity of the 3D sample is divided per almost two compared to that of thermocompressed one. This result makes sense because of the low thermal conductivity of gases (encapsulated air): the higher the porosity, the lower the thermal conductivity [273]. Therefore, based on these three hypotheses, the entangled network is differently organized in both cases, which could explain the thermal behavior differences.

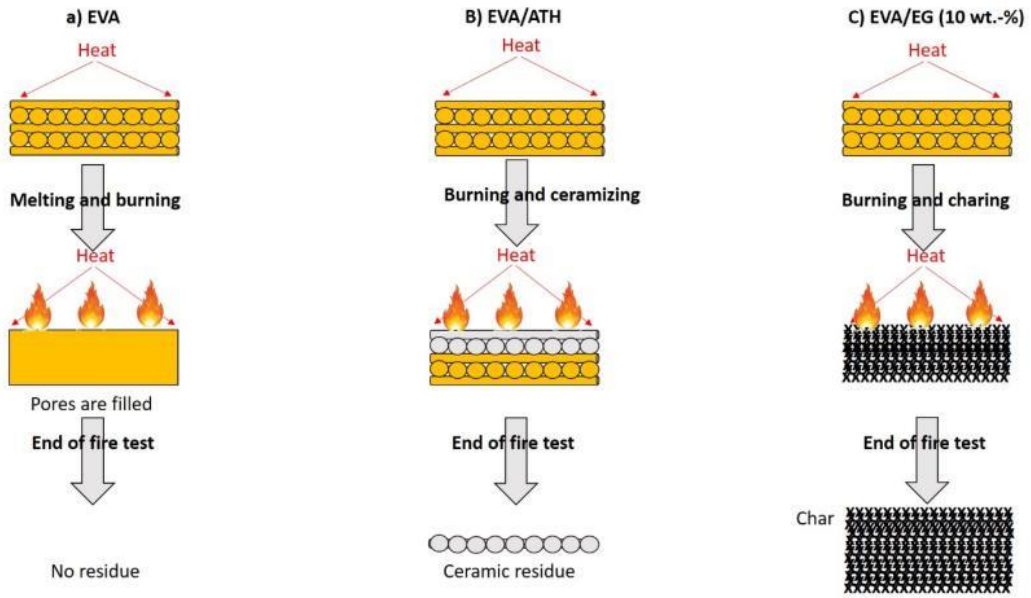

Figure A2- 8. Illustration of the 3D printed polymer matrices thermal behavior (a) EVA, b) EVA/ATH, c) EVA/EG (10 wt.-%)).

© 2020 Tous droits réservés.

lilliad.univ-lille.fr

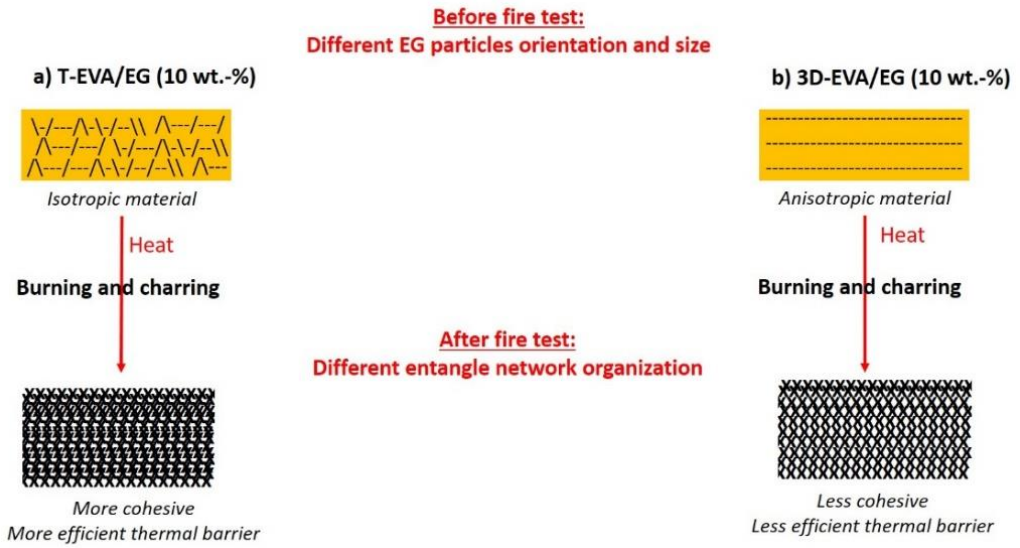

Figure A2- 9. Illustration of EVA/EG (10 wt.-%) thermal behavior (a) Thermocompressed plates, b) 3D printed plates).

3. Conclusion

This work compared two shaping process, i.e. thermocompression and 3D fused polymer deposition technique, to design flame retardant systems. Results show that it is possible to design flame retardant matrices by 3D printing, and that their fire behavior is not particularly affected by the shaping process. The porosity inherent to the successive filaments deposition during the 3D printing process has no influence on the burning mechanism of the EVA and EVA/ATH polymer matrices studied. However, the porosity combined with the nozzle size and "re-extrusion" of the filaments inside the 3D printer can have some harmful influence on some flame retardant fillers, such as expandable graphite. For example, the smaller size of the EG particles as well as the horizontal preferential orientation induced by filaments deposition, lead to decreased fire-retardant properties of the 3D printed plates compared to thermocompressed ones.

This work considered as a preliminary study opens up the fields of possibilities about the use of 3D printing in flame retardancy field.

© 2020 Tous droits réservés.
lilliad.univ-lille.fr

Appendix – Appendix 1

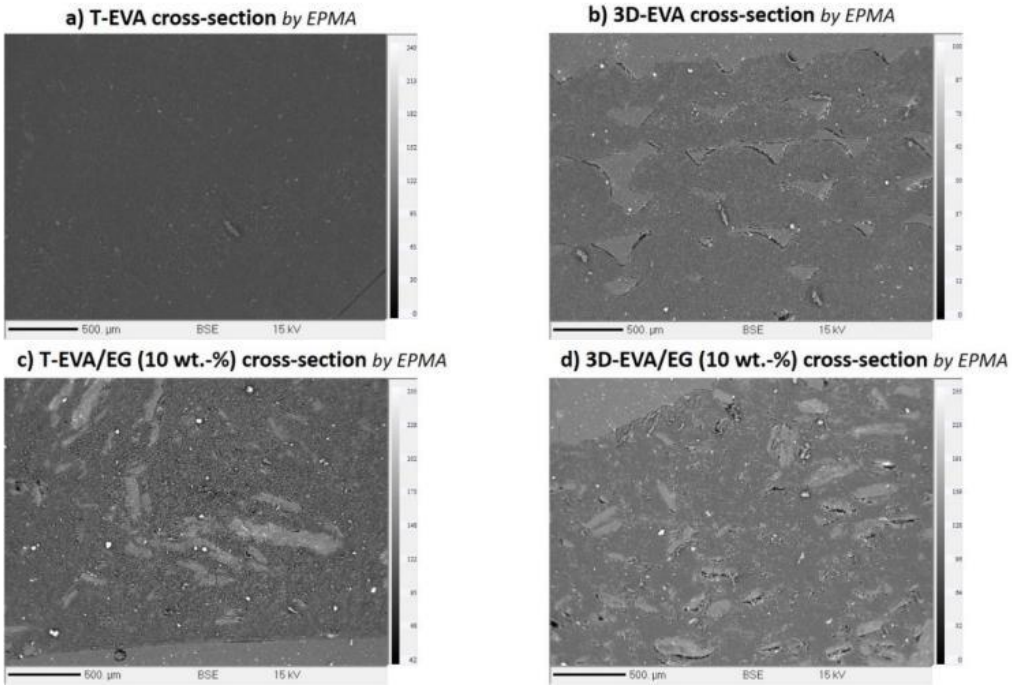

Figure A2- A 1. EPMA cross-section observations (a)T-EVA, b) 3D-EVA, c) T-EVA/EG (10%), d) 3D-EVA/EG (10%)).

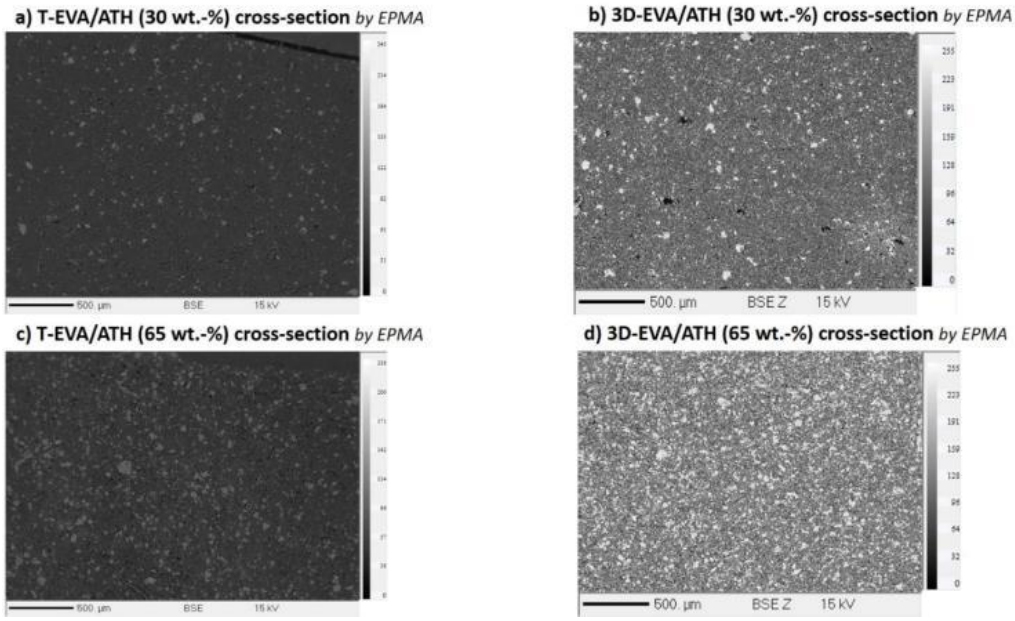

Figure A2- A 2. EPMA cross-section observation (a) T-EVA/ATH (30%), b) 3D-EVA/ATH (30%), c) T-EVA/ATH (65%), d) 3D-EVA/ATH (65%)).

© 2020 Tous droits réservés.

lilliad.univ-lille.fr

Appendix 3 – Part 2, chapter 3

Table A3- 1. Fire protection performances values of each system studied.

Polymer matrix	TTI (s)	THR (MJ/m²)	pHRR (kW/m²)
3D-air	26 ± 1	49.4 ± 0.3	225 ± 13
3D-$K_2CO_{3\ sat.-liquid}$	34 ± 6 (x1.3)	18 ± 1 (-63%)	52 ± 4 (-77%)
3D-H A	168 ± 6 (x6.5)	57 ± 2 (16%)	253 ± 5 (-12%)
3D-H A+VMT	196 ± 2 (x7.5)	46 ± 1 (-2%)	203 ± 7 (-15%)
3D-H A +VMT+K_2CO_3	50 ± 6 (x1.9)	5.65 ± 0.09 (-88%)	32 ± 1 (-86%)
3D-H B	74 ± 6 (x2.8)	63 ± 4 (28%)	226 ± 6 (0.4%)
3D-H B+VMT	31 ± 2 (x1.2)	7.1 ± 0.3 (-86%)	81 ± 3 (-64%)
3D-H C	26.5 ± 0.7 (x1)	48 ± 5 (-2%)	219 ± 4 (-3%)
3D-H C+VMT	38 ± 6 (x1.5)	9.5 ± 0.2 (-82%)	144 ± 5 (-36%)

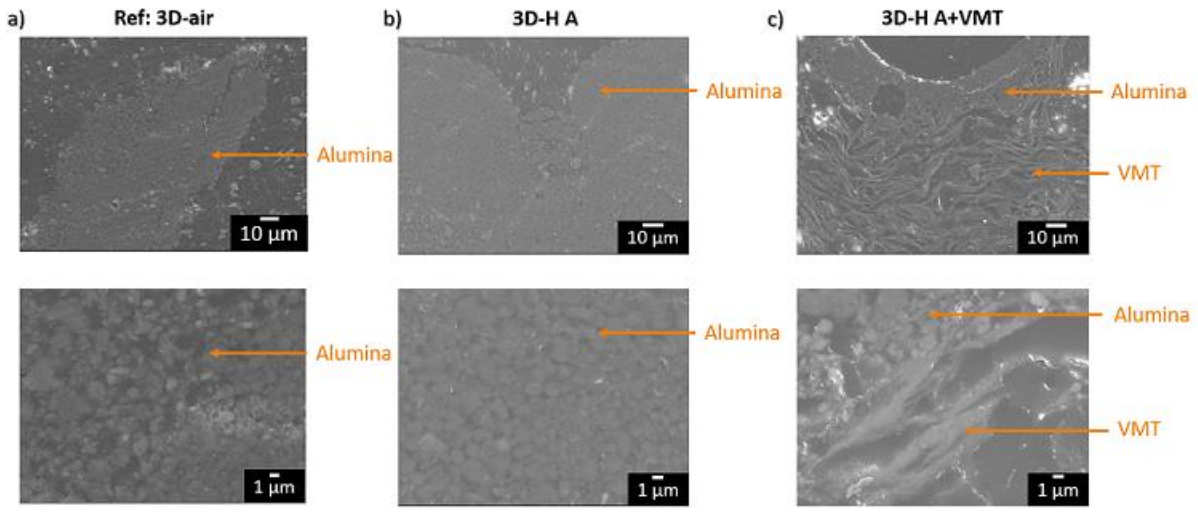

Figure A3- 1. Cross-section of (a) 3D-air, b) 3D-H A and c) 3D-H A+VMT), using SEM observation.

© 2020 Tous droits réservés.
lilliad.univ-lille.fr

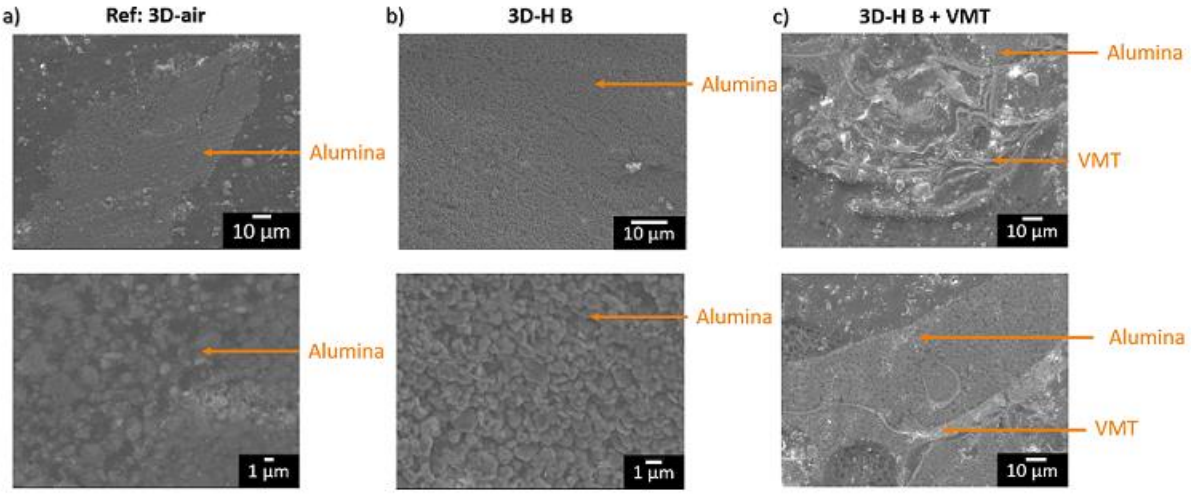

Figure A3- 2. Cross-section of (a) 3D-air, b) 3D-H B and c) 3D-H B+VMT), using SEM observation.

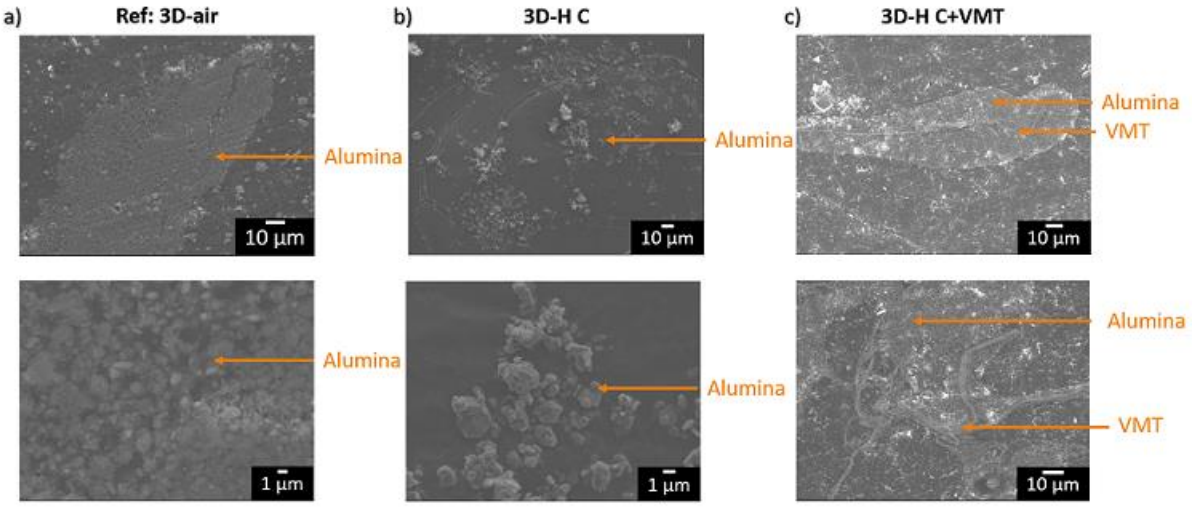

Figure A3- 3. Cross-section of (a) 3D-air, b) 3D-H C and c) 3D-H C+VMT), using SEM observation.

© 2020 Tous droits réservés.

lilliad.univ-lille.fr

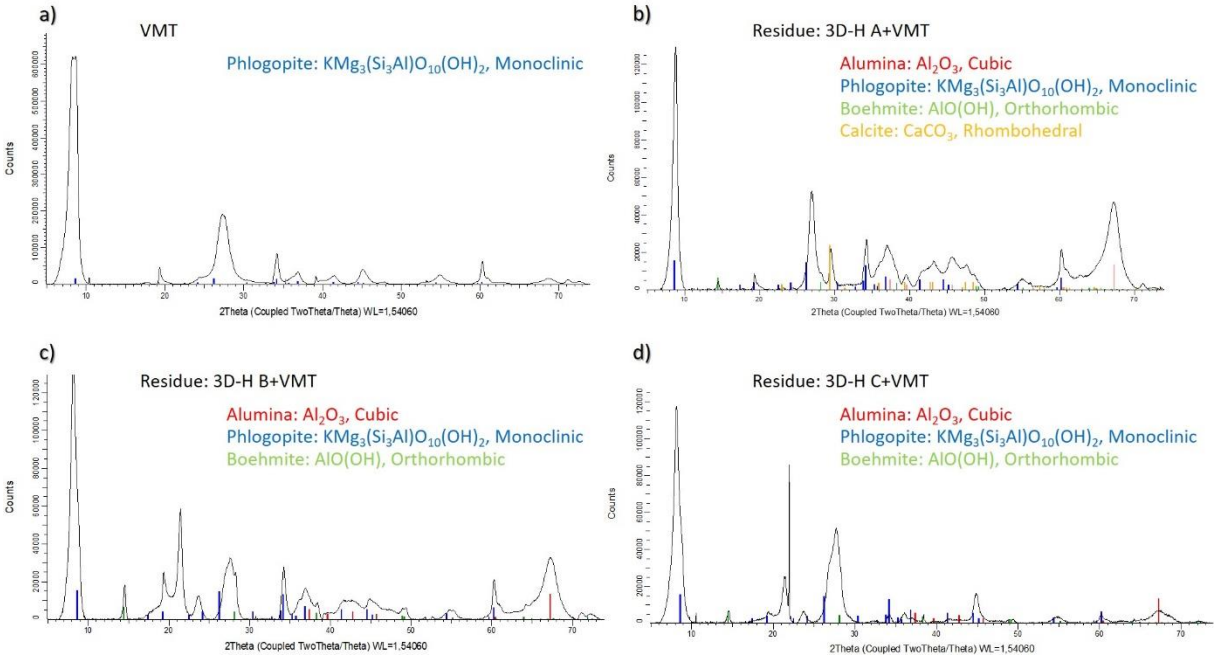

Figure A3- 4. XRD of (a) VMT, b) residue 3D-H A+VMT, c) residue 3D-H B+VMT, d) residue 3D-H C+VMT).

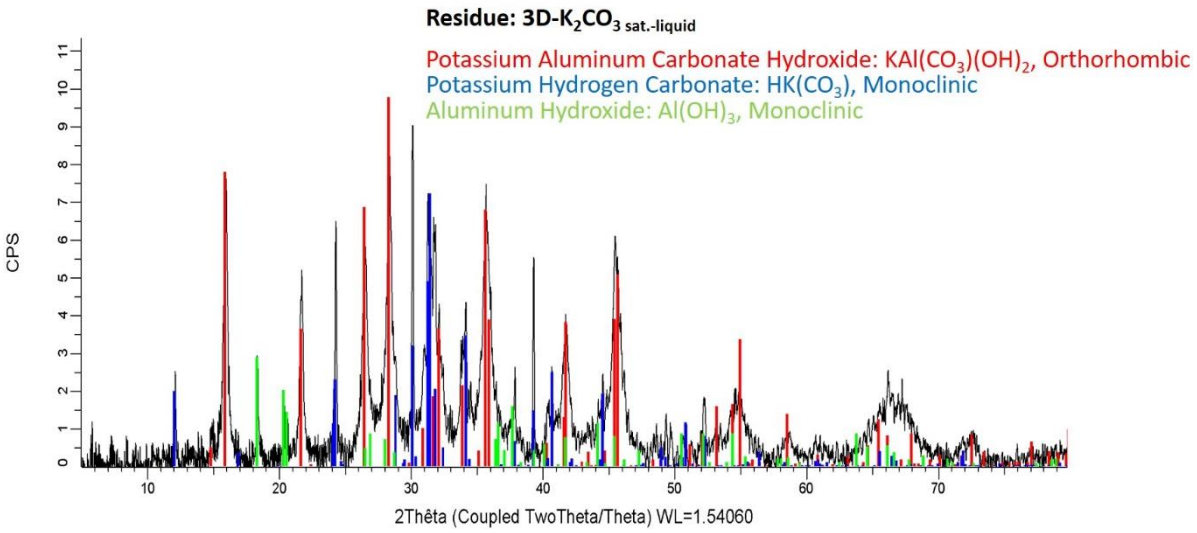

Figure A3- 5. XRD of residue 3D-K_2CO_3 sat.-liquid.

© 2020 Tous droits réservés.
lilliad.univ-lille.fr

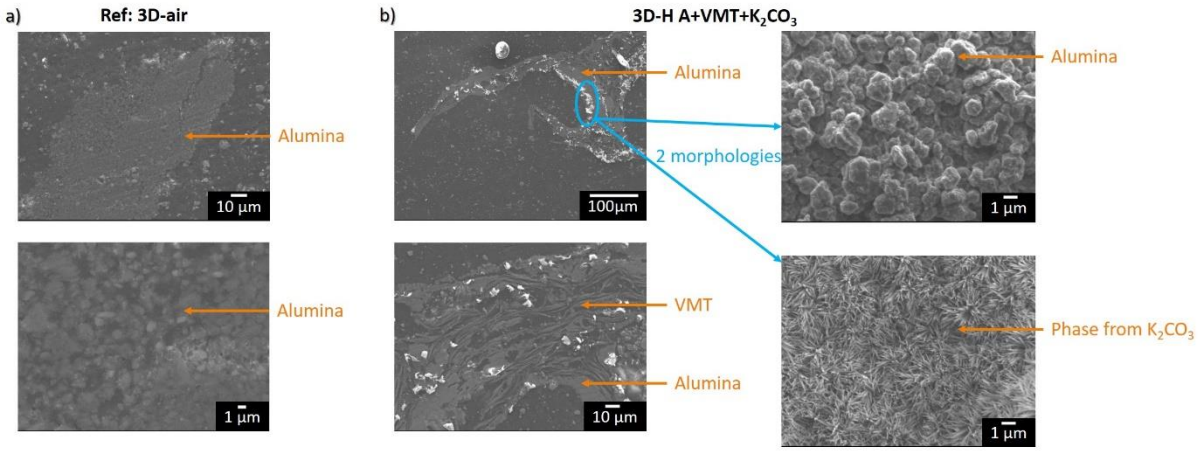

Figure A3- 6. Cross-section of (a) 3D-air, b) 3D-H A+VMT+K_2CO_3), using SEM observation.

© 2020 Tous droits réservés.

lilliad.univ-lille.fr

Appendix 4 – Part 3, chapter 2

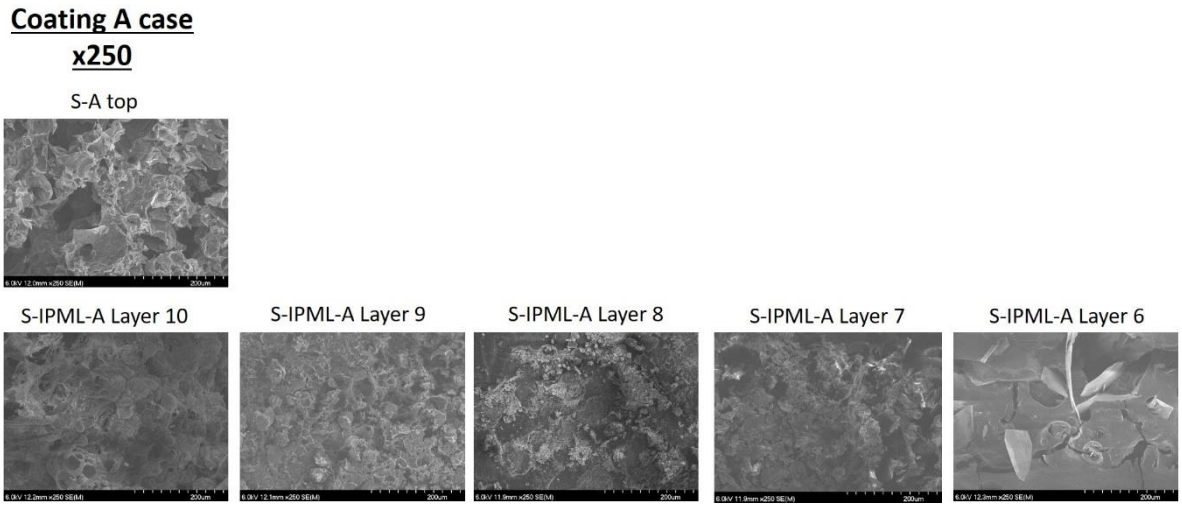

Figure A4- 1. SEM pictures comparing S-A char to S-IPML-A chars (taken from layers 10 to 6).

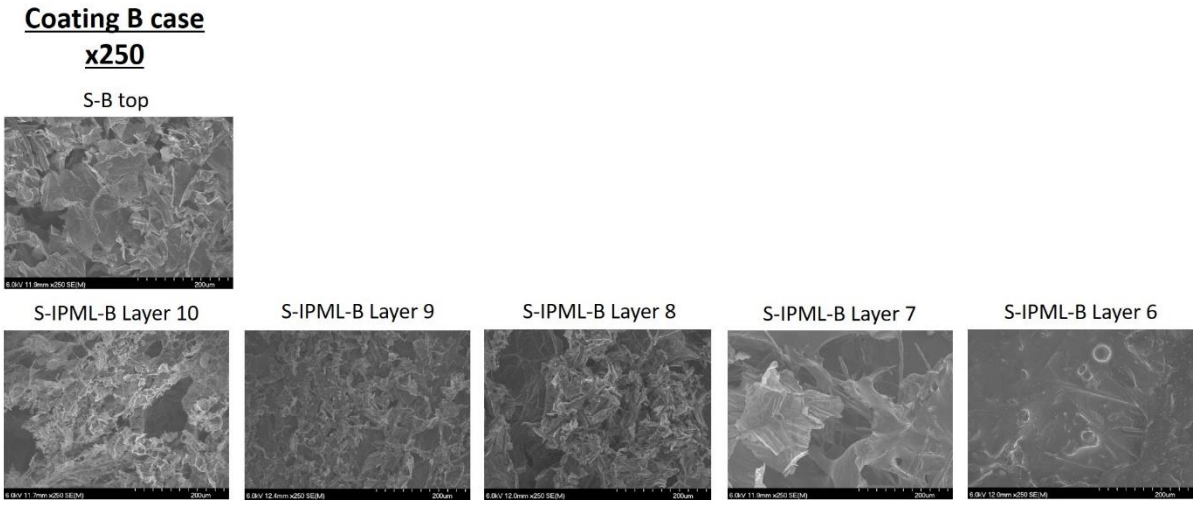

Figure A4- 2. SEM pictures comparing S-B char to S-IPML-B chars (taken from layers 10 to 6).

© 2020 Tous droits réservés.
lilliad.univ-lille.fr

Appendix 5 – Part 3, chapter 3

In addition to this work, an optimization of the IBPML design elaborated in part 3 chapter 3 was tested to try to reduce the steady state temperature reached at the end of the fire testing. The objective was to maintain the reduction of heat propagation at the beginning, and at the same time reduce the temperature reached at the end of fire exposure. The strategy to reach this goal was to replace aluminum foils by another material with high or low thermal conductivity such as copper and mica foils (Figure A5- 1), respectively. Thus, samples studied were named S-AlA+AlB, S-MiA+MiB and S-CuA+CuB. By this approach, a heat dissipater (copper) or an insulator (mica) material is tested, and may give more information of the best assembly for having the best fire protection performances.

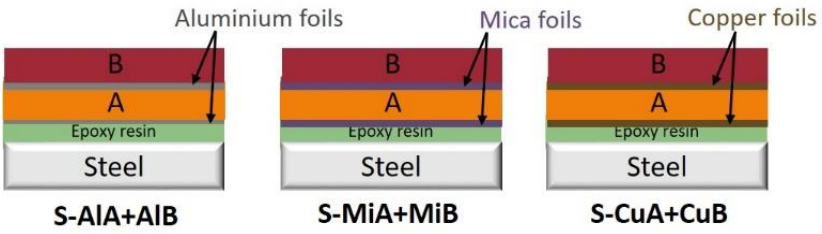

Figure A5- 1. Illustration of samples studied.

To design S-MiA+MiB and S-CuA+CuB, the same process as that used for S-AlA+AlB is employed (described in materials & methods part (page 177)). The only difference is that aluminum foils used for S-AlA+S-AlB is substituted by copper and mica foils for S-CuA+CuB and S-MiA+MiB, respectively. Cross-section pictures of S-AlA+AlB, S-CuA+CuB and S-MiA+MiB, were observed using optical microscopy (Figure A5- 2).Figure A5- 2, reveals that no bubble or void is observed between coating A, coating B and metal foils (aluminum, copper, mica foils for Figure A5- 2 a, Figure A5- 2 b and Figure A5- 2 c, respectively). The adhesion between layers is homogeneous regardless the metal foils used. Moreover, the coating A and coating B thicknesses are globally the same for each sample observed and the average corresponds to 740 µm and 650 µm, respectively.

© 2020 Tous droits réservés.

lilliad.univ-lille.fr

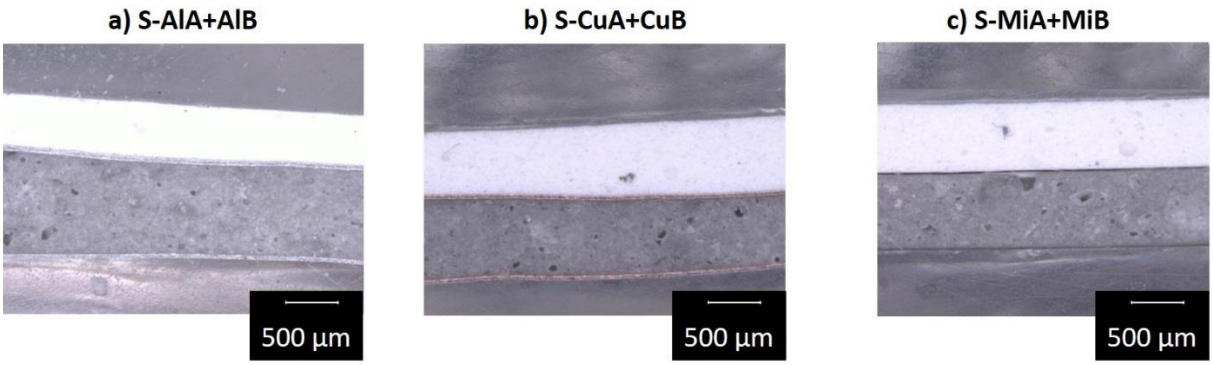

Figure A5- 2. Optical microscopy before fire testing of a) S-AlA+AlB, b) S-CuA-CuB, c) S-MiA+MiB.

Temperature evolution versus time was shown on Figure A5- 3. Replacing aluminum by copper or mica does not allow to significantly reduce the temperature evolution versus time at the backside of the steel plate. Indeed, the temperature evolution of S-AlA+AlB, S-CuA+CuB and S-MiA+MiB is rather the same with a low temperature rise from the beginning to 5 min, with a slope almost equal at 12°C/min, from 2 to 4 min. After 5 min fire exposure, no stabilization occurs, and temperature still increases to reach a temperature around 270°C, after 30 min fire exposure. Therefore, the modification of aluminum with copper or mica does not allow to significantly improve the fire protection performances, nor to stabilize the temperature evolution at the end of the test. Therefore, it is possible to conclude that the thermal conductivity of interlayer materials has not a significant influence in term of temperature rise during the fire exposure.

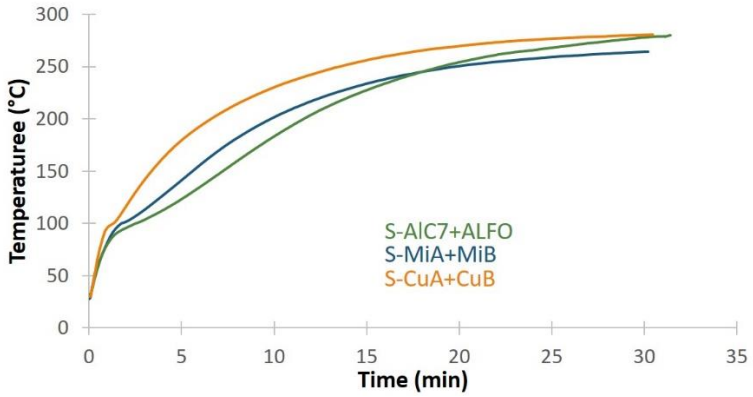

Figure A5- 3. Fire behavior of system with other interlayer materials.

© 2020 Tous droits réservés.
lilliad.univ-lille.fr

Appendix 6 – Part 3, chapter 4

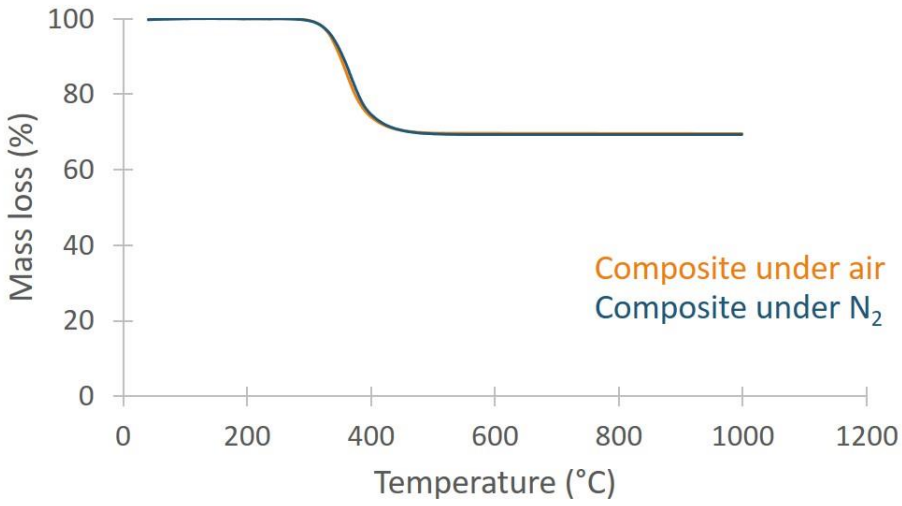

Figure A6- 1. TGA of composite under air and N_2.

© 2020 Tous droits réservés.

lilliad.univ-lille.fr

References

[1] M.-Y. Lyu and T. G. Choi, "Research trends in polymer materials for use in lightweight vehicles," *Int. J. Precis. Eng. Manuf.*, vol. 16, pp. 213–220, 2015.

[2] A. Dessarthe, "Usinage des polymères," *Tech. l'ingénieur*, 1998.

[3] C. Vagner, M. Cochez, H. Vahabi, and M. Ferriol, "Chimie de la combustion des polymères et ignifugation," *Tech. l'ingénieur*, 2016.

[4] C. Vovelle and J. L. Delfau, "Combustion des plastiques," *Tech. l'ingénieur*, 1997.

[5] T. R. Hull and A. A. Stec, "Polymers and fire," in *Fire Retardancy of Polymers: new Strategies and Mechanisms*, 2009, pp. 1–14.

[6] J. Lentini, "Chapter 2 - The Chemistry and Physics of Combustion," in *Scientific Protocols for Fire Investigation*, Protocols., 2012, pp. 50–58.

[7] S. Boryniec and W. Pzrygocki, "Polymer combustion processes. 3. Flame Retardants for Polymeric Materials," *Prog. Rubber, Plast. Recycl. Technol.*, 2001.

[8] T. Kashiwagi, "Polymer combustion and flammability - Role of the condensed phase," *Symp. Combust.*, vol. 25, no. 1, pp. 1423–1437, 1994.

[9] W. Yong, I. Burgess, and F. Wald, "Chapter 5 - Material Properties," in *Performance-Based Fire Engineering of Structures*, 2012, pp. 132–140.

[10] M. Lackner, F. Winter, and A. K. Agarwal, *Handbook of Combustion, Volume 5*. 2010.

[11] S. B. C. Chlon, S. Piquet, "Le projet de recherche 'FireBar-Concept' lauréat de l' ERC Advanced Grant," 2015.

[12] "World Fire Statistics," *CTIF Center of Fire Statistics*, 2017. [Online]. Available: https://www.ctif.org/world-fire-statistics.

[13] Colin Todd, "Legislation, guidance and enforcing authorities relevant to fire safety measures at Grenfell tower," 2018.

[14] J. Watts, "Amazon rainforest fires: global leaders urged to divert Brazil from 'suicide path," *The Guardian*, 2019. [Online]. Available: https://www.theguardian.com/environment/2019/aug/23/amazon-fires-global-leaders-urged-divert-brazil-suicide-path.

[15] "Notre-Dame: Massive fire ravages Paris cathedral," *BBC news*, 2019. [Online]. Available: https://www.bbc.com/news/world-europe-47941794.

[16] S. T. Lazar, T. J. Kolibaba, and J. C. Grunlan, "Flame-retardant surface treatments," *Nat. Rev. Mater.*, 2020.

[17] W. E. Wilson, J. Fristom, and R. M. Fristrom, "Radicals in flame," *APL Tech. Dig.*, vol. 2, pp. 10–15, 1963.

[18] Ian Sutton, "Chapter 12 Firefighting," in *Plant Design and Operation (Second Edition)*, 2017, pp. 353–379.

© 2020 Tous droits réservés.
lilliad.univ-lille.fr

Thèse de Laura Geoffroy, Université de Lille, 2020

[19] Frank Lees, "Chapter 16 - Fire," in *Less'Loss Prevention in the Process Industries (Third Edition)*, 2005, pp. 1–16.

[20] P. Cancelliere, "Design of oxygen reduction systems in active fire protection," in *SFPE conference Fire Safety Engineering*, 2018.

[21] B. Schartel, C. A. Wilkie, and G. Camino, "Recommendations on the scientific approach to polymer flame retardancy: Part 1—Scientific terms and methods," *J. Fire Sci.*, vol. 34, no. 6, pp. 447–467, 2016.

[22] Global, "Fire Resistance and Reaction to Fire," *IFSEC Global*, 2008. [Online]. Available: https://www.ifsecglobal.com/uncategorized/fire-resistance-and-reaction-to-fire/.

[23] E. D. Weil, "Fire-Protective and Flame-Retardant Coatings - A State-of-the-Art Review," *J. Fire Sci.*, vol. 29, no. 3, pp. 259–296, 2011.

[24] J. Alongi, Z. Han, and S. Bourbigot, "Intumescence: Tradition versus novelty. A comprehensive review," *Prog. Polym. Sci.*, vol. 51, pp. 28–73, 2014.

[25] X. H. Dai, Y. C. Ã. Wang, and C. G. Bailey, "Effects of partial fire protection on temperature developments in steel joints protected by intumescent coating," *Fire Saf. J.*, vol. 44, pp. 376–386, 2009.

[26] K. Petersen, K. Dam-johansen, P. Català, and S. Kiil, "Investigation of char strength and expansion properties of an intumescent coating exposed to rapid heating rates," *Prog. Org. Coatings*, vol. 76, no. 12, pp. 1851–1857, 2013.

[27] R. G. Puri and A. S. Khanna, "Intumescent coatings : A review on recent progress," *J. Coatings Technol. Res.*, vol. 14, pp. 1–20, 2016.

[28] T. Mariappan, "Recent developments of intumescent fire protection coatings for structural steel : A review," *J. fire*, vol. 34 (2), pp. 120–163, 2016.

[29] N. Didane, S. Giraud, E. Devaux, G. Lemort, and G. Capon, "Thermal and fire resistance of fibrous materials made by PET containing flame retardant agents," *Polym. Degrad. Stab.*, vol. 97, no. 12, pp. 2545–2551, 2012.

[30] N. Didane, S. Giraud, E. Devaux, and G. Lemort, "Development of fire resistant PET fibrous structures based on phosphinate-POSS blends," *Polym. Degrad. Stab.*, vol. 97, no. 6, pp. 879–885, 2012.

[31] D.-Y. Wang, *Novel Fire Retardant polymers and Composite Materials*, Elsevier S. 2016.

[32] G. A. Mouritz AP, "Fire properties of polymer composite materials," *Solid Mech. Its Appl.*, vol. 143, 2006.

[33] S. Bourbigot and S. Duquesne, "Fire retardant polymers: recent developments and opportunities," *J. Mater. Chem.*, vol. 17, no. 22, pp. 2283–2300, 2007.

[34] S. Bourbigot, M. Lebras, S. Duquesne, and M. Rochery, "Recent Advances for Intumescent Polymers," *Macromol. Mater. Eng.*, vol. 289, no. 6, pp. 499–511, 2004.

[35] K. A. Salmeia, J. Fage, S. Liang, and S. Gaan, "An Overview of Mode of Action and Analytical Methods for Evaluation of Gas Phase Activities of Flame Retardants," *Polymers (Basel).*, vol. 7, pp. 504–526, 2015.

© 2020 Tous droits réservés.

lilliad.univ-lille.fr

[36] S. D. Shaw *et al.*, "Halogenated Flame Retardants: Do the Fire Safety Benefits Justify the Risks ?," *Rev. Enciron. Heal.*, vol. 25, no. 4, pp. 261–305, 2010.

[37] B. Schartel, "Phosphorus-based Flame Retardancy Mechanisms- Old Hat or a Starting Point for Future Development ?," *Mater.*, vol. 3, no. 10, pp. 4710–4745, 2010.

[38] K. A. Salmeia, S. Gaan, and G. Malucelli, "Recent Advances for Flame Retardancy of Textiles Based on Phosphorus Chemistry," *Polymers (Basel).*, vol. 8, no. 319, pp. 1–36, 2016.

[39] M. M. Velencoso, A. Battig, J. C. Markwart, B. Schartel, and F. R. Wurm, "Molecular Firefighting—How Modern Phosphorus Chemistry Can Help Solve the Challenge of Flame Retardancy," *Angew Chem Int Ed Engl*, vol. 57, no. 33, pp. 10450–10467, 2018.

[40] B. Schartel, C. Wilkie, and G. Camino, "Recommendations on the scientific approach to polymer flame retardancy: Part 2--Concepts," *J. Fire Sci.*, vol. 35, no. 1, pp. 3–20, 2016.

[41] M. Klatt, "Nitrogen-Based Flame Retardants," in *Non-Halogenated Flame Retardant Handbook*, 2014.

[42] H. Horacek and R. Grabner, "Advantages of flame retardants based on nitrogen compounds," *Polym. Degrad. Stab.*, vol. 54, no. 2–3, pp. 205–215, 1996.

[43] T. Ishii, H. Kokaku, and A. Nagai, "Calcium Borate Flame Retardation System for Epoxy Molding Compounds," *Polym. Eng. Sci.*, pp. 800–8006, 2006.

[44] M. Dogan and S. M. Unlu, "Flame retardant effect of boron compounds on red phosphorus containing epoxy resins," *Polym. Degrad. Stab.*, vol. 99, pp. 12–17, 2014.

[45] X. Zhang, Q. Shen, X. Zhang, H. Pan, and Y. Lu, "Graphene oxide-filled multilayer coating to improve flame-retardant and smoke suppression properties of flexible polyurethane foam," *J. Mater. Sci.*, vol. 51, pp. 10361–10374, 2016.

[46] H. Pan, Y. Lu, L. Song, X. Zhang, and Y. Hu, "Construction of layer-by-layer coating based on graphene oxide/β-FeOOH nanorods and its synergistic effect on improving flame retardancy of flexible polyurethane foam," *Compos. Sci. Technol.*, vol. 129, pp. 116–122, 2016.

[47] Y. S. Kim and R. Davis, "Multi-walled carbon nanotube layer-by-layer coatings with a trilayer structure to reduce foam flammability," *Thin Solid Films*, vol. 550, pp. 184–189, 2014.

[48] M. Gao, W. Wu, and Z. Xu, "Thermal Degradation Behaviors and Flame Retardancy of Epoxy Resins with Novel Silicon-Containing Flame Retardant," *J. Appl. Polym. Sci.*, pp. 1842–1847, 2013.

[49] J. Li, H. Zhu, J. Li, X. Fan, and X. Tian, "Thermal Degradation Behaviors of Phosphorus – Silicon Synergistic Flame-Retardant Copolyester," *J. Appl. Polym. Sci.*, vol. 122, pp. 1993–2003, 2011.

[50] F. Laoutid, "New prospects in flame retardant polymer materials: From fundamentals to nanocomposites," *F. Laoutid L. Bonnaud M. Alexandre J.-M. Lopez-Cuesta Ph. Dubois*, vol. 63, no. 3, pp. 100–125, 2009.

[51] J. Green, "Mechanisms for Flame Retardancy and Smoke suppression -A Review," *J. Fire Sci.*, vol. 14, pp. 426–442, 1996.

© 2020 Tous droits réservés.
lilliad.univ-lille.fr

Thèse de Laura Geoffroy, Université de Lille, 2020

[52] G. Camino, L. Costa, and M. P. L. di Cortemiglia, "Overview of fire retardant mechanisms," *Polym. Degrad. Stab.*, vol. 33, no. 2, pp. 131–154, 1991.

[53] D. P. A. Richard Horrocks, *Fire Retardant Materials*. 2001.

[54] C. A. Wilkie and A. B. Morgan, "Fire Retardancy of Polymeric Materials, Second Edition." 2009.

[55] L. Ferry and J.-M. Lopez-Cuesta, "Retardateurs de flammes RF des matériaux polymères," *Tech. l'ingénieur*, 2016.

[56] H. D. Tyner, "Fire-Extinguishing Effectiveness of Chemicals in Water Solution," *Ind. Eng. Chem. Res.*, vol. 33, pp. 60–65, 1941.

[57] R. Tay and R. Moynihan, "Samsung designed a vase that can be thrown at fires to extinguish them," *Buisness Insider*, 2019.

[58] B. Schartel *et al.*, "Flame Retardancy of Polymers: The Role of Specific Reactions in the Condensed Phase," *Macromol. Mater. Eng.*, vol. 301, no. 1, pp. 9–35, 2016.

[59] Y. Li, Y. S. Kim, J. Shields, and R. Davis, "Controlling polyurethane foam flammability and mechanical behaviour by tailoring the composition of clay-based multilayer nanocoatings," *J. Mater. Chem. A*, vol. 1, no. 41, pp. 12987–12997, 2013.

[60] H. Pan, Y. Pan, W. Wang, L. Song, Y. Hu, and K. M. Liew, "Synergistic Effect of Layer-by-Layer Assembled Thin Films Based on Clay and Carbon Nanotubes To Reduce the Flammability of Flexible Polyurethane Foam," *Ind. Eng. Chem. Res.*, vol. 53, no. 37, pp. 14315–14321, 2014.

[61] Y. Yang, Y. Li, J. Shields, and R. D. Davis, "Layer double hydroxide and sodium montmorillonite multilayer coatings for the flammability reduction of flexible polyurethane foams," *J. Appl. Polym. Sci.*, vol. 132, no. 4, 2014.

[62] G. Jones and S. Soll, "US patent 2452054," 1984.

[63] H. L. Vandersall, "Intumescent coating systems, their development and chemistry," *J. Fire Flammabl.*, pp. 94–140, 1971.

[64] L. G. Camino, Costa and L. Trossarelli, "Study of the Mechanism of Intumescence in Fire Retardant Polymers : Part l--Thermal Degradation of Ammonium Polyphosphate-Pentaerythritol Mixtures," *Polym. Degrad. Stab.*, vol. 6, pp. 243–252, 1984.

[65] A. Dessarthe, "Usinage des composites à matrice polymère," *Tech. l'ingénieur*, 1999.

[66] A. B. M. Supian, S. M. Sapuan, M. Y. M. Zuhri, E. S. Zainudin, and H. H. Ya, "Hybrid reinforced thermoset polymer composite in energy absorption tube application : A review," *Def. Technol.*, vol. 14, pp. 291–305, 2018.

[67] D. Feldman, "Polymer History," *Des. Monomers Polym.*, vol. 11, pp. 1–15, 2008.

[68] J. Alongi, Z. Han, and S. Bourbigot, "Progress in Polymer Science Intumescence : Tradition versus novelty. A comprehensive review," *Prog. Polym. Sci.*, vol. 51, pp. 28–73, 2015.

[69] K. M. Holder, R. J. Smith, and J. C. Grunlan, "Review A review of flame retardant nanocoatings prepared using layer-by-layer assembly of polyelectrolytes," *J. Mater. Sci.*, 2017.

© 2020 Tous droits réservés.

lilliad.univ-lille.fr

[70] S. Duquesne, *Multifunctional Barriers for Flexible Structure*, Springer. 2007.

[71] P. R. Hornsby, "Fire retardant fillers for polymers," *J. Int. Mater. Rev.*, vol. 46, no. 4, pp. 199–210, 2013.

[72] M. Gomes, D. Martino, A. J. Pontes, and J. C. Viana, "Co-injection Molding of Immiscible Polymers: Skin-Core Structure and Adhesion Studies," *Polym. Eng. Sci.*, vol. 51, no. 12, pp. 2398–2407, 2011.

[73] J. Liu, Z. Yu, Y. Shi, and C. Lu, "A preliminary study on the thermal degradation behavior and flame retardancy of high impact polystyrene/magnesium hydroxide/microencapsulated red phosphorus composite with a gradient structure," *Polym. Degrad. Stab.*, vol. 105, no. 1, pp. 21–30, 2014.

[74] Z. YU, J. Liu, Y. Zhang, J. Luo, C. Lu, and B. Pan, "Thermo-oxidative degradation behavior and fire performance of high impact polystyrene/magnesium hydroxide/microencapsulated red phosphorus composite with an alternating layered structure," *Polym. Degrad. Stab.*, vol. 115, pp. 54–62, 2015.

[75] L. Xie, L. Shen, and B. Jiang, "Chapter 11: Modelling and Simulation for Micro Injection Molding Process," in *Computational Fluid Dynamics Technologies and Applications*, 2011, pp. 317–332.

[76] M. P. Groover, "Chapter 13: Shapping Processes for plastics," in *Fundamentals of Modern Manufacturing: Materials, processes and Systems*, 2009, pp. 268–340.

[77] J. Agassant and M. R. Mackley, "Principles of polymer processing molding," in *NUMIFORM*, 2016, pp. 1–6.

[78] A. N. Wilkinson, A.J. Ryan, "Chapter 2: Introduction to polymer processing tehnologies," in *Polymer Processing and Structure Development*, pp. 9–153.

[79] N. D. Polychronopoulos and J. Vlachopoulos, "Polymer Processing and Rheology," in *Functional Polymers*, Springer Nature, 2019, pp. 1–45.

[80] J. Gardan, "Smart materials in additive manufacturing : state of the art and trends," *Virtual Phys. Prototyp.*, pp. 1–18, 2018.

[81] Z. Low, Y. T. Chua, B. M. Ray, D. Mattia, I. S. Metcalfe, and D. A. Patterson, "Perspective on 3D printing of separation membranes and comparison to related unconventional fabrication techniques," *J. Memb. Sci.*, vol. 523, pp. 596–613, 2017.

[82] V. G. Gokhare, D. N. Rault, and D. K. Shinde, "A Review paper on 3D-Printing Aspects and Various Processes Used in the 3D-Printing," *Int. J. Eng. Res. &Technology*, vol. 6, no. 6, pp. 953–958, 2017.

[83] T. C. Lee, R. Ramlan, N. Shahrubudin, T. C. Lee, and R. Ramlan, "An Overview on 3D Printing Technology : Technological , Materials , and Applications," *Procedia Manuf.*, vol. 35, pp. 1286–1296, 2019.

[84] J. Gardan, "Chapter 10: Additive manufacturing technologies," in *Additive Manufacturing Handbook: Product Development for the Defense Industry*, 2017.

[85] T. D. Ngo, A. Kashani, G. Imbalzano, K. T. Q. Nguyen, and D. Hui, "Additive manufacturing (3D printing): A review of materials , methods , applications and challenges," *Compos. Part B*, vol. 143, pp. 172–196, 2018.

© 2020 Tous droits réservés.
lilliad.univ-lille.fr

Thèse de Laura Geoffroy, Université de Lille, 2020

[86] J. Z. Gul, M. Sajid, M. M. Rehman, and G. Uddin, "3D printing for soft robotics – a review," *Sci. Technol. Adv. Mater.*, vol. 19, no. 1, pp. 243–262, 2018.

[87] Y. Wei *et al.*, "3D printing trends in building and construction industry : a review," *Virtual Phys. Prototyp.*, vol. 12, no. 3, pp. 261–276, 2017.

[88] X. Wang, M. Jiang, Z. Zhou, J. Gou, and D. Hui, "3D printing of polymer matrix composites : A review and prospective," *Compos. Part B*, vol. 110, pp. 442–458, 2017.

[89] H. Wu *et al.*, "Recent Developments in Polymers/Polymer Nanocomposites for Additive Manufacturing," *Prog. Mater. Sci.*, vol. 111, no. April 2019, p. 100638, 2020.

[90] A. D. Valino *et al.*, "Advances in 3D printing of thermoplastic polymer composites and nanocomposites," *Prog. Polym. Sci.*, vol. 98, no. 101162, pp. 1–18, 2019.

[91] T. Sakai, "Screw extrusion technology — past , present and future," *Polimery*, vol. 58, no. 11–12, pp. 847–857, 2013.

[92] P. Mitchell, "Chapter 3: Selection of manufacturing methods," in *Tool and Manufacturing Engineers Handbook: Plastic Part Manufacturing vol.8*, 1996, pp. 3-1-3–6.

[93] S. C. Ligon, R. Liska, M. Gurr, and R. Mu, "Polymers for 3D Printing and Customized Additive Manufacturing," *Chem. Rev.*, 2017.

[94] ASTM international, *ASTM International Technical Committee F42 on Additive Manufacturing Technologies Quick Facts*. 2009, p. 1.

[95] A. Bacciaglia, A. Ceruti, and A. Liverani, "Additive Manufacturing Challenges and Future Developments in the Next Ten Years," in *Design Tools and Methods in Industrial Engineering*, 2019, pp. 891–902.

[96] "Selective deposition lamination," *3D printing basics*, 2020. [Online]. Available: https://3dprintingindustry.com/3d-printing-basics-free-beginners-guide.

[97] Y. S. Zhang *et al.*, "3D Bioprinting for Tissue and Organ Fabrication," *Ann. Biomed. Eng.*, vol. 45, no. 1, pp. 148–163, 2017.

[98] H. Maleki *et al.*, "Mechanically Strong Silica-Silk Fibroin Bioaerogel: A Hybrid Scaffold with Ordered Honeycomb Micromorphology and Multiscale Porosity for Bone Regeneration," *ACS Appl. Mater. Interfaces*, vol. 11, pp. 17256–17269, 2019.

[99] Z. X. Khoo, J. Ee, M. Teoh, Y. Liu, and C. K. Chua, "3D printing of smart materials : A review on recent progresses in 4D printing," *Virtual Phys. Prototyp.*, vol. 10, no. 3, pp. 103–122, 2015.

[100] Z. Zhang, K. G. Demir, and G. X. Gu, "Developments in 4D-printing : a review on current smart materials , technologies , and applications," *Int. J. Smart Nano Mater.*, pp. 1–20, 2019.

[101] J. Ryan, C. Dizon, A. H. Espera, Q. Chen, and R. C. Advincula, "Mechanical Characterization of 3D-Printed Polymers," *Addit. Manuf.*, vol. 20, pp. 44–67, 2018.

[102] C. Kaynak and S. D. Varsavas, "Performance comparison of the 3D-printed and injection-molded PLA and its elastomer blend and fiber composites," *J. Thermoplast. Compos. Mater.*, vol. 32, no. 4, pp. 501–520, 2019.

© 2020 Tous droits réservés.

lilliad.univ-lille.fr

[103] R. Zou, Y. Xia, S. Liu, P. Hu, W. Hou, and Q. Hu, "Isotropic and anisotropic elasticity and yielding of 3D printed material," *Compos. Part B*, vol. 99, pp. 506–513, 2016.

[104] B. O'Neal, "PLA in FDM 3D Printing: Studying the Effects of Porosity & Crystallinity," *3D print*, 2019. [Online]. Available: https://3dprint.com/254978/pla-fff-3d-printing-studying-effects-porosity-crystallinity/.

[105] S. Saunders, "Reducing High Porosity and Improving Sealing Properties in Extrusion-Based 3D Printing," *3D print*, 2018. [Online]. Available: https://3dprint.com/216369/high-porosity-extrusion-3d-print/.

[106] H. A. Habeeb, M. R. Alkahari, F. R. Ramli, R. Hasan, and S. Maidin, "Strength and porosity of additively manufactured PLA using a low cost 3D printing," in *Procedings of Medical Engineering Researd Day*, 2016, pp. 69–70.

[107] X. WANG, L. Zhao, J. Y. H. Fuh, and H. P. Lee, "Effect of Porosity on Mechanical Properties of 3D Printed Polymers: Experiments and Micromechanical Modeling Based on X-ray Computed Tomography Analysis," *Polymers (Basel).*, vol. 11, no. 7, pp. 1–20, 2019.

[108] S. Guessasma, S. Belhabib, H. Nouri, and O. Ben, "Anisotropic damage inferred to 3D printed polymers using fused deposition modelling and subject to severe compression," *Eur. Polym. J.*, vol. 85, pp. 324–340, 2016.

[109] E. Canti and M. Aydin, "Effects of micro particle reinforcement on mechanical properties of 3D printed parts Article information :," *Rapid Prototyp. J.*, vol. 24, no. 1, pp. 171–176, 2018.

[110] N. W. Pensa *et al.*, "3D printed mesh reinforcements enhance the mechanical properties of electrospun scaffolds," *Biomater. Res.*, vol. 23, no. 22, pp. 1–7, 2019.

[111] D. Türk, F. Brenni, M. Zogg, and M. Meboldt, "Mechanical characterization of 3D printed polymers for fiber reinforced polymers processing," *Mater. Des.*, vol. 118, pp. 256–265, 2017.

[112] C. Ziemian, M. Sharma, and S. Ziemian, "Chapter 7: Anisotropic Mechanical Properties of ABS Parts Fabricated by Fused Deposition Modelling," in *Mechanical Engineering*, 2012, pp. 159–180.

[113] I. Durgun and R. Ertan, "Experimental investigation of FDM process for improvement of mechanical properties and," *Rapid Prototyp. J.*, vol. 20, no. 3, pp. 228–235, 2014.

[114] S.-H. Ahn, M. Montero, D. Odell, S. Roundy, and P. K. Wright, "Anisotropic material properties of fused deposition modeling ABS," *Rapid Prototyp.*, vol. 8, no. 4, pp. 248–257, 2002.

[115] A. K. Sood, R. K. Ohdar, and S. S. Mahapatra, "Parametric appraisal of mechanical property of fused deposition modelling processed parts," *Mater. Des.*, vol. 31, no. 1, pp. 287–295, 2010.

[116] A. K. Sood, R. K. Ohdar, and S. S. Mahapatra, "Experimental investigation and empirical modelling of FDM process for compressive strength improvement," *J. Adv. Res.*, vol. 3, no. 1, pp. 81–90, 2012.

[117] T. Letcher and M. Waytashek, "Material property testing of 3D-printed specimen in PLA on an entry-level 3D printer," in *ASME International Mechanical Engineering Congress*

© 2020 Tous droits réservés.
lilliad.univ-lille.fr

Thèse de Laura Geoffroy, Université de Lille, 2020

& Exposition, 2014, pp. 1–8.

[118] B. Rankouhi, S. Javadpour, and T. Letcher, "Experimental Study of Mechanical Properties of Additively Manufactured ABS Plastic as a Function of Layer Parameters," in *ASME International Mechanical Engineering Congress and Exposition*, 2015, pp. 1–8.

[119] B. H. Lee, J. Abdullah, and Z. A. Khan, "Optimization of rapid prototyping parameters for production of flexible ABS object," *J. Mater. Process. Technol.*, vol. 169, pp. 54–61, 2005.

[120] K. Lee, S. Wang, B. C. Fox, E. L. Ritman, M. J. Yaszemski, and L. Lu, "Poly(propylene fumarate) Bone Tissue Engineering Scaffold Fabrication Using Stereolithography : Effects of Resin Formulations and Laser Parameters," *Biomacromolecules*, vol. 8, pp. 1077–1084, 2007.

[121] B. Rankouhi, S. Javadpour, F. Delfanian, and T. Letcher, "Failure Analysis and Mechanical Characterization of 3D Printed ABS With Respect to Layer Thickness and Orientation," *J. Fail. Anal. Prev.*, vol. 16, pp. 467–481, 2016.

[122] C. W. Ziemian, R. D. Ziemian, and K. V Haile, "Characterization of stiffness degradation caused by fatigue damage of additive manufactured parts," *Mater. Des.*, vol. 109, pp. 209–218, 2016.

[123] K. M. Rahman, R. Reese, and T. Letcher, "Mechanical Properties of Additively Manufactured PEEK Components Using Fused Filament Fabrication," in *ASME International Mechanical Engineering Congress & Exposition*, 2015, pp. 1–11.

[124] Arkema, "3D printing materials: our solutions," 2020. [Online]. Available: https://www.arkema.com/en/markets-solutions/3d-printing/.

[125] Solvay, "Additive Manufacturing Solutions," 2020. [Online]. Available: https://www.solvay.com/en/chemical-categories/specialty-polymers/additive-manufacturing.

[126] S. M. Kraft, B. Y. Lattimer, and C. B. Williams, "Flammability of 3-D Printed Polymers - Composition and Geometry Factors," in *Solid Freeform Fabrication Symposium - An Additive Manufacturinf Conference*, 2016, pp. 2407–2422.

[127] H. Wu, M. Sulkis, J. Driver, A. Saade-castillo, A. Thompson, and J. H. Koo, "Multi-functional ULTEM ™ 1010 composite filaments for additive manufacturing using Fused Filament Fabrication (FFF)," *Addit. Manuf.*, vol. 24, pp. 298–306, 2018.

[128] T. Z. Fabian, "Influence of 3D printing by Material Extrusion on UL 94 and UL 746A Material Properties," 2018.

[129] Y. Guo *et al.*, "Engineering fl ame retardant biodegradable polymer nanocomposites and their application in 3D printing," *Polym. Degrad. Stab.*, vol. 137, pp. 205–215, 2017.

[130] S. Dul, L. Fambri, and A. Pegoretti, "Fused deposition modelling with ABS – graphene nanocomposites," *Compos. Part A*, vol. 85, pp. 181–191, 2016.

[131] Z. Weng, J. Wang, T. Senthil, and L. Wu, "Mechanical and thermal properties of ABS/montmorillonite nanocomposites for fused deposition modeling 3D printing," *Mater. Des.*, vol. 102, pp. 276–283, 2016.

[132] T. Sathish, M. D. Vijayakumar, and A. Krishnan, "Design and Fabrication of Industrial

© 2020 Tous droits réservés.

lilliad.univ-lille.fr

Components Using 3D Printing," in *Materials Today: Proceedings*, 2018, vol. 5, no. 6, pp. 14489–14498.

[133] M. J. Richardson, H. Wu, T. J. Wilcox, M. Broaddus, and P. C. Lin, "Flame Retardant Nylon 6 Nanocomposites for Fused Deposition Modeling (FDM) Applications," in *Society for the Advancement of Material and Process Engineering*, 2017.

[134] C. Materials and R. O. Vol, "Investigation of properties of nanocomposite polyimide samples obtained by fused deposition modeling," *Mech. Compos. Mater.*, vol. 54, no. 1, pp. 33–40, 2018.

[135] L. Chen *et al.*, "3D printable robust shape memory PET copolyesters with fire safety via p-stacking and synergistic crosslinking," *J. Mater. Chem.*, vol. 7, pp. 17037–17045, 2019.

[136] Y. Weng *et al.*, "Printability and fire performance of a developed 3D printable fibre reinforced cementitious composites under elevated temperatures," *Virtual Phys. Prototyp.*, vol. 2759, pp. 1–9, 2018.

[137] H. Maleki, S. Montes, N. Hayati-roodbari, F. Putz, and N. Huesing, "Compressible , Thermally Insulating , and Fire Retardant Aerogels through Self-Assembling Silk Fibroin Biopolymers Inside a Silica Structure An Approach towards 3D Printing of Aerogels," *ACS Appl. Mater. Interfaces*, vol. 10, pp. 22718–22730, 2018.

[138] S. C. Lao *et al.*, "Flame-retardant Polyamide 11 and 12 Nanocomposites: Processing, Morphology, and Mechanical Properties," *J. Compos. Mater.*, vol. 44, no. 25, pp. 2933–2950, 2010.

[139] S. Mubarak, D. Dhamodharan, N. Divakaran, and M. B. Kale, "Enhanced Mechanical and Thermal Properties of Stereolithography 3D Printed Structures by the Effects of Incorporated Controllably Annealed Anatase TiO2 Nanoparticles," *nanomaterials*, vol. 10, no. 79, pp. 1–24, 2020.

[140] D. Moreno, V. Casal, and S. Ignacio, "Large-format polymeric pellet-based additive manufacturing for the naval industry," *Addit. Manuf.*, vol. 23, pp. 79–85, 2018.

[141] Clariant, "PA6 FR using Exolit," 2020. [Online]. Available: https://www.clariant.com/en/Solutions/Products/2018/01/22/04/34/PA6_FR_Exolit_3D PrinterFilamet.

[142] R. A. Paggi, V. E. Beal, and G. V Salmoria, "Process optimization for PA12/MWCNT nanocomposite manufacturing by selective laser sintering," *Int. J. Adv. Manuf. Technol.*, vol. 66, pp. 1977–1985, 2013.

[143] A. Manthiram, H. Marcus, and D. Bourell, "US 5431967 Selective laser sintering using nanocomposite materials," 1995.

[144] M. A. Caminero, J. M. Chacon, E. Garcia-Plaza, P. J. Nunez, J. M. Reverte, and J. P. Becar, "Additive Manufacturing of PLA-Based Composites Using Fused Filament Fabrication: Effect of Graphene Nanoplatelet Reinforcement on Mechanical Properties, Dimensional Accuracy and Texture," *Polymers (Basel).*, vol. 11, no. 799, pp. 1–22, 2019.

[145] N. Wu, G. Fu, Y. Yang, M. Xia, H. Yun, and Q. Wang, "Fire safety enhancement of a highly efficient flame retardant poly(phenylphosphoryl phenylenediamine) in biodegradable poly(lactic acid)," *J. Hazard. Mater.*, vol. 363, pp. 1–9, 2019.

© 2020 Tous droits réservés.
lilliad.univ-lille.fr

Thèse de Laura Geoffroy, Université de Lille, 2020

[146] A. Regazzi, M. F. Pucci, L. Dumazert, B. Gallard, S. Buonomo, and R. Ravel, "Controlling the distribution of fire retardants in poly(lactic acid) by fused filament fabrication in order to improve its fire behaviour," *Polym. Degrad. Stab.*, vol. 163, pp. 143–150, 2019.

[147] A. Regazzi *et al.*, "Development of flame-retarded PLA compositions by 3D printing of core-skin structures," in *ECCM18 - 18th European Conference on Composite Materials*, 2019, pp. 1–8.

[148] L. Geoffroy and S. Bourbigot, "Additive manufacturing of fire - retardant ethylene - vinyl acetate," *Polym. Adv. Technol.*, vol. 30, no. 7, pp. 1878–1890, 2019.

[149] S. Rehn, "Vertical Bunsen Burner Testing of 3-D Printed Material," in *International Aircraft Materials Fire Test Forum*, 2018.

[150] B. Girardin, G. Fontaine, S. Duquesne, M. Försth, and S. Bourbigot, "Characterization of Thermo-Physical Properties of EVA / ATH : Application to Gasification Experiments and Pyrolysis Modeling," pp. 7837–7863, 2015.

[151] C. Hoffendahl, G. Fontaine, S. Duquesne, F. Taschner, M. Mezger, and S. Bourbigot, "The fire retardant mechanism of ethylene vinyl acetate elastomer (EVM) containing aluminium trihydroxide and melamine phosphate," *RSC Adv.*, vol. 4, no. 39, pp. 20185–20199, 2014.

[152] F. Taschner, C. Hoffendahl, S. Duquesne, M. Mezger, and S. Bourbigot, "Decomposition mechanism of fi re retarded ethylene vinyl acetate elastomer (EVA) containing aluminum trihydroxide and melamine," vol. 113, pp. 168–179, 2015.

[153] L. Gay, S. Bourbigot, and F. Ngohang, "Smoke composition using MLC / FTIR / ELPI : Application to fl ame retarded ethylene vinyl acetate," vol. 115, pp. 89–109, 2015.

[154] S. Bourbigot, J. Sarazin, F. Samyn, and M. Jimenez, "Intumescent ethylene-vinyl acetate copolymer : Reaction to fi re and mechanistic aspects," *Polym. Degrad. Stab.*, vol. 161, pp. 235–244, 2019.

[155] L. Geoffroy, F. Samyn, M. Jimenez, and S. Bourbigot, "Innovative 3D printed design to conceive highly fi re-retardant," *Polym. Degrad. Stab.*, vol. 169, p. 108992, 2019.

[156] C. T. Ewing, F. R. Faith, J. T. Hughes, and H. W. Carhart, "Flame Extinguishment Properties of Dry Chemicals : Extinction Concentrations for Small Diffusion Pan Fires," *Fire Technol.*, pp. 134–149, 1989.

[157] D. Grossman, "Samsung's 'Firevase' Is a Smashing Fire Extinguisher," *Popular Mechanics*, 2019. [Online]. Available: https://www.popularmechanics.com/technology/infrastructure/a26974315/samsungs-firevase-throwable-fire-extinguisher/.

[158] S. Kang, J. Y. Choi, and S. Choi, "Mechanism of Heat Transfer through Porous Media of Inorganic Intumescent Coating in Cone Calorimeter Testing," *Polymers (Basel).*, vol. 11, no. 2, 2019.

[159] A. M. Helmenstine, "How Flame Test Colors Are Produced," *Science, Tech, Math*, 2020. [Online]. Available: https://www.thoughtco.com/how-flame-test-colors-are-produced-3963973.

[160] G. Okyay, S. Bellayer, F. Samyn, M. Jimenez, and S. Bourbigot, "Characterization of

© 2020 Tous droits réservés.

lilliad.univ-lille.fr

in- flame soot from balsa composite combustion during mass loss cone calorimeter tests," *Polym. Degrad. Stab.*, vol. 154, pp. 304–311, 2018.

[161] D. E. Newbury and N. W. M. Ritchie, "Is Scanning Electron Microscopy / Energy Dispersive X-ray Spectrometry (SEM/EDS) Quantitative ?," *J. scanning Microsc.*, vol. 35, no. 3, pp. 141–168, 2013.

[162] J. A. Aad, "Dégradation chimique et mécanique de l'alumine en phase aqueuse : mécanisme et inhibition en conditions ambiantes et hydrothermales To cite this version : HAL Id : tel-01913067 Université Pierre et Marie Curie Dégradation chimique et mécanique de l ' al," 2018.

[163] Z. Tianwei, L. Hao, H. Zhiyue, D. Zhiming, and W. Yong, "Active substances study in fire extinguishing by water mist with potassium salt additives based on thermoanalysis and thermodynamics," *Appl. Therm. Eng.*, vol. 122, pp. 429–438, 2017.

[164] V. I. Babushok, G. T. Linteris, P. Hoorelbeke, D. Roosendans, and K. van Wingerden, "Flame Inhibition by Potassium-Containing Compounds," *Combust. Sci. Technol.*, vol. 189, no. 12, pp. 2039–2055, Dec. 2017.

[165] J. D. Birchah, "On the Mechanism of Flame Inhibition by Alkali Metal Salts," *Combust. Flame*, vol. 14, pp. 85–96, 1970.

[166] J. W. Hastie, "Molecular Basis of Flame Inhibition," *J. Res. Nationl Bur. Stand.*, vol. 77, no. 0, pp. 733–754, 1973.

[167] W. Cheng, X. Hu, J. Xie, and Y. Zhao, "An intelligent gel designed to control the spontaneous combustion of coal: Fire prevention and extinguishing properties," *Fuel*, vol. 210, pp. 826–835, 2017.

[168] X. Ren *et al.*, "Novel sodium silicate/polymer composite gels for the prevention of spontaneous combustion of coal," *J. Hazard. Mater.*, vol. 371, pp. 643–654, 2019.

[169] W. R. K. Illeperuma, P. Rothemund, Z. Suo, and J. J. Vlassak, "Fire-Resistant Hydrogel-Fabric Laminates : A Simple Concept That May Save Lives," *ACS Appl. Mater. Interfaces*, vol. 8, pp. 2071–2077, 2016.

[170] X. F. Cui *et al.*, "Water-retaining, though and self-healing hydrogels and their uses as fire-resistant materials," *Polym. Chem.*, vol. 10, pp. 5151–5158, 2019.

[171] L. Hsiao, L. Jing, K. Li, H. Yang, Y. Li, and P. Chen, "Carbon nanotube-integrated conductive hydrogels as multifunctional robotic skin," *Carbon N. Y.*, vol. 161, pp. 784–793, 2020.

[172] Q. Ren, Y. Zhang, J. Li, and J. C. Li, "Synergistic Effect of Vermiculite on the Intumescent Flame Retardance of Polypropylene," *J. Appl. Polym. Sci.*, vol. 120, no. 2, pp. 1225–1233, 2010.

[173] R. Hanken *et al.*, "Effect of natural and expanded vermiculite clays on the properties of eco-friendly biopolyethylene-vermiculite clay biocomposites," *Compos. Part B Eng.*, vol. 175, no. 107184, 2019.

[174] A. A. Cain, M. G. B. Plummer, S. E. Murray, L. Bolling, O. Regev, and J. C. Grunlan, "Iron-containing, high aspect ratio clay as nanoarmor that imparts substantial thermal/flame protection to polyurethane with a single electrostatically-deposited bilayer," *J. Mater. Chem. A*, vol. 2, no. 41, pp. 17609–17617, 2014.

© 2020 Tous droits réservés.
lilliad.univ-lille.fr

Thèse de Laura Geoffroy, Université de Lille, 2020

[175] S. Lazar, F. Carosio, A. L. Davesne, M. Jimenez, S. Bourbigot, and J. Grunlan, "Extreme Heat Shielding of Clay/Chitosan Nanobrick Wall on Flexible Foam," *ACS Appl. Mater. Interfaces*, vol. 10, no. 37, pp. 31686–31696, 2018.

[176] L. Geoffroy, A. Davesne, S. Bellayer, and F. Blanchard, "3D printed sandwich materials filled with hydrogels for extremely low heat release rate," *Polym. Degrad. Stab.*, no. 109269, 2020.

[177] M. M. Martin and L. Lindqvist, "The pH dependence of fluorescein fluorescence," *J. Lumin.*, vol. 10, pp. 381–390, 1975.

[178] E. K. Lavrent, S. G. Starodubtsev, A. R. Khokhlov, V. V Volkov, and K. A. Dembo, "Effect of Polymer Nature on the Structure and Properties of Gel Composites with Incorporated Bentonite Particles," *Colloid J.*, vol. 70, no. 5, pp. 604–608, 2008.

[179] S. G. Starodoubtsev, E. K. Lavrentyeva, A. R. Khokhlov, G. Allegra, A. Famulari, and S. V Meille, "Mechanism of Smectic Arrangement of Montmorillonite and Bentonite Clay Platelets Incorporated in Gels of Poly (Acrylamide) Induced by the Interaction with Cationic Surfactants," *Langmuir*, vol. 22, pp. 369–374, 2006.

[180] P. Porion, M. Al Mukhtar, S. Meyer, A. M. Fauge, and J. R. C. Van Der Maarel, "Nematic Ordering of Suspensions of Charged Anisotropic Colloids Detected by 23Na Nuclear Magnetic Resonance," *J. Phys. Chem. B*, vol. 105, pp. 10505–10514, 2001.

[181] G. Schmidt, A. I. Nakatani, P. D. Butler, and C. C. Han, "Small-Angle Neutron Scattering from Viscoelastic Polymer - Clay Solutions," *Macromolecules*, vol. 35, pp. 4725–4732, 2002.

[182] M. Huang, Y. Hou, Y. Li, D. Wang, and L. Zhang, "High performances of dual network PVA hydrogel modified by PVP using borax as the structure- forming accelerator," *Des. Monomers Polym.*, vol. 20, no. 1, pp. 505–513, 2017.

[183] K. Haraguchi, K. Murata, and Y. Kimura, "Uniaxial and plane orientations of clay platelets in nanocomposite gels with different compositions during stretching and recovery," *Polymer (Guildf).*, vol. 116, pp. 439–446, 2017.

[184] G. W. Brindley, "Part III - Methods of Identifying Clays and the Interpretation of Results," in *Calys and Clay Minerals*, 1952, pp. 119–129.

[185] C. Marcos, Y. C. Arango, and I. Rodriguez, "X-ray diffraction studies of the thermal behaviour of commercial vermiculites," *Appl. Clay Sci.*, vol. 42, no. 3–4, pp. 368–378, 2009.

[186] X. Gong, Z. Guo, and Z. Wang, "Variation of Char Structure during Anthracite Pyrolysis Catalyzed by Fe 2 O 3 and Its Influence on Char Combustion Reactivity," *Energy Fuels*, vol. 36, no. 10, pp. 1–6, 2009.

[187] B. Bellich, M. Borgogna, M. Cok, and A. Cesaro, "Release Properties of Hydrogels : Water Evaporation from Alginate Gel Beads," *Food Biophys.*, vol. 6, no. June, pp. 259–266, 2011.

[188] D. R. Rohindra, A. V Nand, and J. R. Khurma, "Swelling properties of chitosan hydrogels," *South Pacific J. Nat. Sci.*, vol. 22, pp. 32–35, 2004.

[189] B. Schartel, U. Beck, H. Bahr, A. Hertwig, U. Knoll, and M. Weise, "Sub-micrometre coatings as an infrared mirror : A new route to flame retardancy," *Fire Mater.*, vol. 36,

© 2020 Tous droits réservés.

lilliad.univ-lille.fr

pp. 671–677, 2012.

[190] M. Försth, S. Zhao, and A. Roos, “Spectrally selective and adaptive surfaces for protection against radiative heating : ITO and VO 2,” *Fire Mater.*, vol. 38, pp. 111–124, 2014.

[191] A. L. Davesne *et al.*, “Low-Emissivity Metal/Dielectric Coatings as Radiative Barriers for the Fire Protection of Raw and Formulated Polymers,” *ACS Appl. Polym. Mater.*, 2020.

[192] G. Okyay, A. D. Naik, F. Samyn, M. Jimenez, and S. Bourbigot, “Fractal conceptualization of intumescent fire barriers , toward simulations of virtual morphologies,” *Nat. Sci. Reports*, vol. 9, no. 1872, pp. 1–16, 2019.

[193] Z. Li, L. Liu, A. J. Gonzalez, and D. Y. Wang, “Bioinspired polydopamine-induced assembly of ultrafine Fe(OH)3 nanoparticles on halloysite toward highly efficient fire retardancy of epoxy resin via an action of interfacial catalysits,” *Polym. Chem.*, vol. 8, no. 3926, pp. 3926–3936, 2017.

[194] D. Wang *et al.*, “Biomimetic structural cellulose nano fi ber aerogels with exceptional mechanical , flame-retardant and thermal-insulating properties,” *Chem. Eng. J.*, vol. 389, no. 124449, pp. 1–9, 2020.

[195] L. Liu *et al.*, “A novel strategy for simultaneously improving the fire safety, water resistance and compatibility of thermoplastic polyurethane composites through the construction of biomimetic hydrophobic structure of intumescent flame retardant synergistic system,” *Compos. Part B*, vol. 176, no. June, p. 107218, 2019.

[196] A. P. Mouritz, S. Feih, E. Kandare, and A. G. Gibson, “Thermal-mechanical modelling of laminates with fire protection coating,” *Compos. Part B Eng.*, vol. 48, pp. 68–78, 2013.

[197] A. P. Mouritz *et al.*, “Review of fire structural modelling of polymer composites,” *Compos. Part A*, vol. 40, no. 12, pp. 1800–1814, 2009.

[198] A.P. Mouritz, A.G. Gibson, *Fire Properties of Polymer Composite Materials*, Springer. 2006.

[199] G. M. Fohlen, J. A. Parker, and S. R. R. P. M. Sawko, “Intumescence: An In Situ Approach to Thermal Protection,” in *Conference on Materials for Improved Fire Safety*, 1970, pp. 111–119.

[200] R. BEAUREGARD, “The USS FORRESTAL (CVA-59) fire and munition explosions _ The History of Insensitive Munitions,” 2011.

[201] M. Jimenez, S. Bellayer, A. Naik, P. Bachelet, S. Duquesne, and S. Bourbigot, “Topcoats versus Durability of an Intumescent Coating,” *Ind. Eng. Chem. Res.*, vol. 55, no. 36, pp. 9625–9632, 2016.

[202] G. Wang and J. Yang, “Influences of binder on fire protection and anticorrosion properties of intumescent fire resistive coating for steel structure,” *Surf. Coat. Technol.*, vol. 204, no. 8, pp. 1186–1192, 2010.

[203] Z. Ma, J. Wang, S. Chen, X. Li, and H. Ma, “Synthesis and characterization of water borne intumescent fire retardant varnish based on phosphate resin acid cold cured amino resin,” *Prog. Org. Coatings*, vol. 74, no. 3, pp. 608–614, 2012.

© 2020 Tous droits réservés.
lilliad.univ-lille.fr

Thèse de Laura Geoffroy, Université de Lille, 2020

[204] G. Wang and J. Yang, "Thermal degradation study of fire resistive coating containing melamine polyphosphate and dipentaerythritol," *Prog. Org. Coatings*, vol. 72, no. 4, pp. 605–611, 2011.

[205] G. Wang, Y. Wang, and J. Yang, "Influences of polymerization degree of ammonium polyphosphate on fire protection of waterborne intumescent fire resistive coating," *Surf. Coat. Technol.*, vol. 206, no. 8–9, pp. 2275–2280, 2012.

[206] G. Wang and J. Yang, "Influences of glass flakes on fire protection and water resistance of waterborne intumescent fire resistive coating for steel structure," *Prog. Org. Coatings*, vol. 70, no. 2–3, pp. 150–156, 2011.

[207] F. Fan, Z. Xia, Q. Li, and Z. Li, "Effects of inorganic fillers on the shear viscosity and fire retardant performance of waterborne intumescent coatings," *Prog. Org. Coatings*, vol. 76, no. 5, pp. 844–851, 2013.

[208] C. Chou, S. Lin, and C. Wang, "Preparation and characterization of the intumescent fire retardant coating with a new flame retardant," *Adv. Powder Technol.*, vol. 20, no. 2, pp. 169–176, 2009.

[209] S. Duquesne, S. Magnet, C. Jama, and R. Delobel, "Thermoplastic resins for thin film intumescent coatings e towards a better understanding of their effect on intumescence efficiency," *Polym. Degrad. Stab.*, vol. 88, pp. 63–69, 2005.

[210] M. Jimenez, S. Bellayer, B. Revel, S. Duquesne, and S. Bourbigot, "Comprehensive Study of the Influence of Different Aging Scenarios on the Fire Protective Behavior of an Epoxy Based Intumescent Coating," *Ind. Eng. Chem. Res.*, vol. 52, no. 2, pp. 729–743, 2013.

[211] K. A. Salmeia *et al.*, "Comprehensive study on flame retardant polyesters from phosphorus additives," *Polym. Degrad. Stab.*, vol. 155, pp. 22–34, 2018.

[212] B. Gardelle, S. Duquesne, V. Rerat, and S. Bourbigot, "Thermal degradation and fi re performance of intumescent silicone-based coatings," no. March 2012, 2013.

[213] B. Gardelle, S. Duquesne, C. Vu, and S. Bourbigot, "Thermochimica Acta Thermal degradation and fire performance of polysilazane-based coatings," vol. 519, pp. 28–37, 2011.

[214] S. Bourbigot, B. Gardelle, and P. Vandereecken, "Protecting substrates against damage by fire. WO 2013/150121," 2013.

[215] B. Gardelle, S. Duquesne, P. Vandereecken, S. Bellayer, and S. Bourbigot, "Resistance to fire of curable silicone/expandable graphite based coating: Effect of the catalyst," *Eur. Polym. J.*, vol. 49, no. 8, pp. 2031–2041, 2013.

[216] B. Gardelle, S. Duquesne, P. Vandereecken, S. Bellayer, and S. Bourbigot, "Progress in Organic Coatings Resistance to fire of intumescent silicone based coating : The role of organoclay," *Prog. Org. Coatings*, vol. 76, no. 11, pp. 1633–1641, 2013.

[217] B. Gardelle, S. Duquesne, P. Vandereecken, and S. Bourbigot, "Characterization of the carbonization process of expandable graphite/silicone formulations in a simulated fire," *Polym. Degrad. Stab.*, vol. 98, no. 5, pp. 1052–1063, 2013.

[218] A. M. Pereyra, G. Canosa, and C. A. Giudice, "Nanostructured protective coating systems, fireproof and environmentally friendly, suitable for the protection of metallic

© 2020 Tous droits réservés.

lilliad.univ-lille.fr

substrates," *Ind. Eng. Chem. Res.*, vol. 49, no. 6, pp. 2740–2746, 210AD.

[219] G. Decher and J. B. Schlenoff, *Multilayer Thin Films: Sequential Assembly of Nanocomposite Materials, 2nd Edition*. 2012.

[220] Z. Wang, E. Han, F. Liu, and W. Ke, "Fire and Corrosion Resistances of Intumescent Nano-coating Containing Nano-SiO 2 in Salt Spray Condition," *Mater. Sci. Technol.*, vol. 26, no. 1, pp. 75–81, 2010.

[221] M. C. Yew and N. H. R. Sulong, "Fire-resistive performance of intumescent flame-retardant coatings for steel," *Mater. Des.*, vol. 34, pp. 719–724, 2012.

[222] B. Gardelle, S. Duquesne, P. Vandereecken, S. Bellayer, and S. Bourbigot, "Resistance to fire of intumescent silicone based coating : The role of organoclay," *Prog. Org. Coatings*, vol. 76, no. 11, pp. 1633–1641, 2013.

[223] R. J. Smith *et al.*, "Environmentally benign halloysite nanotube multilayer assembly significantly reduces polyurethane flammability," *Adv. funtional Mater.*, vol. 28, no. 27, 2017.

[224] Z. Wang, E. Han, and W. Ke, "Influence of nano-LDHs on char formation and fire-resistant properties of flame-retardant coating," *Prog. Org. Coatings*, vol. 53, pp. 29–37, 2005.

[225] J. Galos, "Thin-ply composite laminates : a review," *Compos. Struct.*, vol. 236, no. 111920, pp. 1–12, 2020.

[226] R. C. Alderliesten and R. Benedictus, "Fiber/Metal Composite Technology for Future Primary Aircraft Structures," *J. Aricr.*, vol. 45, no. 4, pp. 1182–1194, 2008.

[227] A. Asundi and A. Y. N. Choi, "Fiber Metal Laminates : An Advanced Material for Future Aircraft," *J. Mater. Process. Technol.*, vol. 63, pp. 384–394, 1997.

[228] L. B. Vogelesang and A. Vlot, "Development of fibre metal laminates for advanced aerospace structures," *J. Mater. Process. Technol.*, vol. 103, no. 1, pp. 1–5, 2000.

[229] G. H. J. J. Roebroeks, "Fibre-metal laminates: Recent developments and applications," *Fatigue*, vol. 16, no. 1, pp. 33–42, 1994.

[230] S. Timme, V. Trappe, M. Korzen, and B. Schartel, "Fire stability of carbon fiber reinforced polymer shells on the intermediate-scale," *Compos. Struct.*, vol. 178, pp. 320–329, 2017.

[231] S. Christke, A. G. Gibson, K. Grigoriou, and A. P. Mouritz, "Multi-layer polymer metal laminates for the fire protection of lightweight structures," *Mater. Des.*, vol. 97, pp. 349–356, 2016.

[232] A. Salve, R. Kulkarni, and A. Mache, "A Review: Fiber Metal Laminates (FML's) - Manufacturing, Test methods and Numerical modeling," *Int. J. Eng. Technol. Sci.*, vol. 6, no. 1, pp. 71–84, 2016.

[233] P. Chang, P. Yeh, and J. Yang, "Fatigue crack initiation in hybrid boron/glass/aluminum fiber metal laminates," *Mater. Sci. Eng. A*, vol. 496, pp. 273–280, 2008.

[234] T. Sinmazçelik, E. Avcu, M. Ö. Bora, and O. Çoban, "A review: Fibre metal laminates, background, bonding types and applied test methods," *Mater. Des.*, vol. 32, no. 7, pp. 3671–3685, 2011.

© 2020 Tous droits réservés.
lilliad.univ-lille.fr

Thèse de Laura Geoffroy, Université de Lille, 2020

[235] C. Meola, S. Boccardi, and G. maria Carlomagno, "Chapter 1 - Composite Materials in the Aeronautical Industry," in *Infrared Thermography in the Evaluation of Aerospace Composite Materials*, 2017, pp. 1–24.

[236] A. Mouritz, "Chapter 1 - Introduction to aerospace materials," in *Introduction to Aerospace Materials*, 2012, pp. 1–14.

[237] V. Vasiliev and E. Morozov, "Chapter 3 - Mechanics of Laminates," in *Advanced Mechanics of Composite Materials and Structures (Fourth Edition)*, 2018, pp. 191–242.

[238] L. Geoffroy, F. Samyn, M. Jimenez, and S. Bourbigot, "Intumescent Polymer Metal Laminates for Fire Protection," *Polymers (Basel).*, vol. 10, no. 9, pp. 1–16, 2018.

[239] M. Jimenez, S. Duquesne, and S. Bourbigot, "Characterization of the performance of an intumescent fire protective coating," *Surf. Coatings Technol.*, vol. 201, no. 3–4, pp. 979–987, 2006.

[240] M. Jimenez, S. Duquesne, and S. Bourbigot, "Multiscale experimental approach for developing high-performance intumescent coatings," *Ind. Eng. Chem. Res.*, vol. 45, no. 13, pp. 4500–4508, 2006.

[241] M. Jimenez, S. Duquesne, and S. Bourbigot, "High-throughput fire testing for intumescent coatings," *Ind. Eng. Chem. Res.*, vol. 45, no. 22, pp. 7475–7481, 2006.

[242] M. Jimenez, S. Duquesne, and S. Bourbigot, "Kinetic analysis of the thermal degradation of an epoxy-based intumescent coating," *Polym. Degrad. Stab.*, vol. 94, no. 3, pp. 404–409, 2009.

[243] L. Geoffroy, F. Samyn, M. Jimenez, and S. Bourbigot, "Bi-layer intumescent paint metal laminate : a novel design for a high performance fire barrier Abstract :," *Ind. Eng. Chem. Res.*, 2020.

[244] P. Tranchard *et al.*, "Fire behaviour of carbon fibre epoxy composite for aircraft: Novel test bench and experimental study," *J. Fire Sci.*, vol. 33, no. 3, pp. 247–266, 2015.

[245] R. Joven, R. Das, A. Ahmed, P. R. Van, and B. M. Ie, "Thermal properties of carbon fiber-epoxy composites with different fabric weaves," in *SAMPE International Symposium Proceeding*, 2012, pp. 1–13.

[246] A. Akni, "Modelisation généralisée du procédé de la coulée continue," 2015.

[247] D. P. K. Sakkas, A. Sofianos, P. Nomikos, "Behaviour of Passive Fire Protection K-Geopolymer under Successive Severe Fire Incidents," *Materials (Basel).*, vol. 8, pp. 6096–6104, 2015.

[248] K. Sakkas, D. Panias, P. P. Nomikos, and A. I. Sofianos, "Potassium based geopolymer for passive fire protection of concrete tunnels linings," *Tunn. Undergr. Sp. Technol.*, vol. 43, pp. 148–156, 2014.

[249] K. Hussin, A. A. Kadir, and E. A. Azimi, "Manufacturing of Fire Resistance Geopolymer : A Review," pp. 4–9, 2016.

[250] M. Watolla, G. J. G. Gluth, P. Sturm, W. D. A. Rickard, S. Krüger, and B. Schartel, "Intumescent Geopolymer-Bound Coatings for Fire Protection of Steel," *J. Ceram. Sci. Technol.*, vol. 8, no. 3, pp. 351–363, 2017.

[251] X. Peng, H. Li, Q. Shuai, and L. Wang, "Fire Resistance of Alkali Activated

© 2020 Tous droits réservés.

lilliad.univ-lille.fr

Geopolymer," *Materials (Basel).*, vol. 13, no. 535, pp. 1–8, 2020.

[252] Y. Uematsu, T. Kitamura, and R. Ohtani, "Creep-Fatigue Interaction in Delamination Crack Propagation of Advanced CFRPs at High Temperatures," in *High Temperature and Environmental Effect on Polymeric Composites Volume 2*, 1997, pp. 110–130.

[253] A. Lucherini, J. P. Hidalgo, J. L. Torero, and C. Maluk, "Influence of heating conditions and initial thickness on the effectiveness of thin intumescent coatings," *Fire Saf. J.*, vol. 103078, pp. 1–18, 2020.

[254] Arkema Functional Polyolefins, "Evatane 28-05: Ethylene-Vinyl Acetate (VA) copolymer with high VA content," 2014.

[255] Sigma-aldrich, "Product Specification: Sodium alginate," 2015.

[256] Sigma-aldrich, "Poly(vinyl alcohol)," 2020. [Online]. Available: https://www.sigmaaldrich.com/materials-science/material-science-products.html?TablePa.

[257] Agargel, "What is agar-agar," 2020. [Online]. Available: https://agargel.com.br/en/agar-agar/.

[258] M. M. Perez-Madrigal, J. Torras, J. Casanovas, M. Häring, C. Aleman, and D. D. Diaz, "Paradigm Shift for Preparing Versatile M 2+ -Free Gels from Unmodified Sodium Alginate," *Biomacromolecules*, vol. 18, pp. 2967–2979, 2017.

[259] C. Riedo, F. Caldera, T. Poli, and O. Chiantore, "Poly(vinylalcohol)-borate hydrogels with improved features for the cleaning of cultural heritage surfaces," *Herit. Sci.*, vol. 3, no. 23, pp. 1–11, 2015.

[260] C. Karakasyan *et al.*, "Cold gelation of alginates induced by monovalent cations," *Biomacromolecules*, vol. 11, no. 11, pp. 2966–2975, 2010.

[261] "Norme ISO 13927. Plastic-simple heat release test using a conical radiant heater and a thermopile detector," 2014. [Online]. Available: https://www.iso.org/standard/52841.html.

[262] "Norme ISO 5660-1. Reaction-to-fire-tests-heat release, smoke production and mass loss rate," 2002. [Online]. Available: https://www.iso.org/obp/ui/#iso:std:iso:5660:-1:ed-2:v1:en.

[263] B. Schartel and T. R. Hull, "Development of fire-retarded materials — Interpretation of cone calorimeter data," no. May, pp. 327–354, 2007.

[264] S. E. Gustafsson and S. E. Gustafsson, "Transient plane source techniques for thermal conductivity and thermal diffusivity measurements of solid materials Transient diffusivity plane source techniques for thermal conductivity measurements of solid materials and thermal," *Rev. Sci. instrumentscientific instruments*, vol. 797, no. 1991, 2000.

[265] J. V. Beck, "Thermocouple Temperature Disturbances in Low Conductivity Materials," *J. Heat Transfer*, vol. 84, no. 2, pp. 124–131, 1962.

[266] W. D. Brewer, "Effect of thermocouple wire size and configuration on internal temperature measurements in a charring ablator," 1967.

[267] "What is Plastic Extrusion," 2018. [Online]. Available:

© 2020 Tous droits réservés.
lilliad.univ-lille.fr

Thèse de Laura Geoffroy, Université de Lille, 2020

https://cnzhmachinery.com/blog/what-is-plastic-extrusion/.

[268] “Blow Molding.” [Online]. Available: https://www.custompartnet.com/wu/blow-molding.

[269] “The rotational Moulding process.” [Online]. Available: https://www.excalibur-rm.co.uk/RotationalMouldingProcess.aspx.

[270] E. G. Gordeev, A. S. Galushko, and V. P. Ananikov, “Improvement of quality of 3D printed objects by elimination of microscopic structural defects in fused deposition modeling,” *journal.pone*, 2018.

[271] Y. Li *et al.*, “Effect of Expandable Graphite Particle Size on the Flame Retardant , Mechanical , and Thermal Properties of Water-Blown Semi-Rigid Polyurethane Foam,” *J. Appl. Polym. Sci.*, 2013.

[272] J. Li, X. Mo, Y. Li, H. Zou, and M. Liang, “Influence of expandable graphite particle size between expandable graphite and ammonium,” *Polym. Bull.*, pp. 5287–5304, 2018.

[273] J. S. Reid *et al.*, “Stefan ’ s measurement of the thermal conductivity of air,” *Eur. J. Phys.*, vol. 5, 1984.

[274] M. M. Hirschler, “Flame retardants: Background and effectiveness,” *Fire protection engineering*, 2014. [Online]. Available: https://www.sfpe.org/page/2014_Q3_3.

© 2020 Tous droits réservés.

lilliad.univ-lille.fr

Thèse de Laura Geoffroy, Université de Lille, 2020

List of Figures

Figure 1. Scientific approach and strategies. 3
Figure 2. Illustration of thermal decomposition and combustion of flammable materials. 5
Figure 3. Active and passive fireproofing solutions. 6
Figure 4. Design of flame retardant material. 11
Figure 5. Polymer processing. 15
Figure 6. Classification of standard polymer processing. 16
Figure 7. Steps of 3D printing process. 18
Figure 8. Illustration of vat photo-polymerization 3D printing techniques: a) Stereolithography (SLA), b) Digital Light Processing (DLP), c) Continuous Liquid Interface Production (CLIP), d) Two Photon Polymerization (TPP). 20
Figure 9. Illustration of powder bed 3D printing techniques: a) Selective Lase Sintering (SLS), b) Electron Beam melting (EBM). 22
Figure 10. Illustration of material extrusion 3D printing techniques: a) Fused Deposition Modelling (FDM), b) Fused pellets polymer deposition. 23
Figure 11. Illustration of lamination 3D printing techniques: a) Laminated Object Manufacturing (LOM), b) Selective Deposition Lamination (SDL) [96]. 24
Figure 12. Illustration of material jetting 3D printing techniques a) Drop On Demand, and b) Binder Jetting. 24
Figure 13. Illustration of the number of papers and patents on “3D printing” and “3D printing fire” according to web of science databased accessed April 13th 2020. 27
Figure 14. Illustration of a) printing parameters and b) raster angle (b_1) 0°, b_2) 90°, b_3) 45°). 28
Figure 15. Illustration of different printing directions (a) horizontal, b) vertical, c) perpendicular). 33
Figure 16. Concepts of flame-retardant designs printed using additive manufacturing (a) Design combining various flame-retardants, b) Design concentrating flame-retardants, c) Sandwich design inspired from honeycomb structure). 37
Figure 17. Top section observation using optical microscopy (x20) before MLCC test (a_1) 3D-EVA/EG (10 wt.-%)-0% air, a_2) 3D-EVA/EG (10 wt.-%)-50%, a_3) 3D-EVA/EG (10 wt.-%)-70% air, b_1) 3D-EVA/ATH (30 wt.-%)-0% air, b_2) 3D-EVA/ATH (30 wt.-%)-50% air, b_3) 3D-

© 2020 Tous droits réservés.
lilliad.univ-lille.fr

Thèse de Laura Geoffroy, Université de Lille, 2020

EVA/ATH (30 wt.-%)-70% air, c_1) 3D-EVA/ATH (65 wt.-%)-0%air, c_2) 3D-EVA/ATH (65 wt.-%)-50%air, c_3) 3D-EVA/ATH (65 wt.-%)-70% air). 40

Figure 18. Cross section observations using optical microscopy (x50) before MLCC test (a_1) 3D-EVA/EG (10 wt.-%)-0% air, a_2) 3D-EVA/EG (10 wt.-%)-50%, a_3) 3D-EVA/EG (10 wt.-%)-70% air, b_1) 3D-EVA/ATH (30 wt.-%)-0% air, b_2) 3D-EVA/ATH (30 wt.-%)-50% air, b_3) 3D-EVA/ATH (30 wt.-%)-70% air, c_1) 3D-EVA/ATH (65 wt.-%)-0% air, c_2) 3D-EVA/ATH (65 wt.-%)-50% air, c_3) 3D-EVA/ATH (65 wt.-%)-70% air). 41

Figure 19. Compacity difference and influence in heat propagation for system (a) 3D-EVA/EG (10 wt.-%)-70% air, b) 3D-EVA/EG (10 wt.-%)-0% air). 43

Figure 20. Influence of the design and the amount of empty cells on fire behavior (a) 3D-EVA/EG (10 wt.-%), b) 3D-EVA/ATH (30 wt.-%), c) 3D-EVA/ATH (65 wt.-%)). 45

Figure 21. Residue after fire testing (a_1) 3D-EVA/EG (10 wt.-%)-0% air, a_2) 3D-EVA/EG (10 wt.-%)-50% air, a_3) 3D-EVA/EG (10 wt.-%)-70% air, b_1) 3D-EVA/ATH (30 wt.-%)-0% air, b_2) 3D-EVA/ATH (30 wt.-%)-50% air, b_3) 3D-EVA/ATH (30 wt.-%)-70% air, c_1) 3D-EVA/ATH (65 wt.-%)-0% air, c_2) 3D-EVA/ATH (65 wt.-%)-50% air, c_3) 3D-EVA/ATH (65 wt.-%)-70% air). 46

Figure 22. Comparison of the fire behavior of biphasic sandwich multi-materials. 49

Figure 23. Evolution of temperature vs time for each biphasic sandwich multi-material studied. 50

Figure 24. Residues after fire testing (a) 3D-EVA/ATH (30 wt.-%)-70% air, b) 3D-EVA/ATH (30 wt.-%)-70% water, c) 3D-EVA/ATH (30 wt.-%)-70% $K_2CO_{3\ solid}$, d) 3D-EVA/ATH (30 wt.-%)-70% $K_2CO_{3\ sat.-liquid}$). 52

Figure 25. Flame aspect after almost 40s MLCC test (a) 3D-EVA/ATH (30 wt.-%), b) 3D-EVA/ATH (30 wt.-%)-70%-$K_2CO_{3\ solid}$, c) 3D-EVA/ATH (30 wt.-%)-70% $K_2CO_{3\ sat.-liquid}$). 53

Figure 26. Soot particles EDS spectra of: a) 3D-EVA/ATH (30 wt.-%)-70% air, b) 3D-EVA/ATH (30 wt.-%)-70% water, c) 3D-EVA/ATH (30 wt.-%)-70% $K_2CO_{3\ solid}$, d) 3D-EVA/ATH (30 wt.-%)-70% $K_2CO_{3\ sat.-liquid,}$ e) Mirror polished stainless steel. 54

Figure 27. Amount of gas release during MLCC test for each sample studied (a) for CO, b) for CO_2, c) for H_2O). 55

Figure 28. Residue EDS spectra of: a) 3D-EVA/ATH (30 wt.-%)-70% air, b) 3D-EVA/ATH (30 wt.-%)-70% water, c) 3D-EVA/ATH (30 wt.-%)-70% $K_2CO_{3\ solid}$, d) 3D-EVA/ATH (30 wt.-%)-70% $K_2CO_{3\ sat.-liquid}$. 56

© 2020 Tous droits réservés.

lilliad.univ-lille.fr

Figure 29. EDS mapping of K after MLCC test in residue of: a) 3D-EVA/ATH (30 wt.-%)-70% air, b) 3D-EVA/ATH (30 wt.-%)-70% water, c) 3D-EVA/ATH (30 wt.-%)-70% K_2CO_3 solid, d) 3D-EVA/ATH (30 wt.-%)-70% K_2CO_3 sat.-liquid. 57
Figure 30. XDR spectra comparison between 3D-EVA/ATH (30 wt.-%)-70% K_2CO_3 solid residue and 3D-EVA/ATH (30 wt.-%)-70% K_2CO_3 sat.-liquid residue. 58
Figure 31. XDR spectrum of 3D-EVA/ATH (30 wt.-%)-70% K_2CO_3 solid residue. 58
Figure 32. XDR spectrum of 3D-EVA/ATH (30 wt.-%)-70% K_2CO_3 sat.-liquid residue. 59
Figure 33. Illustration of fire behavior mechanism for 3D printed plate with 30%polymer (70% voids inside materials) for a) 3D-EVA/ATH (30 wt.-%), b) 3D-EVA/ATH (65 wt.-%), c) 3D-EVA/EG (10 wt.-%). 60
Figure 34. Illustration of fire behavior mechanism of new biphasic sandwich multi-materials (a) 3D-EVA/ATH (30 wt.-%)-70% air, b) 3D-EVA/ATH (30 wt.-%)-70% water, c) 3D-EVA/ATH (30 wt.-%)-70% K_2CO_3 powdered, d) 3D-EVA/ATH (30 wt.-%)-70% K_2CO_3 liquid). 61
Figure 35. Concepts of sandwich flame retardant 3D printed multi-materials filled with hydrogel. 65
Figure 36. 3D printing process and design elaboration. 66
Figure 37. VMT particles dispersion using confocal microscopy (a) Liquid A+VMT, b) Hydrogel A+VMT+K_2CO_3, c) Hydrogel B+VMT, d) Hydrogel C+VMT). 69
Figure 38. Fire behavior of each system studied (a) for systems with hydrogel A, b) for systems with hydrogel B, c) for systems with hydrogel C, d) evolution of temperature versus time for all systems studied. 72
Figure 39. Fire protection performances values of each system studied. 72
Figure 40. Top and cross-section pictures of residue after MLCC test (a) 3D-air, b) 3D-H A, c) 3D-H A+VMT, d) 3D-H A+VMT+K_2CO_3, e) 3D-H B, f) 3D-H B+VMT, g) 3D-H C, h) 3D-H C+VMT). 74
Figure 41. X-rays mappings of (a_1) Al element of 3D-air, a_2) Al element of 3D-H A, a_3) Al element of 3D-H A+VMT, b) Fe element of 3D-H A+VMT, c) Mg element of 3D-H A+VMT, d) K element of 3D-H A+VMT) cross-sections, using EPMA measurements. 76
Figure 42. X-rays mappings of (a_1) Al element of 3D-air, a_2) Al element of 3D-H B, a_3) Al element of 3D-H B+VMT, b) Fe element of 3D-H B+VMT, c) Mg element of 3D-H B+VMT, d) K element of 3D-H B+VMT) cross-sections, using EPMA measurements. 76
Figure 43. X-rays mappings of (a_1) Al element of 3D-air, a_2) Al element of 3D-H C, a_3) Al element of 3D-H C+VMT, b) Fe element of 3D-H C+VMT, c) Mg element of 3D-H C+VMT, d) K element of 3D-H C+VMT) cross-sections, using EPMA measurements. 77

© 2020 Tous droits réservés.
lilliad.univ-lille.fr

Thèse de Laura Geoffroy, Université de Lille, 2020

Figure 44. XRD of residues: 3D-H A+VMT, 3D-H B+VMT, and 3D-H C+VMT. 78
Figure 45. High Temperature X-ray Diffraction of VMT. 79
Figure 46. Visual observation of flame color (a) for 3D-H A+VMT, b) 3D-H A+VMT+K_2CO_3). 80
Figure 47. XRD of residue 3D-H A+VMT+K_2CO_3. 81
Figure 48. Cross-section X ray mapping in a) Al element, b) Fe element, c) Mg element, d) K element, using EPMA measurements of (1) 3D-air, 2) 3D-H A+VMT+K_2CO_3). 81
Figure 49. Illustration of fire behavior mechanism of new hydrogel sandwich multi-materials (a) 3D-H B, b) 3D-H B+VMT, c) 3D-H C, d) 3D-H C+VMT). 84
Figure 50. Illustration of fire behavior mechanism of new hydrogel sandwich multi-materials (a) 3D-H A, b) 3D-H A+VMT, c) 3D-H A+VMT+K_2CO_3). 85
Figure 51. Concept of low emissivity hydrogel sandwich flame retardant design using additive manufacturing. 88
Figure 52. Description of (a) air, b) hydrogel) sandwich multi-materials elaboration. 89
Figure 53. Top section pictures of each sandwich multi-material studied (a) 3D-air, b) IR-3D-air, c) 3D-H B+VMT, d) IR-3D-H B+VMT). 90
Figure 54. Cross-section X-rays mapping of (a) O element, b) Al element, c) Si element) or the low emissivity coating deposed on a glass slide using SEM-EDS analysis. 91
Figure 55. Fire behavior of each material studied (a) Heat release rate versus time, b) Temperature rise versus time). 93
Figure 56. Top residue surface pictures of each material studied (a) 3D-air, b) IR-3D-air, c) 3D-H B+VMT, d) IR-3D-H B+VMT). 94
Figure 57. Illustration of fire behavior mechanism of each sandwich multi-material studied (a) 3D-air, b) IR-3D-air, c) 3D-H B+VMT, d) IR-3D-H B+VMT). 95
Figure 58. Other 3D printed design thinking: Fractal design. 98
Figure 59. Design of fire protective barrier. 99
Figure 60. Some passive fireproofing solutions. 102
Figure 61. Illustration of an intumescent material behavior against fire exposure. 103
Figure 62. Residue obtained after fire testing (a) for acrylic-based intumescent coating, b) for epoxy-based intumescent coating, c) for silicon-based intumescent coating). 105
Figure 63. Number of scientific papers and patents from 1970 to 2019 related to the term “intumescent” and “intumescent coating” (based on the SciFinder database). 106
Figure 64. Illustration of Fiber Metal Laminate (FML). 107
Figure 65. Fire behavior of Polymer Metal Laminate. 108

© 2020 Tous droits réservés.

lilliad.univ-lille.fr

Figure 66. Number of scientific papers and patents from 1970 to 2019 related to the therm "composite and Polymer Metal Laminate" (based on the SciFinder databased). 108
Figure 67. Illustration of different types of design elaborated. 109
Figure 68. Illustration of (a) intumescent coatings, (b) polymer metal laminate (PML), and (c) intumescent polymer metal laminate (IPML) systems. 110
Figure 69. Illustration of studied samples. 111
Figure 70. Cross section pictures obtained by microscopic analyses of (a) IPML A, (b) IPML-B, and (c) IPML-C, before burn-through test. 112
Figure 71. Evolution of temperature versus time for each system ((a) Temperature vs. time for A system, (b) Temperature vs. time for B system, (c) Temperature vs. time for C system). 114
Figure 72. Slope comparison of thermal profile curve at the beginning of burn-through test. 115
Figure 73. Cross-section of IPML after 15 min burn-through test exposition ((a) S-IPML-A before fire test, (b) S-IPML-B before fire test, (c) S-IPML-C before fire test, (d) S-IPML-A after 15 min fire test, (e) S-IPML-B after 15 fire test, and (f) S-IPML-C after 15 min fire test). 116
Figure 74. Expansion versus time curves for S-A, S-B, S-IPML-A and S-IPML-B systems. 117
Figure 75. Thermal gradient evolution in S-IPML-A and S-IPML-B. 119
Figure 76. Carbonization gradient evolution in S-IPML-A and B, compared to S-A and S-B chars (Layer 10 is the top layer (directly exposed to fire) for S-IPML-A and S-IPML-B). .. 119
Figure 77. TG curves for each char layer of S-IPML-A and for S-A char layer, obtained after 15 min burn-through test exposure. 121
Figure 78. TG curves for each char layer of S-IPML-B and for S-B char layer, obtained after 15 min burn-through test. 121
Figure 79. Evolution of carbonization gradient depending on the IPML layer number. 122
Figure 80. Illustration of the thermal behavior when ((a) intumescent coating, (b) PML, and (c) IPML) are exposed to a high heat flux fire test. 124
Figure 81. Development of Intumescent Bilayer Polymer Metal Laminate materials. 127
Figure 82. Intumescent bilayer metal laminate: Samples studied. 128
Figure 83. Optical microscopy observation in cross-section of the studied samples. 129
Figure 84. Fire protection performance comparison of each system studied (a) for the standard overlay without aluminum foils, b) for the overlay A (steel side) and B (A side), c) for the overlay B (steel side) and A (B side), d) for the two best systems). 131

© 2020 Tous droits réservés.
lilliad.univ-lille.fr

Thèse de Laura Geoffroy, Université de Lille, 2020

Figure 85. Comparison of coating B expansion between a) S-B+AlA and b) S-A+AlB..... 132
Figure 86. Expansion evolution versus time for each sample studied. 135
Figure 87. Fire tests stopped at different exposure times for the systems (a) S-A+B, b) S-A, c) S-B). 136
Figure 88. Fire tests stopped at different exposure times for the designs (a) S-AlA+AlB, b) S-A+AlB, c) S-AlA+B). 137
Figure 89. Mechanism of protection during the fire test for a) S-AlA+AlB, b) S-A+AlB, c) S-AlA+B, d) S-A+B. 138
Figure 90. Observation of the wavy shape of coating A after 2 min fire testing. 139
Figure 91. Optimization of the concept by changing metal foils or substrate..... 142
Figure 92. Cross section optical microscopy analysis before fire testing of Composite-AlA+AlB. 143
Figure 93. Fire behavior of S-AlA+AlB and of systems deposited on composite substrate. 145
Figure 94. Residues aspect after 30 min fire exposure for a) Composite, b) S-AlA+AlB, c) Composite-A, d) Composite-B, e) Composite-AlA+AlB. 148
Figure 95. Illustration of perspectives which could be considered. 152
Figure 96. Example of the development of a multi-fireproofing concept. 156
Figure 97. Illustration of Material, methods and characterizations. 159
Figure 98. Extrusion process. 163
Figure 99. Thermocompression process. 164
Figure 100. 3D printing process. 165
Figure 101. Hydrogel sandwich multi-materials elaboration (a) 3D-H A or 3D-H A+VMT, b) 3D-H A+VMT+K_2CO_3, c) 3D-H B or 3D-H B+VMT, d) 3D-H C or 3D-H C+VMT)..... 169
Figure 102. Fire testing: Mass Loss Cone calorimeter test. 171
Figure 103. IPML elaboration process. 177
Figure 104. Elaboration process of intumescent bilayer metal laminate..... 178
Figure 105. Burn-through test bench illustration [244] (a) Flame calibration, (b) Switch between calibration to sample: fire testing. 179
Figure 106. Illustration of thermal gradient measurement in IPML. 181
Figure 107. Description of pull-off test 182

Figure A1- 1. Illustration of polymer extrusion process [267]..... 183
Figure A1- 2. Illustration of injection molding process [75]. 184
Figure A1- 3. Illustration of blow molding process [268]. 185

© 2020 Tous droits réservés.

lilliad.univ-lille.fr

Figure A1- 4. Illustration of a) thermoforming under vacuum and b) thermocompression processes. 186
Figure A1- 5. Illustration of rotational molding process [269]. 187

Figure A2- 1. Illustration of a) thermocompression vs b) 3D printing by fused polymer deposition. 189
Figure A2- 2. Surface observations of thermocompressed and 3D printed samples using optical microscopy x20 (a) T-EVA, b) 3D-EVA, c) T-EVA/ATH (30 wt.-%), d) 3D-EVA/ATH (30 wt.-%), e) T-EVA/ATH (65 wt.-%), f) 3D-EVA/ATH (65 wt.-%), g) T-EVA/EG (10 wt.-%), h) 3D-EVA/EG (10 wt.-%)). 191
Figure A2- 3. Cross-section observations of thermocompressed and 3D printed samples using optical microscopy x50 (a) T-EVA, b) 3D-EVA, c) T-EVA/ATH (30 wt.-%), d) 3D-EVA/ATH (30 wt.-%), e) T-EVA/ATH (65 wt.-%), f) 3D-EVA/ATH (65 wt.-%), g) T-EVA/EG (10 wt.-%), h) 3D-EVA/EG (10 wt.-%)). 193
Figure A2- 4. Cross-section X-ray mapping in Al element using EPMA measurements of (a) T-EVA/ATH (30 wt.-%), b) 3D-EVA/ATH (30 wt.-%), c) T-EVA/ATH (65 wt.-%), d) 3D-EVA/ATH (65 wt.-%). 193
Figure A2- 5. Cross-section X-ray mapping in S element using EPMA measurements of (a) T-EVA/EG (10 wt.-%), b) 3D-EVA/EG (10 wt.-%)). 194
Figure A2- 6. Fire behavior comparison between thermocompression and 3D printing process (a) EVA, b) EVA/ATH (30 wt.-%), EVA/ATH (65 wt.-%), d) EVA/EG (10 wt.-%)). 195
Figure A2- 7. Visual aspect of residues after MLCC test for (a) EVA, b) EVA/ATH (30 wt.-%), c) EVA/ATH (65 wt.-%), and d) EVA/EG (10 wt.-%)). 196
Figure A2- 8. Illustration of the 3D printed polymer matrices thermal behavior (a) EVA, b) EVA/ATH, c) EVA/EG (10 wt.-%)). 198
Figure A2- 9. Illustration of EVA/EG (10 wt.-%) thermal behavior (a) Thermocompressed plates, b) 3D printed plates). 199

Figure A2- A 1. EPMA cross-section observations (a)T-EVA, b) 3D-EVA, c) T-EVA/EG (10%), d) 3D-EVA/EG (10%)). 200
Figure A2- A 2. EPMA cross-section observation (a) T-EVA/ATH (30%), b) 3D-EVA/ATH (30%), c) T-EVA/ATH (65%), d) 3D-EVA/ATH (65%)). 200

© 2020 Tous droits réservés.
lilliad.univ-lille.fr

Thèse de Laura Geoffroy, Université de Lille, 2020

Figure A3- 1. Cross-section of (a) 3D-air, b) 3D-H A and c) 3D-H A+VMT), using SEM observation. 201
Figure A3- 2. Cross-section of (a) 3D-air, b) 3D-H B and c) 3D-H B+VMT), using SEM observation. 202
Figure A3- 3. Cross-section of (a) 3D-air, b) 3D-H C and c) 3D-H C+VMT), using SEM observation. 202
Figure A3- 4. XRD of (a) VMT, b) residue 3D-H A+VMT, c) residue 3D-H B+VMT, d) residue 3D-H C+VMT). 203
Figure A3- 5. XRD of residue 3D-$K_2CO_{3\ sat.-liquid}$. 203
Figure A3- 6. Cross-section of (a) 3D-air, b) 3D-H A+VMT+K_2CO_3), using SEM observation. 204

Figure A4- 1. SEM pictures comparing S-A char to S-IPML-A chars (taken from layers 10 to 6). 205
Figure A4- 2. SEM pictures comparing S-B char to S-IPML-B chars (taken from layers 10 to 6). 205

Figure A5- 1. Illustration of samples studied. 206
Figure A5- 2. Optical microscopy before fire testing of a) S-AlA+AlB, b) S-CuA-CuB, c) S-MiA+MiB. 207
Figure A5- 3. Fire behavior of system with other interlayer materials. 207

Figure A6- 1. TGA of composite under air and N_2. 208

© 2020 Tous droits réservés.

lilliad.univ-lille.fr

List of Tables

Table 1. Examples of fire resistant passive fire protections. 8
Table 2. Examples of fire reaction passive fire protections. 9
Table 3. Polymer processing comparison [91], [92]..... 17
Table 4. 3D printing techniques [95]. 19
Table 5. Advantages and disadvantages of vat photo-polymerization 3D printing techniques. 25
Table 6. Examples of flame-retardant 3D printed materials developed. 31
Table 7. Name and description of samples prepared. 39
Table 8. Quantitative characterization of each sample studied. 42
Table 9. Fire performance values of each design studied for the different formulations. 45
Table 10. Mass loss comparison between different design studied for each material (3D-EVA/EG (10 wt.-%), 3D-EVA/ATH (30 wt.-%), 3D-EVA/ATH (65 wt.-%)). 47
Table 11. Quantitative values of each biphasic sandwich multi-material studied. 48
Table 12. Fire protection performances values of each system studied. 49
Table 13. Rate of change of temperature for each sample studied. 51
Table 14. Mass loss comparison between each sample studied. 52
Table 15. Name and description of samples prepared. 67
Table 16. Composition of sandwich multi-materials. 68
Table 17. Description and composition of materials studied. 89
Table 18. Quantitative values of each sandwich multi-material studied. 90
Table 19. Fire protection performances values of each material studied. 93
Table 20. Examples of carbonization agent, acid source, blowing agent and catalyst used in intumescent material. 104
Table 21. Monolayer of intumescent coating and IPML characterization. 111
Table 22. Temperature reached after 2, 10, and 15 min burning, for each sample studied... 113
Table 23. Organic residue of S-IPML-A and S-IPML-B for each layer. 120
Table 24. Quantitative characterization of each sample studied. 129
Table 25. Rates of change of temperature according to different times, and temperatures reach after 30 min fire exposure. 134
Table 26. Name and composition of sample studied. 142
Table 27. Quantitative characterization of all samples studied before fire testing. 144

© 2020 Tous droits réservés.
lilliad.univ-lille.fr

Thèse de Laura Geoffroy, Université de Lille, 2020

Table 28. Rate of temperature and temperature reached during fire test for each sample studied. 146
Table 29. Mass loss and expansion after 30 min fire exposure for each sample studied. 149
Table 30. Materials' formulation. 163
Table 31. Printing parameters. 166
Table 32. Intumescent coatings characteristics. 176
Table 33. The steps of the process according to the intumescent bilayer metal laminate samples. 179

Table A2- 1. Name and composition of samples. 189
Table A2- 2. Thermocompression vs 3D printing: samples comparison before fire test. 190
Table A2- 3. Comparison of MLCC results between thermocompression and 3D printing depending on the polymer materials' studied. 196
Table A2- 4. Comparison of residual mass after MLCC test for thermocompressed and 3D printed plates. 197

Table A3- 1. Fire protection performances values of each system studied. 201

© 2020 Tous droits réservés.

lilliad.univ-lille.fr

Abstract

Design of new fire protective multi-materials

KEYWORDS: Design, Multi-materials, Flame retardancy, Fire resistance, Additive manufacturing, Polymer metal laminate.

Fire can cause severe material damage as well as human casualties. The development of new fire protective systems is thus of prime importance. In order to conceive new and more efficient systems, an innovative scientific approach has been considered within this PhD work. It consists in combining various concepts and materials while changing their design rather than their chemistry to achieve superior fire protection. In this way, two novel fireproofing multi-materials were developed and aimed on the one hand to limit the reaction to fire, and on the other hand to increase the fire resistance of a substrate. In the first part, additive manufacturing was selected as a process of choice for designing a material with a low reaction to fire. An original bio-inspired sandwich design (honeycomb-like structure) was elaborated, 3D printed and optimized by the combination of numerous concepts (oxygen inhibitor system, physical barrier, low emissivity coating). Thanks to this association of design and concepts, the multi-material exposed to an external radiant heat flux of 50 kW/m^2 based on the ISO 13927 standard of the mass loss cone calorimeter has shown a very low reaction to fire with a fast flame extinguishment and an extremely low total rate of heat release rate (less than 10 kW/m^2) evidencing its outstanding efficiency. In a second part, a system acting as a fire barrier was developed to protect a substrate against a fire exposure of 116 kW/m^2 (burn-through fire testing mimicking the aeronautical standard ISO2685). Intumescence and delamination phenomena were combined within the same design to elaborate this barrier. This new and optimized assembly dramatically reduces heat propagation and protects the substrate, its backside temperature remaining below 250°C after more than 15 minutes of fire exposure. The effectiveness of this fire barrier was finally tested on other substrates to extend its use. This study proves that modifying the design of various materials can be a promising way to design new and very effective fire protective systems.

Nouveaux multi-matériaux de protection contre le feu

MOTS-CLES : Design, Multi-matériaux, Ignifugation, Résistance au feu, Fabrication additive, Stratifié polymère métal.

Le feu peut causer de graves dégâts matériels et humains. Par conséquent, il est important de mettre au point de nouvelles protections contre le feu. Pour concevoir de nouveaux systèmes toujours plus efficaces, une approche scientifique innovante a été envisagée au sein de cette thèse. Elle consiste à combiner différents concepts et matériaux, tout en jouant sur leur design plutôt que leur formulation pour atteindre de meilleures propriétés de protection thermique. Ainsi, deux nouveaux multi-matériaux de protection contre le feu ont été élaborés, visant dans un cas à limiter la réaction au feu, et dans l'autre cas à augmenter la résistance au feu d'un substrat. Dans une première partie, la fabrication additive s'est révélée être un procédé de choix pour concevoir le matériau ayant une faible réaction au feu. Un design à structure sandwich original inspiré du vivant (nid d'abeille) a été conçu, imprimé en 3D, et optimisé par la combinaison de nombreux concepts (système inhibiteur d'oxygène, barrière physique, revêtement basse émissivité). Grâce à cette association de design et concepts, le multi-matériau, exposé à un flux de chaleur radiatif externe de 50 kW/m^2 basé sur la norme ISO 13927 du cône calorimètre, a montré une très faible réaction au feu avec notamment une rapide extinction de flamme et un faible dégagement de chaleur total (inférieur à 10 kW/m^2), témoignant de son excellente efficacité. Dans une seconde partie, un système faisant office de barrière thermique a été développé afin de protéger un substrat face à une exposition au feu de 116 kW/m^2 (test « burn-through » représentatif du standard aéronautique ISO2685). Cette barrière, combinant les phénomènes d'intumescence et de délamination au sein d'un même design, a permis de réduire considérablement la propagation de la chaleur au sein du système. Le substrat a ainsi été protégé, avec une température en face arrière restant inférieure à 250°C après plus de 15 minutes d'exposition au feu. L'efficacité de ce système optimisé a ensuite été validée sur d'autres substrats. Cette étude prouve que la modification du design de divers matériaux constitue une voie prometteuse pour améliorer la performance des systèmes de protection contre le feu.

© 2020 Tous droits réservés.